PONTIFICIA UNIVERSIDAD CATÓLICA DE CHILE

FACULTAD DE QUÍMICA Y DE FARMACIA

DEPARTAMENTO DE QUÍMICA-FÍSICA

LABORATORIO DE QUÍMICA TEÓRICA COMPUTACIONAL (QTC)

ESTUDIO TEÓRICO DE CARBENOIDES METÁLICOS Y SUS REACCIONES DE INSERCIÓN EN ENLACES N-H Y O-H

ROCÍO BELÉN DURÁN GUAJARDO

Tesis

Directores:

Dra. Bárbara Herrera

Dr. Alejandro Toro Labbé

Comité de Tesis:

Dra. María Leonor Contreras

Dra. Angélica Fierro

Dr. Pablo Jaque

Dr. Jorge Martínez

PONTIFICIA UNIVERSIDAD CATÓLICA DE CHILE
FACULTAD DE QUÍMICA Y DE FARMACIA
DIRECCIÓN DE INVESTIGACIÓN Y POSTGRADO

ESTUDIO TEÓRICO DE CARBENOIDES METÁLICOS Y SUS REACCIONES DE INSERCIÓN EN ENLACES N-H Y O-H

Tesis presentada por:

ROCÍO BELÉN DURÁN GUAJARDO

Para optar al Grado Académico de Doctor en Química.

APROBADA POR:

Dra. MARÍA LEONOR CONTRERAS
Prof. Examinador .....

Dra. ANGÉLICA FIERRO
Prof. Examinador .....

Dr. PABLO JAQUE
Prof. Examinador .....

Dr. JORGE MARTÍNEZ
Prof. Director de Tesis .....

JULIO - 2020

Índice general

Índice de Figuras

Índice de Tablas

Lista de Acrónimos

- ASM: modelo de activación y distorsión, del inglés ASM, *Activation Strain Model*.
- BOX: bis(oxazolina).
- CIR: Coordenada Intrínseca de Reacción, del inglés IRC, *Intrinsic Reaction Coordinate*.
- DLPNO-CCSD(T): del inglés, *Domain-based Local Pair-Natural Orbital- Coupled Cluster Singles Doubles perturbatives triples*.
- EDA: análisis de descomposición de energía, del inglés EDA, *Energy Descomposition Analysis*.
- EDG: grupo dador de electrones, del inglés, *Electron Donating Group*.
- ELF: función de localización electrónica, del inglés, *Electron Localization Function*.
- ET: estado de transición, del inglés TS, *Transition State*.
- EWG: grupo atractor de electrones, del inglés, *Electron Withdrawing Group*.
- GGA: aproximación del gradiente generalizado, del inglés, *Generalized Gradient Approximation*.
- HOMO: del inglés, *Highest Occupied Molecule Orbital*.
- I: efecto inductivo, +I efecto inductivo dador, -I efecto inductivo receptor.
- I_σ: efecto inductivo mediante enlace σ.
- I_π: efecto inductivo mediante enlace π.

- LUMO: del inglés, *Lowest Unoccupied Molecular Orbital*.
- NAO: orbitales naturales atómicos, del inglés, *Natural Atomic Orbital*.
- NBO: orbitales naturales de enlace, del inglés, *Natural Bond Orbital*.
- NCI: índice de interacciones no covalentes, del inglés, *Non-Covalent Interaction*.
- NO: orbitales naturales, del inglés, *Natural Orbital*.
- P: producto.
- PC: complejo producto.
- R: reactante.
- RC: complejo reactante.
- SEP: Superficie de Energía Potencial, del inglés PES, *Potential Energy Surface*.
- SPE: Superficie de Potencial Electrostático, del inglés EPS, *Electrostatic Potential Surface*.
- SCRF: del inglés, *Self-Consistent Reaction Field*.
- SMD: modelo de solvatación basado en la densidad, del inglés, *Solvation Model based on Density*.
- TFD: Teoría de Funcionales de la Densidad, del inglés DFT, *Density Functional Theory*.
- X: heteroátomo.

Resumen

Debido a los desafíos que presenta la construcción de enlaces C-X (X: heteroátomo), especialmente en la síntesis de productos de interés industrial, se han propuesto estrategias a esta problemática como la reacción de inserción de carbenoides metálicos en enlaces X-H. En el presente trabajo de tesis, se estudió a nivel teórico, el mecanismo de reacción de inserción del carbenoide de cobre en enlaces X-H (X: N, O), ya que esta reacción proporciona procesos directos y eficientes hacia la formación de enlaces carbono-X y, además, corresponde a un método atractivo, ya que la activación X-H inducida por el metal no interactúa directamente con éste, sino más bien, con el carbono electrofílico del carbenoide. Los resultados indicaron que la reacción ocurre mediante el acercamiento posterior del sustrato (anilina/fenol) siguiendo un mecanismo concertado, el cual presenta tres pasos importantes: (i) proceso sin barrera de energía llevando a un complejo reactante inicial, (ii) transferencia protónica del sustrato al carbenoide, que genera la salida del complejo de cobre (paso elemental) y (iii) ruptura de interacciones no covalentes entre el producto de inserción y el complejo de cobre. La inserción en el enlace O-H es favorecida tanto desde el punto de vista cinético como termodinámico con respecto al enlace N-H, donde la enantioselectividad de la inserción está dada por el ligando PhBOX mediante repulsiones estéricas, favoreciendo la formación del enantiómero R como producto de inserción. Para el paso elemental de la reacción, se utilizaron los modelos de fuerza de reacción (F(ξ)) y de activación y distorsión (ASM), encontrándose que la energía de activa-

ción para ambas reacciones es dominada por repulsiones estéricas entre el ligando y el sustrato utilizado. La fuerza de reacción indica que una gran contribución de la barrera energética en N-H es producto de la mayor contribución de W_2, que impide el proceso de inserción. Adicionalmente, un estudio del efecto del sustituyente fue hecho para la reacción en el enlace O-H, modificando la estructura del carbenoide y del sustrato fenólico, de modo que, se favorece la cinética cuando se utilizan sustituyentes atractores de electrones en la posición orto o para al OH del fenol.

Capítulo 1

Introducción

La formación de enlaces C-X (X: N, O) corresponden a una transformación química importante dentro del área de síntesis orgánica, debido a que enlaces C-X son encontrados en la gran mayoría de los compuestos orgánicos y además, constituyen bloques fundamentales dentro del área de la química orgánica [1, 2]. Por lo que, el conocimiento sobre la construcción de enlaces C-X se hace fundamental, debido a la reactividad que estos enlaces pueden presentar.

Existen varias reacciones químicas que llevan a la formación de enlaces C-X [3–8]; sin embargo, muchas de ellas presentan un corto rango de selectividad o son reacciones que no proceden con el uso de grupos funcionales [9]. La gran mayoría de estas reacciones se llevan a cabo mediante mecanismos comunes, tales como: adición oxidativa/eliminación reductiva, metátesis de enlace σ o activación electrofílica; los que se caracterizan por la participación directa de un catalizador metálico en la reacción, donde la activación del enlace X-H se introduce directamente en la esfera de coordinación interna del metal, para posteriormente llevar a la formación de los enlaces C-X y C-H [9, 10].

La ruta más eficiente para llevar a cabo la formación de enlaces C-X sin experimentar reacciones secundarias o bajos rendimientos, corresponde al uso de catalizadores de metales de transición, utilizando diazocompuestos como ligandos [11–13], lo que resulta en la formación de una especie intermediaria denominada carbenoide, capaz de llevar a cabo un amplio rango de reacciones [2, 10]. Estos intermediarios formados a partir de la coordinación de un complejo metálico con un carbono divalente, son especies muy reactivas debido a su carácter dual, electrofílico y nucleofílico, que permite su participación en una amplia gama de transformaciones químicas [2], sirviendo de este modo, para ser aplicados en una amplia serie de reacciones no convencionales, y siendo ideales para iniciar reacciones en cascada llevando a la rápida generación de productos de alta complejidad estructural [14, 15].

Durante los últimos años, las reacciones de inserción de carbenoides en enlaces X-H han sido ampliamente estudiadas [16–20], ya que son identificadas como un método atractivo, donde el carbenoide es capaz de activar e insertarse en el enlace X-H, sin participación directa del metal, sino más bien, de la interacción con el carbono carbenoide (C*) (ver Figura 1.1) [21].

Estudios experimentales y computacionales previos [13, 21–25] han propuesto un mecanismo general para la inserción del carbenoide en el enlace X-H (ver Figura 1.2), el que incluye la formación de un carbenoide intermediario (c) mediante la descomposición de un diazocompuesto (b) y un catalizador metálico activo (a), para posteriormente llevar a cabo la inserción del carbenoide deficiente en electrones en el enlace X-H (d) y de esta manera, formar dos nuevos enlaces C*-X y C*-H (e). Sin embargo,

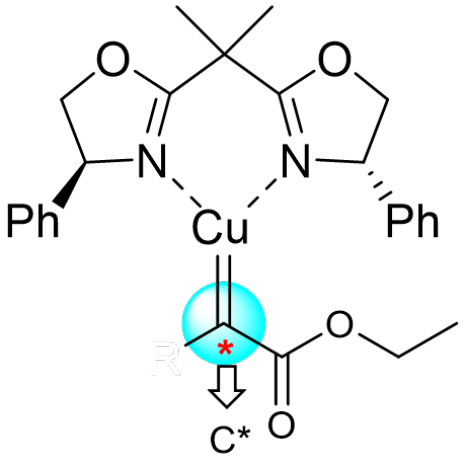

Figura 1.1: Estructura del complejo carbenoide de cobre, representando el carbono carbenoide (C*) mediante una esfera de color celeste.

en la actualidad aún sigue en debate, si el último paso de este mecanismo (Figura 1.2 en negrita) se lleva a cabo mediante un mecanismo concertado o en etapas. Es importante destacar este paso, ya que se propone en esta tesis caracterizar el mecanismo correspondiente al intermediario carbenoide ya formado, hasta la recuperación del catalizador metálico activo.

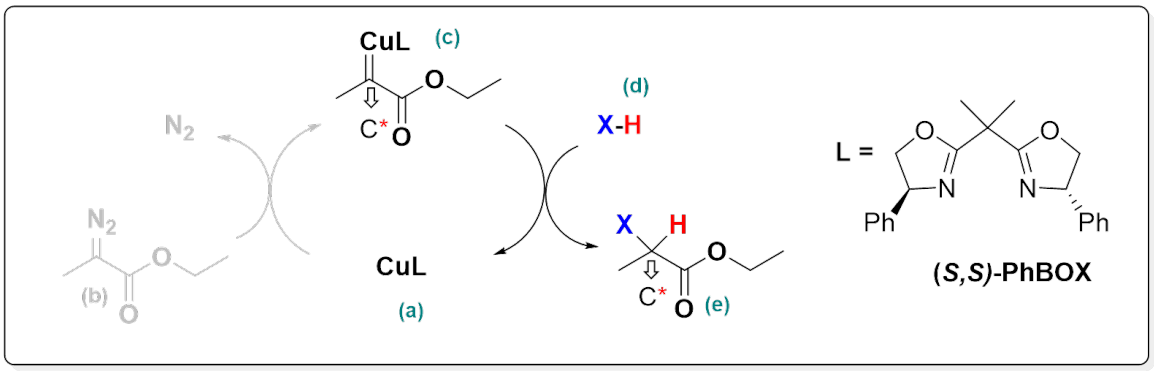

Figura 1.2: Mecanismo general propuesto para la inserción del carbenoide de cobre en el enlace X-H. Adaptado de la referencia 13.

En particular, en esta tesis nos centraremos en la inserción del carbenoide de naturaleza electrofílica en el enlace heteroátomo-hidrógeno (X-H). Es conocido que la reactividad electrofílica de los carbenoides es altamente dependiente de su estructura

[19, 21, 26], debido a los grupos sustituyentes al carbono del carbenoide (C*) y a la naturaleza del complejo metálico activo catalíticamente (ver Figura 1.3). Es por esto, que la caracterización de factores electrónicos y orbitalarios/estéricos corresponden a un objetivo importante en este trabajo de tesis.

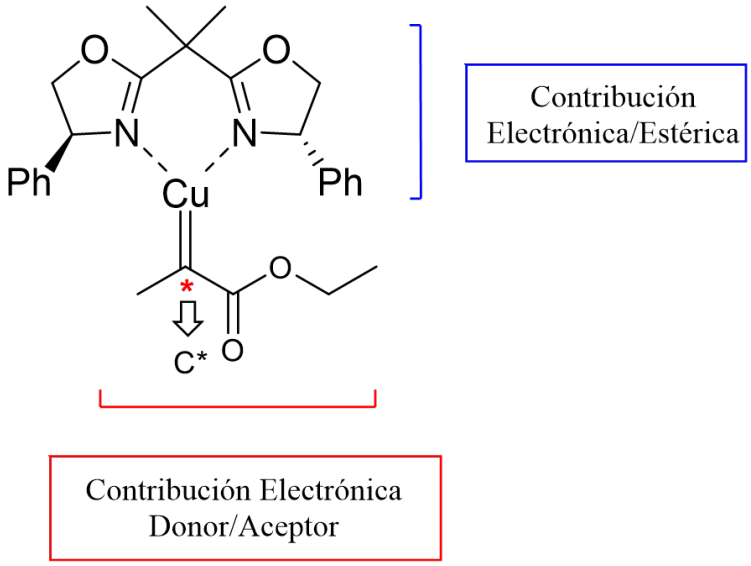

Figura 1.3: Estructura del carbenoide de cobre estudiado en este trabajo de tesis, representando la contribución electrónica por parte de los grupos donor/aceptor, y la contribución electrónica por parte del complejo metálico.

Dentro de este contexto, se estudiarán reacciones de inserción intermoleculares asimétricas (ver Figura 1.4), catalizadas mediante el complejo de cobre(I) tetracoordinado con un ligando bidentado de bis(oxazolina) ((S,S)-2,2-Bis(4-fenil-2-oxazolin-2-il) propano) y dos ligandos cloruro para completar la esfera de coordinación. En este caso, se utilizó la bis(oxazolina) (PhBOX) debido a que es conocido que induce la enantioselectividad y mejora el rendimiento de la reacción, llevando a procesos altamente eficientes [27, 28]. Como diazocompuesto, se utilizó α-diazoester construido mediante una combinación de sustituyentes tanto donor como aceptor de electrones (donor: CH_3 y aceptor: $C_3H_5O_2$). La elección de estos sustituyentes se sustenta en estudios experimentales [2, 19, 29] los cuales indican que la combinación donor/atractor con-

ducen a resultados altamente favorables en rendimiento y selectividad [30, 31].

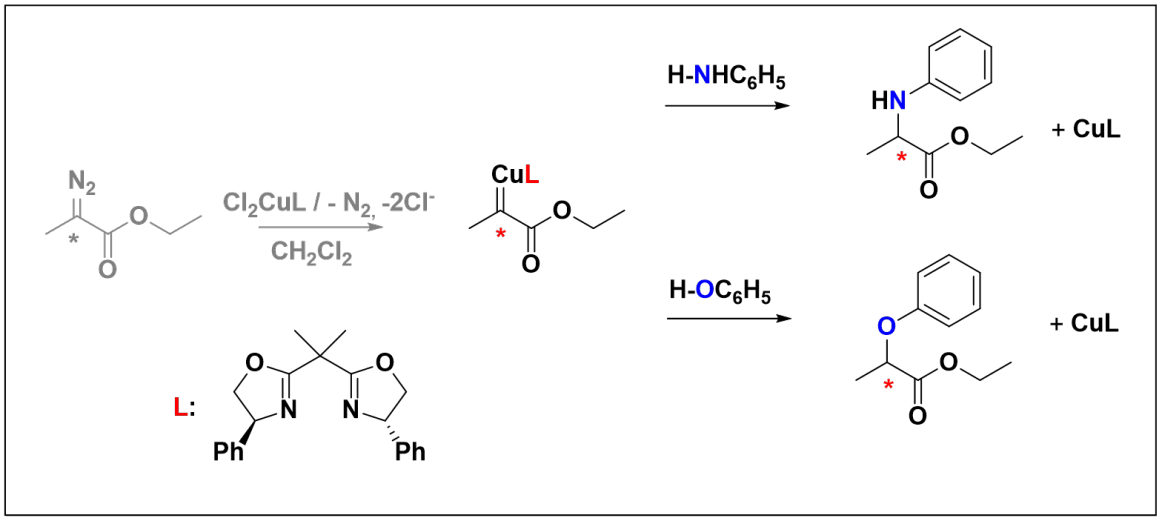

Figura 1.4: Reacción de inserción del carbenoide de cobre en enlaces N-H y O-H. La notación de * se utiliza para señalar al carbono carbenoide (C*).

Trabajos experimentales previos [32, 33] han señalado que la inserción del carbenoide de cobre con el ligando PhBOX en enlaces O-H llevan a resultados favorables, con alta enatioselectividad y rendimiento químico; sin embargo, estudios modificando el heteroátomo del enlace (X-H) y manteniendo la estructura del carbenoide, aún no han sido realizados. Por esta razón, este trabajo de tesis se centra principalmente en un estudio computacional del mecanismo de reacción de inserción enantioselectiva, mediante la Teoría de Funcionales de la Densidad (TFD). Presentando un estudio en detalle del mecanismo de reacción, a partir de un análisis energético, electrónico y de interacciones no covalentes. Proponemos dos mecanismos que pueden tomar lugar en la reacción: un mecanismo concertado (R1-XH) y uno en etapas (R2-XH) mostrados en la Figura 1.5. Ambos mecanismos serán analizados en detalle en el Capítulo 7.

Además, a partir de la fuerza de reacción (F(ξ)) y el modelo de activación y distorsión

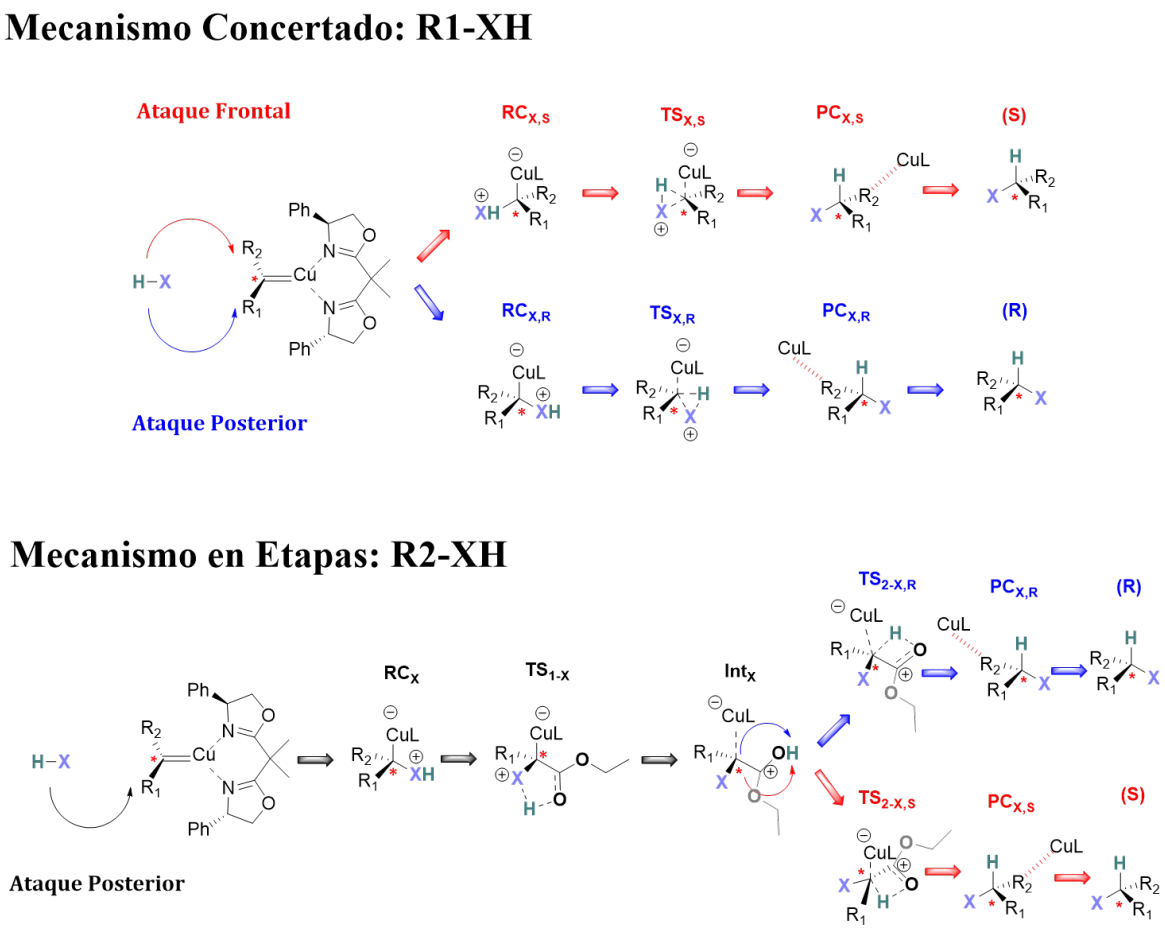

Figura 1.5: Mecanismos propuestos (R1-XH y R2-XH) para la reacción de inserción del carbenoide de Cu en los enlaces X-H (X:N,O). Utilizando como sustituyentes al carbenoide R_1: CH_3 y R_2: $C_3H_5O_2$.

(ASM) se caracterizará la naturaleza de la barrera de energía del paso determinante de cada mecanismo. En esta tesis se propone, estudiar el efecto que tiene el grupo funcional en la activación de enlaces O-H y N-H, y la eficiencia del carbenoide de cobre tanto desde un punto de vista energético como electrónico. Para ello, se utilizó como sustratos la anilina ($C_6H_5\mathbf{NH_2}$) y el fenol ($C_6H_5\mathbf{OH}$) para estudiar la reacción de inserción del carbenoide de cobre en los enlaces N-H y O-H, respectivamente. Es importante señalar que estas reacciones se estudiarán tanto en fase gas como en solvente diclorometano (CH_2Cl_2), este último es elegido debido a que resultados experimentales [2, 26] demuestran que el uso del solvente CH_2Cl_2 en reacciones de

inserción aumenta la velocidad y mejora el rendimiento de la reacción. Adicionalmente, estudios experimentales [2, 13, 19, 29] demuestran que los grupos sustituyentes juegan un rol clave tanto en la estabilidad, como en la naturaleza electrónica de las especies involucradas en la reacción de inserción, por lo que en esta tesis proponemos un estudio energético del efecto del sustituyente tanto el carbenoide como en el sustrato fenólico, con la finalidad de mejorar el proceso de inserción del carbenoide de cobre en el enlace O-H.

Capítulo 2

Base Teórica

2.1. Superficie de Energía Potencial y Perfil de Energía

Para realizar un estudio cinético y termodinámico de una reacción química, es necesario caracterizar reactantes (R), estados de transición (ET) y productos (P), explorando una superficie de energía potencial.

La superficie de energía potencial (SEP) (ver Figura 2.1) describe la manera como la energía de un sistema molecular cambia según las variaciones en la distribución espacial de los átomos. Se construye considerando los 3M-6 grados de libertad para moléculas no lineales y 3M-5 para aquellas lineales, donde M es el número de átomos. Su obtención es posible gracias a la aplicación de la aproximación de Born-Oppenheimer [34], que permite desacoplar el movimiento nuclear del electrónico. Debido a su complejidad y al elevado costo computacional que demanda su obtención, el estudio de una reacción química puede ser reducido al análisis del camino de mínima energía que conecta a reactantes y productos pasando por un estado de transición.

Tanto reactantes y productos son mínimos en la superficie, mientras que el estado de transición se identifica como un punto de silla o un máximo local energéticamente inestable en la dirección en que la reacción transcurre [35].

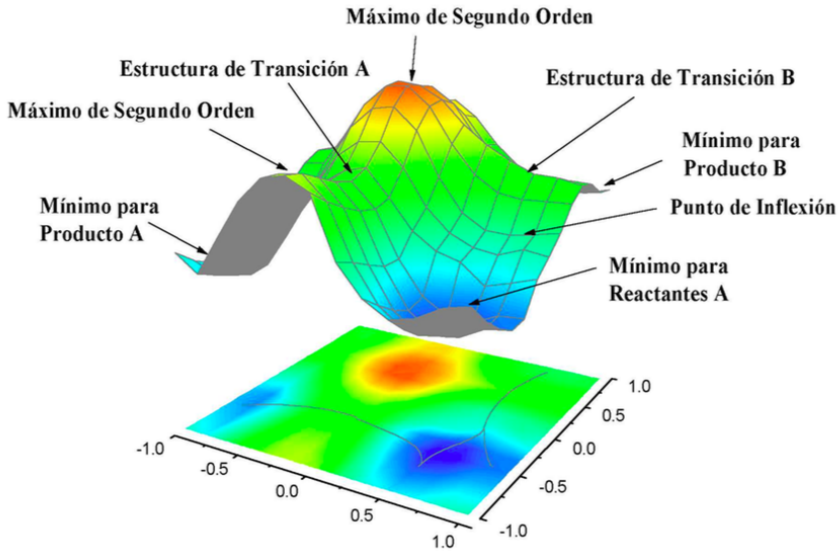

Figura 2.1: Esquema de superficie de energía potencial (SEP).

Este camino de mínima energía puede ser calculado a través del método de la coordenada intrínseca de reacción (CIR) [36, 37] condensando los cambios multidimensionales en el parámetro de coordenada de reacción (ξ). De esta forma, la energía potencial pasa a ser una función sólo dependiente de la CIR. El perfil de energía ($E(\xi)$) puede ser determinado y con esto la energía de reacción ΔE° y la energía de activación ($\Delta E^{\neq}$) (ver Figura 2.2).

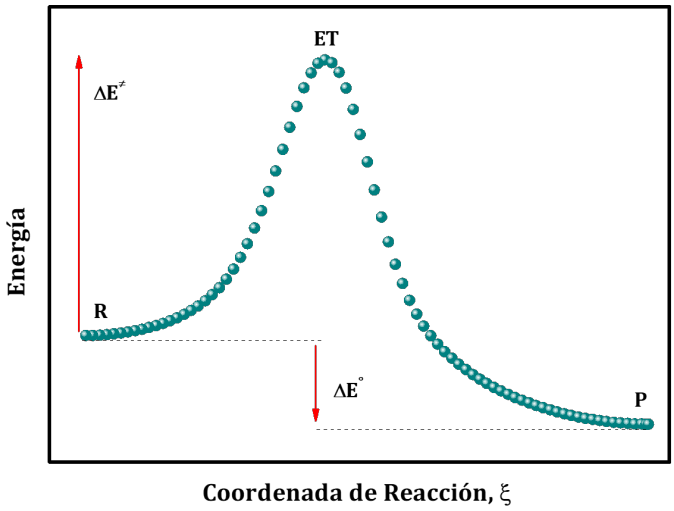

Figura 2.2: Perfil energético para paso elemental a lo largo de la coordenada intrínseca de reacción (ξ).

2.2. Fuerza de Reacción, $F(\xi)$

El análisis del perfil de energía entrega información termodinámica y cinética de la reacción; sin embargo, no proporciona información sobre el mecanismo de reacción propiamente dicho. El concepto de mecanismo de reacción está estrechamente relacionado con los desplazamientos nucleares que ocurren al avanzar desde reactantes a productos. Estos desplazamientos están relacionados con las fuerzas netas que actúan sobre el sistema a medida que la reacción avanza, que definen el mecanismo de la reacción en cada punto a lo largo de la coordenada de reacción. En este contexto, la fuerza de reacción, que se define como el negativo de la derivada de la energía potencial respecto a la coordenada de reacción (ξ) [38–41], está intrínsecamente ligada a los desplazamientos atómicos específicos que van configurando el proceso de transformación química:

$$F(\xi) = -\frac{\partial E(\xi)}{\partial \xi} \tag{2.1}$$

La fuerza de reacción entrega una partición racional del perfil de energía, que permite identificar la activación y desactivación de propiedades locales y globales a lo largo de la coordenada de reacción. F(ξ) presenta dos puntos críticos ξ_{min} y ξ_{max}; estos puntos definen tres regiones reactivas [42–44] (ver Figura 2.3). La región de reactantes que se define en el intervalo $\xi_R \leqslant \xi \leqslant \xi_{min}$, la región de transición en el intervalo $\xi_{min} < \xi < \xi_{max}$ y, por último, la región de productos que está definida para $\xi_{max} \leqslant \xi \leqslant \xi_P$.

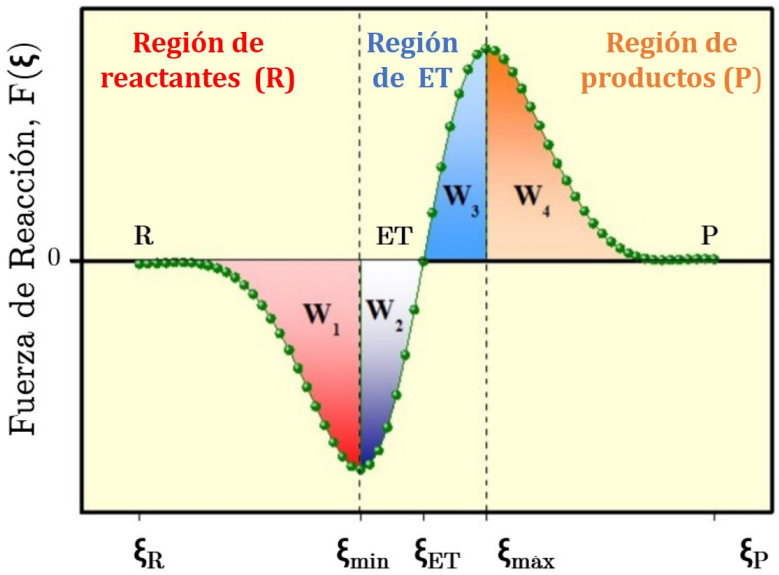

Figura 2.3: Esquema de fuerza de reacción para un paso elemental a lo largo de la coordenada intrínseca de reacción (ξ).

A partir de trabajos anteriores se ha mostrado que en la región reactantes y productos se producen mayormente reordenamientos de tipo estructural; tales como la

variación de ángulos y distancias de enlaces; en cambio, la región de transición se caracteriza por una intensa actividad electrónica debido a la ruptura y formación de enlaces [45–48]. En la Figura 2.3 se puede observar un perfil de fuerza para un paso elemental, donde se muestran las regiones de reacción anteriormente mencionadas.

Al integrar la fuerza en cada región, es posible cuantificar las contribuciones a la barrera energética para las reacciones tanto directa como reversa del proceso y, por lo tanto obtener los trabajos de reacción que miden la energía que se obtiene o libera en cualquier etapa de la reacción.

$$\Delta E^{\neq} = [E(\xi_{ET}) - E(\xi_R)] = W_1 + W_2 \tag{2.2}$$

Por lo tanto;

$$\Delta E^{\circ} = [E(\xi_P) - E(\xi_R)] = W_1 + W_2 + W_3 + W_4 \tag{2.3}$$

donde:

$$W_1 = -\int_{\xi_R}^{\xi_{min}} F(\xi)\ d\xi > 0 \qquad W_2 = -\int_{\xi_{min}}^{\xi_{ET}} F(\xi)\ d\xi > 0 \tag{2.4}$$

$$W_3 = -\int_{\xi_{ET}}^{\xi_{max}} F(\xi)\ d\xi < 0 \qquad W_4 = -\int_{\xi_{max}}^{\xi_P} F(\xi)\ d\xi < 0 \tag{2.5}$$

De esta forma, el análisis de la fuerza de reacción produce una partición racional de

las energías de activación y reacción, $\Delta E^{\neq}$ y ΔE° [39] en términos de contribuciones estructurales y electrónicas.

Más allá del análisis energético, la división unívoca de la coordenada CIR permite superponer las zonas reactivas con los perfiles de diversas propiedades del sistema, tanto electrónicas como estructurales, creando una interesante metodología para analizar los factores responsables de la activación o inhibición del mecanismo estudiado, y cuantificar la energía involucrada en procesos específicos que ocurren en el curso de la reacción.

2.3. Modelo de Activación y Distorsión, ASM

El modelo de activación y distorsión, ASM (*Activation Strain Model*), es un modelo de reactividad basado en la fragmentación de la densidad electrónica, el que, fue desarrollado por Bickelhaupt y colaboradores [49–52] con el objetivo de explicar la naturaleza física de las energías de activación y las diferencias energéticas que se observan en determinadas reacciones químicas. A partir del ASM, la energía total de un sistema queda expresada en función de dos contribuciones, energía de distorsión (ΔE_{dist}) y energía de interacción (ΔE_{int}), según:

$$\Delta E(\xi) = \Delta E_{dist}(\xi) + \Delta E_{int}(\xi) \tag{2.6}$$

El primer término ΔE_{dist} corresponde al costo energético asociado a la distorsión geométrica de los reactantes por separado a medida que la reacción toma lugar, es decir, a lo largo de la coordenada de reacción. El segundo, ΔE_{int} cuantifica la energía

de interacción entre las especies distorsionadas en cada punto de la coordenada de reacción.

Politzer y colaboradores [53] mostraron que ambos modelos, F(ξ) y ASM, permiten identificar y cuantificar las fuerzas retardantes y conductoras que gobiernan las reacciones químicas, siendo útiles para describir en detalle el mecanismo de reacciones químicas.

2.4. Método de Análisis de Descomposición de Energía, EDA

El método de análisis de descomposición de energía (EDA del inglés, *Energy Decomposition Analysis*) desarrollado independientemente por Morokuma [54] y por Ziegler y Raunk [55], es una poderosa herramienta que introduce elementos básicos de interpretación para la energía de interacción entre dos sistemas moleculares.

La energía de interacción (ΔE_{int}) entre los sistemas A y B se define como la diferencia de energía entre la energía de la supermolécula (AB) y la energía de los monómeros A y B aislados:

$$\Delta E_{int} = E_{AB} - (E_A + E_B) \tag{2.7}$$

ΔE_{int} se puede descomponer en tres componentes físicamente significativos, los cuales representan diferentes pasos hacia la formación de un complejo a partir de sus dos

fragmentos.

$$\Delta E_{int} = \Delta V_{elts} + \Delta E_{Pauli} + \Delta E_{orb} \tag{2.8}$$

El primer término, ΔV_{elts}, es mayormente de carácter atractivo y corresponde a la interacción electrostática clásica entre los fragmentos superpuestos con su distribución de carga congelada en la geometría del complejo (ρ_A y ρ_B). El segundo término, ΔV_{Pauli}, representa la energía de repulsión de Pauli que comprende la interacción desestabilizadora entre orbitales ocupados y, la repulsión estérica que resulta del principio de exclusión de Pauli. El tercer término, ΔE_{orb}, es siempre atractiva y corresponde a la energía de interacción orbitalaria, la cual explica la transferencia de carga, la polarización entre fragmentos y el enlace de par electrónico.

Finalmente, se debe agregar el término empírico ΔE_{disp} para tener en cuenta los efectos de dispersión de largo alcance [56, 57]. De esta manera, la suma de todas las contribuciones a la energía de interacción entre los fragmentos A y B queda descrita como:

$$\Delta E_{int} = \Delta V_{elts} + \Delta E_{Pauli} + \Delta E_{orb} + \Delta E_{disp} \tag{2.9}$$

Es importante notar que el EDA introduce componentes físicos de la energía de interacción, siendo una herramienta interpretativa; mientras que el análisis de la fuerza de reacción no introduce elementos de interpretación física, más bien particiona la coordenada de reacción en regiones donde se localizan efectos específicos, estructurales y electrónicos.

2.5. Función de localización electrónica, ELF

La función de localización electrónica (ELF) fue desarrollada por Becke y Edgecombe [58], y posteriormente utilizada para el estudio de moléculas por Silvi y Savin [59]. Se basa en la búsqueda de electrones localizados dentro de un sistema molecular a partir del estudio de la densidad de energía cinética. Savin demostró que la probabilidad de encontrar electrones localizados tenía relación con la diferencia entre la densidad de energía cinética del sistema de partículas no interactuantes de Kohn-Sham y la definida por von Weizsacker [60] (que es exacta para un sistema de bosones).

$$D = \frac{1}{2}\sum_i (\bigtriangledown \phi_i)^2 - \frac{1}{8}\frac{\mid \bigtriangledown \rho(r) \mid}{\rho(r)} \tag{2.10}$$

De esta forma, regiones con valores de D cercanos a cero indican una alta probabilidad de encontrar electrones localizados (en ese caso la expresión de von Weizsacker es una buena aproximación para la energía cinética del sistema en ese punto). Se propuso utilizar la densidad de energía cinética del modelo de Thomas-Fermi del gas de electrones homogéneo (D^0) como referencia, definiendo así el parámetro $\chi = \frac{D}{D^0}$, y además, debido a que la función D varía de cero a infinito, la ELF se quedó expresada como:

$$ELF = \frac{1}{1+\chi^2} \tag{2.11}$$

Donde $0 \leq$ ELF ≤ 1. La ELF mide el exceso de energía cinética del sistema debido al

principio de exclusión de Pauli que obedecen los electrones, interpretándose el concepto de localización electrónica como una manifestación de este principio. El análisis topológico de la ELF permite identificar y caracterizar regiones de alta localización electrónica, las cuales, son consistentes con la visión de Lewis de la estructura molecular (permite identificar pares de electrones libres, pares de electrones enlazantes, etc).

2.6. Índice de Interacciones No Covalentes, NCI

El índice de interacciones no covalentes (NCI) desarrollado por Yang y Contreras-García [61–64] es un índice de visualización de interacciones no covalentes basado en la densidad electrónica (ρ) y el gradiente reducido de la densidad (RDG, s), el cual corresponde a la primera derivada de la densidad electrónica y se encuentra definido como [65]:

$$s = \frac{1}{2(3\pi^2)^{1/3}} \frac{\mid \nabla\rho \mid}{\rho^{4/3}} \tag{2.12}$$

La localización de regiones de baja densidad y bajo gradiente permite la identificación de interacciones débiles en un sistema molecular; de esta manera, las regiones de baja densidad están relacionadas con las interacciones más débiles, como van der Waals, mientras que aquellas con densidades más altas están relacionadas con interacciones más fuertes (estabilizadoras o desestabilizadoras) [66]. Sin embargo, pueden aparecer diferentes tipos de interacciones fuertes en la misma región de densidad y gradiente reducido, tales como los puentes de hidrógeno y apilamientos estéricos, los cuales no

pueden ser distinguidos sólo a partir de la densidad y el gradiente reducido. Por lo que, para distinguir entre estos tipos de interacción, es necesario considerar las segundas derivadas de la densidad.

El signo del laplaciano de la densidad, $\nabla^2\rho$, es una herramienta ampliamente utilizada para distinguir entre diferentes tipos de interacciones fuertes [67]. Para comprender la vinculación con más detalle, el laplaciano a menudo se descompone en una suma de contribuciones a lo largo de los tres ejes principales de variación máxima. Estos componentes son los tres valores propios λ_i de la matriz hessiana de la densidad electrónica (segunda derivada), de modo que $\nabla^2\rho = \lambda_1 + \lambda_2 + \lambda_3$ ($\lambda_1 \leq \lambda_2 \leq \lambda_3$). El análisis de estos componentes es ampliamente utilizada para explicar el enlace químico [68].

En los núcleos (o atractores no nucleares), la densidad alcanza un máximo local, y los tres valores propios son negativos. De esta manera, las regiones interatómicas entre átomos unidos (puntos silla) son caracterizados por la presencia de un valor propio positivo y dos negativos ($\lambda_1 < 0$, $\lambda_2 < 0$, $\lambda_3 > 0$). En el caso de interacciones covalentes, las contribuciones negativas son dominantes y el laplaciano resultante es negativo. Mientras que para interacciones más débiles y no covalentes, el laplaciano en la región interatómica está dominado por la contribución positiva [67], independientemente si son estabilizadoras o desestabilizadoras. Las interacciones fuertes estabilizadoras, como los puentes de hidrógeno, pueden identificarse por el signo negativo de λ_2. Por el contrario, las interacciones fuertes desestabilizadoras, como las repulsiones estéricas, son representadas por el signo positivo de λ_2 en la región interatómica (donde $\lambda_3 > 0$ y λ_1 puede ser positivo o negativo).

La principal importancia de este índice es la comprensión de la estabilidad o inestabilidad de los sistemas químicos, basado en el contrapeso que existe entre las interacciones de naturaleza atractiva (estabilizadora) y repulsiva (desestabilizadora). De esta forma, el NCI puede ser obtenido como una función de la densidad electrónica (ρ) orientada por el signo de λ_2. Donde para valores de $\rho > 0.01$ a.u. y $\lambda_2 < 0$ se considera como fuertes interacciones de tipo estabilizadoras, mientras que valores de $\rho > 0.01$ a.u. y $\lambda_2 > 0$ se identifican como fuertes interacciones de tipo desestabilizadoras y, finalmente para valores bajos de densidad se le asignan a interacciones débiles van der Waals. Estas interacciones débiles son definidas para valores de $\rho > 0.01$ a.u. y $\lambda_2 \sim 0$.

En esta metodología es posible obtener gráficos 2D y 3D, donde los tipos de interacciones son coloreados (ver Figura 2.4). De esta manera fuertes interacciones repulsivas son representadas en color rojo, fuertes interacciones atractivas en color azul, e interacciones débiles van der Waals son graficadas en color verde.

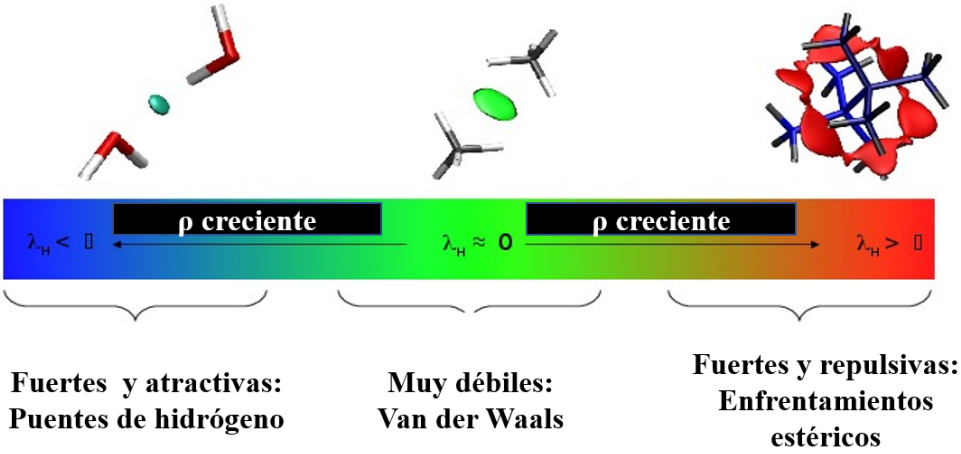

Figura 2.4: Representación genérica del tipo de interacción no covalente según el signo de λ_2. Adaptada de la referencia 64.

2.7. Electrofilia global, ω

La electrofilia global [69–71], corresponde a un índice global que entrega una medida de la estabilización energética de un sistema químico cuando se satura de electrones que provienen del medio externo. La electrofilia se expresa como:

$$\omega = \frac{\mu^2}{2\eta} \tag{2.13}$$

Donde μ y η corresponden al potencial químico electrónico y dureza química, respectivamente. El índice de electrofilia indica simultáneamente tanto la tendencia del electrófilo para adquirir una densidad electrónica adicional impulsado por μ^2 (el cuadrado de la electronegatividad), como la resistencia del sistema al intercambio

electrónico con el medio externo, descrito por η.

El concepto electrofília global ha sido recientemente generalizado para definir una electrofilia local (ω_k) condensada en el átomo k en la molécula. Este índice ofrece información local de un sitio atómico en particular para una molécula que puede ser propenso a ataques nucleofílicos. Este índice es definido como: [70, 72]

$$\omega_k = \frac{\mu^2 S}{2} f_k^+ = \omega f_k^+ \tag{2.14}$$

Donde se utiliza la relación exacta $s_k^+ = f_k^+ S$, relacionando la blandura local s_k^+ con la función de Fukui electrofílica f_k^+ y la blandura global S ($S = \frac{1}{\eta}$). La Ecuación 2.14 implica tanto que el sitio más electrofílico en la molécula coincidirá con el sitio más blando, como también conlleva que el sitio más electrofílico será el que presenta el mayor valor de la función de Fukui, es decir, el sitio activo de la molécula.

2.8. Análisis Poblacional, NBO

Para el análisis poblacional se analizarán los órdenes de enlace de Wiberg [73] a lo largo de la coordenada de reacción por medio de un estudio de orbitales naturales de enlace (NBO, *Natural Bond Orbital*).

En la década de 1980, Weinhold [74] retoma el trabajo de Löwdin, sobre orbitales naturales, creando una técnica de análisis poblacional para el estudio de hibridación y covalencia desde una función de onda polielectrónica. Se trata de una rutina computacional (presente en muchos paquetes computacionales), diseñada para recuperar la

estructura orbital responsable de los patrones de enlace y distribución electrónica del sistema, reencontrando los principios de enlace molecular introducidos por los científicos Lewis y Pauling.

Löwdin [75] introduce los orbitales naturales NO (ϕ) (*Natural Orbital*), como orbitales propios del operador de densidad de primer orden $\hat{\Gamma}$, para una función de onda polielectrónica Ψ, con p_ϕ el número de ocupación:

$$\hat{\Gamma}(1|1') = N \int \Psi(1,2,..,N)\Psi^*(1',2,..,N)d_{\tau_2}..d_{\tau_N} \tag{2.15}$$

$$\hat{\Gamma}\phi_i = p_\phi \phi_i (i = 1, 2..) \tag{2.16}$$

El procedimiento variacional de análisis NBO [76], se inicia al generar un conjunto de orbitales naturales atómicos (NAO, *Natural Atomic Orbital*) que a diferencia de los NO (ortonormales moleculares y deslocalizados), son orbitales ortonormales centrados en los átomos.

Cada orbital NBO [77], está compuesto de orbitales atómicos híbridos h_A, normalizados, generados a partir de combinaciones lineales de NAOs centrados en los átomos:

$$h_A = \sum_i c_i \phi_i^A \tag{2.17}$$

Una vez obtenidos los orbitales híbridos h_A, los orbitales naturales de enlace NBO

son construidos como combinación lineal de los orbitales híbridos centrados en los átomos involucrados en un enlace (A y B), tal como se muestra en la ecuación 2.18.

$$\sigma_{AB} = c_A h_A + c_B h_B \tag{2.18}$$

El valor de los coeficientes de polarización (c_A y c_B) otorgará una medida del carácter del enlace, siendo covalente para $c_A \approx c_B$ y iónico para $c_A << c_B$, bajo la condición: $c_A^2 + c_B^2 = 1$.

El orden de enlace de Wiberg es definido en términos del cuadrado de los elementos no diagonales de la matriz de densidad obtenida con una base de orbitales ortonormalizados, específicamente los orbitales naturales atómicos (NAOs), según:

$$I_{AB} = \sum_{a \in A} \sum_{b \in B} P_{ab}^2 \tag{2.19}$$

Donde P_{ab}^2 corresponde al cuadrado del elemento no diagonal de la matriz de densidad asociado al orbital a y b, centrados en los átomos A y B, respectivamente. El orden de enlace de Wiberg asegura valores positivos de éste y además se caracteriza por aproximarse al orden de enlace clásico proveniente de la teoría de enlace de pares de electrones de Lewis.

Cabe destacar que el orden de enlace se relaciona directamente con el número de enlaces existentes entre dos átomos, y también con la longitud del enlace y la energía del mismo. Por lo general, a mayor orden de enlace, mayor es la energía y la fuerza

de dicho enlace y menor su longitud. Estos factores también están asociados a su estabilidad.

Es importante notar que para sistemas químicos con átomos pesados y estructuras moleculares complejas, el análisis NBO presenta valores que pueden estar lejos del real [78]; no obstante, para elementos de las primeras filas que poseen estados de valencia bien definidos, es probablemente una de las herramientas más completas para realizar un análisis poblacional.

Con el uso de estas herramientas teóricas y computacionales, se espera avanzar en el entendimiento y caracterización del mecanismo de reacción en estudio, el que será desarrollado en los Capítulos 6, 7 y 8. En los siguientes capítulos se presentarán Hipótesis, Objetivos y Detalles Computacionales.

Capítulo 3

Hipótesis

El uso complementario de la fuerza de reacción y el modelo de activación y distorsión permitirá caracterizar el mecanismo de reacción detallado del proceso de inserción del carbenoide de cobre en enlaces N-H y O-H.

La naturaleza electrofílica/nucleofílica del sistema carbenoide es un criterio fundamental para entender su reactividad sobre el enlace X-H. En este sentido, el análisis de interacción donor aceptor proveniente de los orbitales naturales de enlace (NBO), basado en el análisis de la densidad electrónica, nos ayudarán a identificar y entender la naturaleza electrónica del carbenoide y las interacciones orbitalarias presentes entre el carbenoide y el sustrato (anilina/fenol).

Capítulo 4

Objetivos

4.1. Objetivos Generales

Se propone un estudio computacional en la reacción de inserción del carbenoide en los enlaces N-H y O-H, determinando propiedades estructurales y electrónicas con la finalidad de caracterizar el mecanismo de reacción. Además, se describirán estos sistemas desde la perspectiva de la reactividad y selectividad química, basadas en la estructura electrónica de cada sistema. Con esta información, en una segunda etapa se explorará el mecanismo de la reacción de inserción bajo el efecto del sustituyente, principalmente con el enfoque en las barreras de energía. En particular proponemos:

1. Caracterizar la reactividad del sistema carbenoide mediante el uso de índices de reactividad globales y locales.

2. Avanzar en el entendimiento de reacciones de inserción del carbenoide de cobre en enlaces X-H (X= N, O), identificando aquellos factores estructurales y electrónicos que conducen los procesos de inserción.

4.2. Objetivos Específicos

1. Validar metodologías computacionales, para describir las energías de reacción y los estados de transición sobre la superficie de energía potencial.

2. Analizar la reactividad intrínseca de los reactantes.

3. Obtener el mecanismo de reacción en reacciones de inserción del carbenoide de cobre en el enlace X-H.

4. Describir la naturaleza de las barreras de energía y cuantificar los efectos estructurales y electrónicos mediante los modelos de fuerza de reacción y ASM.

5. Determinar el efecto de la modificación estructural de los reactantes (carbenoide y fenol) en la reacción de inserción del carbenoide en el enlace O-H.

Capítulo 5

Detalles Computacionales

Los cálculos fueron realizados utilizando la Teoría de Funcionales de la Densidad (TFD), de manera de tomar en cuenta los efectos de intercambio y correlación electrónica en los sistemas moleculares. Se realizó un estudio *benchmark* para validar la metodología a utilizar. Entre los funcionales TFD analizados, se utilizaron dos funcionales híbridos-GGA: B3LYP [79, 80] y PBE0 [80], el funcional híbrido meta-GGA M06-2X [81, 82] y el funcional híbrido-GGA con correcciones de largo alcance ωB97X-D3 [83]. Todos estos funcionales fueron comparados con el método *ab initio* DLPNO-CCSD(T)[84], eligiendo el funcional M06-2X para estudiar los sistemas de interés (ver Apéndice).

Es importante destacar que el funcional M06-2X fue diseñado para mejorar el rendimiento en la obtención de propiedades de los sistemas que involucran interacciones no covalentes, tales como puentes de hidrógeno, interacciones de van der Waals, apilamiento $\pi-\pi$, transferencias de carga débiles, etc. Además, es altamente recomendado para el estudio de la termodinámica y cinética de reacciones químicas [82, 85, 86]. Se utilizó un conjunto de funciones base estándar del tipo DZP (doble zeta) cc-pVDZ

para tratar aquellos átomos no metálicos, mientras que para átomos metálicos se utilizó el LANL2DZ como pseudopotencial cuasirelativista y set de base. El efecto del solvente fue tomado en cuenta utilizando el método SCRF (*Self-Consistent Reaction Field*), aplicando el modelo SMD (*Solvation Model based on Density*)[87], utilizando diclorometano como solvente ($\varepsilon = 8.93$), para tomar en cuenta las condiciones experimentales. Para determinar la estructura electrónica de los sistemas estudiados, se realizó el análisis de la densidad electrónica, cargas atómicas, orden de enlace, orbitales moleculares y la superficie de potencial electrostático (SPE). Las cargas atómicas fueron obtenidas a partir del esquema de partición de Hirshfeld-I, las cuales fueron calculadas utilizando el método implementado en el programa Multiwfn 3.5 [88]. El uso de las cargas de Hirshfeld-I se deriva de la buena reproducibilidad respecto a los momentos dipolares, robustez con respecto a los cambios geométricos y obtención cualitativa correcta del SPE [89, 90].

Para estudiar las interacciones intermoleculares, se utilizó el índice de interacciones no covalentes (NCI) [61, 63], definido en la Sección 2.6, mediante el programa NCIPLOT 3.0 [61, 63, 91, 92]. El cálculo de pK_a se realizó utilizando la ecuación $pK_a = \Delta G^*_{aq}/2.303\ RT$, donde $\Delta \mathrm{G}^*_{aq}$ se calculó directamente a partir de las energías libres de Gibbs acuosas del ácido y la base conjugada, utilizando las correcciones de solvatación desarrolladas por Peng [93] para construir la cavidad del soluto.

El análisis armónico vibracional fue llevado a cabo para confirmar reactantes y productos como un mínimo sobre la superficie de energía potencial y el estado de transición (ET) como un punto de silla de primer orden con un único valor propio negativo en su matriz hessiana.

Mientras que para estudiar el mecanismo detallado de la inserción del carbenoide de cobre (I) en los enlaces N-H y O-H se aplicó el método basado en la coordenada intrínseca de reacción (CIR) [36, 37]. Además, se realizó el análisis de orbitales naturales de enlace (NBO) [74, 76, 77], tanto para la obtención de los órdenes de enlace, como para el análisis de interacción donor-aceptor. Todos los cálculos fueron realizados usando el paquete de programas Gaussian 16 [94] como también el programa Orca 4.0.0.2 [95]. La visualización y generación de estructuras moleculares fueron performadas con el programa Chemcraft [96] y las figuras fueron generadas con el programa CYLview [97].

Capítulo 6

Reactividad Intrínseca en el Carbenoide y los Sustratos

En este primer capítulo de resultados, como punto de partida en este trabajo de tesis, nos centraremos en analizar la reactividad de cada sistema por separado, con el fin de obtener información de los sitios y átomos activos de cada sistema interactuante.

6.1. Reactividad del Carbenoide

En esta tesis, el estudio se centró en un carbenoide de cobre (I), sustituido con un grupo dador de electrones por efecto inductivo, CH_3, y un grupo aceptor de electrones tanto por efecto resonante como inductivo, $C_3H_5O_2$. Ambos efectos electrónicos (dador y aceptor) llevan a un C^* con características electrofílicas. Este carbenoide es un intermediario reactivo que comparte características similares a las de un carbeno, sin embargo, es una especie mucho más estable. Esta estabilidad es otorgada tanto por la incorporación del complejo metálico, como también por la variación de los grupos

adyacentes al carbono carbenoide (C*) (ver Figura 1.3). Para comprobar dicho efecto, se realizó un estudio electrónico del sistema carbenoide, centrándose en el estudio de la superficie de potencial electrostático (SPE). La SPE ilustra la distribución de la densidad electrónica en la molécula en tres dimensiones, permitiendo la visualización de regiones con carga variable dentro de una molécula. El conocimiento de la distribución de carga se puede utilizar para determinar cómo las moléculas interactúan entre sí.

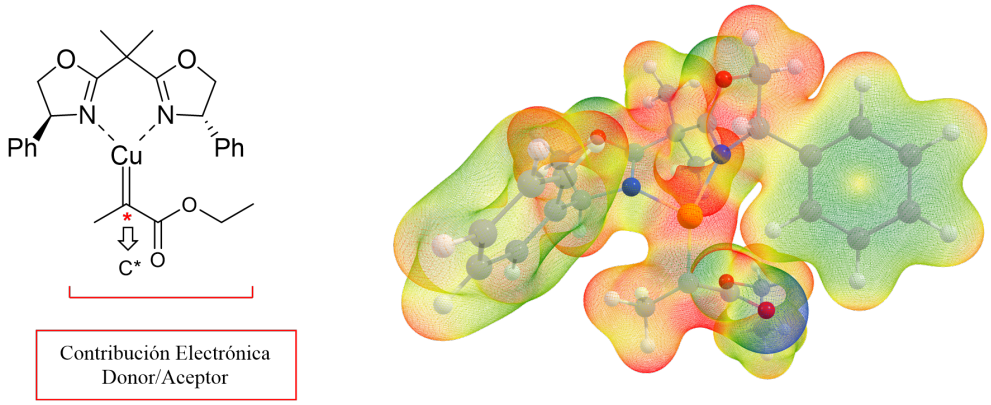

Figura 6.1: Superficie de potencial electrostático para el sistema carbenoide, utilizando un isovalor de 0.01 a.u. calculado a nivel M06-2X/cc-pVDZ. La notación * corresponde al carbono electrofílico (C*). El color rojo indica déficit de electrones, y el color azul exceso de electrones.

La Figura 6.1 contiene la estructura del carbenoide de cobre y la superficie de potencial electrostático del carbenoide bajo estudio. En ésta se observa un déficit de electrones (isosuperficie de color rojo) localizado en centro del carbenoide, de esta forma el C* posee carga de +0.03 |e|, mientras que el exceso de electrones (isosuperficie de color azul) se localiza en aquellos átomos que tienen una mayor electronegatividad, como lo son los oxígenos del formiato de etilo (grupo atractor de electrones).

Por otro lado, el complejo de cobre ((S,S)-2,2-bis(4-fenil-2-oxazolin-2-il)propano cobre

(I)) cumple un rol clave en las características electrofílicas del C*, por lo que es necesario dilucidarlo a partir de un análisis orbitalario. El estudio de los orbitales de enlace natural (NBOs) permite determinar interacciones orbitalarias responsables de la naturaleza electrofílica del C*, a partir de un análisis de interacción donor-aceptor, el cual es representado en la Figura 6.2, donde se presenta una alta donación σ desde del orbital sp^2 del C* al orbital s del cobre, con una energía de estabilización de 106.8 kcal/mol. Mientras que por otro lado, una baja retrodonación π se presenta desde el orbital d_{xy} del cobre al orbital p_y vacío del C*, con una energía de estabilización de 18.8 kcal/mol. La alta donación σ junto con la baja retrodonación π en el enlace Cu−C* resulta en un C* con características electrofílicas.

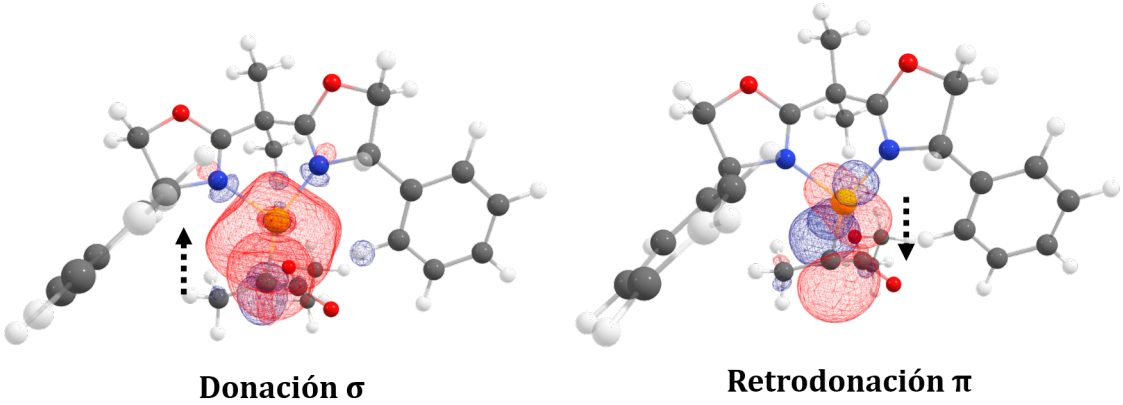

Figura 6.2: Orbitales de enlace natural (NBOs) asociados con la interacción donor-aceptor en el enlace Cu−C*. El color azul y rojo representan las diferentes fases existentes en los orbitales naturales.

6.2. Reactividad de los Sustratos

La reactividad de los sustratos también juega un rol clave en el proceso de inserción, debido a que el carbenoide electrofílico debe insertarse en el enlace X-H proveniente del sustrato, siendo esencial que éste presente una naturaleza nucleofílica. En esta sección se analizarán dos sustratos, anilina ($C_6H_5NH_2$) y fenol (C_6H_5OH), para es-

tudiar los enlaces N(sp^3)-H y O(sp^3)-H, respectivamente, utilizando en ambos casos el mismo carbenoide de cobre. Para estudiar la naturaleza nucleofílica, en primer lugar se realizó un estudio electrostático, a partir de la SPE y las cargas atómicas de Hirshfeld-I. La Figura 6.3 muestra que en la SPE, el exceso de electrones se localiza en el heteroátomo con cargas de -0.18 |e| para anilina y -0.19 |e| para el fenol, indicando que existe una mayor densidad de electrones en el átomo de oxígeno del sustrato fenólico.

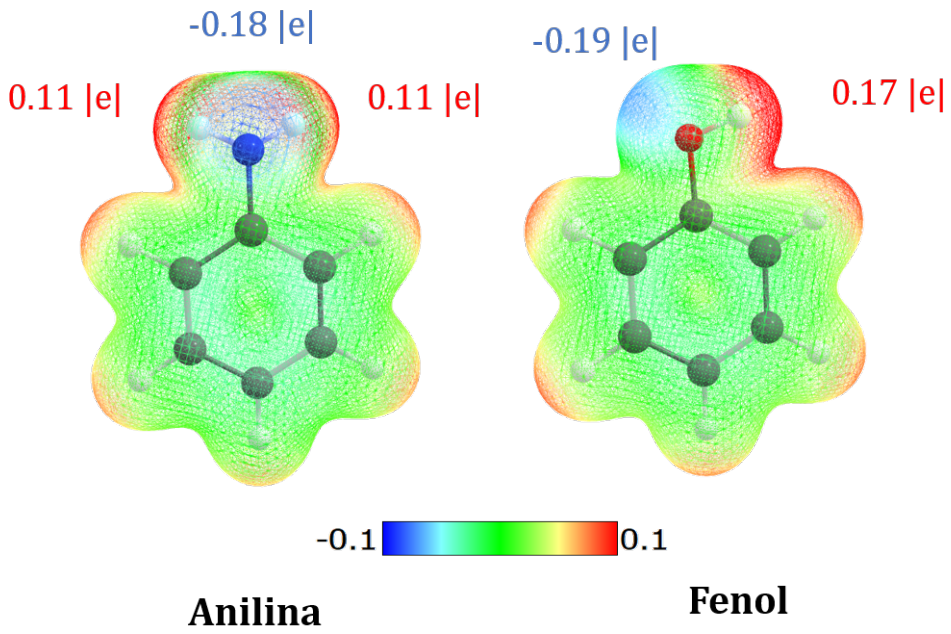

Figura 6.3: Superficie de Potencial Electrostático (SPE) para los sustratos en estudio, utilizando un isovalor de 0.01 a.u.. La isosuperficie de color rojo señala deficiencia de electrones, mientras que la de color azul un exceso de electrones.

Adicionalmente, la SPE muestra que el déficit de electrones se encuentra en el(los) átomo(s) de hidrógeno enlazado(s) al heteroátomo, por lo que se calculó la carga para el átomo de hidrógeno correspondiente al enlace X-H, donde el fenol presentó un hidrógeno con un mayor carácter deficiente en electrones, con carga de +0.17 |e|, mientras que los hidrógenos proveniente de la anilina poseen carga de +0.11 |e|. Esta

característica juega un rol clave para la posterior formación del enlace C*-H y salida del complejo metálico, que se lleva a cabo en la reacción de inserción, la cual estudiaremos con mayor profundidad en el Capítulo 7.

En resumen, los resultados de este capítulo mostraron que ambas especies (carbenoide y sustrato) tienen un comportamiento electrónico favorable para llevar a cabo una interacción orbitalaria entre ambas especies. Donde el carbenoide de cobre presentó características electrofílicas, las cuales son resultantes tanto de la contribución electrónica de los sustituyentes (donor y atractor de electrones), como de la contribución orbitalaria del metal, siendo esta última producto de alta donación σ y baja retrodonación π. Mientras que, los sustratos mostraron un carácter nucleofílico, proveniente de la acumulación de densidad electrónica en los heteroátomos de interés (N y O), debido a la mayor electronegatividad que estos átomos presentan.

Capítulo 7

Mecanismo de Reacción

En este segundo capítulo de resultados, nos enfocaremos en estudiar en detalle el mecanismo por el cual procede la reacción de inserción del carbenoide de cobre en los enlaces N-H y O-H. Sin embargo, antes de presentar los resultados, es importante destacar que el mecanismo de una reacción corresponde a una descripción detallada de la transformación de reactantes a productos, esta descripción incorpora tanto el movimiento de electrones como las relaciones espaciales de los átomos durante dichos procesos químicos. Adicionalmente, los eventos químicos relacionados con la transformación química pueden ser llevados a cabo tanto en un paso elemental como en una secuencia de pasos elementales, por lo que cuando el proceso químico es llevado a cabo en un único paso cinético, el mecanismo de reacción es definido como concertado, mientras que si éste procede en dos o más pasos cinéticamente diferentes a través de uno o más intermediarios, se puede definir como un mecanismo en etapas. Es importante notar, que un mecanismo concertado puede involucrar una serie de cambios, lo que lleva a definir un mecanismo concertado sincrónico o asincrónico. El sincrónico se refiere a un proceso donde los eventos de formación y ruptura de enlace proceden de manera simultánea, mientras que el asincrónico se refiere a una reacción

en la que los eventos químicos tienen lugar en forma secuencial.

Como mencionamos anteriormente, en este capítulo, se analizarán las distintas rutas de reacción que se pueden llevar a cabo en la reacción de inserción del carbenoide de cobre en los enlaces X-H (X: N, O). De esta manera la reacción de inserción bajo estudio es mostrada en la Figura 7.1, donde es importante tener en cuenta que para términos de esta tesis, sólo se centró el estudio en la reacción involucrada desde el carbenoide ya formado hasta la formación del producto de inserción y la regeneración del complejo de cobre catalíticamente activo (destacado en la Figura 7.1).

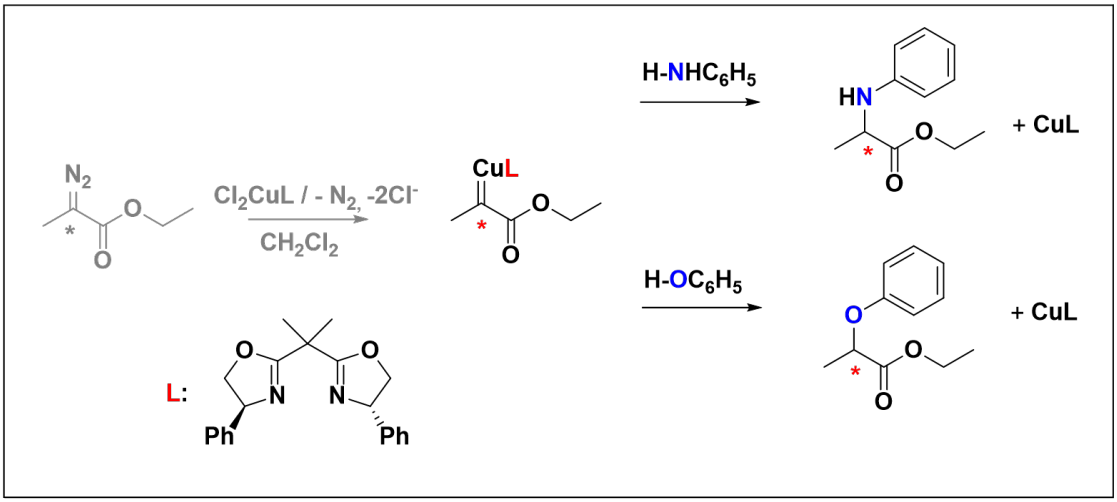

Figura 7.1: Reacción de inserción del carbenoide de cobre en los enlaces X-H (X: N y O). La notación * corresponde al carbono electrofílico C*.

Se realizaron los cálculos de los estados estacionarios en las reacciones de inserción y, a partir de las energías de todos los sistemas, se encontró dos mecanismos posibles, un mecanismo concertado y un mecanismo en etapas. En ambos mecanismos, el primer paso ocurre mediante un proceso sin barrera, formándose un compuesto zwitteriónico ($\mathbf{RC}_X$), sistema molecular donde la carga formal negativa es localizada en el átomo de cobre, mientras que la carga formal positiva se localiza en el heteroátomo (X). Esta

especie, es formada a partir de una interacción inicial entre el (C^*) del carbenoide y el heteroátomo del sustrato, generando la formación de un enlace covalente C^*-X con una baja población electrónica en el orbital molecular enlazante.

Por otro lado, como se mencionó anteriormente, el carbenoide se forma a partir de un diazocompuesto y un complejo metálico, donde a partir de la PhBOX la reacción es enantioselectiva (ligando utilizado experimentalmente para este fin), por lo que, en ambos caminos de reacción, ya sea en etapas o concertado, se obtienen dos isómeros ópticos como producto de inserción, los que están relacionados directamente con los efectos estéricos provenientes de los grupos fenilo del ligando con el sustrato en estudio.

7.1. Mecanismo Concertado

En esta sección, se describirá de forma detallada el mecanismo de la reacción de inserción del carbenoide de cobre en los enlaces N-H y O-H mediante un mecanismo concertado (**R1-XH**). Como se mencionó anteriormente, es posible formar dos isómeros ópticos como producto de la reacción a partir de la orientación en la que el sustrato se acerca al carbenoide. De esta manera, cuando el sustrato (anilina o fenol) se acerca mediante una orientación frontal, se obtiene como producto un enantiómero S, mientras que si el sustrato ataca mediante una orientación posterior, el producto obtenido es el R (ver Figura 7.2).

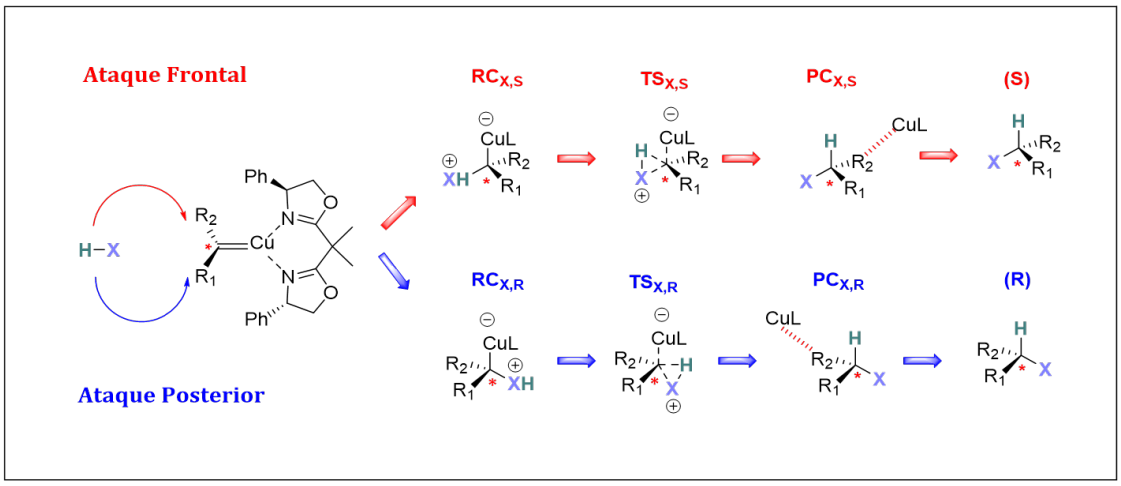

Figura 7.2: Mecanismo propuesto para la reacción **R1-XH** señalando las dos orientaciones que se acerca el sustrato al carbenoide. La notación * corresponde al carbono electrofílico (C*). R_1: CH_3 y R_2: $C_3H_5O_2$. X: C_6H_5**N**H, C_6H_5**O**.

A partir de esta información, se procedió a obtener las rutas por las que se obtienen ambos isómeros. La Figura 7.3 muestra un diagrama de energía, donde las energías (ΔG_{sol}) fueron calculadas incorporando el efecto del solvente. En el diagrama se presenta sólo un paso elemental, es decir, sólo un paso cinético. Sin embargo existen tres procesos químicos importantes dentro de este paso, ya sea tanto para la inserción que

toma lugar en la anilina (**R1-NH**), como para la inserción que procede en el sustrato fenólico (**R1-OH**).

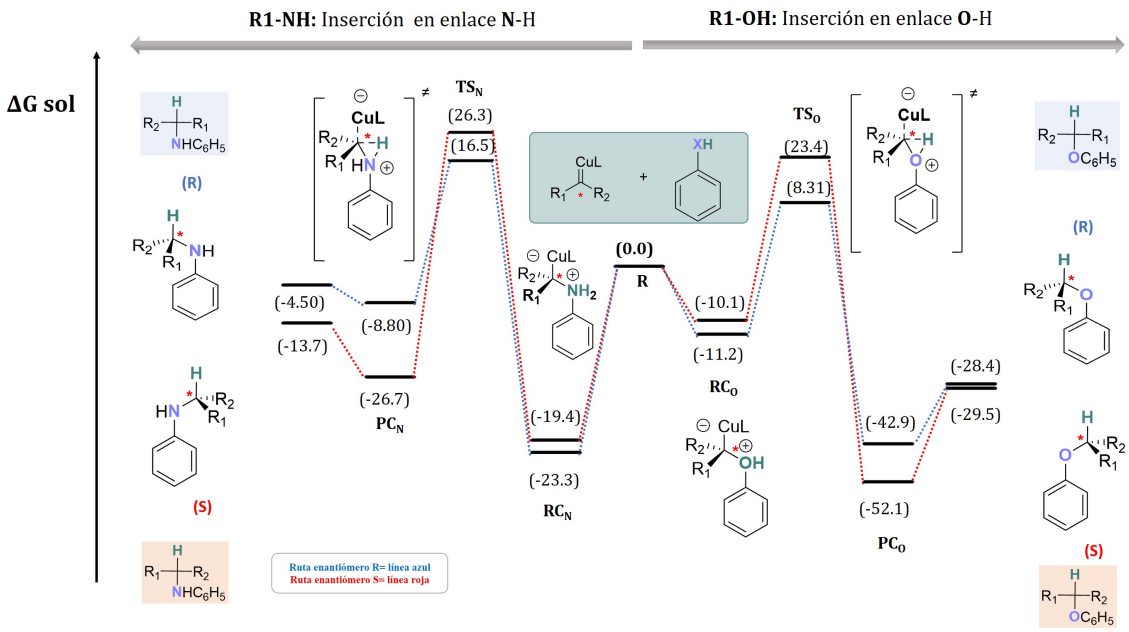

Figura 7.3: Caminos de reacción competitivos para las reacciones **R1-NH** (R y S) y **R1-OH** (R y S). La notación * corresponde al carbono electrofílico (C*). R_1: CH_3 y R_2: $C_3H_5O_2$. El camino de reacción que lleva a la formación del producto con configuración S es representado mediante la línea roja, mientras que la línea azul representa la ruta que lleva a la formación del producto con configuración R. La energía corresponde a la energía libre de Gibbs tomando en cuenta el efecto del solvente diclorometano (CH_2Cl_2). Todos los valores se encuentran en kcal/mol.

Para analizar en detalle las reacciones, vamos a separar cada proceso asociado a cada paso. El primer proceso corresponde a un paso sin barrera de energía, el cual involucra el ataque del nucleófilo hacia al carbono electrofílico del carbenoide (C*) para llevar posteriormente a la formación de un enlace covalente (C*-X), generando un compuesto zwitteriónico, denominado en esta tesis como complejo reactante (**RC**$_X$). El segundo proceso de la reacción incluye tanto la transferencia protónica desde el sustrato hacia el C*, como la ruptura del enlace Cu-C* llevando a la formación del complejo producto (**PC**$_X$), donde el producto de inserción (R o S) y el complejo metálico (CuL)

permanecen unidos por medio de interacciones no covalentes. Finalmente, el último proceso corresponde a la ruptura de las interacciones intermoleculares presentes en $\mathbf{PC}_X$ para así obtener separadamente el producto de inserción y el complejo de cobre catalíticamente activo. Los tres procesos químicos son mostrados en la Figura 7.3.

7.1.1. Primer proceso: Proceso sin barrera de energía

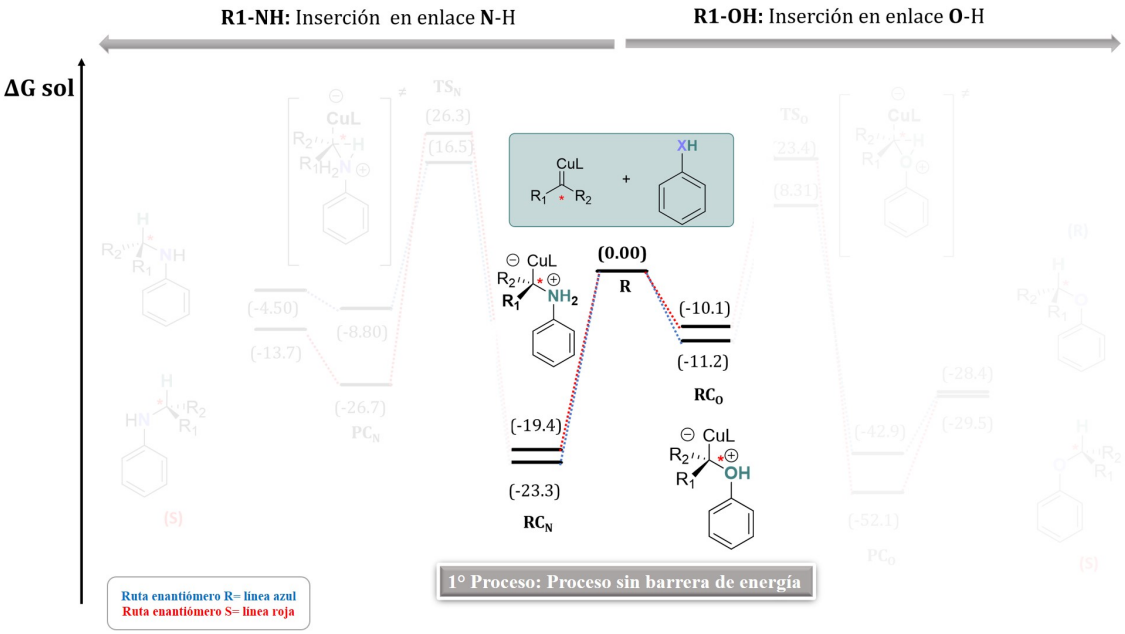

Figura 7.4: Caminos de reacción competitivos para el primer proceso, correspondiente a un proceso sin barrera para las reacciones **R1-NH** (R y S) y **R1-OH** (R y S). La notación * corresponde al carbono electrofílico (C*). R_1: CH_3 y R_2: $C_3H_5O_2$. El camino de reacción que lleva a la formación del producto con configuración S es representado mediante la línea roja, mientras que la línea azul representa la ruta que lleva la formación del producto con configuración R. La energía corresponde a la energía libre de Gibbs tomando en cuenta el efecto del solvente diclorometano (CH_2Cl_2). Todos los valores se encuentran en kcal/mol.

El primer proceso mostrado en la Figura 7.4, corresponde a la formación de un enlace C*-X con órdenes de enlace de 0.84 (R) y de 0.77 (S) para **R1-NH** y 0.67 (R) y 0.55

(S) para **R1-OH**, lo que sugiere la formación de un enlace covalente; además de la pérdida de saturación del enlace Cu-C* (R) y ruptura del doble enlace para Cu-C* (S). El estudio detallado de este proceso químico es esencial para el análisis del mecanismo concertado, debido a que determina la enantioselectividad de la reacción. Para cada inserción (**R1-NH** y **R1-OH**) se tienen dos procesos sin barrera, llevando a la formación de dos diferentes complejos reactantes ($\mathbf{RC}_X$), donde cada uno de ellos origina un isómero óptico específico. El ataque posterior del sustrato origina las especies $\mathbf{RC}_{X,R}$, mientras que las especies $\mathbf{RC}_{X,S}$ son obtenidas mediante el ataque frontal del sustrato hacia el carbenoide. Las energías de interacción para cada $\mathbf{RC}_X$ fueron obtenidas a partir de la siguiente ecuación:

$$\Delta E_{RC} = E_{carbenoide-sustrato}(RC_X) - E_{carbenoide} - E_{sustrato} \tag{7.1}$$

Donde se encontró que tanto para **R1-NH** como para **R1-OH** ΔE_{RC} es mayor para aquellas especies formadas a partir de un ataque posterior, es decir, para las conformaciones que llevan a la formación del isómero R ($\mathbf{RC}_{X,R}$). Siendo $\mathbf{RC}_{X,R}$ más estable en 13.3 kcal/mol para **R1-NH** y 9.70 kcal/mol en **R1-OH** con respecto a $\mathbf{RC}_{X,S}$.

Tabla 7.1: Energías de interacción del complejo reactivo (ΔE_{RC}), energía de interacción (ΔE_{int}) y energía de distorsión (ΔE_{dist}) calculadas mediante el ASM. Los porcentajes son calculados como $\%_{dist} = \frac{\mid \Delta E_{dist} \mid}{\mid \Delta E_{dist} \mid + \mid \Delta E_{int} \mid}$ x 100. Todos los valores están en unidades de kcal/mol y además corresponden a energías electrónicas.

	R1-NH		**R1-OH**	
	$\boldsymbol{RC}_{N,R}$	$\boldsymbol{RC}_{N,S}$	$\boldsymbol{RC}_{O,R}$	$\boldsymbol{RC}_{O,S}$
ΔE_{RC}	-27.6	-14.3	-20.3	-10.6
ΔE_{dist}	56.9 (40 %)	103.2 (47 %)	32.1 (38 %)	73.8 (47 %)
ΔE_{int}	-84.5 (60 %)	-117.5 (53 %)	-52.4 (62 %)	-84.4(53 %)

Para entender e identificar la naturaleza de las energías de formación del complejo reactante, ésta se descompuso tanto en ΔE_{dist} como en ΔE_{int}, las energías de distorsión y de interacción, y su contribución a la energía de formación del complejo reactante (ΔE_{RC}) son mostradas en la Tabla 7.1. Donde se observa que ΔE_{int} (de naturaleza estabilizadora) tiene una mayor contribución en todos los casos, siendo mucho más importante para el ataque posterior, con una contribución de más del 60 % de la suma de los valores absolutos de las componentes de ΔE_{RC}. Los resultados indican que en ambas especies químicas ($\mathbf{RC}_{X,R}$ y $\mathbf{RC}_{X,S}$) la energía del complejo reactante (ΔE_{RC}) es dominada por la energía de interacción ΔE_{int} (60 % (R)) y 53 % (S)). La menor estabilidad encontrada en los complejos reactantes $\mathbf{RC}_{X,S}$ se explica por el incremento en ΔE_{dist}, producto de la alta energía utilizada para permitir la deformación geométrica de los sistemas S y, de su mayor reactividad hacia la formación del producto final de la reacción.

Adicionalmente, la Figura 7.5 muestra las correspondientes estructuras para cada orientación del sustrato, para **R1-NH** y **R1-OH**, donde se observa que en ambas estructuras $\mathbf{RC}_{N,S}$ y $\mathbf{RC}_{O,S}$ se presenta una importante deformación de la geometría respecto al carbenoide inicial. Esto es producto de la pérdida de saturación y rompimiento del enlace Cu-C* (d: 3.34 Å para **R1-NH** y 3.41 Å para **R1-OH**), conduciendo al fortalecimiento del enlace C*-X (d: 1.46 Å para C*-N y 1.48 Å para C*-O), por lo que gran parte de la energía que se libera en la formación del enlace C*-X es utilizada para romper el enlace Cu-C*, lo que explica la mayor energía de interacción del complejo reactivo conduciendo a una menor estabilidad. Además, la ruptura del enlace Cu-C* lleva consigo la pérdida de contribución orbitalaria (ver Tabla 7.2), proveniente del átomo de cobre, resultando en la formación de especies inestables.

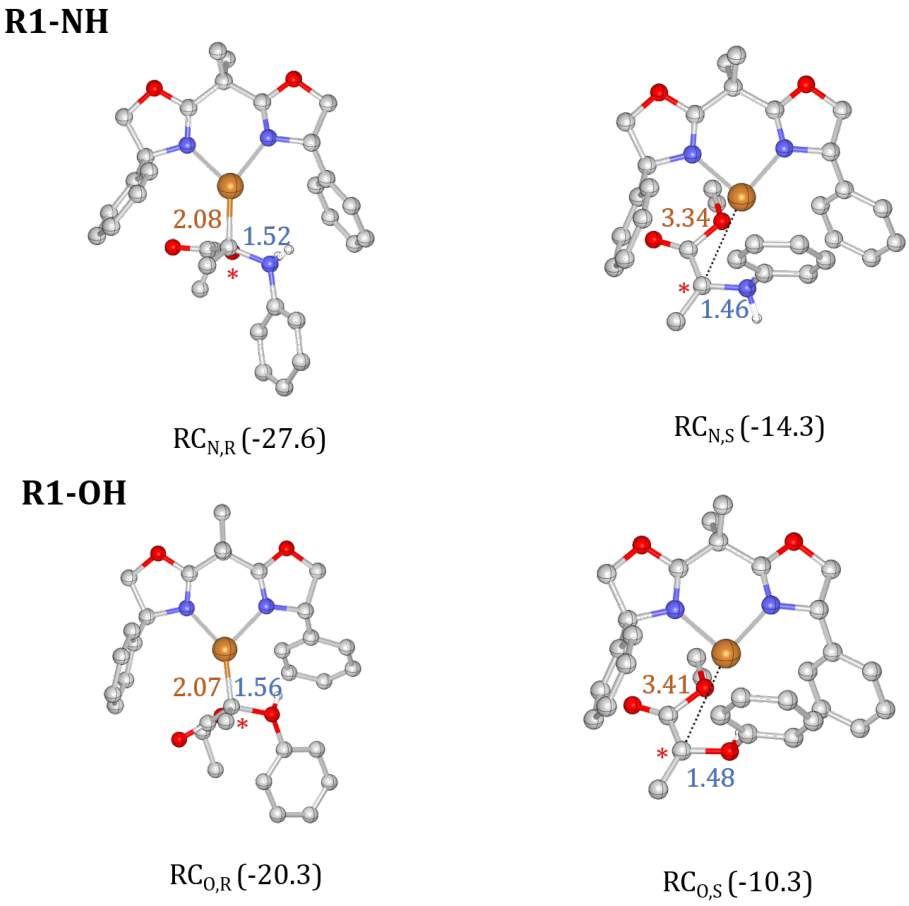

Figura 7.5: Estructuras del complejo reactante $\mathbf{RC}_{X,R}$ y $\mathbf{RC}_{X,S}$ en la reacción **R1-XH** (X: N, O). El valor entre paréntesis corresponde a la energía electrónica de formación del complejo reactante (ΔE_{RC}). Todos los valores están en kcal/mol.

Tabla 7.2: Orden de enlace Cu-C* y distancia de enlace Cu-C* medida en Å para los complejos reactantes $\mathbf{RC}_X$

Sistema	Orden de enlace Cu-C*	Distancia de enlace Cu-C*
$\mathbf{RC}_{N,R}$	0.50	2.08
$\mathbf{RC}_{N,S}$	0.00	3.34
$\mathbf{RC}_{O,R}$	0.54	2.07
$\mathbf{RC}_{O,S}$	0.00	3.41

Para estudiar el comportamiento de ΔE_{int}, se estudió el método de descomposición de energía EDA sobre las energías de interacción ΔE_{int} de $\mathbf{RC}_{X,R}$ y $\mathbf{RC}_{X,S}$, donde

ΔE $_{int}$ puede escribirse como:

$$\Delta E_{int} = \Delta V_{elstat} + \Delta E_{Pauli} + \Delta E_{orb} \tag{7.2}$$

Los resultados a partir de la EDA (Figura 7.6 **(a)**) exponen un alto porcentaje de repulsión de Pauli entre el carbenoide y el sustrato en $\mathbf{RC}_{N,S}$ y $\mathbf{RC}_{O,S}$, siendo un 3 % más alto que $\mathbf{RC}_{N,R}$ para **R1-NH** y 2 % más alto que $\mathbf{RC}_{O,R}$ para **R1-OH**. Este aumento en la repulsión de Pauli explica la menor contribución de ΔE$_{int}$ en ΔE$_{RC}$ para las estructuras $\mathbf{RC}_{X,S}$ respecto a $\mathbf{RC}_{X,R}$. El porcentaje de la repulsión de Pauli fue calculado como $\%_{Pauli} = \frac{\mid \Delta E_{Pauli} \mid}{\mid \Delta V_{elstat} \mid + \mid \Delta E_{Pauli} \mid + \mid \Delta E_{orb} \mid}$x 100.

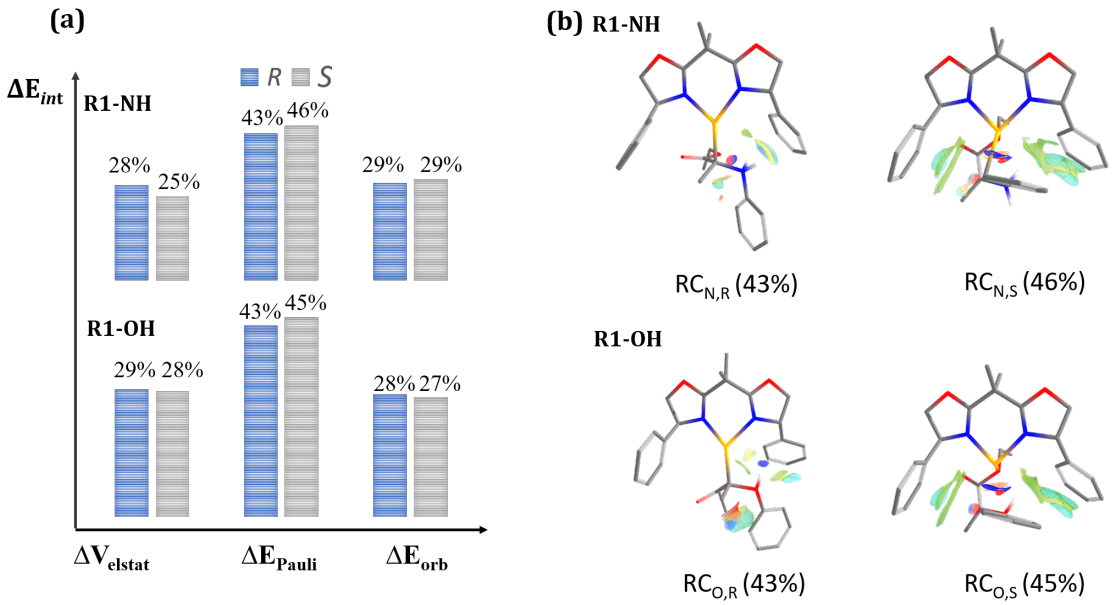

Figura 7.6: (a) EDA para la energía de interacción ΔE$_{int}$ en el complejo reactante ($\mathbf{RC}_X$), expresadas en porcentaje de ΔE$_{int}$, la columna azul corresponde al enantiómero R, mientras que la columna en color gris corresponde al enantiómero S. **(b)** Gráficos NCI de las estructuras $\mathbf{RC}_X$, en paréntesis se encuentra el porcentaje de ΔE$_{Pauli}$. En color rojo se encuentran las interacciones repulsivas, en color verde las interacciones van der Waals y en azul se representan las interacciones atractivas.

Para entender la naturaleza de la repulsión de Pauli, se realizó el análisis de inter-

acciones no covalentes (NCI). Los resultados son mostrados en la Figura 7.6 **(b)**, donde el ligando quiral (PhBOX) otorga la selectividad a la reacción. En esta figura, se observa que el ataque frontal del sustrato al carbenoide es mayoritariamente impedido mediante repulsiones van der Waals, lo que se refleja en la alta repulsión de Pauli encontrada en estos sistemas. Contrariamente, el ataque posterior es favorecido principalmente por la configuración que tiene el ligando quiral.

7.1.2. Segundo Proceso: Paso elemental

El segundo proceso para **R1-NH** y **R1-OH** mostrado en la Figura 7.7, involucra un estado de transición, característico de una reacción concertada, que corresponde a una transferencia protónica, cuyo átomo donor es el heteroátomo (X: N, O), mientras que el átomo aceptor es el carbono C*, formándose el enlace C*-H y las consiguientes rupturas de X-H y Cu-C*, resultando en la salida del complejo de cobre.

La altura de la barrera nuevamente está sujeta a la orientación del ataque proveniente del sustrato. Las energías de activación para **R1-NH** corresponden a 39.2 (R) y 47.5 (S) kcal/mol, mientras que en la reacción **R1-OH** las barreras son de 20.0 (R) y 33.8 (S) kcal/mol, indicando que la enantioselectividad es favorecida cinéticamente. Las estructuras de $\mathbf{TS}_{X,R}$ y $\mathbf{TS}_{X,S}$ son mostradas en la Figura 7.8, donde para $\mathbf{TS}_{X,S}$ se observa que el complejo de cobre se libera antes que ocurra la transferencia protónica, presentando distancias de enlace Cu-C* de 3.42 Å en **R1-NH** y 3.51 Å en **R1-OH**. En $\mathbf{TS}_{X,R}$, la salida del complejo de cobre y la transferencia protónica se realizan simultáneamente (d Cu-C*: 2.16 Å (**R1-NH**) y 2.19 Å **R1-OH**). Esta diferencia se debe a que la geometría molecular adoptada por $\mathbf{TS}_{X,S}$ presenta una deformación geométrica importante producto de la repulsión entre el ligando PhBOX y el sustra-

to, lo que desfavorece un ataque frontal.

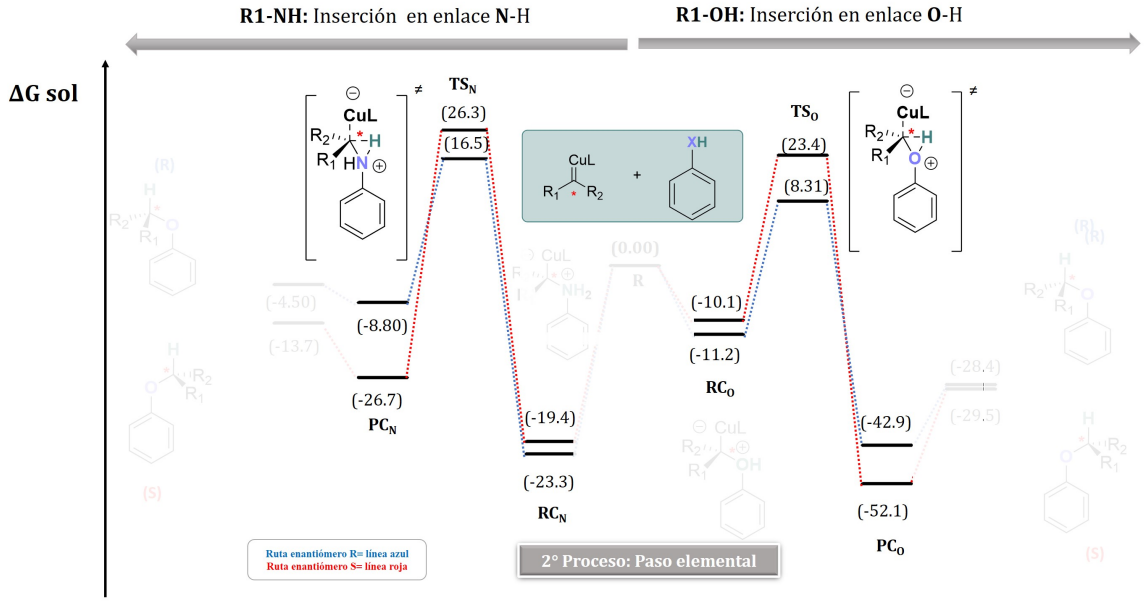

Figura 7.7: Caminos de reacción competitivos para el paso elemental, para las reacciones **R1-NH** (R y S) y **R1-OH** (R y S). La notación * corresponde al carbono electrofílico (C*). R_1: CH_3 y R_2: $C_3H_5O_2$. El camino de reacción que lleva a la formación del producto con configuración S es representado mediante la línea roja, mientras que la línea azul representa la ruta que lleva a la formación del producto con configuración R. La energía corresponde a la energía libre de Gibbs tomando en cuenta el efecto del solvente diclorometano (CH_2Cl_2). Todos los valores se encuentran en kcal/mol.

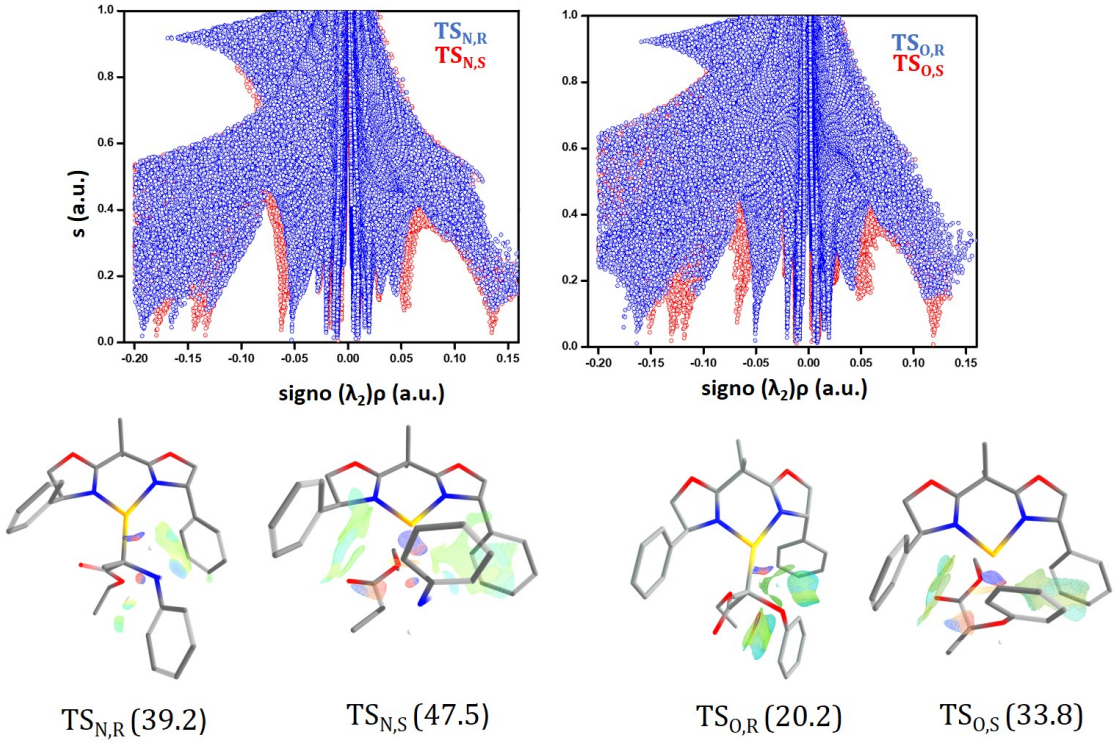

Figura 7.8: Gráficos NCI 2D y 3D para las estructuras del estado de transición (TS), correspondiente a las reacciones **R1-NH** y **R1-OH**. En los gráficos 2D (panel superior), los puntos de color azul corresponden a las estructuras del estado de transición $\mathbf{TS}_{X,R}$, mientras que los de color rojo representan a las estructuras del estado de transición $\mathbf{TS}_{X,S}$. X corresponde al heteroátomo (X: N, O). En los gráficos 3D (panel inferior), los valores entre paréntesis corresponden a la energía electrónica de activación en kcal/mol.

El índice de interacciones no covalentes (NCI) ha sido calculado para entender la naturaleza de la enantioselectividad de las reacciones en estudio. Los gráficos de NCI, tanto 2D y 3D, son mostrados en la Figura 7.8 en los estados de transición $\mathbf{TS}_{X,R}$ y $\mathbf{TS}_{X,S}$. En $\mathbf{TS}_{X,S}$ se observa un mayor número interacciones van der Waals repulsivas entre el grupo fenilo de PhBOX y el sustrato, reflejándose en el incremento de la barrera de energía para aquellas reacciones que proceden mediante la orientación frontal del sustrato. Por otro lado, en las estructuras $\mathbf{TS}_{X,R}$ existe un menor número de interacciones desfavorables entre ambas especies, haciendo que el paso que conduce a sistemas con configuración R ocurra con menor energía de activación.

Mecanismo de Reacción

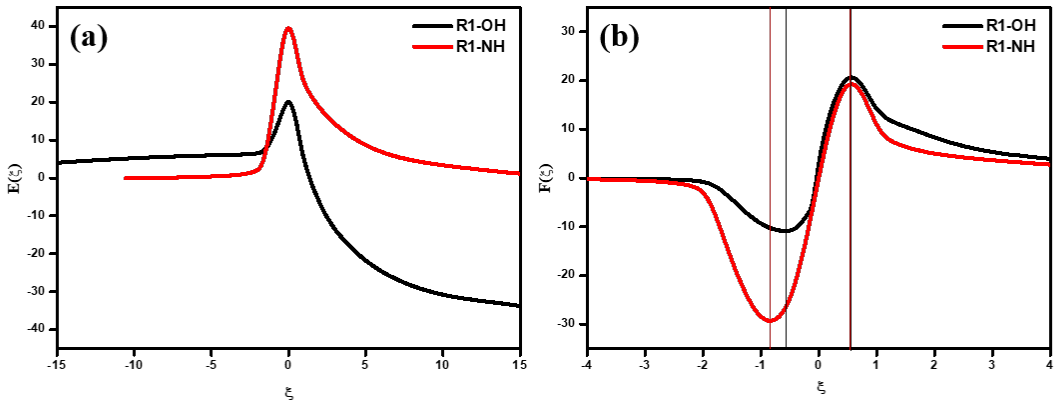

Figura 7.9: (a) Perfil de energía potencial con respecto a la coordenada de reacción ξ. **(b)** Perfil de fuerza de reacción con respecto a ξ. Ambos perfiles corresponden al paso elemental de **R1-XH** en cada caso. La línea en rojo representa la reacción **R1-NH**, mientras que la línea en negro la reacción **R1-OH**. La coordenada de reacción del perfil F(ξ) se graficó de -4 a 4, para una mejor visualización de la región de transición.

Debido a la relevancia del segundo proceso dentro de la reacción de inserción, se realiza el análisis del mecanismo de reacción con el fin de entender el significado físico de la energía de activación a partir de la RF y el ASM. Con este objetivo, se tomaron aquellas reacciones más favorables basadas en el análisis realizado con el modelo EDA y NCI, las que resultan en el ataque posterior que conducen a isómeros con configuración R. La Figura 7.9 muestra los perfiles de energía potencial y de fuerza de reacción para **R1-NH** (línea de color rojo) y **R1-OH** (línea de color negro).

Los resultados correspondientes a la altura de la barrera de energía indican que la reacción es favorecida cinéticamente cuando la reacción toma lugar en el sustrato fenólico ($\Delta E^{\neq}$ = 20.0 kcal/mol vs 39.2 kcal/mol para **R1-OH** y **R1-NH**, respectivamente). Para explicar este comportamiento se analizaron los trabajos de reacción, los cuales

son obtenidos a partir del perfil de RF considerando especialmente los trabajos W_1 y W_2, ya que ellos toman en cuenta el costo energético asociado a la transformación de reactantes a productos. Los trabajos de reacción son mostrados en la Tabla 7.3, donde se observa una importante contribución de W_2 a la energía de activación en **R1-NH** en contraste a **R1-OH** (34 % *vs.* 19 %). Para explicar la diferencia entre los trabajos de reacción W_1 y W_2, se complementó el análisis de RF con ASM para así comparar tanto la energía de interacción como la distorsión en términos de los trabajos de reacción (W_{1-dist}, W_{1-int}, W_{2-dist} y W_{2-int}). Los resultados se presentan en la Tabla 7.3 e indican que la mayor contribución a W_1 corresponde a la repulsión estérica entre el grupo fenilo del ligando y el sustrato (W_{1-int} es positivo, es decir, de naturaleza repulsiva), mientras que W_2 se encuentra dominado principalmente por una distorsión geométrica del sustrato. Por lo que, el mayor W_2 encontrado en **R1-NH** corresponde a una mayor deformación estructural que es producto de la ruptura de los enlaces N-H y Cu-C*, resultando en un incremento de la energía de activación con respecto a **R1-OH**.

Tabla 7.3: Trabajos W_1 y W_2 con sus contribuciones en W_{dist} y W_{int} para **R1-NH** y **R1-OH**. Todos los valores se encuentran en kcal/mol y corresponden a energías electrónicas.

R1-NH (39.2)				**R1-OH** (20.0)			
W_1 26.4 (66 %)		W_2 12.8 (34 %)		W_1 16.2 (81 %)		W_2 3.83 (19 %)	
W_{1-dist}	W_{1-int}	W_{2-dist}	W_{2-int}	W_{1-dist}	W_{1-int}	W_{2-dist}	W_{2-int}
5.95	20.4	35.2	-22.4	-9.37	25.5	21.0	-17.2

Adicionalmente, se realizó un análisis cualitativo del modelo de activación y distorsión (ASM) cuyos resultados se muestran en la Figura 7.10 **(a)**. La línea de color azul en la figura corresponde a la energía de interacción ΔE_{int}, que corresponde a la suma de todos los efectos energéticos que resultan de la combinación y mezcla

de la distribución de carga de los fragmentos. La línea de color verde representa la energía de distorsión ΔE_{dist}, la que es identificada como la distorsión geométrica de los fragmentos aislados, mientras que la línea roja corresponde a la energía total. Los perfiles ASM muestran que la región de reactantes es dominada por una energía de interacción positiva, asociada a la energía de repulsión de Pauli, generando una desestabilización del sistema. Esta tendencia se observa en ambas reacciones siendo mayor en **R1-OH**; sin embargo, ésta va acompañada de una alta estabilización asociada a la energía de distorsión, la cual es vinculada con los reordenamientos de tipo estructural que están tomando lugar en la reacción.

Para entrar en mayor detalle sobre la contribución de estabilización otorgada por la energía de distorsión en **R1-OH**, se graficó la energía de distorsión asociada a ambos fragmentos (carbenoide y sustrato) en la Figura 7.10 **(b)**. Los resultados señalan que la estabilización de la energía de distorsión en **R1-OH** tiene una mayor contribución en la deformación geométrica que sufre el carbenoide, siendo estabilizado a medida que la reacción transcurre, hasta las cercanías del estado de transición. Estos resultados pueden ser complementados con un análisis de orden de enlace mediante el perfil de orden de enlace (Figura 7.10 **(c)**), donde en **R1-OH** aparecen importantes variaciones en la región de reactantes, principalmente asociados al fortalecimiento del enlace Cu-C*, evento químico que libera energía y contribuye a la estabilización del carbenoide, tal como fue discutido para la energía de distorsión asociada al carbenoide.

Adicionalmente, el enlace O-H se refuerza produciendo una leve estabilización en el fenol. Contrariamente en **R1-NH** los enlaces se mantienen sin variación en la región

de reactantes, por lo que, al no haber una estabilización en el carbenoide, resulta en una energía de distorsión cercana a cero en la región de reactantes.

Estos resultados indican que la menor energía de activación que presenta **R1-OH** se debe principalmente a la estabilización que experimenta el carbenoide en la región de reactantes. Además de la baja contribución de W_2 asociada a la energía de distorsión desestabilizadora asociada a la distorsión geométrica del sustrato, producto de la ruptura del enlace O-H.

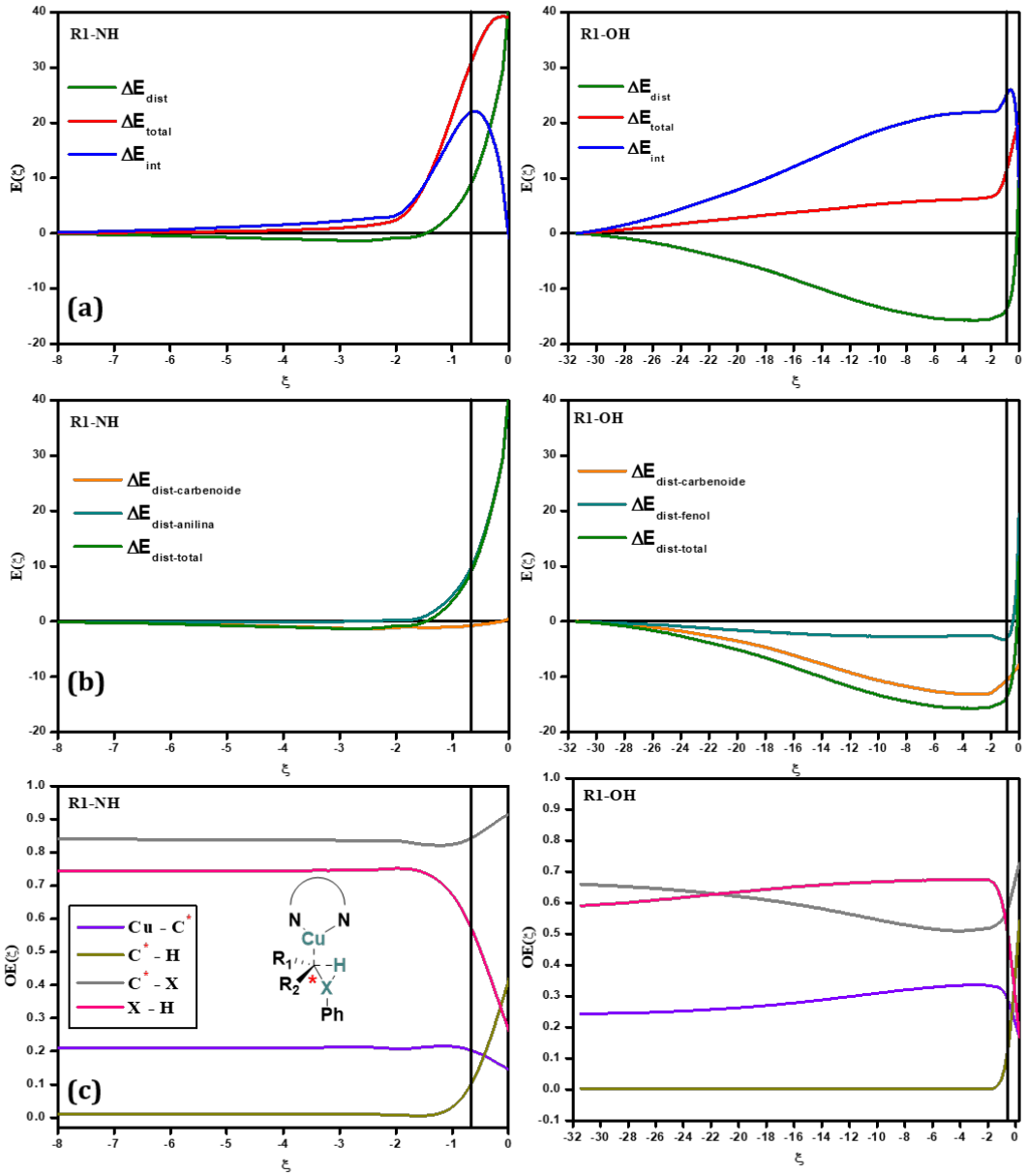

Figura 7.10: **(a)** Perfil del modelo de activación y distorsión. **(b)** Perfil de energía correspondiente a distorsión en ambos fragmentos aislados (carbenoide y sustrato), la energía de distorsión asociada al carbenoide es representada por la línea de color naranjo, la energía asociada al sustrato se graficó en color celeste y la energía total de distorsión se presenta en color verde. **(c)** Perfil de orden de enlace de los enlaces participantes del paso elemental. Los tres perfiles son graficados desde la coordenada de los reactantes ξ_R hasta la coordenada del estado de transición ξ_{ET}. Todos los valores energéticos se encuentran en kcal/mol.

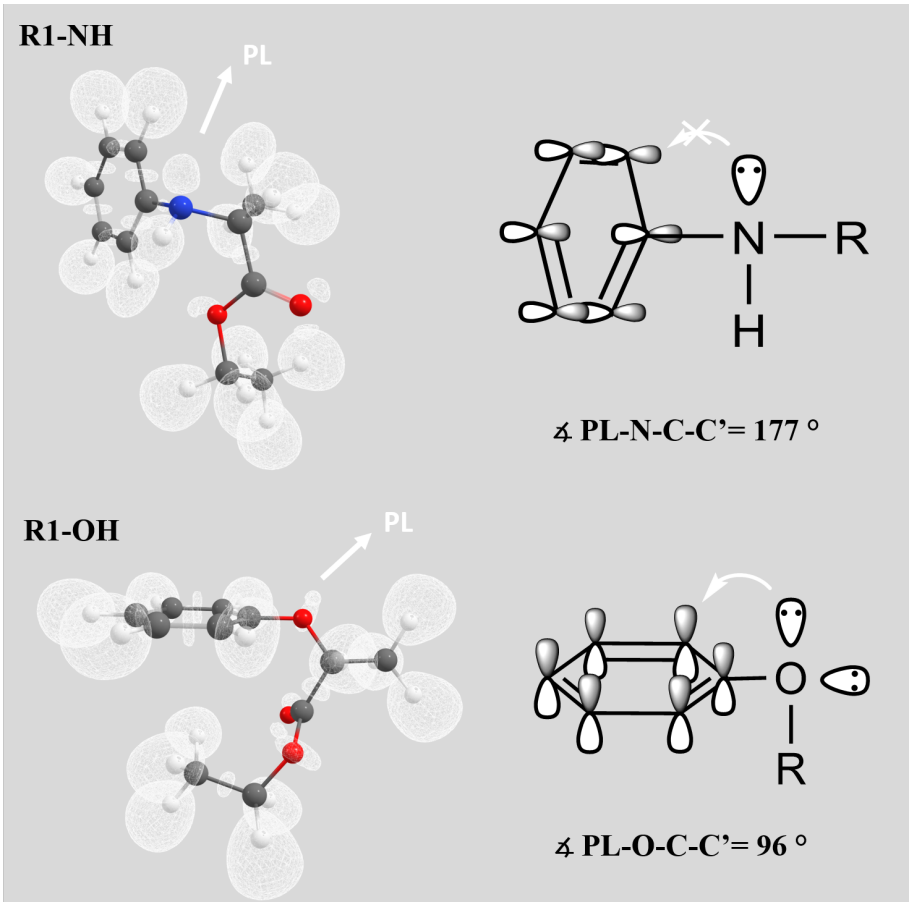

Figura 7.11: Función de localización electrónica (ELF) para las estructuras de los productos obtenidos en las reacciones **R1-NH** y **R1-OH** con isovalor de 0.9 a.u., la notación PL corresponde a los pares de electrones no compartidos. C representa al átomo de carbono adyacente a X (X:N,O) y C' al carbono en posición para al C.

Con respecto a la termodinámica de la reacción, $\Delta E°$ indica que ambas reacciones son favorables llevando a la formación de productos estables ($\Delta E°$ = -9.61 y -39.8 kcal/mol para **R1-NH** y **R1-OH**, respectivamente). Sin embargo, **R1-OH** resultó ser más favorable al analizar los resultados de la función de localización electrónica (ELF, *Electron localization function*) (Figura 7.11), la que permite analizar la probabilidad de encontrar electrones localizados en una determinada región del espacio, donde se observa que un par electrones libres del átomo de oxígeno se encuentra perpendicular al plano del ciclo aromático, con un ángulo diedro de α PL-O-C-C' de 96°, interactuando con los electrones de los enlaces π del benceno y entrando en

conjugación con el anillo aromático, para así formar un producto de inserción más estable. Mientras que, en **R1-NH** el PL del átomo de nitrógeno se encuentra en el mismo plano del benceno, es decir, en una orientación perpendicular al sistema π del anillo, impidiendo la conjugación (α PL-N-C-C'= 177°).

7.1.3. Tercer Proceso: Interacciones no covalentes entre el producto de inserción y el complejo CuL

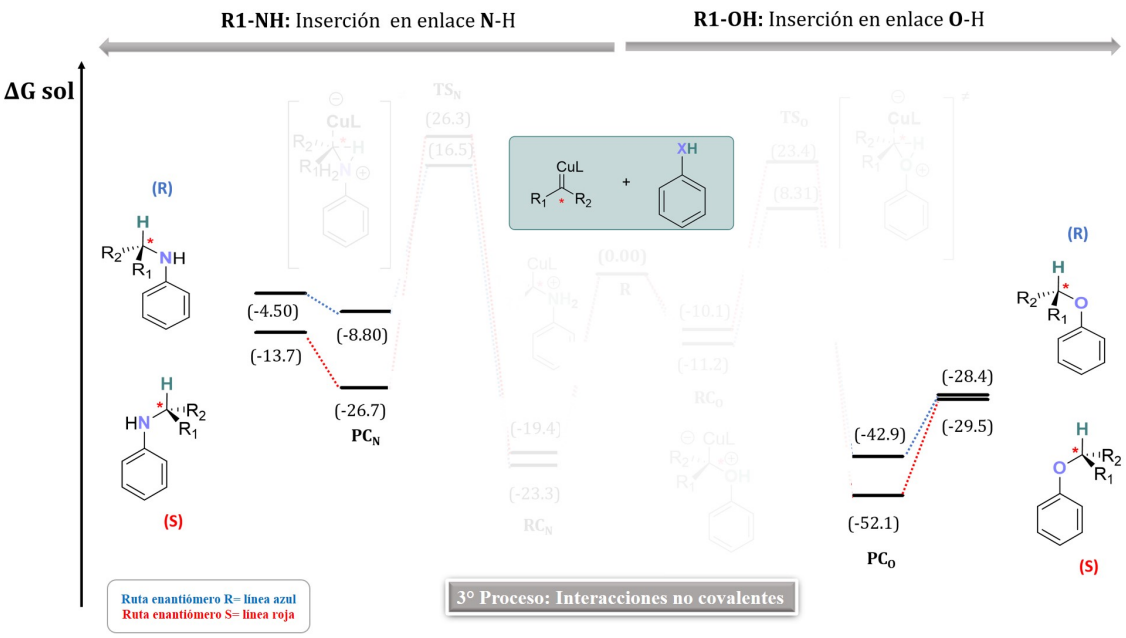

Figura 7.12: Caminos de reacción competitivos para el tercer paso, para las reacciones **R1-NH** (R y S) y **R1-OH** (R y S). La notación * corresponde al carbono electrofílico (C*). R_1: CH_3 y R_2: $C_3H_5O_2$. El camino de reacción que lleva a la formación del producto con configuración S es representado mediante la línea roja, mientras que la línea azul representa la ruta que lleva a la formación del producto con configuración R. La energía corresponde a la energía libre de Gibbs tomando en cuenta el efecto del solvente diclorometano (CH_2Cl_2). Todos los valores se encuentran en kcal/mol.

Finalmente, el último paso del mecanismo concertado mostrado en la Figura 7.12, corresponde a la ruptura de las interacciones no covalentes presentes en $\mathbf{PC}_X$, para obtener separadamente el producto de inserción y el complejo de cobre (CuL). El costo energético asociado con este proceso es de 4.30 y 13.0 kcal/mol en **R1-NH** para los productos R y S respectivamente y, de 14.5 (R) y 22.6 (S) kcal/mol para **R1-OH**. Esta energía es usada en las estructuras $\mathbf{PC}_{X,R}$ para romper las interacciones no covalentes entre el átomo de cobre y el átomo de oxígeno del carbonilo (formiato de etilo). Mientras que en las estructuras $\mathbf{PC}_{X,S}$ esta energía se utiliza para romper la interacción atractiva entre el átomo de cobre del complejo metálico y los enlaces dobles provenientes del anillo aromático del sustrato (ver Figura 7.13).

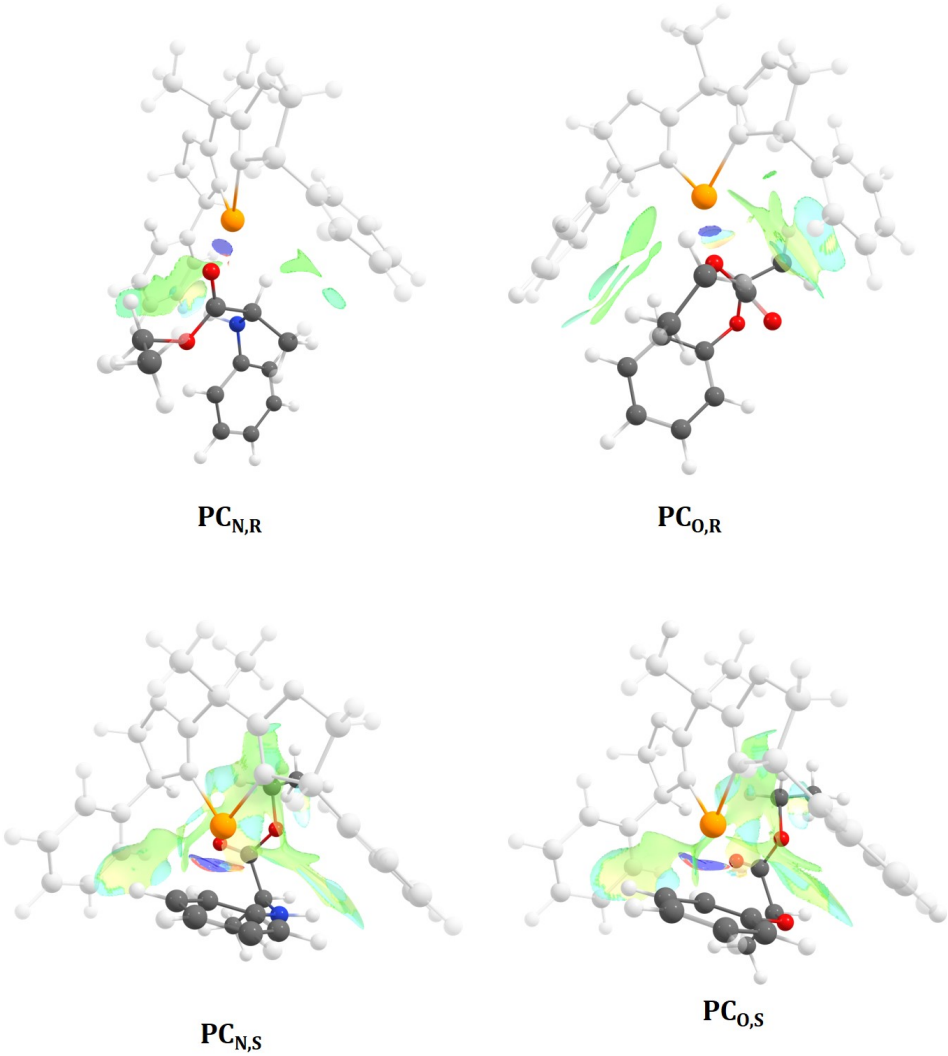

Figura 7.13: NCI 3D para las estructuras de los complejos producto $\mathbf{PC}_{X,R}$ y $\mathbf{PC}_{X,S}$ obtenidos en las reacciones **R1-NH** y **R1-OH**.

En resumen, los resultados de esta sección indicaron que la reacción más favorable cinéticamente, ocurre mediante un acercamiento posterior del sustrato (anilina/fenol) siguiendo un mecanismo concertado, el cual presenta tres pasos importantes dentro de la reacción. El primer paso, corresponde a proceso sin barrera de energía llevando a un complejo reactante inicial. El segundo paso, presenta una transferencia protónica desde el sustrato hacia el carbenoide, la que genera la salida del complejo de cobre (paso elemental). Finalmente, el tercer paso, corresponde a la ruptura de las interacciones no covalentes entre el producto de inserción y el complejo de cobre. El

análisis del paso elemental de la reacción, indica que la inserción en el enlace O-H es favorecida tanto desde el punto de vista cinético como termodinámico con respecto al enlace N-H, donde la enantioselectividad de la inserción está dada por el ligando PhBOX mediante repulsiones estéricas, favoreciendo de este modo la formación del enantiómero R como producto de inserción. Para el estudio en detalle del paso elemental que lleva a la formación del producto de inserción R, se utilizaron los modelos F(ξ) y ASM. De este modo, la fuerza de reacción indica que una gran contribución de la barrera energética en N-H es producto de la mayor contribución de W_2, que impide el proceso de inserción. Mientras que el ASM, señala que la energía de activación para ambos enlaces es dominada por repulsiones estéricas entre el ligando y el sustrato utilizado.

7.2. Mecanismo en Etapas

Presentamos en esta sección el estudio del mecanismo en etapas en las reacciones de inserción del carbenoide de cobre en los enlaces N-H (**R2-NH**) y O-H (**R2-OH**). El diagrama de energía para este mecanismo se presenta en la Figura 7.14. La principal característica de este mecanismo con respecto al concertado, es la participación directa del grupo formiato de etilo en la reacción. El mecanismo en etapas comienza con el ataque nucleofílico del sustrato al carbenoide (proceso sin barrera de energía), seguido de una transferencia protónica desde el heteroátomo del sustrato al grupo atractor de electrones (primer paso elemental), el que posteriormente dona un protón hacia el C* del carbenoide (segundo paso elemental). El segundo estado de transición (TS_{2-X}) y paso determinante de la reacción presenta ΔG_{sol} superiores a los reportados para el paso elemental del mecanismo concertado (**R1-XH**: 16.5 kcal/mol (**TS**$_{N,R}$) y 8.31 kcal/mol (**TS**$_{O,R}$) *vs.* **R2-XH** 35.7 kcal/mol (**TS**$_{2-N,R}$) y 14.5 kcal/mol (**TS**$_{2-O,R}$)), por lo que el mecanismo en etapas no se encuentra favorecido desde el punto de vista cinético.

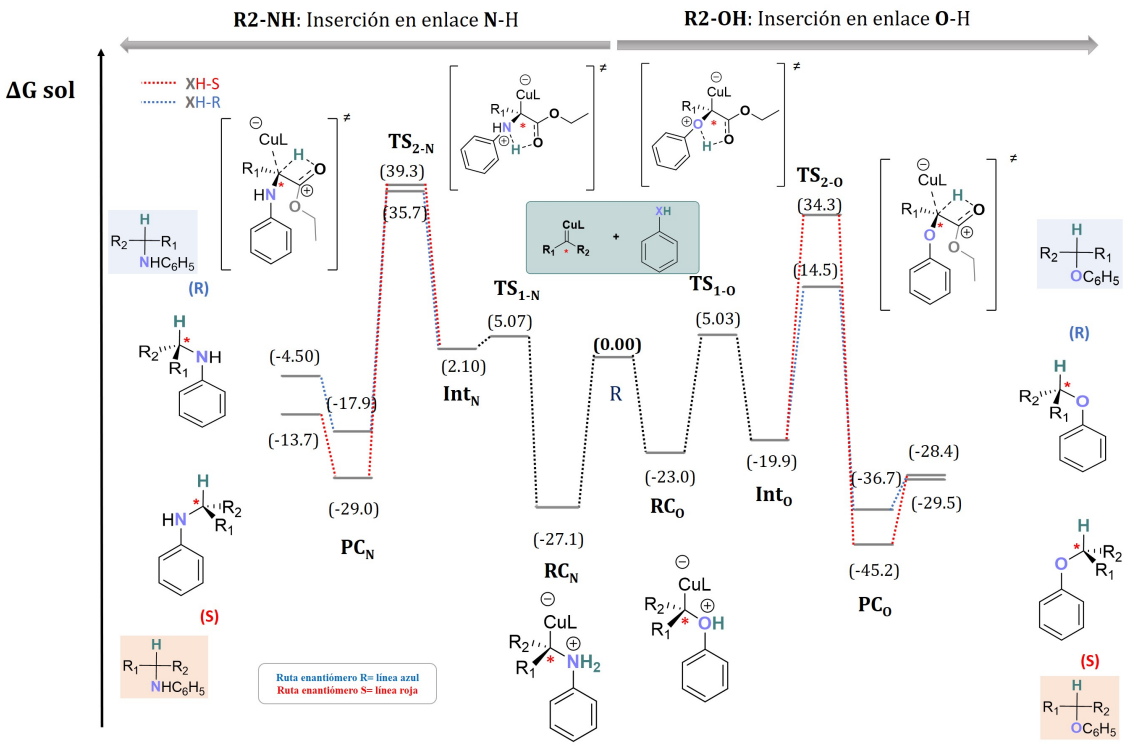

Figura 7.14: Caminos de reacción competitivos para las reacciones **R2-NH** (R y S) y **R2-OH** (R y S). La notación * corresponde al carbono electrofílico (C*). R_1: CH_3 y R_2: $C_3H_5O_2$. El camino de reacción que lleva a la formación del producto con configuración S es representado mediante la línea roja, mientras que la línea azul representa la ruta que lleva a la formación del producto con configuración R. La energía corresponde a la energía libre de Gibbs tomando en cuenta el efecto del solvente diclorometano (CH_2Cl_2). Todos los valores se encuentran en kcal/mol.

7.2.1. Primer proceso: Proceso sin barrera de energía

La Figura 7.14 y 7.15 representan de manera más detallada los pasos nombrados anteriormente de este mecanismo. El primer paso en ambas reacciones corresponde al ataque posterior del sustrato al centro electrofílico C*. Sin embargo, la estereoselectividad de la reacción, a diferencia de **R1-XH**, se define en la formación del $\mathbf{TS}_{2-X}$, caracterizado por la transferencia protónica hacia este mismo carbono C*, la que será discutida más adelante. Este primer paso, al igual que en el caso de **R1-XH** corresponde a un proceso sin barrera de energía llevando a la formación del complejo reactante $\mathbf{RC}_X$. Este sistema reactivo en **R2-NH** es 4.1 kcal/mol más estable que

en **R2-OH** (**RC**$_N$**:** -27.1 kcal/mol *vs.* **RC**$_O$: -23.0 kcal/mol).

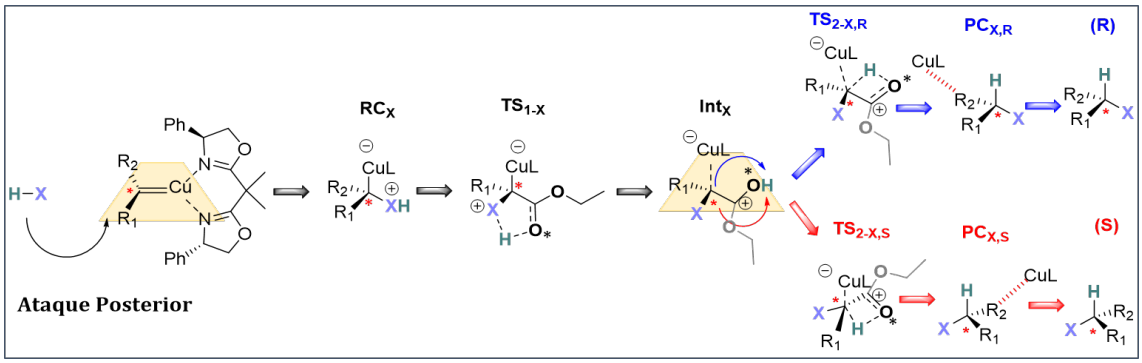

Figura 7.15: Mecanismo propuesto para la reacción **R2-XH**, tomando en cuenta las dos orientaciones en las que la transferencia protónica puede tomar lugar en el segundo paso elemental (**TS**$_{2-X,R}$ y **TS**$_{2-X,S}$, respectivamente). La notación * en color rojo corresponde al carbono electrofílico (C*), mientras que la notación * en color negro corresponde al oxígeno del grupo carbonilo del formiato de etilo (R_2). R_1: CH_3 y R_2: $C_3H_5O_2$. X: C_6H_5**N**H, C_6H_5**O**.

La Figura 7.16 presenta las estructuras de los complejos reactante formados (**RC**$_N$ y **RC**$_O$), donde se observa la conformación espacial que adoptan las estructuras **RC**$_N$ y **RC**$_O$, indicando la participación del oxígeno (O*) proveniente del grupo carbonilo del formiato de etilo ($C_3H_5O_2$) en la reacción, lo que conlleva a la formación de un ciclo de 5 miembros (C*-X-H-O*-C), por medio de un puente de hidrógeno entre el oxígeno (O*) y el H del sustrato. En esta figura, se aprecia además que a mayor estabilidad del complejo reactante **RC**$_N$ formado, se observa un fortalecimiento del enlace C*-N, debido a que la distancia de enlace es menor que en el caso de C*-O (1.51 Å *vs.* 1.57 Å). Los órdenes de enlace asociados a los enlaces C*-N y C*-O son 0.71 y 0.53, respectivamente, confirmando la estabilidad del primer enlace.

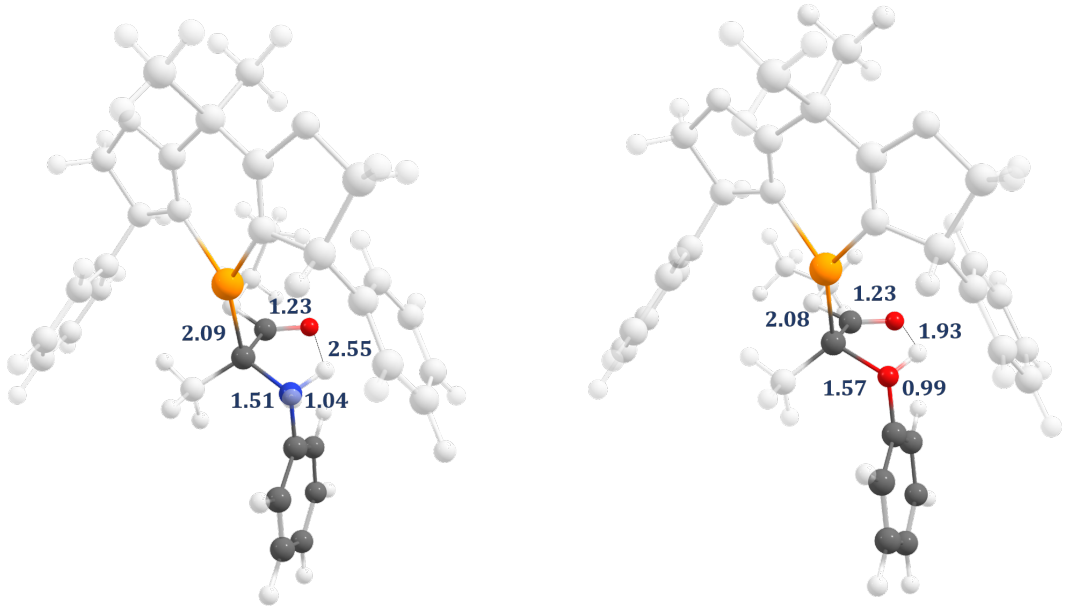

RC$_N$ (-46.2) **RC$_O$** (-23.0)

Figura 7.16: Estructuras de los complejos reactante **RC**$_N$ y **RC**$_O$ en la reacción **R2-XH**, para cada inserción en los enlaces N-H y O-H. El valor entre paréntesis corresponde a la energía libre de Gibbs tomando en cuenta el efecto del solvente (CH_2Cl_2). Todos los valores se encuentran en kcal/mol.

7.2.2. Segundo Proceso: Primer paso elemental

En este paso, se lleva a cabo la primera transferencia protónica (**TS**$_{1-X}$) y el consiguiente debilitamiento del enlace Cu-C*. La transferencia protónica toma lugar desde el heteroátomo (X) al átomo de oxígeno (O*) del grupo R_2. Este primer paso cinético presenta energías libres relativas (ΔG_{sol}) de 5.07 y 5.03 kcal/mol para **R2-NH** y **R2-OH**, respectivamente. Sin embargo, la altura de la barrera de energía correspondiente a este paso (desde **RC**$_X$ a **TS**$_{1-X}$) es mayor para **R2-NH** que para **R2-OH** ($\Delta G^{\neq}_{sol}$: 32.2 *vs.* 28.0 kcal/mol), lo cual es producto tanto de la mayor estabilización que presenta el complejo reactante en **RC**$_N$, como también de la naturaleza electrónica del protón que participa de la transferencia protónica, donde en **TS**$_{1-N}$ el protón transferido presenta una carga de +0.31 |e|, mientras que en **TS**$_{1-O}$ de +0.40 |e|.

De esta forma, en **R2-NH**, al átomo aceptor (O*) le dificulta en mayor medida la abstracción del protón.

Es importarte destacar que en la reacción **R2-NH** el protón participante de la transferencia protónica es distinto al que participa en **R1-NH**, de tal modo que en **R2-NH** se transfiere el protón con menor carga positiva. La Figura 7.17 muestra que para el caso de **R1-NH**, es decir, cuando la reacción toma lugar por un mecanismo concertado, el protón que participa de la reacción corresponde al protón más electropositivo (+0.35 |e|), mientras que si la reacción se lleva a cabo mediante un mecanismo en etapas (**R2-NH**) el protón menos electropositivo (+0.31 |e|) es aquel que se transfiere.

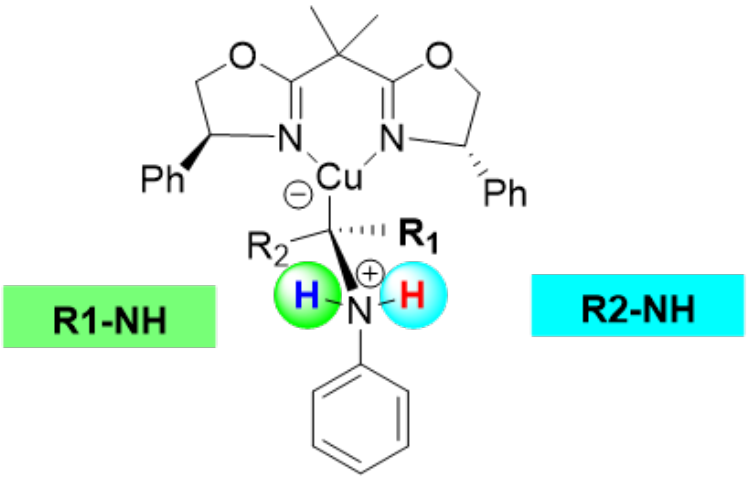

Figura 7.17: Estructura del complejo reactante $\mathbf{RC}_N$. La esfera de color verde corresponde al protón que participa de la reacción **R1-NH**, mientras que la esfera de color celeste corresponde la protón que participa de la reacción **R2-NH**.

La primera transferencia protónica lleva a la formación de los intermediarios $\mathbf{Int}_N$ y $\mathbf{Int}_O$, que son mostrados en la Figura 7.18. Estos intermediarios presentan un enlace Cu-C* debilitado, con órdenes de enlace de 0.25 para **R2-NH** y 0.24 para **R2-OH**, dando cuenta del comienzo de la salida del complejo metálico, y generando por lo tanto interacciones no covalentes entre el átomo de cobre y el C*.

Los intermediarios presentan energías de 2.10 kcal/mol para **R2-NH** y -19.9 kcal/mol para **R2-OH**, por lo que existe una importante diferencia en la termodinámica en ambos procesos. **R2-OH** lleva a la formación de una especie intermediaria con mayor estabilidad que **R2-NH**. Es importante notar que en este paso, el enlace C*-X es más fuerte en el caso de **R2-OH** y tiene mayor estabilidad (distancia de enlace (orden de enlace): 1.40 Å (1.2) en **R2-OH** *vs.* 1.45 Å (1.1) en **R2-NH**). Adicionalmente, la mayor estabilidad del intermediario $\mathbf{Int}_O$, viene dada por la deslocalización electrónica que presenta el anillo aromático del sustrato, lo cual es producto de la conjugación electrónica del par de electrones libres del oxígeno en el anillo aromático.

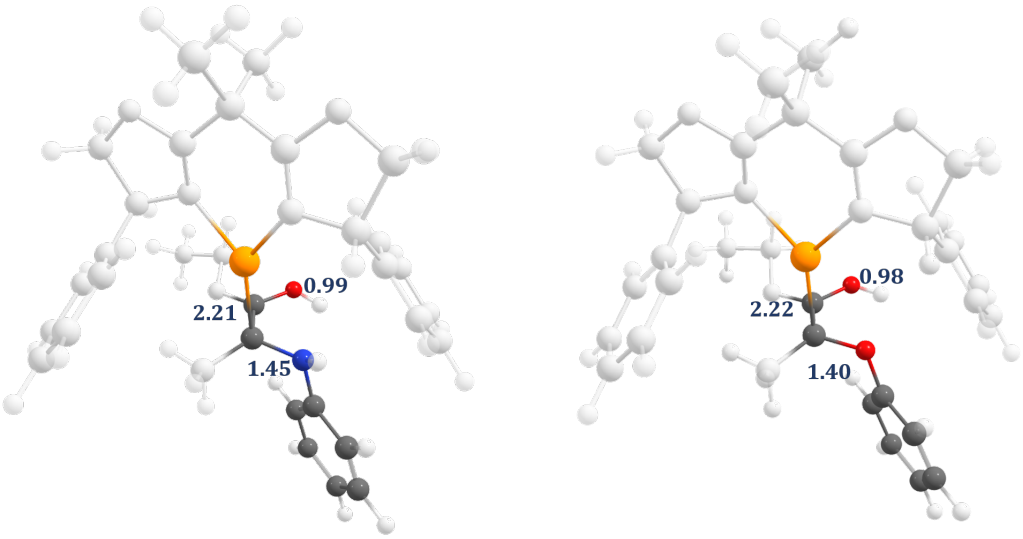

$\mathbf{Int_N}$ (2.10) $\mathbf{Int_O}$ (-19.9)

Figura 7.18: Estructuras de los intermediarios $\mathbf{Int}_N$ y $\mathbf{Int}_O$ en **R2-XH**

7.2.3. Tercer Proceso: Segundo paso elemental

El siguiente paso corresponde al paso determinante de la reacción, el que involucra tanto la transferencia protónica desde el grupo hidroxilo (proveniente del grupo atrac-

tor de electrones) hacia el átomo de carbono (C*), como también la salida definitiva del complejo metálico (CuL), donde ambos eventos químicos ocurren de manera no simultánea.

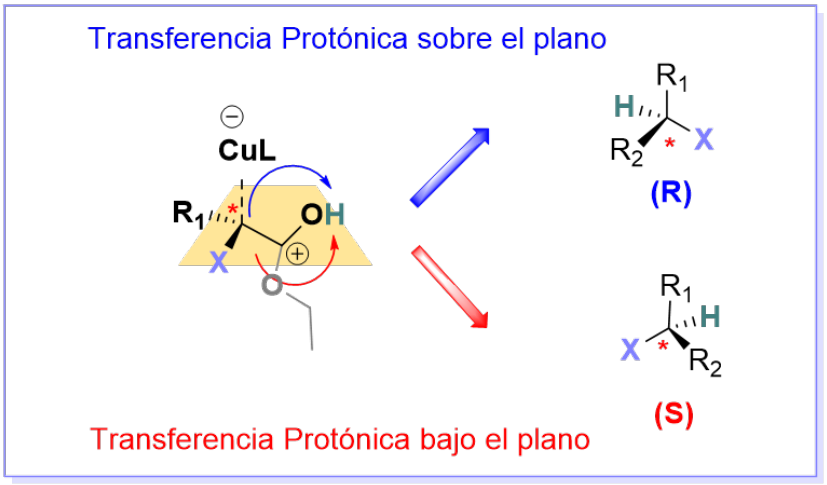

Figura 7.19: Esquema explicativo sobre las dos orientaciones que puede tomar la transferencia protónica, la cual corresponde al segundo paso elemental y paso determinante de la reacción **R2-XH**. R_1:CH_3, R_2: $C_3H_5O_2$, X: N,O.

Este paso es importante debido a que la transferencia protónica puede ocurrir sobre o bajo el plano (coloreado en amarillo en la Figura 7.19), generando dos productos de inserción con configuración enantiomérica distinta (R y S). La formación del enantiómero R tiene energías de 14.5 kcal/mol para **R2-OH** y 35.7 kcal/mol para **R2-NH**, mientras que la formación del enantiómero S presenta energías superiores al primer caso (34.3 kcal/mol en energía para **R2-OH** y 39.3 kcal/mol en energía para **R2-NH**). A partir de estos resultados, podemos confirmar que la enantioselectividad de la reacción se ve favorecida cinéticamente hacia la formación del producto con configuración R. Además, es importante mencionar que en el mecanismo en etapas nuevamente el ligando PhBOX juega un rol clave en la enantioselectividad de la reacción, principalmente en **R2-OH**. La enantioselectividad que otorga el ligando se presenta mediante efectos estéricos tanto entre el grupo fenilo del ligando PhBOX

con el grupo formiato de etilo, como con el anillo aromático del sustrato, cuando la transferencia protónica toma lugar por debajo del plano. Estos resultados se pueden visualizar en la Figura 7.20, a partir del análisis 3D de NCI, donde se presenta un menor número de interacciones van der Waals repulsivas en $\mathbf{TS}_{2-X,R}$ que en $\mathbf{TS}_{2-X,S}$.

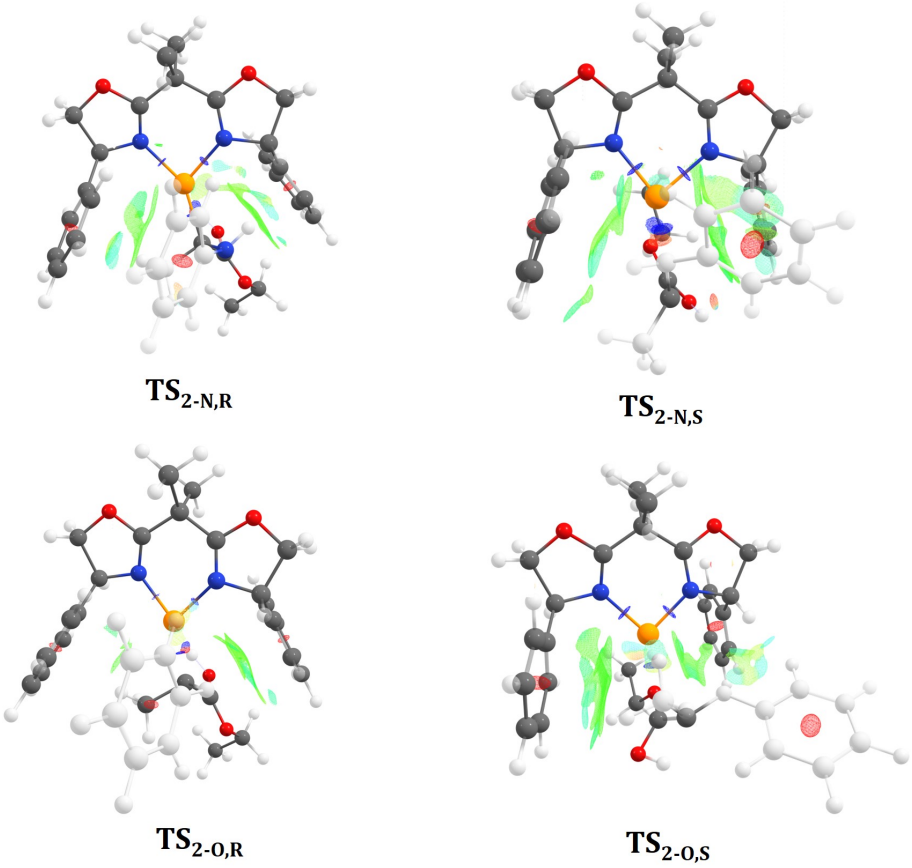

Figura 7.20: Gráficos NCI 3D para las estructuras del estado de transición (**TS**), correspondiente a las reacciones **R2-NH** y **R2-OH**.

Etapa determinante para R2-NH y R2-OH

En este análisis, la discusión se centrará en la reacción más favorable de ambos sistemas, la que corresponde a la transferencia protónica que toma lugar por debajo del plano, ya que es la orientación que ocurre con una menor energía de activación, llevan-

do a la formación del producto de inserción R. Para ello, se utilizó el modelo de fuerza de reacción con la finalidad de analizar la naturaleza física de la energía de activación. Sin embargo, es necesario analizar el perfil de energía potencial con respecto a ξ, el que se muestra en la Figura 7.21 **(a)**. Estos resultados indican que la transferencia protónica corresponde a un proceso favorable para ambas reacciones (**R2-NH** y **R2-OH**) con energías electrónicas de reacción de -26.3 y -32.4 kcal/mol, respectivamente.

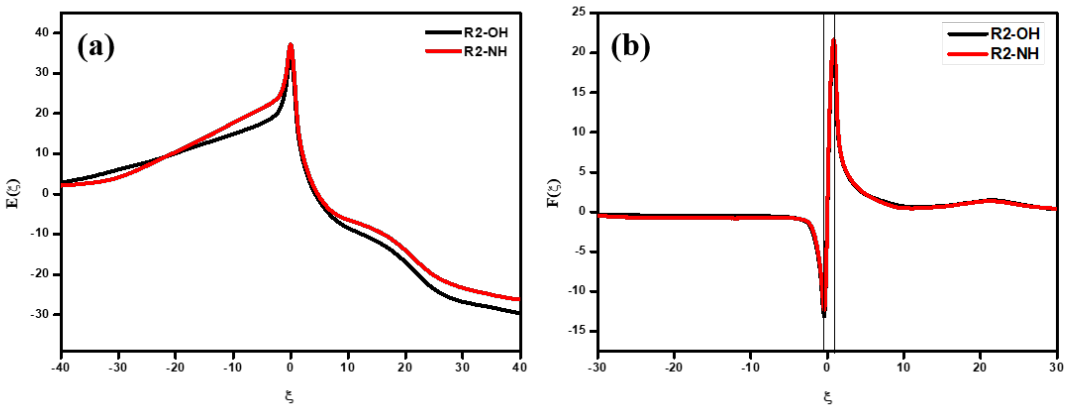

Figura 7.21: (a) Perfil de energía potencial con respecto a la coordenada de reacción ξ. **(b)** Perfil de fuerza de reacción con respecto a ξ. Ambos perfiles correspondientes al paso determinante de **R2-XH**. La línea de color rojo representa la reacción **R2-NH**, mientras que la línea de color negro a la reacción **R2-OH**. Los valores de energía se encuentran en kcal/mol.

La cinética de la reacción representada por la altura de la barrera de energía indica que **R2-NH** tiene una energía de 37.2 kcal/mol, mientras que **R2-OH** de 34.5 kcal/mol. La diferencia en la barrera de energía es pequeña debido a que la naturaleza del heteroátomo proveniente del sustrato (N y O) no afecta directamente a la transferencia protónica, ni tampoco a la salida del complejo de cobre (CuL), sino más bien, sólo afecta a la naturaleza electrónica de los átomos donor (O*)/aceptor(C*) de la transferencia protónica. La Figura 7.22 muestra las cargas atómicas del estado de

transición para ambas reacciones **R2-NH** y **R2-OH**, donde para **R2-NH** el heteráto-mo tiene un efecto electrónico sobre el oxígeno (O*) que permite un leve aumento de la densidad de electrones en este átomo (O*: -0.47 |e| en **R2-NH**, O*: -0.45 |e| en **R2-OH**) y, por lo tanto haciendo levemente más difícil que el átomo donor ceda el protón.

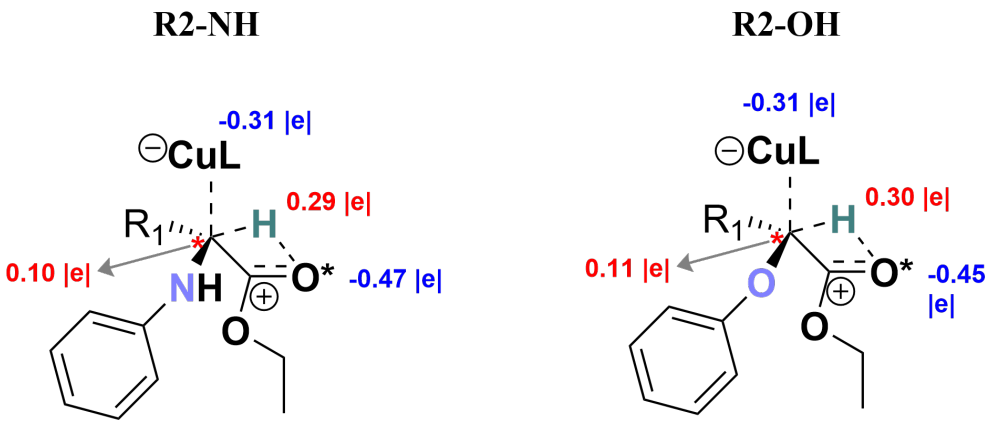

Figura 7.22: Cargas atómicas obtenidas a partir del esquema de partición Hirshfeld-I para la estructura del estado de transición de **R2-NH** y **R2-OH**.

Tabla 7.4: Trabajos de reacción W_1 y W_2 y su contribución porcentual a la energía de activación para las reacciones **R2-NH** y **R2-OH**. Todos los valores se encuentran en kcal/mol y corresponden a energías electrónicas.

R2-NH (37.2)		**R2-OH** (34.5)	
W_1	W_2	W_1	W_2
33.7 (91 %)	3.60 (9 %)	31.1 (90 %)	3.40 (10 %)

En la Figura 7.21 **(b)** se presentan los perfiles de fuerza, donde se puede notar que ambas reacciones proceden prácticamente de la misma forma, los cuales son muy similares entre ellos. Los trabajos de reacción asociados a estas reacciones se muestran en la Tabla 7.4, indicando que la energía asociada a cambios estructurales es la que define la barrera de energía en un 90 %, encontrándose dada por la elongación del ángulo C*-H -O* (ver Figura 7.23 **(c)**). La Figura 7.23 **(a)** muestra que las distancias de enlace O*-H y C*-H se mantienen constantes en la región de reactantes (ξ_R - ξ_{min})

tanto para **R2-NH** como para **R2-OH**, por lo que variaciones en las distancias de enlace no estarían contribuyendo en energía al trabajo de reacción W_1. Adicionalmente, la Figura 7.23 **(b)** muestra que la distancia de enlace Cu-C* en **R2-NH** y **R2-OH**, comienza a disminuir en la región entre ξ_R - ξ_{min}, lo que indica el fortalecimiento del enlace Cu-C* antes de que ocurra la transferencia protónica (2.41 Å a 2.00 Å). Esta disminución de la distancia de enlace corresponde a un fortalecimiento del enlace Cu-C*, proceso que libera energía, por lo que no contribuye al aumento de energía en la región de reactantes (cuantificado en W_1). Es importante mencionar que a partir de la Figura 7.23 **(a)** y **(b)**, se puede señalar que los procesos correspondientes a la transferencia protónica y a la salida del complejo de cobre corresponden a procesos desacoplados, es decir, no se llevan a cabo simultáneamente; donde la transferencia protónica ocurre en la región de transición, mientras que el complejo de cobre se separa en la región de productos.

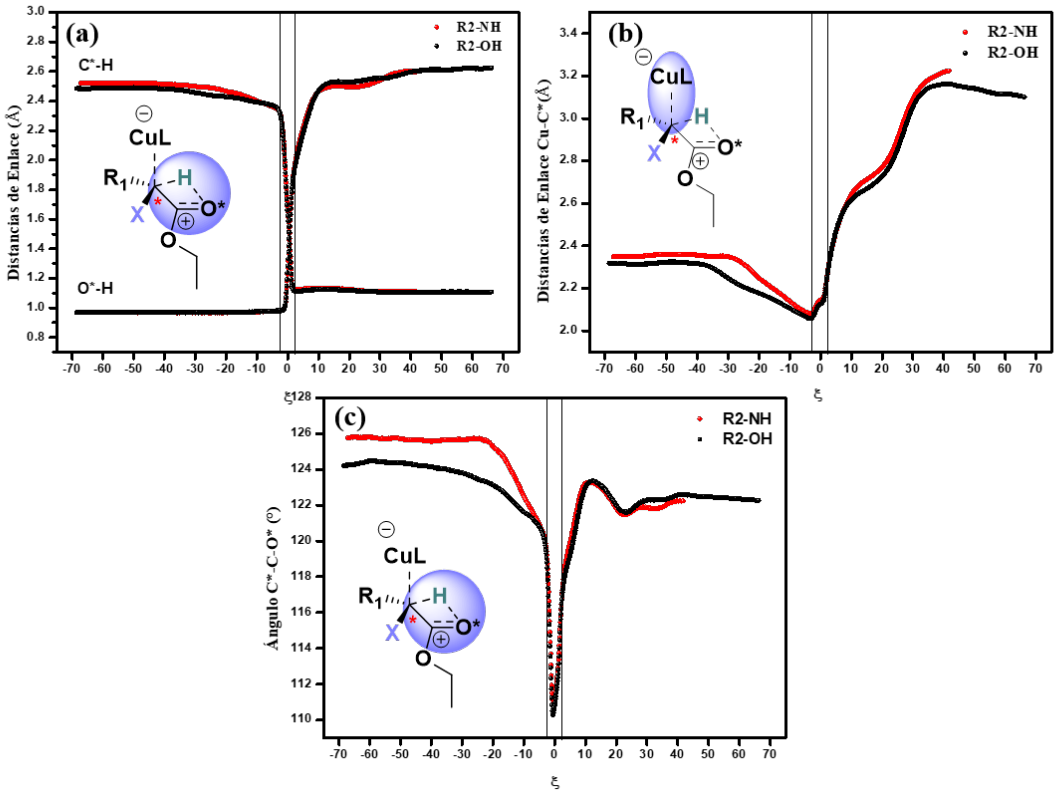

Figura 7.23: **(a)** Perfil de distancia de enlace, correspondiente a enlaces participantes directamente de la transferencia protónica (C*-H y O-H). **(b)** Perfil de distancia de enlace del enlace Cu-C*, característico de la salida del complejo de cobre. **(c)** Perfil de la elongación del ángulo C*-C-O*, característico de la transferencia protónica. Las lineas de color rojo corresponden a la reacción **R2-NH**, mientras que las de color negro a **R2-OH**.

7.2.4. Cuarto Proceso: Interacciones no covalentes entre el producto de inserción y el CuL

El último paso corresponde al rompimiento de las interacciones no covalentes existentes entre el complejo de cobre y el producto de inserción formado. A partir de la Figura 7.14, en **R2-NH** (estructuras $\mathbf{PC}_{N,R}$ y $\mathbf{PC}_{N,S}$) la energía asociada corresponde a 13.4 y 15.3 kcal/mol para llevar al producto de inserción aislado de R y S, respectivamente, mientras que en caso de **R2-OH** (estructuras $\mathbf{PC}_{O,R}$ y $\mathbf{PC}_{O,S}$) son

8.30 y 15.7 kcal/mol en energía para R y S, respectivamente. Estas energías están en el orden de las que se tienen en las interacciones no covalentes, las que dependiendo de la naturaleza de las fuerzas intermoleculares varían de 1.20 a 83.6 kcal/mol [98]. En este contexto, es necesario realizar un análisis de las interacciones intermoleculares que participan en la formación de $\mathbf{PC}_{X,R}$ y $\mathbf{PC}_{X,S}$ a través del uso de NCI.

La Figura 7.24 muestra los gráficos 3D del índice NCI, donde las estructuras $\mathbf{PC}_{N,R}$ y $\mathbf{PC}_{O,R}$, presentan una interacción atractiva (superficie de color azul) entre el átomo de cobre y el oxígeno (O*) del carbonilo (formiato de etilo). Mientras que las estructuras $\mathbf{PC}_{N,S}$ y $\mathbf{PC}_{O,S}$ además de presentar la interacción atractiva entre Cu y O*, presenta otra interacción atractiva entre el átomo de cobre y el hidrógeno proveniente del grupo dador de electrones (CH_3) Cu $\cdots$ H, lo que puede justificar las pequeñas diferencias entre la formación de los isómeros R y S, donde el producto S se ve ligeramente favorecido en ambas inserciones. En este último caso, el producto obtenido a partir de la reacción **R2-OH** es más favorable, debido a que las interacciones son más débiles que en el caso de **R2-NH**.

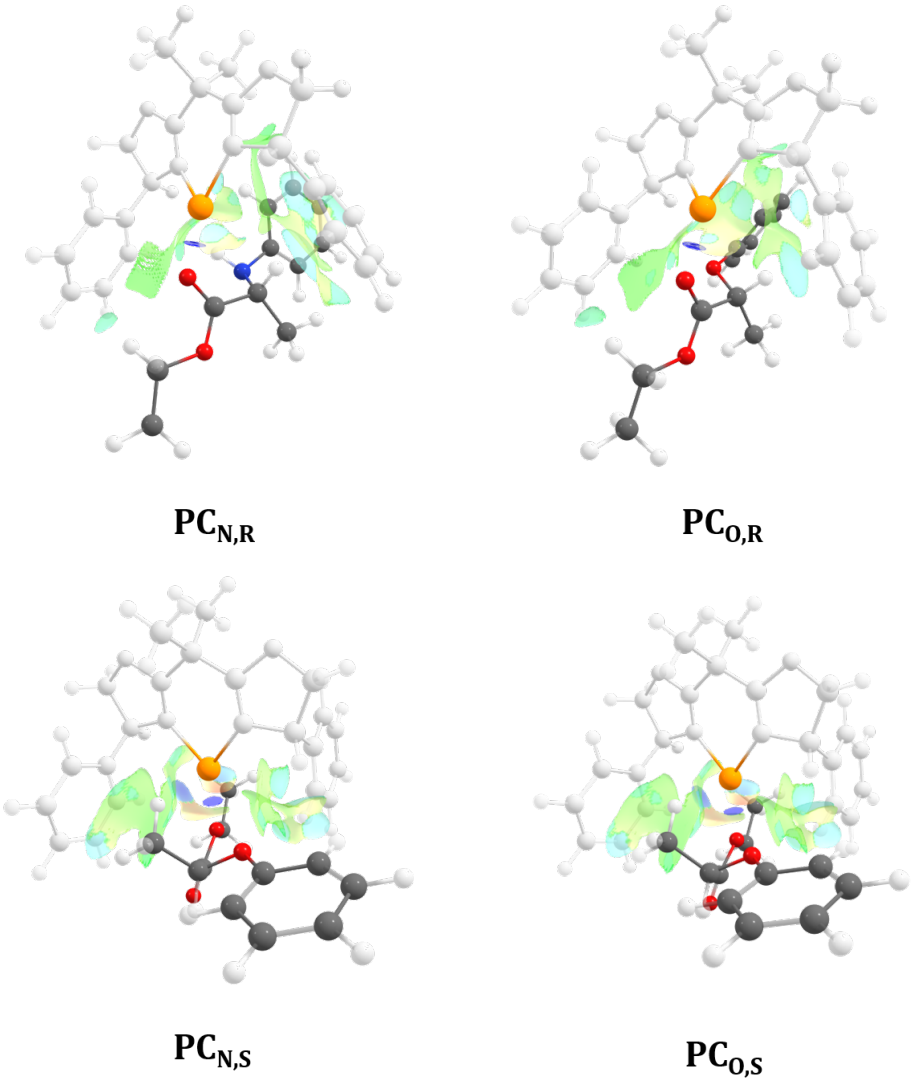

Figura 7.24: Gráficos 3D obtenidos a través del índice NCI para las estructuras de los complejos producto $\mathbf{PC}_{X,R}$ y $\mathbf{PC}_{X,S}$.

En resumen, los principales resultados discutidos en esta sección señalan que este mecanismo presenta cuatro pasos: (i) proceso sin barrera de energía que lleva a la formación de un complejo reactante inicial, mediante un acercamiento posterior del sustrato al carbenoide, (ii) primer paso elemental correspondiente a la primera transferencia protónica, la cual procede desde el heteroátomo al átomo de oxígeno (O*) del sustituyente atractor, (iii) segundo paso elemental y paso determinante de la reacción, correspondiente a la transferencia protónica desde el grupo hidroxilo (sustituyente

atractor) al átomo de carbono C* y (iv) ruptura de interacciones no covalentes entre el producto de inserción y el complejo de cobre. Para el paso determinante los resultados indican que la reacción **R2-OH** se encuentra más favorecida que **R2-NH**, siendo, al igual que en el mecanismo concertado, el sustrato fenólico más favorecido cinética y termodinámicamente. Un aspecto importante que hay que destacar es el hecho de que en la reacción con fenol, la diferencia entre las energías de activación entre los TS que llevan a la formación del enantiómero R y S es de 19.8 kcal/mol, mientras que es de 3.6 kcal/mol para el caso de la anilina, lo que indicaría una reacción con un mayor carácter enantioselectivo si se utiliza fenol como sustrato. Esta enantioselectividad nuevamente se debe, en mayor parte, a la presencia de ligando PhBOX en el complejo de cobre, el cual, genera una mayor presencia de interacciones no covalentes de naturaleza repulsiva en el sistema cuando éste se orienta geométricamente hacia la formación del enantiómero S, especialmente en el caso del sustrato fenólico. Finalmente, la salida del complejo de cobre requiere una menor energía cuando participa el sustrato fenólico que la anilina, favoreciendo aún más el proceso para el caso del fenol.

En síntesis los resultados de este capítulo, señalaron que la reacción de inserción del carbenoide de cobre en los enlaces X-H (X: N, O) se lleva a cabo mediante un mecanismo concertado más que por un mecanismo en etapas, ya que las barreras del paso limitante mostraron ser más bajas para el mecanismo concertado. Por esta razón, en las siguientes secciones del Capítulo 8, el estudio se centrará en las modificaciones estructurales de los reactivos dentro del contexto de un mecanismo concertado.

Capítulo 8

Efecto del Cambio Estructural sobre el Carbenoide y Sustrato

En este capítulo el análisis se centrará principalmente en estudiar como varían las barreras de energía en la reacción de inserción, al modificar el grupo sustituyente en los reactantes; ya que es conocido que el cambio en la estructura de los sistemas reactivos pueden llevar a cambios importantes en la reactividad de las especies químicas y, por lo tanto, modificar las energías involucradas en las transformaciones químicas. En base a esto, es interesante estudiar el efecto del cambio de la reactividad de los sistemas químicos en la reacción de inserción del carbenoide de cobre en el enlace O-H. Para ello, se estudiará el efecto que existe en el mecanismo concertado utilizando fenol como sustrato (**R1-OH**) considerando el ataque posterior. Esta reacción fue escogida debido a que, dentro de este trabajo de tesis, resultó ser la inserción más favorable. Para ello, se presentará el efecto energético que tiene en las barreras de energía el cambio de átomos en los sistemas carbenoide y sustrato. Para el carbenoide se analizará el efecto del cambio del metal y la modificación de los sustituyentes (donor/aceptor), mientras que en el sustrato se estudiará el efecto del cambio del

sustituyente en el anillo aromático.

8.1. Modificación de la estructura en el complejo carbenoide

Como se mencionó anteriormente, la reactividad del complejo carbenoide depende en gran medida de su estructura, ya que cambios en el metal o en los sustituyentes del carbenoide pueden afectar a la naturaleza electrofílica del carbono carbenoide (C*). Existen varios trabajos experimentales que estudian el efecto del cambio en los sustituyentes [2, 13, 19, 29, 99]; sin embargo, en el campo de la química computacional, los estudios teóricos son escasos. Por este motivo, se hace interesante estudiar el efecto del cambio de la estructura del carbenoide desde una perspectiva computacional, enfocándose en estudiar cambios energéticos, electrónicos y orbitalarios.

Efecto del metal en la reactividad del carbenoide

En esta sección se incluye el efecto del metal en la reactividad del sistema carbenoide. Principalmente, se analizaron tres metales del grupo IB: cobre, plata y oro, manteniendo constante el resto de la estructura del carbenoide original (ver Figura 8.1).

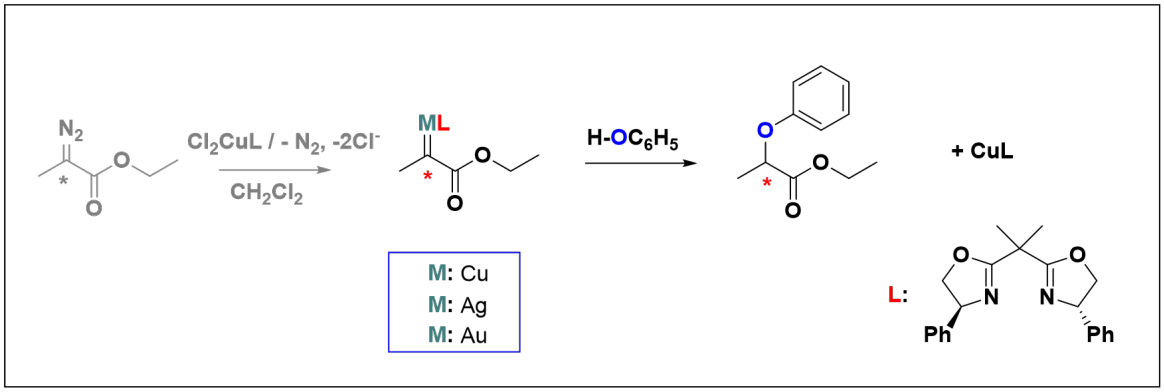

Figura 8.1: Reacción de inserción del carbenoide en el enlace O-H (**R1-OH**). M: Cu, Ag, Au.

La Figura 8.2 **(a)** muestra el perfil de energía potencial para las reacciones **R1-OH-Cu** y **R1-OH-Ag** (**R1-OH-Au** no presenta reactividad hacia la inserción del carbenoide en el enlace O-H). Los resultados mostrados en la figura indican que cuando se modifica el metal de cobre a plata, la barrera de energía disminuye de 20.2 a 14.5 kcal/mol, haciendo más favorable cinéticamente la reacción. Por otro lado, la energía de reacción disminuye de -39.8 a -47.1 kcal/mol señalando que la reacción **R1-OH-Ag** corresponde a una reacción más exotérmica, mientras que, si modificamos el metal de cobre a oro, la reacción no ocurre por el mecanismo concertado propuesto. Esta tendencia está directamente relacionada con la electrofilia local del carbono C* (ver Figura 8.2 **(b)**), donde el carbenoide de Ag presenta una electrofilia local C* de 5.50 eV, mientras que el carbenoide de Cu de 5.09 eV y, por último el carbenoide de oro presenta una electrofilia de 1.99 eV. A partir de estos resultados, se encontró que el carbono C* del carbenoide de oro (**R1-OH-Au**) pierde carácter electrofílico en gran medida, de tal forma que la reacción no presenta las condiciones necesarias para llevarse a cabo; ya que la naturaleza electrofílica del C* corresponde a una condición fundamental para que el carbenoide se inserte en el enlace O-H.

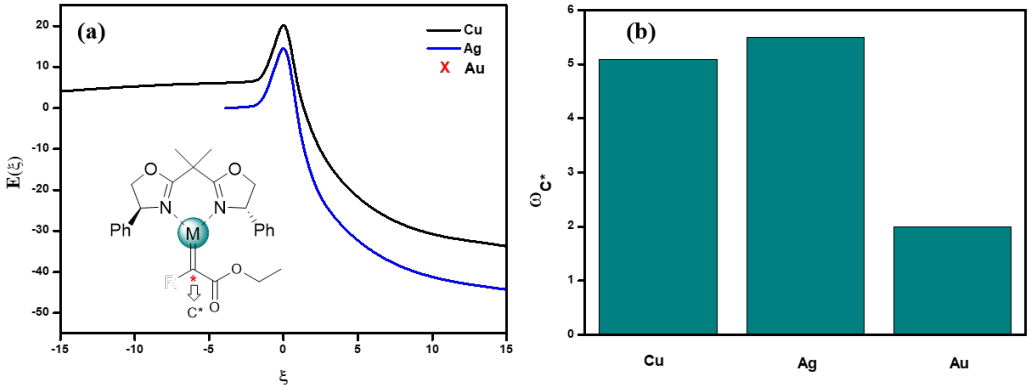

Figura 8.2: (a) Perfil de energía potencial con respecto a ξ. **(b)** Gráfico de barras para la electrofilia local (ω_{C*}) del carbono C* para cada carbenoide estudiado. M: Cu, Ag, Au. Los valores de energía se encuentran en kcal/mol, mientras que la electrofilia local en eV.

Por otro lado, se realizó un análisis de interacción donor-aceptor a partir de los orbitales de enlace natural (NBO) con la finalidad de analizar el mayor carácter electrofílico del carbono C* en el complejo carbenoide de plata. La Figura 8.3 y Tabla 8.1 muestran la interacción orbitalaria correspondiente a la retrodonación π del enlace M - C*, donde el orbital donor corresponde al orbital d_{xy} del metal, mientras que el orbital aceptor corresponde al orbital p_y del C*. En la Figura 8.3 se observa que a medida que existe un mayor solapamiento del orbital d_{xy} con el orbital p_y, la interacción se vuelve más estable (ver Tabla 8.1), de tal forma que el carbenoide de plata presenta un menor solapamiento de los orbitales, lo que implica una menor retrodonación π (9.14 kcal/mol) y, por ende, un carbono central C* deficiente en electrones con un carácter más electrofílico que el carbenoide de Cu y Au.

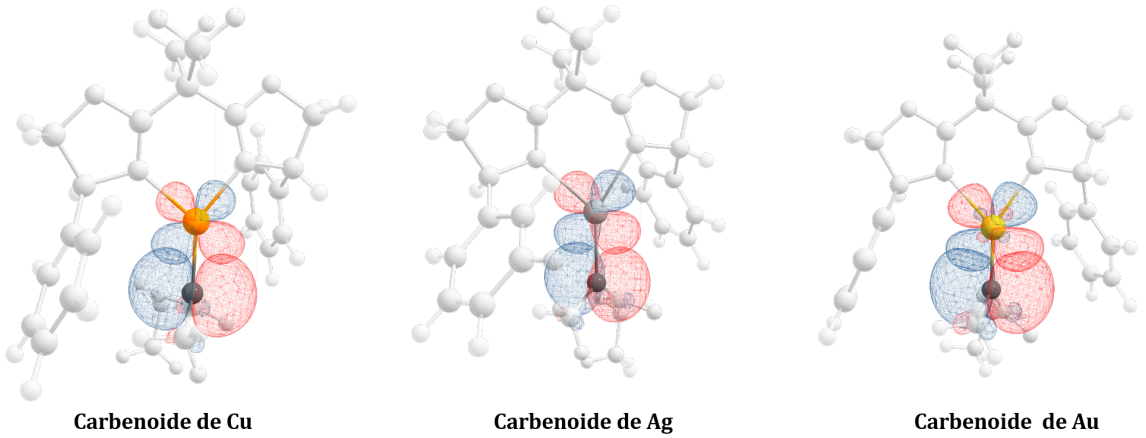

Figura 8.3: Orbitales de enlace natural (NBOs) asociados a la interacción donor-aceptor del enlace M-C* (M: Cu, Ag, Au). El color azul y rojo representan las diferentes fases existentes en los orbitales naturales.

Por otro lado, el carbenoide de oro presenta una retrodonación π con una energía de estabilización de 60.3 kcal/mol y un mayor solapamiento de los orbitales, llevando al carbono central a tener menor carácter electrofílico. El mayor solapamiento de los orbitales en el carbenoide de oro implica un enlace C*-Au más fuerte que C*-Cu y C*-Ag, presentando distancias de enlace de 1.90 Å, 1.96 Å y 2.23 Å, respectivamente. Por esta razón, la mayor retrodonación π es la responsable que se impida el proceso de inserción, ya que el átomo de oro comienza a competir con el C* en la abstracción del protón, tomando lugar la reacción en el metal y, por lo tanto, posiblemente siguiendo otro mecanismo de reacción.

Tabla 8.1: Energía de estabilización (E_{est}) correspondiente a la interacción orbitalaria donor-aceptor del enlace M-C*. Los valores de energías se encuentran en kcal/mol.

Carbenoide	Orbital donor (M)	Orbital aceptor (C*)	E_{est} (kcal/mol)
Cu	d_{xy}	p_y	18.8
Ag	d_{xy}	p_y	9.14
Au	d_{xy}	p_y	60.3

Efecto del sustituyente en la reactividad del carbenoide

Es conocido que los grupos sustituyentes del carbono carbenoide juegan un rol clave tanto en la estabilidad, como en la naturaleza electrofílica del carbono central C*. Estudios experimentales [2, 19, 29] han demostrado que la combinación tanto de un grupo dador junto con un atractor llevan a mejores resultados en rendimiento y selectividad, que la combinación de un grupo atractor/atractor o donor/donor. Esto se debe a que, el grupo atractor de electrones incrementa la electrofilia y reactividad del sistema químico, mientras que el grupo donor de electrones incrementa la selectividad y estabilidad del sistema evitando reacciones laterales competitivas, como lo son las reacciones de ciclopropanación o dimerización [30, 31]. A partir de estos estudios experimentales, se analizará el efecto del cambio del sustituyente tanto del grupo donor como del atractor de electrones, manteniendo constante el resto del carbenoide original.

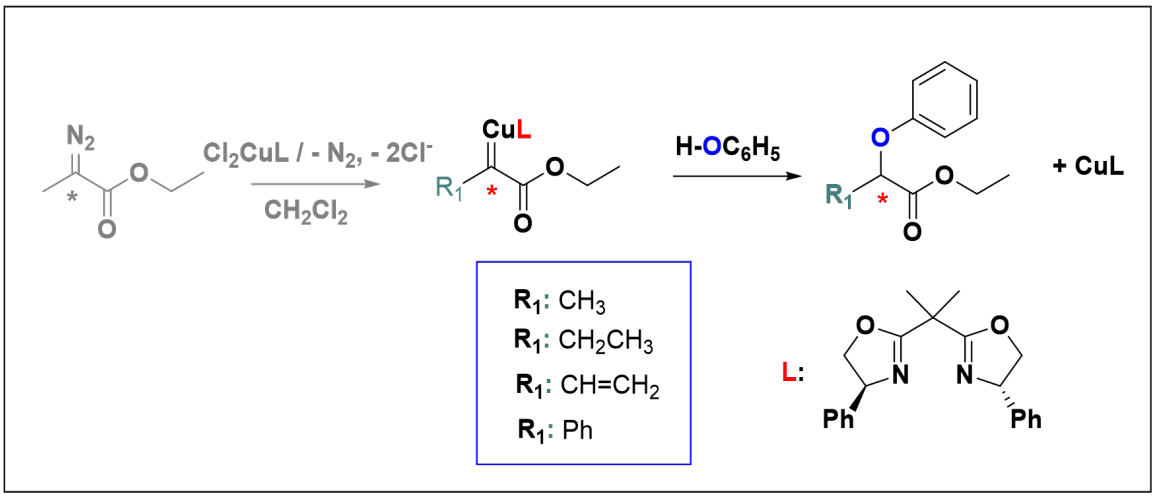

Figura 8.4: Reacción de inserción del carbenoide en el enlace O-H (**R1-OH**), modificando el sustituyente donor de electrones (R_1) del carbenoide y manteniendo constante el grupo atractor de electrones (R_2: $C_3H_5O_2$).

En una primera instancia se analizará el efecto energético que tiene la variación del grupo dador de electrones (R_1) en la reacción **R1-OH**, donde se estudiaron cuatro grupos dadores de electrones, los cuales son mostrados en la Figura 8.4. Los resultados energéticos mostrados en la Tabla 8.2 y Figura 8.5 indican que el grupo fenilo es el grupo dador que tiene un mejor comportamiento respecto a **R1-OH**, disminuyendo la barrera de energía en 2.4 kcal/mol, mientras que los grupos etilo y vinilo aumentan la barrera en 1.1 y 7.2 kcal/mol, respectivamente. Adicionalmente, la reacción se vuelve más favorable a medida que disminuye la energía de activación.

Tabla 8.2: Energía de activación $\Delta E^{\neq}$, energía de reacción ΔE°, energía de interacción del complejo reactante ΔE_{RC}, electrofilia global ω del carbenoide aislado, electrofilia local del C* ω_{C*} en el carbenoide aislado, electrofilia global en la estructura del complejo reactante ω-**RC** y la electrofilia local del C* en la estructura del complejo reactante ω_{C*}-**RC** para la reacción **R1-OH** modificando el sustituyente donor del carbenoide de Cu. El * del grupo CH_3 representa el grupo dador de electrones elegido inicialmente para tratar la reacción. Los valores de energías se encuentran en kcal/mol, mientras que la electrofilia en eV.

R_1	$\Delta E^{\neq}$	ΔE°	ΔE_{RC}	ω	ω_{C*}	ω-**RC**	ω_{C*}-**RC**
Ph	17.8	-48.4	-8.70	12.2	5.25	12.4	2.34
***CH_3**	20.2	-39.8	-20.3	10.4	5.09	5.60	0.65
CH_2CH_3	21.3	-31.3	-21.2	10.3	5.03	5.56	0.60
$CH{=}CH_2$	27.4	-15.4	-21.9	12.7	6.98	5.50	0.52

Para entender los cambios en la barrera energética de la reacción, estudiamos propiedades globales y locales de los sistemas de interés, para ello calculamos la electrofilia global (ω) y la electrofilia local del carbono central (ω_{C*}) del carbenoide sin interactuar con el sustrato (ver Tabla 8.2), donde los resultados indican que existe una correlación entre la disminución de la energía de activación y el aumento de las electrofilias ω y ω_{C*} para los grupos Ph, CH_3 y CH_3CH_2, presentándose electrofilias locales de 5.25, 5.09 y 5.03 eV, respectivamente. Sin embargo, el grupo vinilo no presenta el mismo comportamiento energético, aun así cuando los grupos Ph y $CH{=}CH_2$

comparten un efecto resonante similar (donor), ya que ambos son grupos dadores por resonancia mediante los electrones π del sistema. A partir de estos resultados, se decidió calcular las mismas propiedades que en el estudio anterior (carbenoide y sustrato sin interacción), pero en la geometría del complejo reactante **RC** (interacción con el sustrato), encontrándose que en la geometría **RC** existe una relación importante entre $\Delta E^{\neq}$ y las electrofilias ω-**RC** y ω_{C*}-**RC**, lo que implica que el vinilo pierde en gran medida el carácter electrofílico del carbono C* en la estructura del complejo reactante (**RC**). Esta pérdida de electrofilia viene dada por el efecto electrónico del grupo vinilo, donde los orbitales π del doble enlace se encuentran alineados y conjugados con los orbitales π del grupo atractor de electrones (formiato de etilo).

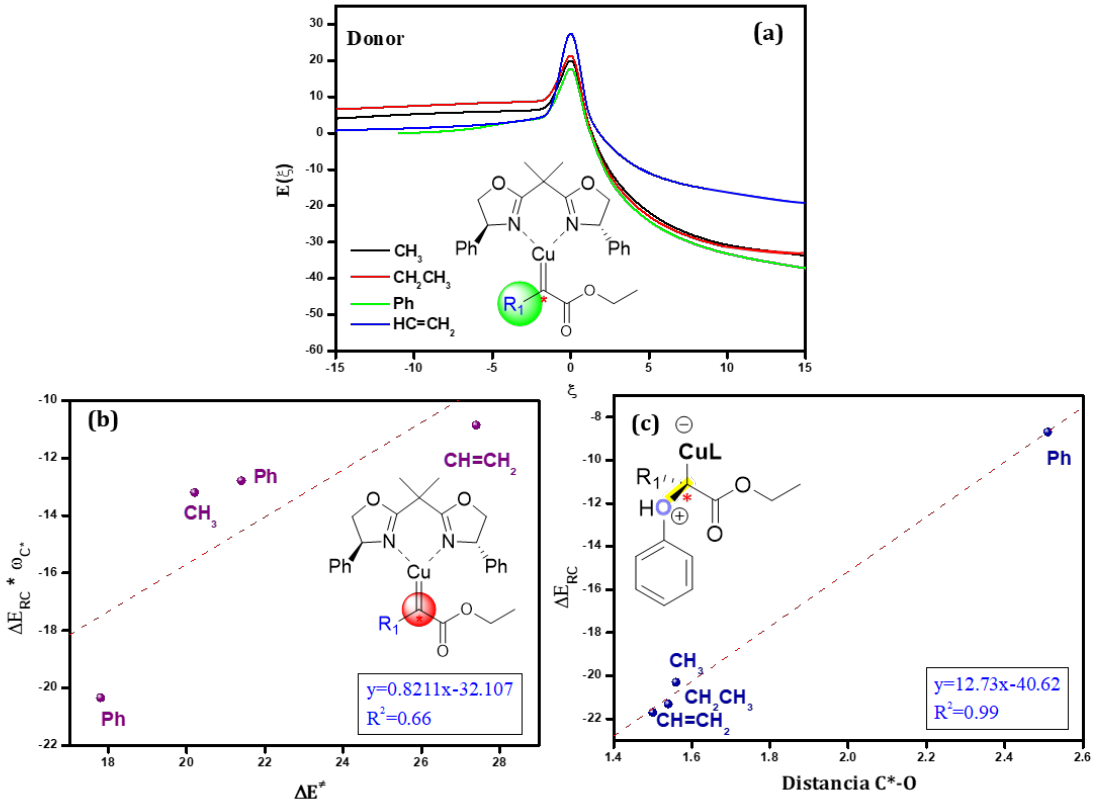

Figura 8.5: **(a)** Perfil de energía potencial para la reacción **R1-OH**, variando el grupo dador de electrones (R_1) y manteniendo constante el R_2 (formiato de etilo). **(b)** Gráfico del producto entre la energía de interacción del complejo reactante y la electrofilia local del C* (ΔE_{RC} x ω_{C*}) *vs.* la energía de activación ($\Delta E^{\neq}$), **(c)** Gráfico de energía de interacción del complejo reactivo (ΔE_{RC}) *vs.* la distancia de enlace C*–O del complejo reactante. Los valores de energía se encuentran en kcal/mol y la electrofilia local está en eV.

Por otra parte, en la Tabla 8.2 se encontró una tendencia importante entre la energía del interacción del complejo rectante (ΔE_{RC}) y la energía de activación ($\Delta E^{\neq}$), donde un aumento de la estabilidad, implica un aumento de energía de activación, de tal modo, que la barrera de energía se encuentra dominada por dos factores igualmente importantes, tales como la estabilización del complejo reactante y la electrofilia local de C*. De esta forma, se graficó el producto entre ΔE_{RC} y ω_{C*}-**RC** *vs.* la energía de activación, donde los resultados mostraron una relación lineal entre ambos factores

(ver Figura 8.5 **(b)**).

Adicionalmente, se estudió el origen de la estabilización del complejo reactante, donde se encontró una buena correlación entre la distancia del enlace (o interacción en algunos casos) de C*- O y la estabilidad de la geometría del complejo reactante **RC** (ver Figura 8.5 **(c)**), de tal modo, que un aumento en la distancia de C*-O conduce a un aumento de ΔE_{RC} y, por ende una pérdida de estabilidad.

Un efecto importante que puede influir en este tipo de reacciones es el efecto atractor de electrones del grupo R_2 manteniendo sin modificación R_1: CH_3, para ello se estudiaron seis sustituyentes, los cuales se muestran en la Figura 8.6.

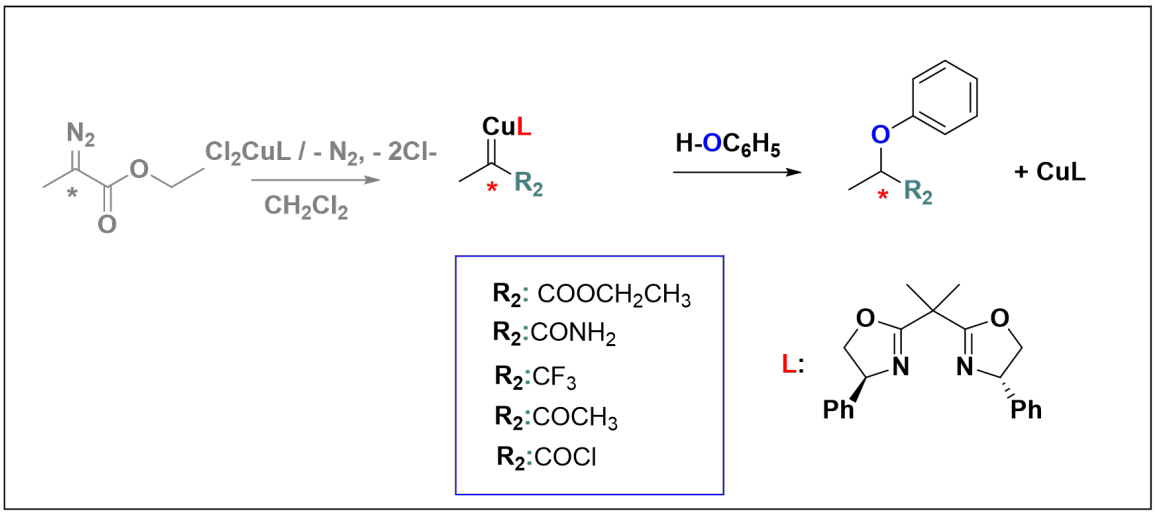

Figura 8.6: Reacción de inserción del carbenoide sobre el enlace O-H (**R1-OH**), modificando el sustituyente atractor de electrones (R_2) del carbenoide de cobre, manteniendo el grupo donor de electrones (R_1: CH_3) constante.

Los resultados energéticos mostrados en la Tabla 8.3 y Figura 8.7 **(a)** señalan que el grupo amida presenta la menor barrera de energía, disminuyendo en 6.1 kcal/mol con respecto a **R1-OH**. Para el resto de los casos, no existe un efecto energético importante hacia la disminución de la barrera de energía.

Por otro lado, a diferencia de la variación del grupo donor de electrones, en este caso no existe una relación clara entre la energía de activación y la electrofilia (global y local) del sistema (ver Tabla 8.3), siendo la estabilización del complejo reactante la que determina las diferencias observadas en la barrera de energía, dado que existe una correlación entre la energía de activación y la distancia del enlace C*-O (ver Figura 8.7 **(b)**).

Tabla 8.3: Energía de activación $\Delta E^{\neq}$ y energía de reacción ΔE° para la reacción **R1-OH** modificando los sustituyentes atractores del carbenoide de Cu. El * del grupo $C_3H_5O_2$ representa el grupo atractor de electrones elegido inicialmente para tratar la reacción. Los valores de energías se encuentran en kcal/mol.

R_2	$\Delta E^{\neq}$	ΔE°	ω	ω_{C*}	ω-**RC**	ω_{C*}-**RC**
$CONH_2$	14.1	-53.6	9.92	4.30	5.92	0.15
CHO	18.9	-49.5	11.3	5.09	6.07	0.44
CF_3	19.0	-45.5	11.7	5.03	5.93	0.06
$*COOCH_2CH_3$	20.2	-39.8	10.4	5.09	5.49	0.65
$COCH_3$	23.3	-21.2	10.5	5.20	5.91	0.19
COCl	30.3	-34.9	12.4	4.70	5.83	0.67

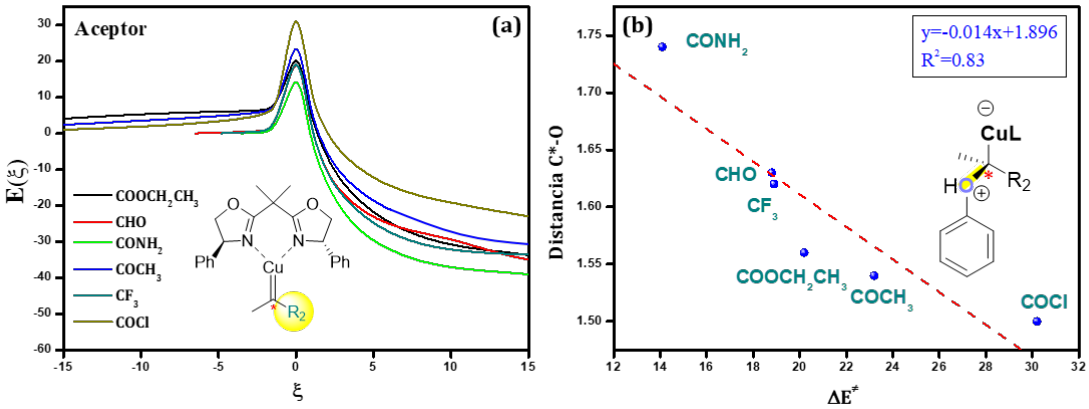

Figura 8.7: **(a)** Perfil de energía potencial para la reacción **R1-OH**, variando el grupo atractor de electrones (R_2) y manteniendo constante el R_1 (metilo). **(b)** Gráfico de la distancia de enlace C*-O del complejo reactante *vs.* la energía de activación ($\Delta E^{\neq}$). Los valores de energía se encuentran en kcal/mol.

En resumen, los resultados de esta sección, correspondientes a la modificación estructural del carbenoide, señalan que los cambios del metal y del sustituyente en el carbenoide pueden llevar a resultados cinéticamente favorables. De tal modo, se mejora la cinética del proceso de inserción cuando cambiamos el metal del carbenoide de cobre a plata, debido a la baja retrodonación π que presenta el carbenoide de plata, llevando a un C* más electrofílico. Por otro lado, dentro de los sustituyentes donores del carbenoide, el grupo fenilo disminuye en 2.4 kcal/mol la energía de activación respecto a **R1-OH** (reacción utilizada como modelo de comparación, R_1:CH_3) mejorando de este modo el proceso de inserción, lo cual es producto tanto de la menor estabilización del complejo reactante, como de la mayor electrofilia que presenta el carbono C*. Mientras que dentro del set de los grupos atractores de electrones, la amida mostró ser la mejor candidata con respecto a la cinética de la reacción, debido a la menor estabilización que presenta la estructura del complejo reactante.

8.2. Modificación en la estructura del sustrato

Estudio de efecto del sustituyente en la reactividad del sustrato

En esta sección nos centraremos en estudiar el efecto energético que tiene en la energía de activación la modificación estructural del sustrato fenólico. Principalmente, porque el cambio en la reactividad del fenol corresponde a un análisis interesante dentro del estudio de la reacción de inserción del carbenoide en el enlace O-H, ya que los cambios en la densidad electrónica del heteroátomo llevan a efectos importantes en la cinética de la reacción. Por lo que, en esta sección se realizará un análisis del efecto que tiene el cambio del sustituyente en el anillo del fenol desde un punto de vista energético, sustituyendo el anillo aromático en las posiciones orto, meta y para

respecto al OH. Para ello, se estudió un set de sustituyentes para cada posición, los cuales son mostrados en la Figura 8.8.

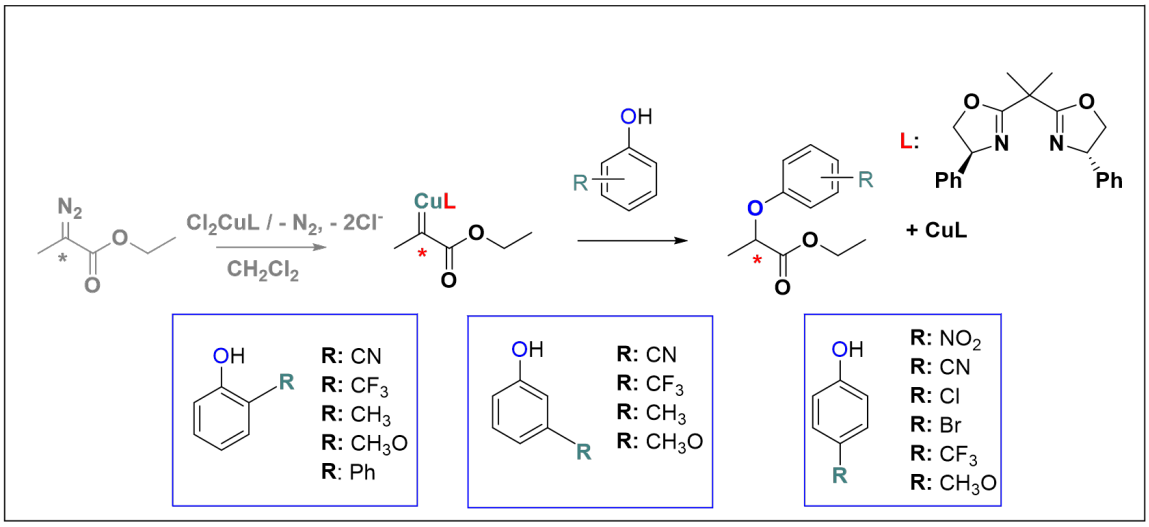

Figura 8.8: Reacción de inserción del carbenoide en el enlace O-H (**R1-OH**). R corresponde al sustituyente en estudio para cada posición (para, meta y orto).

La Figura 8.9 **(a)** muestra el efecto en la energía de activación del sustituyente en posición para, donde los sustituyentes estudiados corresponden principalmente a grupos atractores de electrones (EWG, *Electron Withdrawing Group*), exceptuando al grupo metoxilo que corresponde a un grupo donor de electrones por efecto mesomérico (EDG, *Electron Donating Group*) y EWG por efecto inductivo. Los resultados energéticos indican que al sustituir el fenol, la reacción de inserción toma valores de energía de activación más bajos que el fenol sin sustituir, disminuyendo así la energía del paso elemental entre 7.52 a 6.18 kcal/mol, además la disminución de la barrera de energía lleva consigo un aumento proporcional en la exotermicidad de la reacción (ver Tabla 8.4). Adicionalmente, se estudió el efecto del sustituyente en los trabajos de reacción, donde los resultados son mostrados en la Tabla 8.4, los cuales señalan que el sustituyente ejerce un efecto electrónico importante en la barrera de energía, de tal forma que el aumento en W_2 se traduce en un aumento en la barrera de energía.

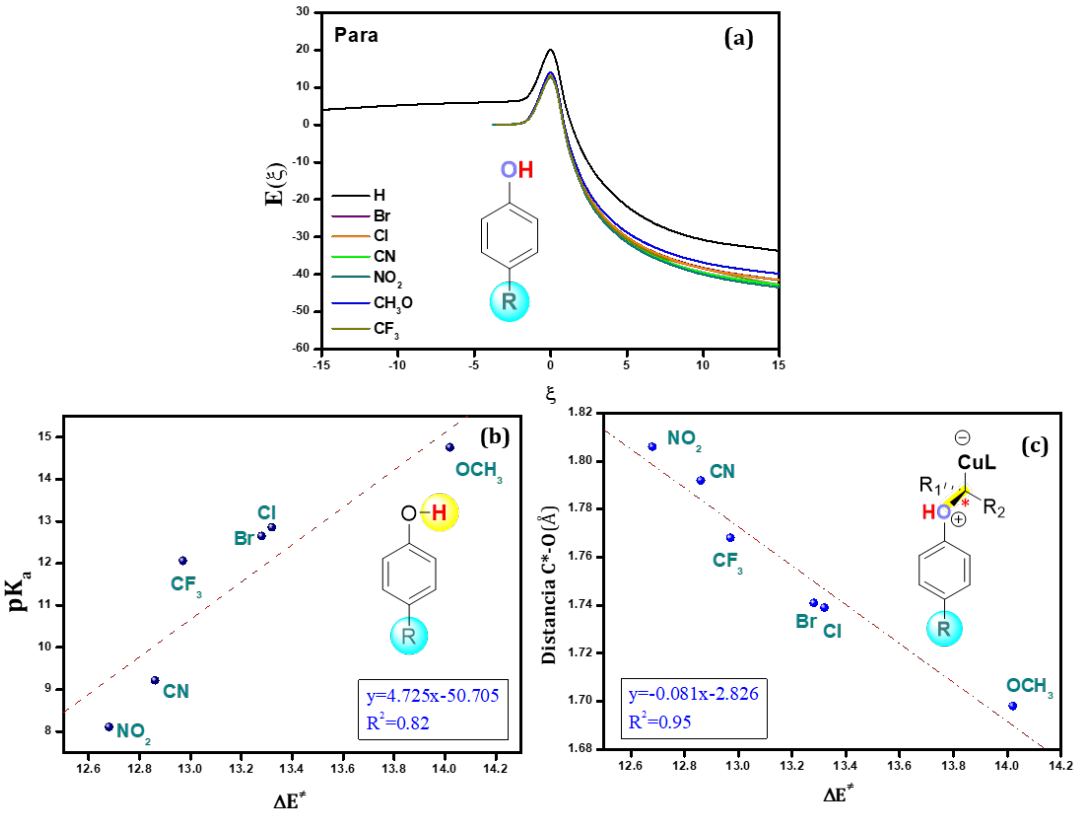

Figura 8.9: **(a)** Perfil de energía potencial respecto a ξ, modificando el sustituyente en posición para. **(b)** Gráfico de pK_a del protón H del fenol sustituido en para *vs.* la energía de activación ($\Delta E^{\neq}$). **(c)** Gráfico de la distancia de enlace C*-O del complejo reactante *vs.* la energía de activación ($\Delta E^{\neq}$) R_1: CH_3, R_2: $C_3H_5O_2$. Todos los valores de energía se encuentran en kcal/mol.

El aumento del efecto electrónico al sustituir el fenol en la posición para fue estudiado tanto desde el punto de vista del cambio de acidez que presenta el protón que se transfiere, como también en la estabilidad que presenta el complejo reactante ($\mathbf{RC}_O$) en cada reacción. El análisis de la acidez del protón que participa del paso elemental de la reacción, fue estudiado mediante el cálculo del pK_a de los sustratos sustituidos (ver Figura 8.9 **(b)**), donde los resultados indican que existe una relación lineal entre pK_a y la energía de activación. De tal forma, que un aumento del pK_a, el cual se re-

laciona con la disminución de la acidez del protón, implica un aumento de la barrera de energía.

Tabla 8.4: Energía de activación $\Delta E^{\neq}$, energía de reacción ΔE°, porcentaje de los trabajos de reacción W_1 y W_2 para la reacción **R1-OH** modificando el sustituyente en la posición para al OH del fenol. Los valores de energías se encuentran en kcal/mol.

Sustituyente en para	$\Delta E^{\neq}$	ΔE°	W_1	W_2
H	20.2	-39.8	80 %	20 %
NO_2	12.7	-53.8	71 %	29 %
CN	12.9	-53.4	66 %	34 %
CF_3	13.0	-52.7	67 %	33 %
Br	13.3	-51.3	67 %	33 %
Cl	13.4	-51.2	67 %	33 %
CH_3O	14.0	-48.6	68 %	32 %

Por otra parte, la estabilidad de complejo reactante también juega un rol importante en la barrera de energía, donde la Figura 8.9 **(c)** muestra la relación lineal que existe entre la distancia de enlace C*- O y la energía de activación. De tal manera, que mientras la distancia de enlace C*-O es más corta se traduce en un enlace más fuerte, correspondiente a un proceso que libera una mayor cantidad de energía. Esta mayor energía liberada al formar el complejo reactante trae consigo un aumento en la barrera de energía. Por lo tanto, mientras mayor estabilidad presenta el complejo reactante, mayor es la energía de activación requerida para transformar las especies químicas en productos.

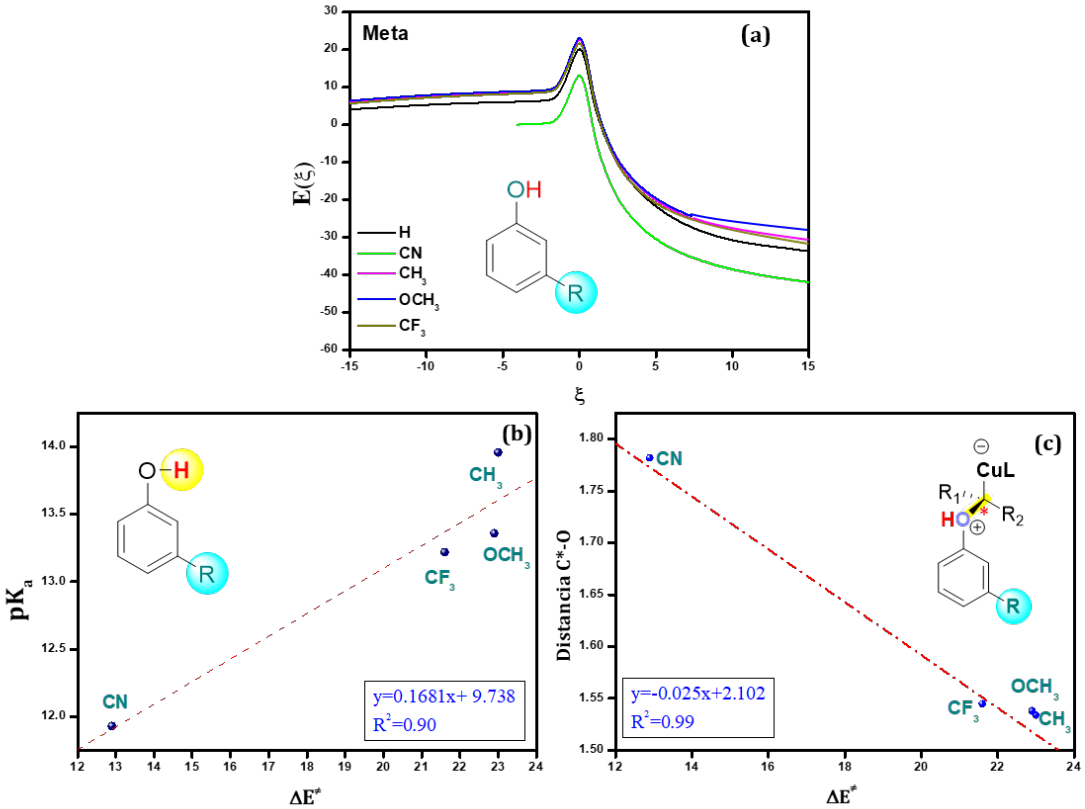

Figura 8.10: **(a)** Perfil de energía potencial respecto a ξ, modificando el sustituyente en posición meta. **(b)** Gráfico de pK_a del protón H del fenol sustituido en meta *vs.* la energía de activación ($\Delta E^{\neq}$). **(c)** Gráfico de distancia de enlace C*-O del complejo reactante *vs.* la energía de activación ($\Delta E^{\neq}$). Todos los valores de energía se encuentran en kcal/mol.

Por otro lado, también se hace interesante estudiar el comportamiento presente en las posiciones meta y orto. Para la posición meta se utilizaron cuatro sustituyentes entre ellos dos grupos EWG: CN, CF_3 y, dos grupos EDG: CH_3, OCH_3 (EWG por efecto inductivo). Los resultados energéticos mostrados en la Figura 8.10 **(a)** y Tabla 8.5 indican que el grupo atractor ciano presenta la menor barrera de energía, con una energía de activación de 12.9 kcal/mol, mientras que el grupo trifluorometilo, metoxilo y metilo presentan barreras de energía cercanas entre ellas pero más altas que la reacción de referencia (R: H, $\Delta E^{\neq}$ = 20.2 kcal/mol), con energías de 21.6, 22.7 y

23.0 kcal/mol, respectivamente. Adicionalmente, los trabajos de reacción mostrados en la Tabla 8.5 señalan que el aumento de la barrera tiene una relación inversa con el aumento del trabajo W_2, de tal modo, que un aumento en este trabajo implica una disminución de la barrera de energía, siendo el grupo ciano el que posee mayor W_2 y una menor barrera de energía.

El comportamiento del trabajo W_2 se comparó con el análisis del pK_a de los sustratos y la estabilidad del complejo reactante. Los resultados mostrados en la Figuras 8.10 **(b)** y **(c)** indican que en el caso del efecto en la posición meta, existe nuevamente una relación lineal de la energía de activación con el pK_a y la distancia de enlace C*-O. Por lo que, el aumento de la energía de activación se debe tanto a la disminución de la acidez del protón, como a la mayor estabilidad presente en la estructura del complejo reactante.

Tabla 8.5: Energía de activación $\Delta E^{\neq}$, energía de reacción ΔE°, porcentaje de los trabajos de reacción W_1 y W_2 para la reacción **R1-OH** modificando el sustituyente en la posición meta al OH del fenol. Los valores de energías se encuentran en kcal/mol.

Sustituyente en meta	$\Delta E^{\neq}$	ΔE°	W_1	W_2
H	20.2	-39.8	80 %	20 %
CN	12.9	-51.5	67 %	33 %
CF_3	21.6	-38.8	80 %	20 %
OCH_3	22.7	-35.9	80 %	20 %
CH_3	23.0	-35.4	80 %	20 %

Dentro del análisis del efecto en la posición meta, es importante mencionar que en esta posición prima principalmente el efecto inductivo. Ya que el efecto mesómerico en posición meta se reduce en gran medida y tiene una baja contribución al efecto que tiene el sustituyente en la barrera de energía. Adicionalmente, el poder del efecto inductivo dentro de los sustituyentes correlaciona adecuadamente con los resultados obtenidos, donde el grupo ciano presenta un efecto inductivo atractor (-I), priman-

do un efecto inductivo π (I_π). Mientras que, el grupo trifluorometilo y el metoxilo también tienen un efecto inductivo atractor, pero un efecto inductivo σ (I_σ) que se desvanece rápidamente y, sólo es significativo a cortas distancias. Por último, el grupo metilo, el cual presenta la mayor barrera, corresponde a un grupo dador por efecto inductivo mediante enlace sigma (I_σ).

Es importante notar, que las variaciones de la energía de activación para las posiciones para y meta no necesariamente pueden ser explicadas aislando las variables pK_a y la estabilidad del complejo reactante, ya que la energía de activación depende simultáneamente de ambas variables. Sin embargo, en la posición orto el comportamiento de la barrera de energía está sujeta a la compensación de ambos efectos.

Tabla 8.6: Energía de activación $\Delta E^{\neq}$, energía de reacción ΔE°, porcentaje de los trabajos de reacción W_1 y W_2 para la reacción **R1-OH** modificando el sustituyente en la posición orto al OH del fenol. Los valores de energías se encuentran en kcal/mol.

Sustituyente en orto	$\Delta E^{\neq}$	ΔE°	W_1	W_2
H	20.2	-39.8	80 %	20 %
CF_3	12.6	-53.5	71 %	29 %
CN	13.5	-51.3	69 %	21 %
CH_3	14.2	-48.9	67 %	33 %
Ph	14.2	-47.3	67 %	33 %
OCH_3	24.0	-43.8	71 %	29 %

La Tabla 8.6 y Figura 8.11 muestran los resultados obtenidos para la posición orto, donde se estudiaron cinco sustituyentes dos de ellos EWG: CF_3, CN y tres EDG: CH_3, Ph y OCH_3 (siendo Ph y OCH_3 también EWG por efecto inductivo). Los resultados indican que no existe una relación directa entre la energía de activación con los trabajos de reacción. Mientras que se encontró una pobre tendencia entre la energía de activación tanto con el pK_a del fenol sustituido, como con la estabilidad del complejo reactante. Sin embargo, excluyendo al grupo ciano la correlación mejora en el

gráfico de $\Delta E^{\neq}$ *vs.* la distancia C*-O, y no así en el gráfico de pK_a, ya que el pK_a es más sensible a efectos inductivos, resonantes y estéricos que se originan en esta posición, por lo que, la tendencia en la barrera de energía indica, que a mayor estabilidad del complejo reactante mayor es la energía de activación que presenta la reacción.

Adicionalmente, los resultados señalan que grupo ciano presenta un comportamiento diferente al resto, ya que al tener un menor valor de pK_a y una distancia más larga de C*–O se esperaría que este sustituyente tuviese la menor barrera de energía; sin embargo, el grupo fluorometil presenta la menor barrera, por esta razón, es necesario comparar los grupos CN y CF_3 con respecto a sus propiedades electrónicas y estructurales que existen en la geometría del complejo reactante y del estado de transición, debido a que se puede extraer una mayor información respecto al comportamiento de estos sustituyentes.

La Figura 8.12 muestra las distancias de enlace C*-H, C*-O y O-H, las cargas atómicas de los átomos de interés (C*, O, H) y la densidad de electrones presente en el anillo aromático del fenol sustituido por CN y CF_3. Los resultados señalan que el grupo ciano tiene un efecto inductivo más fuerte que el CF_3, retirando 0.52 |e| de densidad electrónica del anillo, mientras que el CF_3 sólo retira 0.03 |e| respecto a la estructura del complejo reactante sin sustituír. Esta menor densidad de electrones en el anillo en **RC-CN** hace que en esta geometría el protón tenga una menor acidez (q_H: 0.38 |e| *vs.* 0.43 |e|). Además, se calculó la energía del complejo van der Waals (ΔE_{RC}) para **RC-CN** y **RC-CF$_3$** y los resultados señalaron que **RC-CN** corresponde a un sistema más estable que **RC-CF$_3$** (ΔE_{RC}: -12.2 kcal/mol vs. 11.7 kcal/mol), esta mayor estabilidad tiene también su origen en la menor densidad de electrones que presenta

el anillo aromático, la que permite de mejor manera la conjugación del par de electrones no enlazantes del oxígeno del fenol en el anillo aromático, justificando de este modo el comportamiento del grupo CN en la posición orto al OH del sustrato fenólico.

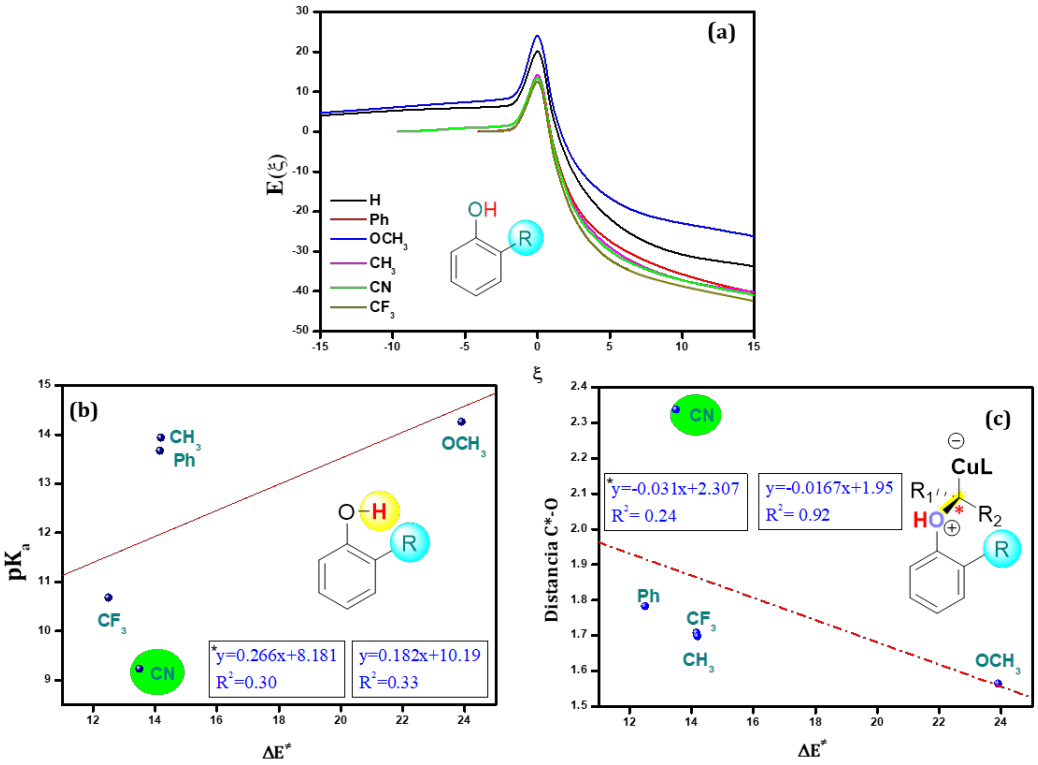

Figura 8.11: **(a)** Perfil de energía potencial respecto a ξ, modificando el sustituyente en posición orto. **(b)** Gráfico de pK_a del protón H del fenol sustituido en orto *vs.* la energía de activación ($\Delta E^{\neq}$). **(c)** Gráfico de distancia de enlace C*-O del complejo reactante *vs.* la energía de activación ($\Delta E^{\neq}$). Los datos estadísticos de la regresión lineal con asterisco (*) corresponden a los valores sin considerar el grupo ciano. Todos los valores de energía se encuentran en kcal/mol.

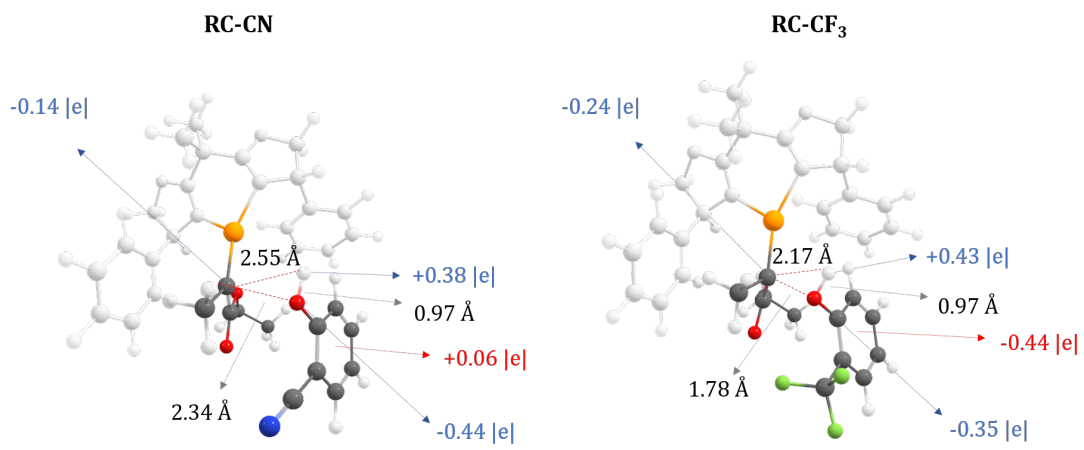

Figura 8.12: Geometría del complejo reactante para el fenol sustituido en orto con los grupos CN y CF_3, las flechas de color rojo representan la carga del anillo aromático del fenol sustituido, las de color azul la carga atómica de los átomos C*, O y H y las de color negro las distancias de enlaces participantes de la transferencia protónica.

En resumen, los resultados correspondientes a la modificación de la estructura del sustrato, indican que la variación de la acidez del protón transferido, junto con la estabilidad del complejo reactante, son puntos importantes para entender el efecto energético que contempla el cambio de sustituyente en el anillo aromático en las posiciones orto, meta y para al OH del fenol. De tal modo, el aumento de la velocidad de la reacción en la posición para se presentó en todos los casos cuando se sustituyó con grupos atractores de electrones, disminuyendo de este modo la barrera de energía entre 6.2 a 7.5 kcal/mol aproximadamente con respecto a **R1-OH** (reacción sin sustituir). Esto se debe tanto a la menor estabilidad del complejo reactante, como al aumento en la acidez del protón que participa de la transferencia protónica, la cual conlleva la salida del complejo de cobre y corresponde al paso elemental del mecanismo de reacción estudiado. Con respecto al efecto energético en la posición meta, los resultados no fueron tan favorables como en la posición para, sin embargo, el grupo ciano mostró ser el mejor candidato, disminuyendo la barrera de energía en 7.3 kcal/mol respecto a **R1-OH**, producto del mayor efecto inductivo que presenta,

el que se relaciona con la mayor acidez del protón y la menor estabilidad del complejo reactante. Finalmente, el efecto energético en la posición orto, presentó un comportamiento favorable en la cinética de la reacción, disminuyendo la energía de activación en todos los sustituyentes estudiados (a excepción del grupo metoxilo) entre 6.0 a 7.6 kcal/mol aproximadamente, producto de la menor estabilidad del complejo reactante.

De este modo, en resumen del capítulo, el estudio sistemático en los cambios estructurales realizados en ambos reactantes indican que la modificación del sustrato tiene un mayor efecto en la cinética de la reacción que la modificación estructural del carbenoide, ya que el cambio en la reactividad del sustrato disminuye la energía de activación en la mayoría de los casos (principalmente en las posiciones orto y para) en aproximadamente entre 6.0 a 7.6 kcal/mol en relación a la reacción **R1-OH**.

Conclusiones

Se validó el nivel de teoría a utilizar para el estudio de la reacción de inserción del carbenoide de cobre en los enlaces X-H, encontrándose que el funcional M06-2X, con el conjunto de funciones base cc-pVDZ, proporciona valores más cercanos a aquellos obtenidos con el método de referencia (DLPNO-CCSD(T)/cc-pVTZ).

Los antecedentes mostrados en el primer capítulo indican que el carbono carbenoide posee características electrofílicas debido a la alta donación σ al metal y pobre retro-donación π desde el metal al carbono carbenoide, tal como fue señalado con el análisis donor-aceptor del método NBO, adquiriendo una carga de +0.03 |e|. Por su parte, los sustratos anilina y fenol, poseen una carga de -0.18 |e| y -0.19 |e| en el nitrógeno y oxígeno, respectivamente, indicando una mayor densidad de electrones en el átomo de oxígeno del sustrato fenólico. Además, la carga del hidrógeno unido al heteroátomo es de +0.11 |e| y +0.17 |e| para anilina y fenol, respectivamente, por lo que el protón del fenol tiene un carácter más ácido, lo que favorecería una transferencia protónica desde aquel sustrato, más que desde la anilina. De esta manera, se logró caracterizar la reactividad intrínseca del complejo carbenoide y de ambos sustratos.

Desde un punto de vista mecanístico, se encontró que la reacción de inserción del carbenoide de cobre en los enlaces X-H puede llevarse a cabo siguiendo un mecanis-

mo concertado o un mecanismo en etapas. El mecanismo concertado presentó tres procesos químicos importantes: el primero, un proceso sin barrera de energía, el segundo, el paso elemental de la reacción y, el último correspondiente al estudio de las interacciones no covalentes entre los productos de reacción.

Para cada inserción en el mecanismo concertado (**R1-NH** y **R1-OH**) dos procesos sin barrera son encontrados, llevando a la formación de dos diferentes complejos reactivos ($\mathbf{RC}_X$), donde cada uno de ellos origina un isómero óptico específico. Un acercamiento frontal del sustrato al carbenoide conduce la reacción hacia un isómero S, mientras que un acercamiento posterior hacia la del isómero R. El análisis de la energía de interacción del complejo reactante (ΔE_{RC}) junto con su descomposición mediante el método ASM y EDA, indicaron que el complejo reactante $\mathbf{RC}_{X,R}$ es 13.3 kcal/mol más estable que $\mathbf{RC}_{X,S}$ en **R1-NH** y 9.70 kcal/mol más estable en **R1-OH**, lo que es producto del incremento en la energía desestabilizadora ΔE_{dist} y el aumento en la energía de repulsión de Pauli en las estructuras $\mathbf{RC}_{X,S}$, utilizando una alta energía en la deformación geométrica, y por ende resultando en la formación de especies más reactivas.

El paso elemental del mecanismo concertado, corresponde tanto a la transferencia protónica desde el heteroátomo al carbono central C*, junto con la salida del complejo de cobre (CuL). Las energías de activación para **R1-NH** corresponden a 39.2 (R) y 47.5 kcal/mol (S), mientras que para **R1-OH** de 20.0 (R) y 33.8 kcal/mol (S). La enatioselectividad está favorecida cinéticamente hacia la formación del isómero R, producto del mayor número de interacciones van der Waals repulsivas presentes entre el fenilo de PhBOX y el sustrato en las estructuras $\mathbf{TS}_{X,S}$.

A partir del análisis de los modelos de F(ξ) y el ASM en el paso elemental del mecanismo concertado (orientación posterior), los resultados indicaron que la mayor contribución al trabajo W_1 corresponde a una repulsión estérica entre el grupo fenilo del ligando y el sustrato, mientras que W_2 se encuentra dominado principalmente por una distorsión geométrica del sustrato. Los análisis en **R1-OH** demostraron que la región de reactantes es dominada por una energía de interacción positiva asociada a la energía de repulsión de Pauli, la que es acompañada de una alta estabilización asociada a la energía de distorsión, teniendo esta última una mayor contribución de la deformación del carbenoide, lo que resulta en una menor energía de activación para **R1-OH**. La termodinámica de este paso elemental, indica que ambas reacciones son favorables; sin embargo, **R1-OH** indicó ser más exotérmica debido a un par de electrones libres del átomo de oxígeno, el cual se encuentra perpendicular al plano del ciclo aromático, siendo de esta forma capaz de interactuar con los electrones de los enlaces π del benceno.

Los resultados del último paso del mecanismo concertado, correspondiente a la ruptura de las interacciones no covalentes entre el complejo de cobre y el producto de inserción, señalaron que en las estructuras $\mathbf{PC}_{X,R}$ y $\mathbf{PC}_{X,S}$ se deben romper distintos tipos de interacciones no covalentes. Para $\mathbf{PC}_{X,R}$ corresponden a la interacción entre el átomo de oxígeno del grupo carbonilo (formiato de etilo) y el cobre, mientras que para $\mathbf{PC}_{X,S}$ corresponden a la interacción entre el átomo de cobre y los enlaces dobles provenientes del anillo aromático del sustrato.

El mecanismo en etapas, resultó tener cuatro pasos importantes, siendo dos de ellos

pasos elementales. La principal característica de este mecanismo corresponde a la participación del sustituyente atractor del carbenoide en la reacción. Donde el paso elemental, correspondiente a la transferencia protónica desde el grupo atractor de electrones al carbono central C*, resultó ser el paso determinante. Este paso determinante origina dos enantiómeros, donde el enantiómero R se produce a partir de la transferencia protónica sobre el plano, mientras que la transferencia protónica por debajo del plano origina el isómero S. Los resultados indicaron que la formación del enantiómero R es favorecido cinéticamente, donde el ligando PhBOX juega un rol importante mediante efectos estéricos. La reacción que toma lugar sobre el plano presentó energías de 37.2 y 34.5 kcal/mol para **R2-NH** y **R2-OH**, respectivamente, donde la diferencia en energía entre ambas reacciones corresponde a la naturaleza electrónica del átomo donor del protón.

De esta manera, se logró una completa caracterización de ambos mecanismos, encontrándose que la barrera de energía de la etapa determinante en el mecanismo en etapas (**R2-OH**) resultó ser mayor que las energías del paso elemental del mecanismo concertado (**R1-OH**), por cual se favorece el mecanismo concertado por sobre el de etapas, desde un punto de vista cinético y termodinámico. Mientras que **R2-NH** a pesar de tener 2 kcal/mol más favorable en energía de activación que **R1-NH**, no favorece en gran medida la cinética de la reacción. Por lo cual, el carbenoide de cobre utilizado no sería un carbenoide eficiente para llevar a cabo la reacción de inserción sobre el enlace N-H.

Se logró determinar el efecto de la modificación estructural de los reactantes estudiados (carbenoide y fenol). Donde el efecto del metal en el carbenoide en **R1-OH**,

indicó que el C* del carbenoide de plata tiene un mayor carácter electrofílico que el C* del carbenoide de cobre, debido al menor solapamiento de orbitales p_y y d_{xy} que conducen a una menor retrodonación π en el enlace Ag-C* generando una disminución de la barrera de energía. El efecto del cambio del sustituyente en el carbenoide, indica que el grupo fenilo como donor de electrones disminuye la barrera de energía, producto del aumento de electrofilia local del C* junto con la menor estabilización de la geometría **RC**, mientras que el sustituyente amida como grupo atractor presenta la menor energía de activación gracias a la menor estabilización de la geometría del complejo reactante. Por otra parte, el estudio del efecto del sustituyente en el sustrato en **R1-OH**, indica que el mayor efecto en la reducción de la altura de la barrera de energía, ocurre cuando se sustituye el anillo del fenol en posición para y meta al OH utilizando grupos atractores de electrones, producto del aumento de acidez del protón transferido en el paso elemental, y la menor estabilización de la geometría del complejo reactante.

Apéndice A

Estudio del rendimiento de los funcionales de la densidad utilizados

Se realizó un estudio del rendimiento de un set de cuatro funcionales DFT para validar la metodología a utilizar. Entre los funcionales analizados dos de ellos corresponden a funcionales híbridos GGA: B3LYP y PBE0, uno híbrido meta-GGA M06-2X, y por último uno híbrido GGA incluyendo correcciones de largo alcance ωB97X-D3. Utilizando en todos los casos un conjunto de funciones base estándar del tipo TZP (triple zeta) cc-pVTZ . Los 4 funcionales fueron confrontados con el método DLPNO-CCSD(T) (del inglés, *Domain-based Local Pair-Natural Orbital- Coupled Cluster Singles, Doubles and perturbatives triples excitations*), utilizando el Programa Orca 4.0.0.2

Los resultados mostrados en la Tablas A.1 y A.2, indican que el funcional M06-2X es aquel funcional más comparable con el método de alta precisión DLPNO-CCSD(T),

tanto en la energía de activación como en la de reacción. Adicionalmente, el funcional M06-2X proporciona cálculos de bajo costo computacional.

Tabla A.1: Energías de activación ($\Delta E^{\neq}$) y energía de reacción (ΔE°) para la reacción de inserción del carbenoide de Cu en el enlace O-H (**R1-OH**), obtenidas con las cuatro metodologías diferentes. Todos los valores están en kcal/mol.

Reacción	**R1-OH**	
Metodología	$\Delta E^{\neq}$	ΔE°
B3LYP/cc-pVTZ	16.51	-34.83
PBE0/cc-pVTZ	16.24	-34.92
M06-2X/cc-pVTZ	19.94	-39.89
ωB97XD-D3	17.56	-36.90
DLPNO-CCSD(T) cc-pVTZ // M06-2X/cc-pVTZ	19. 12	-37.40

Tabla A.2: Tiempo de cómputo para el cálculo de energía y frecuencias vibracionales en la geometría del estado de transición, para los tres metodologías utilizadas. El tiempo de cómputo presentado corresponde al tiempo obtenido con 1 procesador.

Reacción	**R1-OH**
Metodología	Tiempo de Cómputo
B3LYP/cc-pVTZ	27 h 48 m
PBE0/cc-pVTZ	28 h 52 m
M06-2X/cc-pVTZ	52 h 55 m
ωB97XD-D3/ cc-pVTZ	30 h 35 m

Apéndice B

Aspectos Teóricos

El primer postulado de la mecánica cuántica señala que un sistema microscópico está completamente caracterizado por una función de onda Ψ [100] que contiene toda la información que es posible conocer de dicho estado cuántico, mediante la aplicación de los operadores que describen un observable físico y el teorema del valor medio en mecánica cuántica. Sin embargo, la función de onda no posee interpretación física directa y tiene $3N$ dimensiones (para un aproximación estacionaria), lo que representa un problema de resolución en sistemas polielectrónicos. Para conocer la función de onda Ψ, es necesario conocer la ecuación de *Schrödinger* [101] utilizando el operador Hamiltoniano adecuado:

$$\hat{H}\Psi = E\Psi \tag{B.1}$$

Para determinar el Hamiltoniano hay que conocer el número de electrones N y el potencial externo $v(\vec{r})$ del sistema[102].

Durante los últimos años la TFD ha tenido una fuerte influencia en la determinación

de sistemas mecano cuánticos. Basadas en los teoremas de Hohenberg y Kohn, la TFD tiene como idea fundamental que la densidad electrónica ($\rho(r)$) define el estado fundamental de átomos y moléculas, permitiendo así obtener la información acerca de la energía, la estructura y propiedades de un sistema químico en estudio teniendo en cuenta que la energía resulta ser un funcional de $\rho(r)$, $E = E[\rho(r)]$.

Es posible expresar todos los términos del Hamiltoniano electrónico en función de la densidad, según:

$$E[\rho(r)] = T[\rho(r)] + V_{Ne}[\rho(r)] + V_{ee}[\rho(r)] \tag{B.2}$$

$T[\rho(r)]$ da cuenta de la energía cinética de los electrones, $V_{ee}[\rho(r)]$ de la interacción electrón-electrón y $V_{Ne}[\rho(r)]$ de la interacción núcleo electrón, siendo el único conocido gracias a la función de energía potencial de atracción nuclear, de naturaleza coulómbica. De conocerse los otros términos, se obtendría la solución exacta para la densidad electrónica; sin embargo, se cuenta con distintas aproximaciones que modelan la suma de $T[\rho(r)]$ y $V_{ee}[\rho(r)]$, el llamado Funcional Universal $F[\rho(r)]$, por su independencia del potencial externo.

En 1965 *Kohn y Sham* [103] desarrollan un método para poder extraer la información numérica de los postulados de *Hohenberg* y *Kohn*. Por un procedimiento variacional, se optimiza un conjunto de orbitales, los orbitales de *Kohn* y *Sham* (KS), que genera una densidad de prueba, en forma análoga a la metodología de *Hartree-Fock* [75], y se incluye una aproximación para la correlación electrónica en el modelo de Funcional Universal, funcionales de intercambio y correlación. Aún cuando el significado físi-

co de los orbitales KS no está claramente formulado en el desarrollo metodológico, existe evidencia de que su uso es perfectamente aceptable para análisis de resultados electrónicos [104], permitiendo la obtención de manera eficiente de datos energéticos, estructurales y electrónicos para un sistema dado.

La *Teoría de Funcionales de la Densidad* genera las bases para el desarrollo de elementos interpretativos de especial interés, que permite extraer información de un sistema en forma rigurosa y directamente relacionable con los conceptos químicos [105].

B.0.1. Teoría de Funcionales de la Densidad Conceptual

Potencial químico y Dureza molecular

La TFD conceptual centra su interés en la extracción de conceptos y principios relevantes para la química, desde los desarrollos metodológicos en química cuántica [106–108]. La TFD conceptual data de 1980, cuando se comienza a explorar el significado físico-químico de términos matemáticos asociados con la respuesta de un sistema frente a distintas perturbaciones, generados en el marco de la *Teoría de Funcionales de la Densidad*.

Como se mencionó anteriormente, la densidad electrónica ρ nos permite caracterizar en forma completa un sistema químico. Para obtener la densidad correcta a partir de una densidad de prueba $\rho\prime$, debemos seguir el criterio de mínima energía, aplicando el principio variacional para la densidad a potencial externo constante, con la condición de normalización a N, siendo μ el multiplicador de Lagrange asociado a la minimización, cuyo valor será característico del sistema de interés:

$$\delta\{E_v[\rho\prime] - \mu N[\rho\prime]\} = 0 \tag{B.3}$$

Como se ha señalado, la densidad ρ, determina el potencial externo $v(\vec{r})$ y el número de electrones del sistema N, mediante su normalización los que a su vez determinan el Hamiltoniano del sistema, resultando la energía total una funcional de N y $v(\vec{r})$:

$$E = E[N, v(\vec{r})] \tag{B.4}$$

Por otro lado, corresponde señalar que las funciones respuestas en la energía para variaciones en N, y en el potencial externo ($\upsilon(\vec{r})$) generan una familia de descriptores locales y no locales de reactividad. Ambas familias de respuesta se resumen en la Figura B.1.

$$
\begin{tikzcd}
 & & E[\mathrm{N}, \upsilon(\vec{r})] \arrow[dl, "\frac{\partial}{\partial \mathrm{N}}"'] \arrow[dr, "\frac{\delta}{\delta \upsilon(\vec{r})}"] & & \\
 & \left(\frac{\partial \mathrm{E}}{\partial \mathrm{N}}\right)_{\upsilon(\vec{r})} = \mu = -\chi \arrow[dl, "\frac{\partial}{\partial \mathrm{N}}"'] \arrow[dr] & & \left(\frac{\delta \mathrm{E}}{\delta \upsilon(\vec{r})}\right)_{\mathrm{N}} = \rho(\vec{r}) \arrow[dl] \arrow[dr, "\frac{\delta}{\delta \upsilon(\vec{r})}"] & \\
\left(\frac{\partial^2 \mathrm{E}}{\partial \mathrm{N}^2}\right)_{\upsilon(\vec{r})} = \eta & & \left(\frac{\partial^2 \mathrm{E}}{\partial \mathrm{N} \partial \upsilon(\vec{r})}\right) = f(\vec{r}) & & \left(\frac{\delta^2 \mathrm{E}}{\delta \upsilon(\vec{r}) \delta \upsilon(\vec{r}\,')}\right)_{\mathrm{N}} = \chi(\vec{r}, \vec{r}\,')
\end{tikzcd}
$$

Figura B.1: Derivadas superiores de la energía electrónica en un conjunto canónico.

Al analizar la respuesta en la energía para cambios en N hasta segundo orden, se obtiene una serie de términos para el análisis de la reactividad química:

$$
\mu = \left[\frac{\partial E}{\partial N}\right]_{\upsilon(\vec{r})} \quad ; \quad \eta = \left[\frac{\partial^2 E}{\partial N^2}\right]_{\upsilon(\vec{r})} \tag{B.5}
$$

A primer orden, se recupera el multiplicador de Lagrange μ, proveniente de la minimización variacional del funcional de la energía. Éste será definido como el potencial químico electrónico del sistema [109], en analogía al potencial químico termodinámico. Debido a que N es una variable discreta, y la energía es discontínua en N, para obtener valores de μ se debe recurrir a la aproximación de diferencias finitas, la que

indica que la energía varía con N, según:

$$\mu \approx \frac{\Delta E}{\Delta N} = \frac{[E_{N-1} - E_{(N)}] - [E_{N+1} - E_{(N)}]}{[N-1] - [N+1]} = \frac{AE - PI}{2} \tag{B.6}$$

Donde PI corresponde al primer potencial de ionización y AE a la afinidad electrónica. La respuesta de segundo orden para la energía es llamada dureza molecular, η [106, 108, 109]. Ésta también puede ser obtenida mediante aproximación de diferencias finitas [110].

$$\eta = \left[\frac{\partial^2 E}{\partial N^2}\right]_{v(\vec{r})} = \left[\frac{\partial \mu}{\partial N}\right]_{v(\vec{r})} = \frac{PI - AE}{2} \tag{B.7}$$

Los términos μ y η se originan a partir de cambios en el número total de electrones, siendo propiedades globales del sistema. Esto, sumado a que sus fórmulas operacionales están compuestas por cantidades con significado químico, se utilizan como descriptores de reactividad química.

Para facilitar la obtención de estos descriptores, es posible usar el Teorema de *Koopmans* [111], que asocia el valor de la afinidad electrónica con la energía del primer orbital molecular desocupado (LUMO) y el potencial de ionización con la energía del último orbital ocupado (HOMO), obteniéndose μ y η en función de dichas cantidades:

$$PI \approx -\epsilon_H \quad ; \quad AE \approx -\epsilon_L \tag{B.8}$$

$$\mu \approx \frac{1}{2}(\epsilon_L + \epsilon_H) \quad ; \quad \eta \approx \frac{1}{2}(\epsilon_L - \epsilon_H) \tag{B.9}$$

El potencial químico es una medida de la tendencia de escape de los electrones desde el sistema en equilibrio [112] la dureza molecular es una medida de la resistencia del sistema a cambios en su distribución electrónica [113].

Apéndice C

Estudio Teórico de la Tiourea como catalizador en la Piranilación de Metanol

Este trabajo se enmarca en la pasantía de investigación realizada en la Universidad de Brock, St. Catharines, Canadá, con el profesor Travis Dudding. En esta instancia, se estudió el mecanismo de reacción de piralinación de metanol utilizando tiourea como catalizador. Este estudio se realizó computacionalmente apoyado de datos otorgados por el grupo experimental del profesor Dudding.

El campo de la catálisis continúa evolucionando hacia modos de reactividad sostenibles, renovables y menos dependientes de metales preciosos, dentro de este enfoque se enmarca el uso de metodologías organocatalíticas [114–116]. El impulso para este cambio, es la característica intrínseca no metálica de la organocatálisis [117–122] tolerante a los grupos funcionales del sustrato y, a la participación de múltiples interacciones no covalentes. En este contexto, las tioureas son una clase popular de

organocatalizadores con amplia utilidad [123–127], derivadas en parte de su capacidad de emplear múltiples interacciones atractivas para facilitar de este modo las transformaciones químicas. Por esta razón, esta clase privilegiada de organocatalizador continúa ganando atracción en los últimos años mediante mecanismos como la catálisis no covalente, catálisis de ácido de Brønsted [128], catálisis mejorada electrostáticamente [129] y catálisis multifuncional.

Desde un punto de vista mecanístico, el rol multifuncional de las tioureas en la activación del sustrato, corresponde a un punto importante dentro de la organocátalisis [130, 131]. En este caso, la doble función de las tioureas, tales como la disminución de LUMO y la activación de los sustratos (base de Lewis) ha sido considerado como un punto crítico en el rendimiento del catalizador. Adicionalmente, este modo de activación del sustrato se encuentra vinculado a la dinámica conformacional de la tiourea, la cual puede ser efectiva tanto en la activación electrofílica, como en la organización del estado de transición.

Es conocido que los efectos conformacionales de la tiourea desempeñan un rol fundamental en la catálisis (orientaciones *Z,Z*; *E,Z*; *Z,E* y *E,E*), ya que estudios demuestran que estímulos ambientales influyen en las preferencias conformacionales [132, 133] (ver Figura C.1 **A**). Adicionalmente, está establecido que los solventes pueden favorecer la presencia de un confórmero en particular a través de la estabilización [134]. Sin embargo, la estabilización otorgada por solvente, no resulta necesariamente en el confórmero más estable termodinámicamente, como se observaría en el estado sólido, sino más bien conduce a la estabilización de su contraparte catalíticamente activa [135, 136].

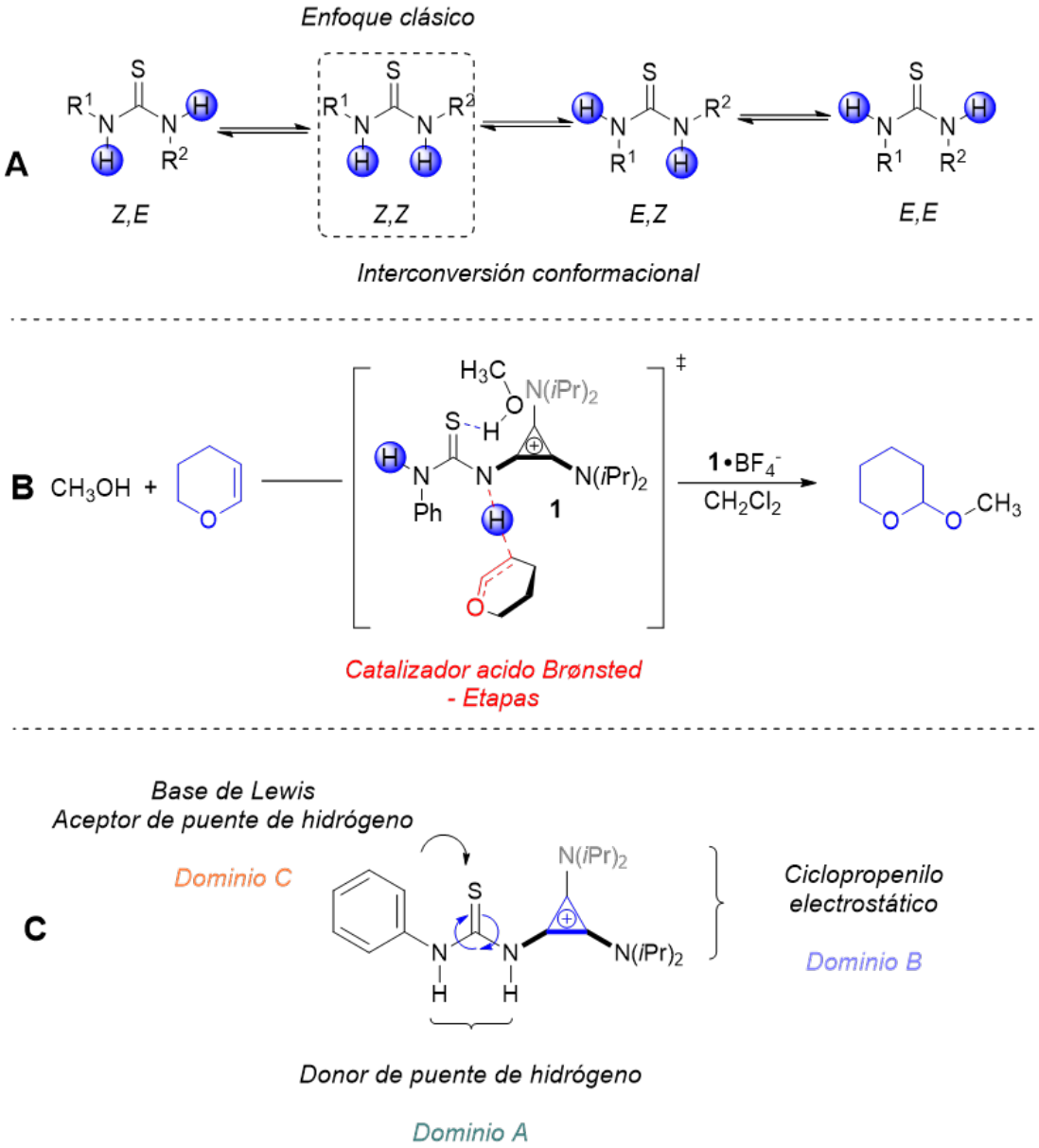

Figura C.1: **(A)** Isómeros conformacionales de la tiourea estudiada. R_1: Ph, R_2: bis(diisopropilamino). **(B)** Trabajos previos reportados por Dudding para la piranilación de alcoholes y fenoles. **(C)** Ciclopropenilo como un nuevo dominio electrostático para el catalizador de tiourea.

Dudding recientemente ha reportado evidencia experimental [137], mediante el uso de sistemas ciclopropenilos en busca de desarrollar un catalizador eficiente para la reacción de piranilación de alcoholes y fenoles (ver Figura C.1 **B**). De esta manera, este nuevo catalizador de tiourea mostrado en la Figura C.1 **C** exhibe tanto un

dominio A donor de puente de hidrógeno, como un mejorado carácter electrostático debido a la presencia del anillo de ciclopropenilo (*dominio B*), además de una base de Lewis (azufre) que actúa como un aceptor de puente de hidrógeno (*dominio C*) .

La protección de los alcoholes a través de la piranilación (protección de THP) es un ejemplo pertinente de las muchas transformaciones sintéticas existentes, que se producen a través de estos intermediarios de oxocarbenio [138]. Este trabajo tiene como objetivo principal estudiar las múltiples vías de reacción que existen, las cuales dependen de la disposición geométrica del complejo catalizador-sustrato activo dentro del estado de transición. Dentro de este enfoque, a partir de nuestros hallazgos computacionales y experimentales, se encontró que existen elementos complementarios que coexisten para dirigir de este modo dos tipos de mecanismos: HBC (del inglés, *Hydrogen Bond Catalyzed*) correspondiente a una catálisis no covalente mediada por interacciones puentes de hidrógeno para activar el sustrato (metanol) y BAC (del inglés, *Brønsted Acid Catalyzed*) donde la tiourea se comporta como un catalizador de ácido de Brønsted (ver Figura C.2).

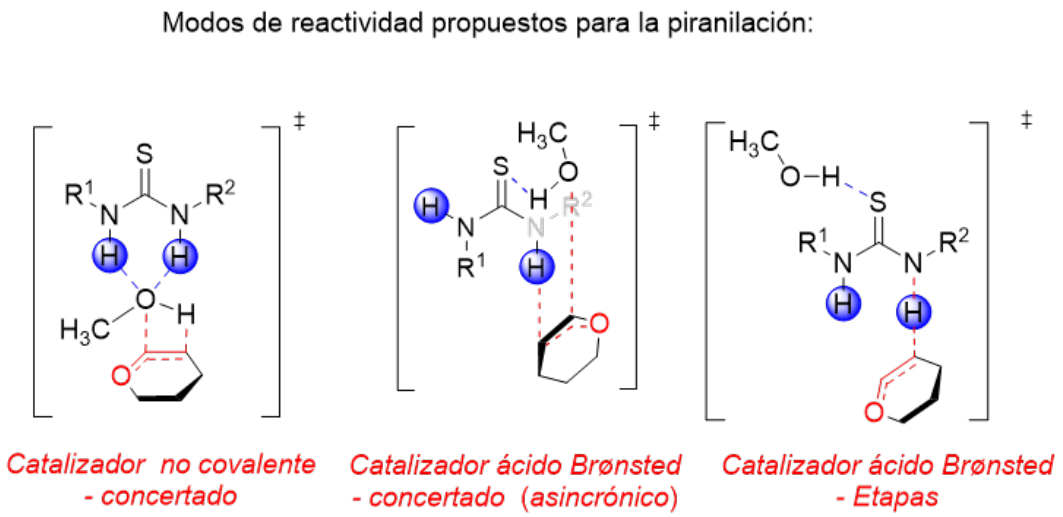

Figura C.2: Investigación computacional de las reacciones de piranilación utilizando la tiourea sintetizada por el grupo de Dudding.

De tal modo, se evaluarán aquellos factores que gobiernan la estabilización del estado de transición tanto para las vías concertadas como en etapas, a partir de un análisis computacional mediante una perpectiva energética, electrónica y de interacciones no covalentes.

C.1. Análisis conformacional

Como punto de partida para nuestros estudios, se optimizó la estructura del estado fundamental del catalizador de tiourea propuesto, utilizando la metodología ωB97XD[139]/6-311G(d,p), lo que resultó en el hallazgo de cuatro conformaciones distintas: *Z,Z, E,Z, Z,E*, y *E,E* mostradas en la Figura C.1, con energías libre de Gibbs ($\Delta G°$) relativas que abarcan hasta 3.57 kcal/mol en solvente DCM (ver Tabla C.1). Entre estos rotámeros calculados, el *E,Z* presentó la menor energía en los tres solventes estudiados: DCM, CH_3CN y DMSO con constante dieléctrica de 8.93, 37.7 y 46.8, respectivamente. Esta preferencia energética de la conformación *E,Z*, se debe a una serie de factores, tales como; el considerable valor del momento dipolar (17.2

D), junto con el menor número de repulsiones estéricas intramoleculares, como se observa en la Figura C.3 mediante los gráficos NCI 2D y 3D.

Tabla C.1: Energía libre de Gibbs ΔG° tomando en cuenta los solventes DCM, CH_3CN y DMSO. MD corresponde al momento dipolar con unidad de Debyes. Los valores de energías se encuentran en kcal/mol.

Confórmero	MD	ΔG°	ΔG°_{DCM}	$\Delta G^{\circ}_{CH_3CN}$	ΔG°_{DMSO}
Z,Z	7.90	1.58	3.15	2.51	1.78
E,E	12.1	5.43	3.57	4.37	4.40
E,Z	15.8	5.47	1.51	1.25	1.41
Z,E	17.2	0.0	0.0	0.0	0.0

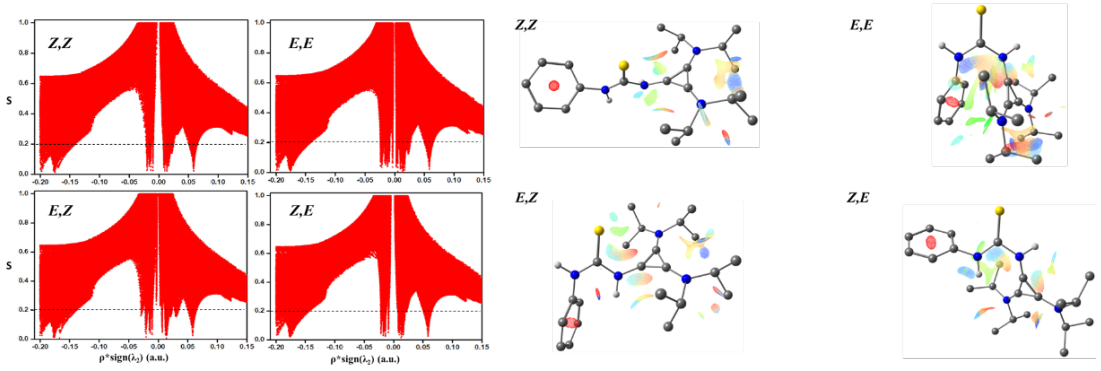

Figura C.3: Gráficos NCI 2D (panel izquierdo) y gráficos NCI 3D (panel derecho) para los rotámeros *Z,Z, E,Z, Z,E* y *E,E* estudiados en la tiourea.

C.2. Mecanismo de reacción

Al tener ya una idea de la dinámica conformacional del catalizador de tiourea, nos enfocamos en explorar el mecanismo de formación de productos piranilados. De estos esfuerzos, surgen dos vías mecanísticas, que implican un paso determinante para la reacción de adición de alcohol: (i) Ruta 1: activación del metanol mediante puentes de hidrógeno bifurcados de la tiourea (Figura C.4), (ii) Ruta 2: adición de alcohol mediante una catálisis por ácido de Brønsted (Figura C.5).

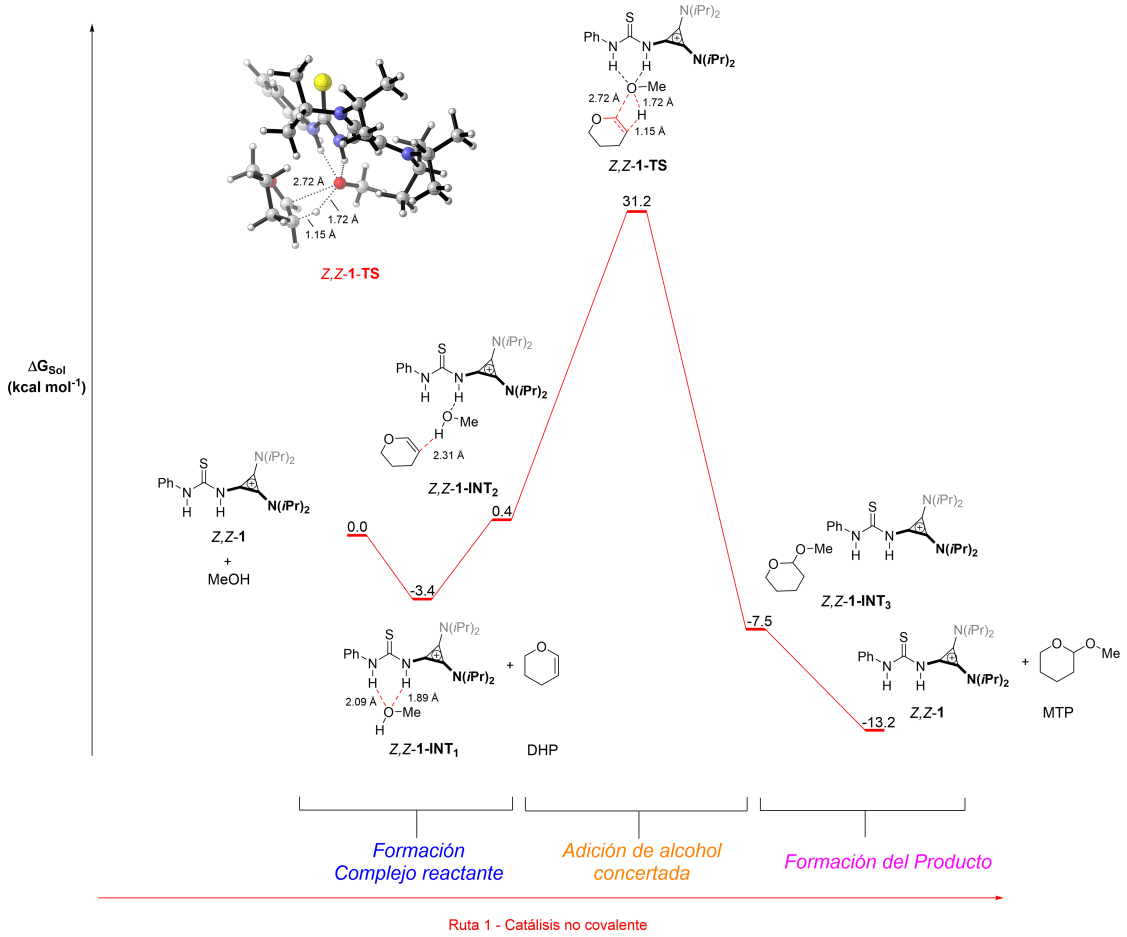

Figura C.4: Ruta 1: activación del metanol mediante puentes de hidrógeno bifurcados del confórmero *Z,Z* de la tiourea.

C.2.1. Mecanismo concertado

La ruta 1 se inicia con la formación de un complejo reactante *Z,Z*-**1-INT1** mediante la participación del confórmero Z,Z, donde se generan interacciones puentes de hidrógeno bifurcados entre la tiourea y el metanol con distancias de 2.09 Å y 1.89Å (Figura C.4). Luego se forma el complejo *Z,Z*-**1-INT2**, donde el átomo de hidrógeno del alcohol reside directamente encima del alqueno del 3,4-dihidro-2H-pirano (DHP) a una distancia de 2.31 Å, generando un alto grado de polarización de carga en los enlaces N-H · · · O-H producto del carácter electrostático del ciclopropenilo (Cargas

NBO N=-0.671 |e| , H=0.459 |e|, O= -0.795 |e|, H=0.510 |e|), y preparando de este modo el escenario para la transferencia protónica hacia el carbono-β del vinil éter proveniente del DHP. En el paso determinante, el estado de transición *Z,Z*-**1-TS** implica tanto la formación del enlace C-O como la transferencia protónica hacia el carbono β, presentando una barrera de energía libre de Gibbs considerable de 30.8 kcal/mol con respecto a *Z,Z*-**1-INT2**. El estado de transición *Z,Z*-**1-TS** presenta un enlace C ··· O alargado con distancia de 2.72 Å, además las distancias de enlace involucradas en la transferencia protónica de C ··· H y O ··· H son de 1.15 Å y 1.72 Å, respectivamente. Finalmente, se forma el complejo producto *Z,Z*-**1-INT3**, para luego ocurrir la separación del producto piranilado 2-metoxitetrahidropirano (MTP) y la salida del catalizador de tiourea *Z,Z*, mediante un proceso exergónico.

C.2.2. Mecanismo en etapas

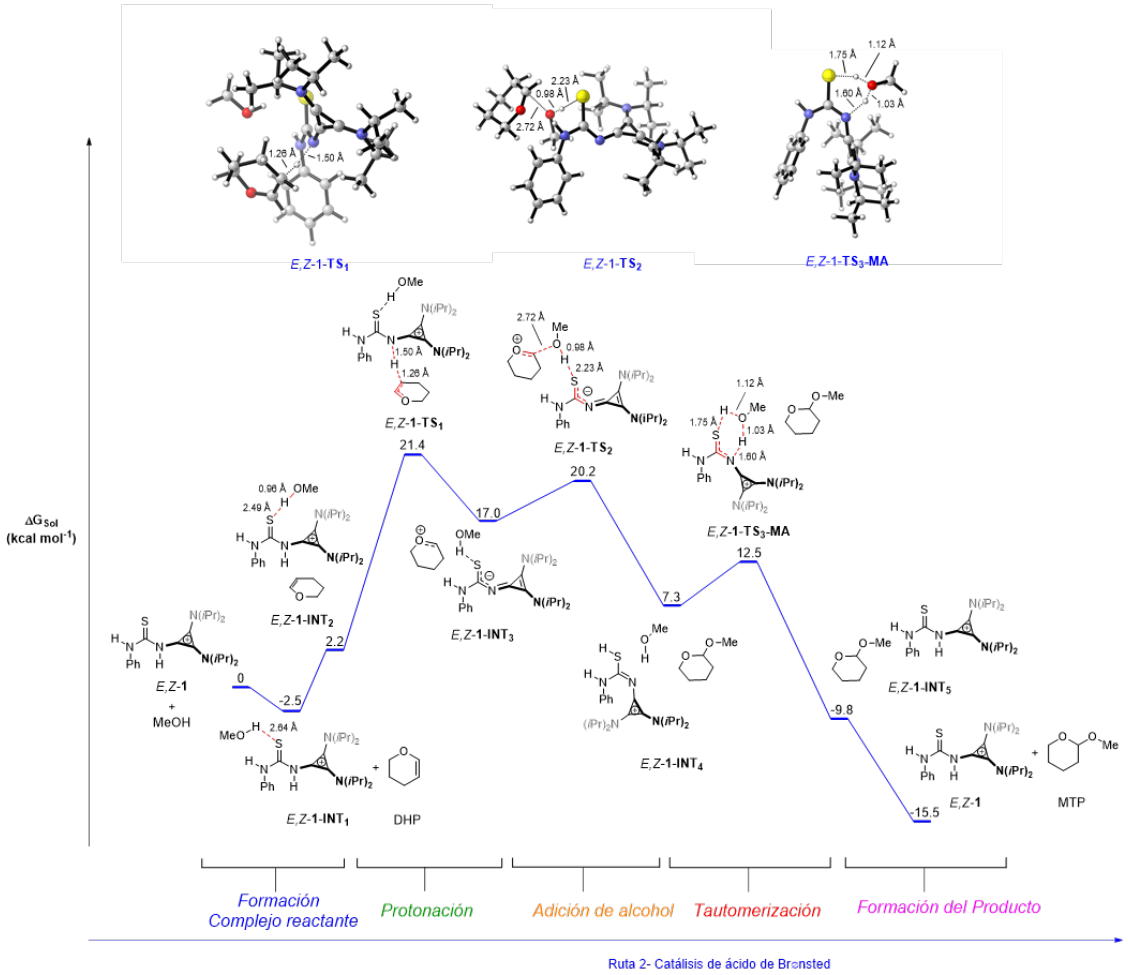

Figura C.5: Ruta 2: adición de alcohol mediante una catálisis de ácido de Brønsted, utilizando el confórmero *E,Z* de la tiourea.

La ruta 2 (catálisis de ácido de Brønsted) comienza con la formación del complejo reactante *E,Z*-**1-INT1**, a partir del confórmero *E,Z* de la tiourea y el metanol. Este complejo presenta un puente de hidrógeno S ··· H-O con distancia de 2.64 Å (ver Figura C.5). Luego, se forma el complejo *E,Z*-**1-INT2** donde el hidrógeno del enlace N-H (cercano al ciclopropenilo) comienza a prepararse para la protonación del alqueno vinil éter del DHP, mientras que el metanol actúa como un puente que acerca el catalizador y el DHP, es decir, el alcohol sirve como una conexión no covalente,

que se origina a partir de interacciones intermoleculares S ··· H – O y C – H ··· O con distancias de 2.49 Å y 0.96 Å, respectivamente. El estado de transición *E,Z*-**1-TS1** correspondiente a la transferencia protónica, ocurre con una barrera de energía libre de Gibbs de 21.4 kcal/mol. Este estado de transición presenta distancias de 1.50 Å y 1.26 Å para la transferencia protónica y 4.52 Å de distancia entre el metanol y el carbono α del vinil éter. Es importante notar, que la transferencia protónica mediante el hidrógeno del enlace N-H (cercano al fenilo) presenta una barrera de energía 4.5 kcal/mol más alta, haciendo que este proceso sea poco probable, por lo que se resalta aún más la importancia del ciclopropenilo en la tiourea, ya que éste aumenta la acidez del protón cercano a él. El primer estado de transición conduce a la formación de un par iónico oxonio-tiourea (*E,Z*-**1-INT3**) con 4.4 kcal/mol menos de energía que *E,Z*-**1-TS1**. Posteriormente, se lleva a cabo la adición de alcohol a través de *E,Z*-**1-TS2** con una distancia de enlace C ··· O de 2.72 Å, seguida de una transferencia protónica hacia el azufre de la tiourea, formando el intermediario *E,Z*-**1-INT4**, que corresponde al tautómero de la tiourea y al producto piranilado (MTP). Luego, toma lugar la tautomerización tiol-nitrógeno en la tiourea, mediante una transferencia protónica asistida por el metanol, pasando por un estado de transición cíclico de 6 miembros *E,Z*-**1-TS4-MA** con una barrera energética de 12.5 kcal/mol, llevando a la formación del complejo *E,Z*-**1-INT5**. Finalmente, esta ruta 2 es energéticamente favorecida con respecto a la ruta 1, la cual termina con la separación del producto piranilado MTP y la liberación del catalizador *E,Z*, quedando este último disponible para otro ciclo catalítico.

Apéndice D

Otras actividades

En el marco de la formación científica en el área de investigación que se ha logrado en estos 5 años de Doctorado en Química, se enmarcan principalmente colaboraciones internacionales y nacionales, como la participación en eventos científicos en modalidad de póster.

D.1. Artículos científicos

Con respecto a las colaboraciones científicas se destaca principalmente la elaboración de siete publicaciones ISI tituladas:

- **Rocío Durán** and Bárbara Herrera, Theoretical Study of the Mechanism of Catalytic Enanteoselective N-H and O-H Insertion Reactions, *The Journal of Physical Chemistry A* , 124, 1 (2020): 2-11.

- Ivor Smajlagic, Matt Guest, **Rocío Durán**, Barbara Herrera and Travis Dudding, Mechanistic Insight Towards Understanding the Role of Charge in Thiourea Organocatalysis, *The Journal of Organic Chemistry*, 85, 2 (2020): 585-593.

- Daniel Villablanca, **Rocío Durán**, Al Mokhtar Lamsabhi, Barbara Herrera, Reaction Mechanism of Li and Mg Carbenoid Cyclopropanations: Metal-π and σ Interactions, *ACS Omega*, 4, 21 (2019): 19452-19461.

- **Rocío Durán**, Nicolás Núñez-Navarro, Flavia C. Zacconi and Barbara Herrera, Theoretical study of C-arylations with Aryl Halides. Determining the reaction mechanism, the effect of substituents and heteroatoms, *Physical Chemistry Chemical Physics*, 21 (2019): 10163-10170.

- Ivor Smajlagic, **Rocío Durán**, Melanie Pilkington and Travis Dudding, Cyclopropenium Enhanced Thiourea Catalysis., *The Journal of Organic Chemistry*, 83, 22 (2018): 13973-13980.

- Nery Villegas-Escobar, Daniela E. Ortega, Diego Cortés-Arriagada, **Rocío Durán**, Diana Yepes, Soledad Gutiérrez-Oliva and Alejandro Toro-Labbé, Why Low Valent Lead (II) Hydride Complex Would be a Better Catalyst for CO_2 Activation than Its 14 Group Analogues?, *The Journal of Physical Chemistry C* , 121.22 (2017): 12127-12135.

- Cristina Ortega-Moo, **Rocío Durán**, Bárbara Herrera, Soledad Gutiérrez-Oliva, Alejandro Toro-Labbé and Rubicelia Vargas, Study of antiradical mechanisms with dihydroxybenzenes using reaction force and reaction electronic flux, *Physical Chemistry Chemical Physics*, 19.22 (2017): 14512-14519.

D.2. Participación en eventos científicos

Por otro lado, la participación en eventos científicos en modalidad de póster se destacan:

- Rocío Durán, Diego Cortés, Barbara Herrera, Alejandro Toro Labbé, *Reactivity of copper carbenoid toward insertion in O-H bonds. A Density Functional Theory Study* 44ª Congreso de Químicos Teóricos de Expresión Latina, Santiago, Chile, 2018.
- Rocio Durán, Bárbara Herrera, Alejandro Toro-Labbé, *Reactivity of copper carbenoid toward insertion in O-H bonds. A Density Functional Theory Study*, The Chemical Bonds at the 21st Century - 2017 CB2017 International conference on chemical bonding, Alemania, Aachen, 2017.

- Rocío Durán, Barbara Herrera, Alejandro Toro-Labbé, *Reactivity of copper carbenoid toward insertion in O-H bonds. A Density Functional Theory Study*, 11th Triennial Congress of the World Association of Theoretical and Computational Chemists, Alemania, Munich, 2017.

- Rocío Durán, Diego Cortés, Barbara Herrera, Alejandro Toro Labbé, *Theoretical study of the isomerization of transition metal complex with azo substituent, from the perspective of the Reaction Electronic Flux and Reaction Force*, 42do Congreso de Químicos Teóricos de Expresión Latina, Uruguay, Montevideo, 2016.

- Rocío Durán, Diego Cortés, Barbara Herrea, Alejandro Toro-labbé, *Theoretical study of the isomerization of transition metal complex with azo substituent, from the perspective of the Reaction Electronic Flux and Reaction Force*, R Bryan Miller Symposium, Estados Unidos, Davis, 2016.

- Cristina Ortega-Moo, Rocío Durán, Patricia Pérez, Eduardo E. Chamorro, Alejandro Toro-Labbé , Rubicelia Vargas, Jorge Garza, *Efecto del sustituyente en la capacidad antioxidante de compuestos relacionados con el pardeamiento enzimático*, Reunión Mexicana de Fisicoquímica Teórica XIV 2015, México, Tonalá, Jalisco, 2015.

- Rocío Durán, Diego Cortes, Barbara Herrera, Alejandro Toro-Labbé, *Theoretical study of the isomerization of the azobenzene, from the perspective of the Reaction Electronic Flux*, 3rd International Conference on Materials Science, Chile, Valdivia, 2015.

Bibliografía

[1] A. K. Yudin, *Catalyzed Carbon-Heteroatom Bond Formation*. Wiley-VCH: Weinheim, Germany, 2011 (2011).

[2] H. Keipour, V. Carreras, T. Ollevier, Recent progress in the catalytic carbene insertion reactions into the silicon-hydrogen bond, *Organic and Biomolecular Chemistry*, 15 (2017) 5441–5456.

[3] N. Martín, M. Dusselier, D. E. De Vos, F. G. Cirujano, Metal-Organic Framework Derived Metal Oxide Clusters in Porous Aluminosilicates: A Catalyst Design for the Synthesis of Bioactive aza-Heterocycles, *ACS Catalysis*, 9 (2019) 44–48.

[4] W. Liu, M. J. Cheng, R. J. Nielsen, W. A. Goddard, J. T. Groves, Probing the C-O Bond-Formation Step in Metalloporphyrin-Catalyzed C-H Oxygenation Reactions, *ACS Catalysis*, 7 (2017) 4182–4188.

[5] T. L. Lohr, Z. Li, T. J. Marks, Thermodynamic Strategies for C-O Bond Formation and Cleavage via Tandem Catalysis, *Accounts of Chemical Research*, 49 (2016) 824–834.

[6] X. F. Cheng, Y. Li, Y. M. Su, F. Yin, J. Y. Wang, J. Sheng, H. U. Vora, X.-S. Wang, J.-Q. Yu, Pd(II)-Catalyzed Enantioselective C-H Activation/C-O Bond Formation: Synthesis of Chiral Benzofuranones, *Journal of the American Chemical Society*, 135 (2013) 1236–1239.

[7] K. Manna, M. L. Kruse, A. D. Sadow, Concerted C-N/C-H Bond Forma-

tion in Highly Enantioselective Yttrium(III)-Catalyzed Hydroamination, *ACS Catalysis*, 1 (2011) 1637–1642.

[8] S. i. Kuwabe, K. E. Torraca, S. L. Buchwald, Palladium-Catalyzed Intramolecular C-O Bond Formation, *Journal of the American Chemical Society*, 123 (2001) 12202–12206.

[9] M. Besora, A. A. Braga, W. Sameera, J. Urbano, M. R. Fructos, P. J. Pérez, F. Maseras, A computational view on the reactions of hydrocarbons with coinage metal complexes, *Journal of Organometallic Chemistry*, 784 (2015) 2–12.

[10] Y. Xia, D. Qiu, J. Wang, Transition-Metal-Catalyzed Cross-Couplings through Carbene Migratory Insertion, *Chemical Reviews*, 117 (2017) 13810–13889.

[11] S. Wang, S. Xu, C. Yang, H. Sun, J. Wang, Formal Carbene C-H Bond Insertion in the Cu(I)-Catalyzed Reaction of Bis(trimethylsilyl)diazomethane with Benzoxazoles and Oxazoles, *Organic Letters*, 21 (2019) 1809–1812.

[12] Y. Xia, Z. Liu, Z. Liu, R. Ge, F. Ye, M. Hossain, Y. Zhang, J. Wang, Formal Carbene Insertion into C-C Bond: Rh(I)-Catalyzed Reaction of Benzocyclobutenols with Diazoesters, *Journal of the American Chemical Society*, 136 (2014) 3013–3015.

[13] S. F. Zhu, Q. L. Zhou, Transition-metal-catalyzed enantioselective heteroatom-hydrogen bond insertion reactions, *Accounts of Chemical Research*, 45 (2012) 1365–1377.

[14] D. Gillingham, N. Fei, Catalytic X-H insertion reactions based on carbenoids., *Chem. Soc. Rev.*, 42 (2013) 4918–31.

[15] Y. Xia, Y. Zhang, J. Wang, Catalytic Cascade Reactions Involving Metal Carbene Migratory Insertion, *ACS Catalysis*, 3 (2013) 2586–2598.

[16] Y. Y. Ren, S. F. Zhu, Q. L. Zhou, Chiral proton-transfer shuttle catalysts for carbene insertion reactions, *Organic and Biomolecular Chemistry*, 16 (2018) 3087–3094.

[17] H. Yuan, T. Nuligonda, H. Gao, C.-H. Tung, Z. Xu, Copper-catalyzed carbene insertion into the sulfur-sulfur bond of benzenesulfonothioate, *Organic Chemistry Frontiers*, 5 (2018) 1371–1374.

[18] S. Hyde, J. Veliks, B. Liégault, D. Grassi, M. Taillefer, V. Gouverneur, Copper-Catalyzed Insertion into Heteroatom-Hydrogen Bonds with Trifluorodiazoalkanes, *Angewandte Chemie*, 128 (2016) 3849–3853.

[19] K. Ramakrishna, C. Sivasankar, Iridium catalyzed acceptor/acceptor carbene insertion into N-H bonds in water, *Organic and Biomolecular Chemistry*, 15 (2017) 2392–2396.

[20] J. M. Fraile, P. López-Ram-de Viu, J. A. Mayoral, M. Roldán, J. Santafé-Valero, Enantioselective C-H carbene insertions with homogeneous and immobilized copper complexes, *Organic and Biomolecular Chemistry*, 9 (2011) 6075.

[21] H. M. L. Davies, R. E. J. Beckwith, Catalytic enantioselective C-H activation by means of metal-carbenoid-induced C-H insertion, *Chemical Reviews*, 103 (2003) 2861–2903.

[22] H. M. L. Davies, J. R. Manning, Catalytic C-H functionalization by metal carbenoid and nitrenoid insertion., *Nature*, 451 (2008) 417–24.

[23] A. Pereira, Y. Champouret, C. Martín, E. Álvarez, M. Etienne, T. R. Belderraín, P. J. Pérez, Copper-Carbene Intermediates in the Copper-Catalyzed Functionalization of O-H Bonds, *Chemistry: A European Journal*, 21 (2015) 9769–9775.

[24] Y. Liu, Z. Luo, J. Z. Zhang, F. Xia, DFT Calculations on the Mechanism of Transition-Metal-Catalyzed Reaction of Diazo Compounds with

Phenols: O-H Insertion versus C-H Insertion, *The Journal of Physical Chemistry A*, 120 (2016) 6485–6492.

[25] Y. Liu, Z. Yu, Z. Luo, J. Z. Zhang, L. Liu, F. Xia, Mechanistic Investigation of Aromatic C(sp)-H and Alkyl C(sp$^{(}$3))-H Bond Insertion by Gold Carbenes, *The Journal of Physical Chemistry A*, 120 (2016) 1925–1932.

[26] D. Zhu, J. Ma, K. Luo, H. Fu, L. Zhang, S. Zhu, Enantioselective Intramolecular C-H Insertion of Donor and Donor/Donor Carbenes by a Nondiazo Approach, *Angewandte Chemie International Edition*, 55 (2016) 8452–8456.

[27] J. T. Aldajaei, J. R. Keeffe, C. a. Swift, S. Gronert, Are Copper(I) Carbenes Capable Intermediates for Cyclopropanations? The Case for Ylide Intermediates, *Chemistry: A European Journal*, 21 (2015) 12702–12708.

[28] R. Rasappan, D. Laventine, O. Reiser, Metal-bis(oxazoline) complexes: From coordination chemistry to asymmetric catalysis, *Coordination Chemistry Reviews*, 252 (2008) 702–714.

[29] H. Keipour, V. Carreras, T. Ollevier, Recent progress in the catalytic carbene insertion reactions into the silicon-hydrogen bond, *Organic and Biomolecular Chemistry*, 15 (2017) 5441–5456.

[30] G. Boche, J. C. W. Lohrenz, The Electrophilic Nature of Carbenoids, Nitrenoids, and Oxenoids, *Chemical Reviews*, 101 (2001) 697–756.

[31] H. M. Davies, E. G. Antoulinakis, Recent progress in asymmetric intermolecular C-H activation by rhodium carbenoid intermediates, *Journal of Organometallic Chemistry*, 617-618 (2001) 47–55.

[32] T. C. Maier, G. C. Fu, Catalytic Enantioselective OH Insertion Reactions, *Journal of the American Chemical Society*, 128 (2006) 4594–4595.

[33] P. Le Maux, D. Carrié, P. Jéhan, G. Simonneaux, Asymmetric O-H insertion reaction of carbenoids catalyzed by chiral bicyclo bisoxazoline copper(I) and (II) complexes, *Tetrahedron*, 72 (2016) 4671–4675.

[34] M. Born, R. Oppenheimer, Zur Quantentheorie der Molekeln, *Annalen der Physik*, 389 (1927) 457–484.

[35] J. Foresman, A. Frisch, *Exploring Chemistry with Electronic Structure Methods. Guassian. INC.* Pittsburgh (1996).

[36] K. Fukui, The path of chemical reactions - the IRC approach, *Accounts of Chemical Research*, 14 (1981) 363–368.

[37] C. Gonzalez, H. B. Schlegel, Reaction path following in mass-weighted internal coordinates, *Journal of Physical Chemistry*, 94 (1990) 5523–5527.

[38] A. Toro-Labbé, Characterization of Chemical Reactions from the Profiles of Energy, Chemical Potential, and Hardness, *The Journal of Physical Chemistry A*, 103 (1999) 4398–4403.

[39] A. Toro-Labbé, S. Gutiérrez-Oliva, M. C. Concha, J. S. Murray, P. Politzer, Analysis of two intramolecular proton transfer processes in terms of the reaction force, *Journal of Chemical Physics*, 121 (2004) 4570–4576.

[40] B. Herrera, A. Toro-Labbe, The role of the reaction force to characterize local specific interactions that activate the intramolecular proton transfers in DNA basis, *Journal of Chemical Physics*, 121 (2004) 7096–7102.

[41] P. Politzer, A. Toro-Labbé, S. Gutiérrez-Oliva, B. Herrera, P. Jaque, M. C. Concha, J. S. Murray, The reaction force: Three key points along an intrinsic reaction coordinate, *Journal of Chemical Sciences*, 117 (2005) 467–472.

[42] S. Gutiérrez-Oliva, B. Herrera, A. Toro-Labbé, H. Chermette, On the Mechanism of Hydrogen Transfer in the HSCH(O) $\rightleftarrows$ (S)CHOH and HSNO

⇄ SNOH Reactions, *The Journal of Physical Chemistry A*, 109 (2005) 1748–1751.

[43] E. Rincón, P. Jaque, A. Toro-Labbé, Reaction Force Analysis of the Effect of Mg(II) on the 1,3 Intramolecular Hydrogen Transfer in Thymine, *The Journal of Physical Chemistry A*, 110 (2006) 9478–9485.

[44] B. Herrera, A. Toro-Labbé, The Role of Reaction Force and Chemical Potential in Characterizing the Mechanism of Double Proton Transfer in the Adenine-Uracil Complex, *The Journal of Physical Chemistry A*, 111 (2007) 5921–5926.

[45] J. V. Burda, A. Toro-Labbé, S. Gutiérrez-Oliva, J. S. Murray, P. Politzer, Reaction Force Decomposition of Activation Barriers To Elucidate Solvent Effects, *The Journal of Physical Chemistry A*, 111 (2007) 2455–2457.

[46] A. Toro-Labbé, S. Gutiérrez-Oliva, J. S. Murray, P. Politzer, The reaction force and the transition region of a reaction, *Journal of Molecular Modeling*, 15 (2009) 707–710.

[47] D. E. Ortega, D. Cortés-Arriagada, A. Toro-Labbé, Mechanistic details of ethylene polymerization reaction using methallyl nickel(II) catalysts, *Physical Chemistry Chemical Physics*, 20 (2018) 22915–22925.

[48] C. Barrales-Martíz, D. Cortés-Arriagada, S. Gutiérrez-Oliva, Molecular hydrogen formation in the interstellar medium: the role of polycyclic aromatic hydrocarbons analysed by the reaction force and activation strain model, *Monthly Notices of the Royal Astronomical Society*, 481 (2018) 3052–3062.

[49] W. J. van Zeist, A. H. Koers, L. P. Wolters, F. M. Bickelhaupt, Reaction Coordinates and the Transition-Vector Approximation to the IRC, *Journal of Chemical Theory and Computation*, 4 (2008) 920–928.

[50] W. J. van Zeist, F. M. Bickelhaupt, The activation strain model of chemical reactivity, *Organic and Biomolecular Chemistry*, 8 (2010) 3118.

[51] L. P. Wolters, F. M. Bickelhaupt, The activation strain model and molecular orbital theory, *Wiley Interdisciplinary Reviews: Computational Molecular Science*, 5 (2015) 324–343.

[52] J. Kubelka, F. M. Bickelhaupt, Activation Strain Analysis of SN2 Reactions at C, N, O, and F Centers, *The Journal of Physical Chemistry A*, 121 (2017) 885–891.

[53] P. Politzer, J. S. Murray, D. Yepes, P. Jaque, Driving and retarding forces in a chemical reaction, *Journal of Molecular Modeling*, 20 (2014) 2351.

[54] K. Morokuma, Molecular Orbital Studies of Hydrogen Bonds. III. C=O···H-O Hydrogen Bond in $H_2CO\cdots H_2O$ and $H_2CO\cdots 2H_2O$, *Journal of Chemical Physics*, 55 (1971) 1236–1244.

[55] T. Ziegler, A. Rauk, On the calculation of bonding energies by the Hartree Fock Slater method, *Theoretical Chemistry Accounts*, 46 (1977) 1–10.

[56] S. Grimme, J. Antony, S. Ehrlich, H. Krieg, A consistent and accurate ab initio parametrization of density functional dispersion correction (DFT-D) for the 94 elements H-Pu, *Journal of Chemical Physics*, 132 (2010) 154104.

[57] S. Grimme, S. Ehrlich, L. Goerigk, Effect of the damping function in dispersion corrected density functional theory, *Journal of Computational Chemistry*, 32 (2011) 1456–1465.

[58] A. D. Becke, K. E. Edgecombe, A simple measure of electron localization in atomic and molecular systems, *The Journal of Chemical Physics*, 92 (1990) 5397–5403.

[59] B. Silvi, A. Savin, Classification of chemical bonds based on topological analysis of electron localization functions, *Nature*, 371 (1994) 683–686.

[60] C. F. v. Weizscker, Zur Theorie der Kernmassen, *Zeitschrift fr Physik*, 96 (1935) 431–458.

[61] A. Otero-de-la Roza, E. R. Johnson, J. Contreras-García, Revealing non-covalent interactions in solids: NCI plots revisited, *Physical Chemistry Chemical Physics*, 14 (2012) 12165.

[62] R. Chaudret, B. de Courcy, J. Contreras-García, E. Gloaguen, A. Zehnacker-Rentien, M. Mons, J.-P. Piquemal, Unraveling non-covalent interactions within flexible biomolecules: from electron density topology to gas phase spectroscopy, *Physical Chemistry Chemical Physics*, 16 (2014) 9876.

[63] R. A. Boto, J. Contreras-García, J. Tierny, J.-P. Piquemal, Interpretation of the reduced density gradient, *Molecular Physics*, 114 (2016) 1406–1414.

[64] C. Narth, Z. Maroun, R. A. Boto, R. Chaudret, M.-L. Bonnet, J.-P. Piquemal, J. Contreras-García, *A Complete NCI Perspective: From New Bonds to Reactivity.* Springer (2016).

[65] E. R. Johnson, S. Keinan, P. Mori-Sánchez, J. Contreras-García, A. J. Cohen, W. Yang, Revealing noncovalent interactions, *Journal of the American Chemical Society*, 132 (2010) 6498–6506.

[66] G. V. Gibbs, D. F. Cox, K. M. Rosso, A Connection between Empirical Bond Strength and the Localization of the Electron Density at the Bond Critical Points of the SiO Bonds in Silicates, *The Journal of Physical Chemistry A*, 108 (2004) 7643–7645.

[67] R. F. W. Bader, H. Essén, The characterization of atomic interactions, *The Journal of Chemical Physics*, 80 (1984) 1943–1960.

[68] R. F. W. Bader, A Bond Path: A Universal Indicator of Bonded Interactions, *The Journal of Physical Chemistry A*, 102 (1998) 7314–7323.

[69] R. G. Parr, L. Szentpály, S. Liu, Electrophilicity Index, *Journal of the American Chemical Society*, 121 (1999) 1922–1924.

[70] E. Chamorro, P. K. Chattaraj, P. Fuentealba, Variation of the Electrophilicity Index along the Reaction Path, *The Journal of Physical Chemistry A*, 107 (2003) 7068–7072.

[71] P. K. Chattaraj, D. R. Roy, Update 1 of: Electrophilicity Index, *Chemical Reviews*, 107 (2007) PR46–PR74.

[72] P. Pérez, A. Aizman, R. Contreras, Comparison between experimental and theoretical scales of electrophilicity based on reactivity indexes, *The Journal of Physical Chemistry A*, 106 (2002) 3964–3966.

[73] K. Wiberg, Application of the pople-santry-segal CNDO method to the cyclopropylcarbinyl and cyclobutyl cation and to bicyclobutane, *Tetrahedron*, 24 (1968) 1083–1096.

[74] A. E. Reed, R. B. Weinstock, F. Weinhold, Natural population analysis, *Journal of Chemical Physics*, 83 (1985) 735–746.

[75] P. O. Löwdin, Quantum Theory of Many-Particle Systems. III. Extension of the Hartree-Fock Scheme to Include Degenerate Systems and Correlation Effects, *Physical Review*, 97 (1955) 1509–1520.

[76] A. E. Reed, L. A. Curtiss, F. Weinhold, Intermolecular interactions from a natural bond orbital, donor-acceptor viewpoint, *Chemical Reviews*, 88 (1988) 899–926.

[77] E. D. Glendening, C. R. Landis, F. Weinhold, NBO 6.0 : Natural bond orbital analysis program, *Journal of Computational Chemistry*, 34 (2013) 1429–1437.

[78] L. Onsager, Electric moments of molecules in liquids, *Journal of the American Chemical Society*, 58 (1936) 1486–1493.

[79] A. D. Becke, Density-functional thermochemistry. III. The role of exact exchange, *Journal of Chemical Physics*, 98 (1993) 5648–5652.

[80] C. Lee, W. Yang, R. G. Parr, Development of the Colle-Salvetti correlation-energy formula into a functional of the electron density, *Physical Review*, 37 (1988) 785–789.

[81] Y. Zhao, D. G. Truhlar, The M06 suite of density functionals for main group thermochemistry, thermochemical kinetics, noncovalent interactions, excited states, and transition elements: two new functionals and systematic testing of four M06-class functionals and 12 other function, *Theoretical Chemistry Accounts*, 120 (2008) 215–241.

[82] N. Mardirossian, M. Head-Gordon, How Accurate Are the Minnesota Density Functionals for Noncovalent Interactions, Isomerization Energies, Thermochemistry, and Barrier Heights Involving Molecules Composed of Main-Group Elements?, *Journal of Chemical Theory and Computation*, 12 (2016) 4303–4325.

[83] Y. S. Lin, G. D. Li, S. P. Mao, J. D. Chai, Long-Range Corrected Hybrid Density Functionals with Improved Dispersion Corrections, *Journal of Chemical Theory and Computation*, 9 (2013) 263–272.

[84] C. Riplinger, F. Neese, An efficient and near linear scaling pair natural orbital based local coupled cluster method, *The Journal of Chemical Physics*, 138 (2013) 034106.

[85] N. Mardirossian, M. Head-Gordon, Characterizing and Understanding the Remarkably Slow Basis Set Convergence of Several Minnesota Density Functionals for Intermolecular Interaction Energies, *Journal of Chemical Theory and Computation*, 9 (2013) 4453–4461.

[86] L. Goerigk, Treating London-Dispersion Effects with the Latest Minnesota Density Functionals: Problems and Possible Solutions, *Journal of Physical Chemistry Letters*, 6 (2015) 3891–3896.

[87] A. V. Marenich, C. J. Cramer, D. G. Truhlar, Universal Solvation Model Based on Solute Electron Density and on a Continuum Model of the

Solvent Defined by the Bulk Dielectric Constant and Atomic Surface Tensions, *Journal of Physical Chemistry B*, 113 (2009) 6378–6396.

[88] T. Lu, F. Chen, Multiwfn: A multifunctional wavefunction analyzer, *Journal of Computational Chemistry*, 33 (2012) 580–592.

[89] S. Van Damme, P. Bultinck, S. Fias, Electrostatic Potentials from Self-Consistent Hirshfeld Atomic Charges, *Journal of Chemical Theory and Computation*, 5 (2009) 334–340.

[90] T. Verstraelen, E. Pauwels, F. De Proft, V. Van Speybroeck, P. Geerlings, M. Waroquier, Assessment of Atomic Charge Models for Gas-Phase Computations on Polypeptides, *Journal of Chemical Theory and Computation*, 8 (2012) 661–676.

[91] J. Contreras-García, E. R. Johnson, S. Keinan, R. Chaudret, J. P. Piquemal, D. N. Beratan, W. Yang, NCIPLOT: A Program for Plotting Noncovalent Interaction Regions, *Journal of Chemical Theory and Computation.*, 7 (2011) 625–632.

[92] R. Chaudret, B. de Courcy, J. Contreras-García, E. Gloaguen, A. Zehnacker-Rentien, M. Mons, J.-P. Piquemal, Unraveling non-covalent interactions within flexible biomolecules: from electron density topology to gas phase spectroscopy, *Physical Chemistry Chemical Physics*, 16 (2014) 9876.

[93] P. Lian, R. C. Johnston, J. M. Parks, J. C. Smith, Quantum Chemical Calculation of pK_as of Environmentally Relevant Functional Groups: Carboxylic Acids, Amines, and Thiols in Aqueous Solution, *The Journal of Physical Chemistry A*, 122 (2018) 4366–4374.

[94] H. Frisch, MJ Trucks, GW and Schlegel, HB and Scuseria, GE and Robb, MA and Cheeseman, JR and Scalmani, G and Barone, V and Petersson, GA and Nakatsuji, Gaussian Inc 16, revision B.01, *Gaussian Inc., Wallingford CT*, (2016).

[95] F. Neese, The ORCA program system, *Wiley Interdisciplinary Reviews: Computational Molecular Science*, 2 (2012) 73–78.

[96] G. Zhurko, D. Zhurko. ChemCraft, Version 1.8 (2017).

[97] C. Legault. CYLview , Version 1.0b http://www.cylview.org (2009).

[98] T. L. Brown, *Chemistry: the central science.* Pearson Education (2009).

[99] H. Keipour, A. Jalba, N. Tanbouza, V. Carreras, T. Ollevier, α-Thiocarbonyl synthesis via the Fe^{II}-catalyzed insertion reaction of α-diazocarbonyls into S-H bonds, *Organic and Biomolecular Chemistry*, 17 (2019) 3098–3102.

[100] C. J. Cramer, *Essentials of computational chemistry: theories and models.* John Wiley & Sons (2013).

[101] R. J. Hinde, Quantum Chemistry, 5th Edition (by Ira N. Levine), *Journal of Chemical Education*, 77 (2000) 1564.

[102] W. A. Yager, E. Wasserman, R. M. R. Cramer, ESR Observation of Δm=1 Transitions of Triplet States in Glasses, *The Journal of Chemical Physics*, 37 (1962) 1148–1149.

[103] W. Kohn, L. J. Sham, Self-Consistent Equations Including Exchange and Correlation Effects, *Physical Review*, 140 (1965) A1133–A1138.

[104] E. J. Baerends, O. V. Gritsenko, A Quantum Chemical View of Density Functional Theory, *The Journal of Physical Chemistry A*, 101 (1997) 5383–5403.

[105] P. W. Ayers, R. G. Parr, Variational Principles for Describing Chemical Reactions: The Fukui Function and Chemical Hardness Revisited, *Journal of the American Chemical Society*, 122 (2000) 2010–2018.

[106] R. G. Parr. Density functional theory of atoms and molecules. *Horizons of Quantum Chemistry*, pp. 5–15. Springer (1980) .

[107] R. G. Parr, W. Yang, Density-Functional Theory of the Electronic Structure of Molecules, *Annual Review of Physical Chemistry*, 46 (1995) 701–728.

[108] P. Geerlings, F. De Proft, W. Langenaeker, Conceptual Density Functional Theory, *Chemical Reviews*, 103 (2003) 1793–1874.

[109] R. G. Parr, R. a. Donnelly, M. Levy, W. E. Palke, Electronegativity: The density functional viewpoint, *Journal of Chemical Physics*, 68 (1978) 3801.

[110] M. Solà, A. Toro-Labbé, The Hammond Postulate and the Principle of Maximum Hardness in Some Intramolecular Rearrangement Reactions, *The Journal of Physical Chemistry A*, 103 (1999) 8847–8852.

[111] G. S. Hammond, A Correlation of Reaction Rates, *Journal of the American Chemical Society*, 77 (1955) 334–338.

[112] J. E. Leffler, Parameters for the Description of Transition States, *Science*, 117 (1953) 340–341.

[113] R. G. Pearson, Recent advances in the concept of hard and soft acids and bases, *Journal of Chemical Education*, 64 (1987) 561.

[114] T. J. Auvil, A. G. Schafer, A. E. Mattson, Design Strategies for Enhanced Hydrogen-Bond Donor Catalysts, *European Journal of Organic Chemistry*, 2014 (2014) 2633–2646.

[115] R. J. Phipps, G. L. Hamilton, F. D. Toste, The progression of chiral anions from concepts to applications in asymmetric catalysis, *Nature Chemistry*, 4 (2012) 603–614.

[116] F. Giacalone, M. Gruttadauria, P. Agrigento, R. Noto, Low-loading asymmetric organocatalysis, *Chemical Society Reviews*, 41 (2012) 2406–2447.

[117] S. E. Root, S. Savagatrup, A. D. Printz, D. Rodriquez, D. J. Lipomi, Mechanical Properties of Organic Semiconductors for Stretchable, Highly Flexible, and Mechanically Robust Electronics, *Chemical Reviews*, 117 (2017) 6467–6499.

[118] Y. Qin, L. Zhu, S. Luo, Organocatalysis in Inert C-H Bond Functionalization, *Chemical Reviews*, 117 (2017) 9433–9520.

[119] J. Alemán, S. Cabrera, Applications of asymmetric organocatalysis in medicinal chemistry, *Chemical Society Reviews*, 42 (2013) 774–793.

[120] S. Bertelsen, K. A. Jørgensen, Organocatalysisafter the gold rush, *Chemical Society Reviews*, 38 (2009) 2178.

[121] D. W. MacMillan, The advent and development of organocatalysis, *Nature*, 455 (2008) 304–308.

[122] P. I. Dalko, L. Moisan, In the Golden Age of Organocatalysis, *Angewandte Chemie International Edition*, 43 (2004) 5138–5175.

[123] R. R. Knowles, E. N. Jacobsen, Attractive noncovalent interactions in asymmetric catalysis: Links between enzymes and small molecule catalysts, *Proceedings of the National Academy of Sciences*, 107 (2010) 20678–20685.

[124] A. G. Doyle, E. N. Jacobsen, Small-Molecule H-Bond Donors in Asymmetric Catalysis, *Chemical Reviews*, 107 (2007) 5713–5743.

[125] S. J. Connon, Organocatalysis Mediated by (Thio)urea Derivatives, *Chemistry - A European Journal*, 12 (2006) 5418–5427.

[126] Y. Takemoto, Recognition and activation by ureas and thioureas: stereoselective reactions using ureas and thioureas as hydrogen-bonding donors, *Organic and Biomolecular Chemistry*, 3 (2005) 4299.

[127] P. R. Schreiner, Metal-free organocatalysis through explicit hydrogen bonding interactions, *Chemical Society Reviews*, 32 (2003) 289.

[128] Á. Madarász, Z. Dósa, S. Varga, T. Soós, A. Csámpai, I. Pápai, Thiourea Derivatives as Brønsted Acid Organocatalysts, *ACS Catalysis*, 6 (2016) 4379–4387.

[129] Y. Fan, S. R. Kass, Electrostatically Enhanced Thioureas, *Organic Letters*, 18 (2016) 188–191.

[130] Y. Park, C. S. Schindler, E. N. Jacobsen, Enantioselective Aza-Sakurai Cyclizations: Dual Role of Thiourea as H-Bond Donor and Lewis Base, *Journal of the American Chemical Society*, 138 (2016) 14848–14851.

[131] C. B. Tripathi, S. Mukherjee, Lewis Base Catalysis by Thiourea: N-Bromosuccinimide-Mediated Oxidation of Alcohols, *The Journal of Organic Chemistry*, 77 (2012) 1592–1598.

[132] A. Supady, S. Hecht, C. Baldauf, About Underappreciated Yet Active Conformations of Thiourea Organocatalysts, *Organic Letters*, 19 (2017) 4199–4202.

[133] Z. Zhang, P. R. Schreiner, (Thio)urea organocatalysisWhat can be learnt from anion recognition?, *Chemical Society Reviews*, 38 (2009) 1187.

[134] C. Cox, T. Lectka, Solvent Effects on the Barrier to Rotation in Carbamates, *The Journal of Organic Chemistry*, 63 (1998) 2426–2427.

[135] A. J. Cruz-Cabeza, J. Bernstein, Conformational Polymorphism, *Chemical Reviews*, 114 (2014) 2170–2191.

[136] J. Garric, J.-M. Léger, A. Grelard, M. Ohkita, I. Huc, Solid state and solution conformation of 2-pyridinecarboxylic acid hydrazides: a new structural motif for foldamers, *Tetrahedron Letters*, 44 (2003) 1421–1424.

[137] I. Smajlagic, R. Durán, M. Pilkington, T. Dudding, Cyclopropenium Enhanced Thiourea Catalysis, *The Journal of Organic Chemistry*, 83 (2018) 13973–13980.

[138] L. Krasnova, C.-H. Wong, Understanding the Chemistry and Biology of Glycosylation with Glycan Synthesis, *Annual Review of Biochemistry*, 85 (2016) 599–630.

[139] J. D. Chai, M. Head-Gordon, Long-range corrected hybrid density functionals with damped atom-atom dispersion corrections, *Physical Chemistry Chemical Physics*, 10 (2008) 6615.

JOC The Journal of Organic Chemistry
Article
Cite This: J. Org. Chem. 2020, 85, 585−593
pubs.acs.org/joc

Mechanistic Insight toward Understanding the Role of Charge in Thiourea Organocatalysis

Ivor Smajlagic,[†] Matt Guest,[†] Rocío Durán,[‡] Barbara Herrera,[‡] and Travis Dudding*[,†]

[†]Brock University, 1812 Sir Isaac Brock Way, St. Catharines, ON L2S 3A1, Canada

[‡]Laboratorio de Química Teórica Computacional (QTC), Departamento de Química-Física, Facultad de Química y de Farmacia, Pontificia Universidad Católica de Chile, Av. Vicuña Mackenna 4860, Macul, Santiago, Chile

Supporting Information

ABSTRACT: Pyranylation and glycosylation are pivotal for accessing a myriad of natural products, pharmaceuticals, and drug candidates. Catalytic approaches for enabling these transformations are of utmost importance and integral to advancing this area of synthesis. In exploring this chemical space, a combined experimental and computational mechanistic study of pyranylation and 2-deoxygalactosylation catalyzed by a cationic thiourea organocatalyst is reported. To this end, a thiourea−cyclopropenium organocatalyst was employed as a model system in combination with an arsenal of mechanistic techniques, including ^{13}C kinetic isotope effect experiments, deuterated labeling studies, variable-temperature ^{1}H NMR spectroscopy, and density functional theory calculations. From these studies, two distinct reaction pathways were identified for this transformation corresponding to either dual hydrogen bond (H-bond) activation or Brønsted acid catalysis. The former involving thiourea orchestrated bifurcated hydrogen bonding proceeded in an asynchronous concerted fashion. In contrast, the latter stepwise mechanism involving Brønsted acid catalysis hinged upon the formation of an oxocarbenium intermediate accompanied by subsequent alcohol addition.

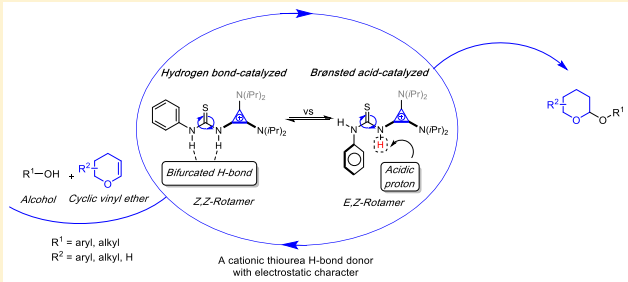

INTRODUCTION

Catalysis is a powerful tool for enabling large-scale manufacturing, fine chemical production, pharmaceutical synthesis, renewable energies, and countless other important processes.[1] For these reasons, the advancement of catalytic technologies is of utmost importance in today's society. On this forefront, mechanistic understanding acquired by computational modeling studies, in combination with experimental validation and testing, continues to gain traction. This synergy, arguably, has sparked numerous innovative approaches, e.g., the burgeoning field of organocatalysis[1a,2] offering a nonmetal feature,[3] functional group (FG) tolerance,[3a,4] and eco-friendliness.

In this context, thiourea organocatalysis has gained widespread popularity and with it broad utility,[2d,5] such as in host−guest (catalyst−substrate) applications involving attractive interactions facilitating chemical transformations. This includes uses in anion-binding catalysis,[6] H-bond donor/Brønsted acid catalysis,[2d,7] charge-enhanced catalysis,[8] and multifunctional catalysis.[9] Furthermore, thioureas equipped with multifunctional catalytic (e.g., Lewis base and H-bond donor) H-bond donor or Brønsted acid character are especially appealing. Often such character and associated reactivity, as well as others, can be attained by structural and electronic fine-tuning of a thiourea organocatalyst[4] with mechanistic understanding serving as a useful guide.

Complicating matters, nevertheless, are conformational dynamics as proposed more and more in emerging reports. For instance, recent efforts investigating the putative role of thiourea *Z,Z*-, *E,Z*-, *Z,E*-, and *E,E*-orientations and their correlated conformational dynamics, highlights the importance of these underappreciated, yet catalytically active conformers[7d,j,10] (Figure 1A). In this respect, thiourea *Z,Z*-orientations have historically been widely invoked in transition-state models; however, contemporary examples in the literature suggest other thiourea rotamers are likely vital for reactivity (Figure 1B). Moreover, critical in this sense are environmental stimuli, e.g., solvent stabilization rigidifying catalyst conformation and with it influencing transition state organization.[5d,c,10−14]

In light of these developments we recently reported the first cyclopropenium charge-enhanced thiourea organocatalyst that as a proof-of-principle application was deployed in pyranylation reactions; notably, this thiourea was found to be superior to current state-of-the-art thiourea organocatalysts, both neutral and charged.[8a] Despite this value, the underpinning mechanistic details of this catalytic reactivity remain uncertain. Considering this uncertainty and the well-established dynamic nature of biomimetic thiourea catalysts, e.g., Schreiner's thiourea, as demonstrated by Schreiner,[7d] Pápai and Varga,[7j]

Received: October 3, 2019
Published: December 2, 2019

DOI: 10.1021/acs.joc.9b02682
J. Org. Chem. 2020, 85, 585−593

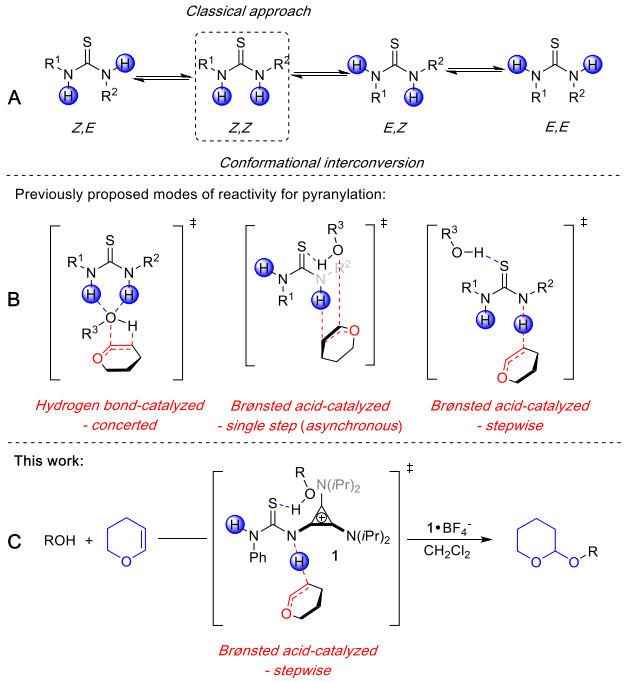

Figure 1. (A) General depiction of thiourea conformers. (B) Previous reported modes of reactivity for pyranylation by thioureas. (C) Computational investigation of pyranylations using thiourea **1**·BF_4^-.

and Baldauf,[10b] we were especially interested in understanding the operative role of our thiourea in pyranylations[15] and other transformations. Further, we anticipated the knowledge acquired from this undertaking would offer insights into hydrogen bond catalysis, Brønsted acid catalysis, charge-enhanced catalysis, multifunctional catalysis, and conformational dynamics broadly applicable in organocatalysis.

In this spirt, we report, vide infra, the first in-depth mechanistic study shedding light into synthetic and biorelevant pyranylation and 2-deoxygalactosylation reactions catalyzed by a cationic thiourea organocatalyst. To this end, multifunctional charged thiourea−cyclopropenium organocatalyst **1**·BF_4^- was employed as a model system (Figure 1C). In a broader context, this work demonstrates the importance of charge in promoting catalysis as well as the crucial impact of catalyst conformational flexibility in organocatalysis.

■ COMPUTATIONAL DETAILS

All calculations were performed with the Gaussian 09[16] suite of programs at the density functional theory (DFT) level employing the range-separated hybrid ωB97X-D functional[17] with a 6-311G(d,p) basis set.[18] This functional was selected as it accounts for dispersion and has been shown to provide accurate thermochemical and kinetic energies. Single-point calculations were also performed at the SMD/ωB97X-D/6-311G(d,p) level on ωB97X-D/6-311G(d,p)-optimized geometries. Thermal corrections from the vibrational frequencies at the ωB97X-D/6-311G(d,p) were added to the electronic energies of the above-mentioned methods to obtain the free energies. All of the optimized geometries (minimum stationary points (reactants, intermediates and products)) were confirmed by frequency computations as minima (zero imaginary frequencies) or transition states (one imaginary frequency) using analytic second derivatives.[19] Intrinsic reaction coordinate (IRC) calculations were performed to ensure that the transition states found were first order saddle points connecting the reactants and the products.[20−22] Solvent dichloromethane (DCM, ε = 8.93) in these calculations was accounted for by the self-consistent reaction field (SCRF) method using the solvation model based on density (SMD) model to gain a more accurate treatment of medium/long ranged attractive noncovalent interactions.[23,24] The Gibbs free energy differences ($\Delta G°$) were taken with respect to the most stable conformer. The 3D images of all optimized geometries were generated with CYLview[25] and natural bond orbital representations were produced using Chemcraft.[26] GaussView[27] was used to construct all structures prior to geometrical optimization. Monte Carlo conformational searches (MCCS) with an OPLS3[28] force field were performed on the full catalyst systems using Macromodel program in Schrodinger.[29]

■ RESULTS AND DISCUSSION

As a point of departure for our studies, we performed computations exploring the ground-state conformer distribution of thiourea catalyst **1** in the absence of a counterion for computational simplicity. Emerging from these calculations were four distinct conformer populations, conforming to *E,Z*-, *E,E*-, *Z,E*-, and *Z,Z*-rotamers of **1** with relative Gibbs free energies ($\Delta G°_{rel}$) spanning 3.5 kcal mol^{-1} in the presence of implicit solvent DCM, respectively (Figure 2). Among these conformers *E,Z*-**1** was lowest in energy, due in part to a smaller 7.59 D dipolar moment and reduced intramolecular (intra-host) steric contacts.

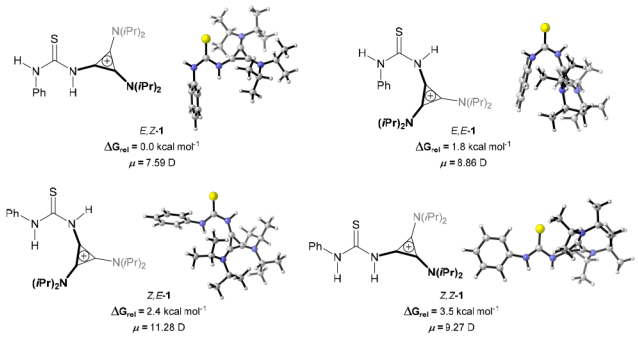

Figure 2. Conformers *E,Z*-**1**, *E,E*-**1**, *Z,E*-**1**, *Z,Z*-**1** with corresponding relative Gibbs free energies ($\Delta G°_{rel}$) and dipole moments (μ, units = debyes (D)).

Building upon these computed findings, we explored the rotamer distribution of **1**·BF_4^- by 1D nuclear Overhauser enhancement spectroscopy (NOESY) and variable-temperature (VT) ^{1}H NMR (600 MHz, CD_2Cl_2) analysis (Figure 3). Irradiation of the adjacent cyclopropenium ring N(3)-H hydrogen atom (green) gave rise to NOE signals correlating to both the N(4)-H (blue) and *o*-aryl C(22)-H (gray) hydrogens with the latter signal being weaker in intensity. A similar trend emerged upon irradiation of the N(4)-H hydrogen, though a stronger correlation to the *o*-aryl C(22)-H (gray) hydrogen was observed. In contrast, correlation between the N(3)-H hydrogen and the hydrogens of the *N*-diisopropyl methyl groups was not observed, thus suggesting a distal spatial relationship between the groups (Figure 3A). Evident from these NOE findings is a preferred solution-phase *Z,Z*-orientation of **1**·BF_4^-consistent with the reported crystal structure.

DOI: 10.1021/acs.joc.9b02682
J. Org. Chem. 2020, 85, 585−593

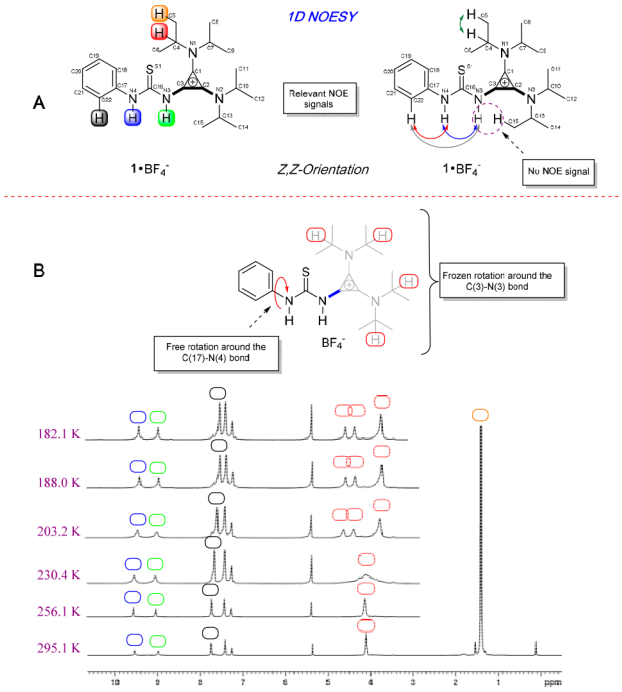

Figure 3. (A) Correlations between hydrogen atoms for **1**·BF_4^- based on 1D NOESY experiments with atoms labeled. (B) Variable-temperature ^{1}H NMR spectra with select thiourea **1**·BF_4^- conformers frozen.

Prompted by these results, we anticipated that VT analysis would reveal the presence of other rotamers of **1**·BF_4^- at lower temperatures (Figure 3B). Initially, a well-resolved methine signal at 4.08−4.12 ppm indicative of rapid conformer exchange at 295.1 K was observed that upon cooling to 230.4 K resulted in a broad signal at ∼4.09 ppm telling of restricted rotation about the C(3)−N(3) bond. Further cooling of the sample to 203.2 K led to splitting of this poorly resolved methine signal to a doublet (4.36−4.60 ppm) and a singlet at 3.74 ppm, supporting the presence of two or possibly more distinct rotamers. Consistent with this was the extrapolated activation barrier ($\Delta G^{\ddagger}$) of 10.2 kcal mol^{-1} and rate constant k_c = 974.1 s^{-1} for this exchange process at coalescence (230.4 K). The nonequivalency of these methine signals we attribute to anisotropic shielding by the π-polarizable cyclopropenium ring and π-electron system of the thiocarbonyl. Likewise, a 1D NOESY experiment conducted at 193.0 K revealed the presence of thiourea *Z,Z*-orientation. Confirming this orientation was an observed N(3)-H and N(4)-H correlation resulting in a strong NOE signal ascribed to interactions with the tetrafluoroborate counterion, rigidifying this conformation.[6] Irrespective, all of these conformers would be accessible experimentally as further supported by the computed 12.5 kcal mol^{-1} rotational barrier for conversion of conformer *E,Z*-**1** to *Z,Z*-**1** (see the SI). In attempting to freeze out additional rotamers the sample was cooled to 182.1 K; however, no further signal separation was observed with respect to the *o*-aryl hydrogen atoms, thus confirming C(17)−N(4) bond rotation was a low barrier process.

Having insight into the conformational dynamics of thiourea catalyst **1** we next explored the mechanism of pyranylated product formation. Emerging from these efforts were mechanistic pathways involving either rate determining (1) alcohol addition by thiourea-bifurcated dual hydrogen bond activation (pathway 1, Scheme 1) or (2) alcohol addition by Brønsted acid catalysis (pathway 2, Scheme 2). Inherent to both pathways was the thiourea conformer pre-equilibrium of Figure 2 as a point of entry for these mechanisms.

Scheme 1. Pathway 1: Dual Hydrogen Bond Activation Catalyzed by Charged Thiourea Conformer *Z,Z*-1

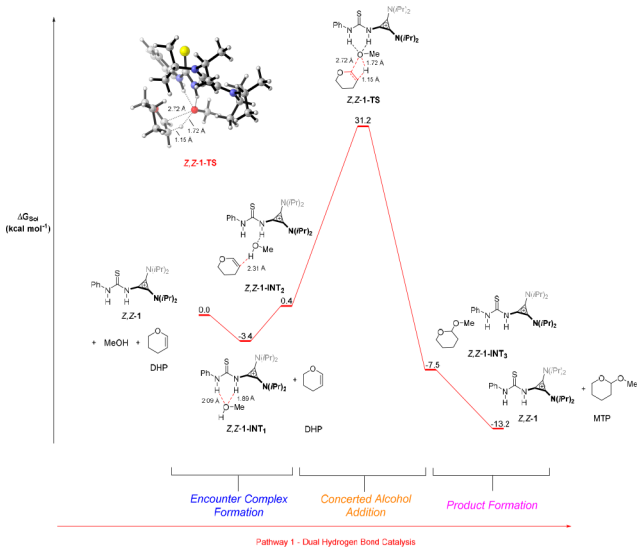

Pathway 1 (dual hydrogen bond activation) proceeds from thiourea **1** in the *Z,Z*-rotamer geometry (as observed by NMR), wherein a bifurcated H-bond complex *Z,Z*-**1-INT$_1$** displaying N−H···O hydrogen bond distances of 2.09 and 1.89 Å occurs (Scheme 1). Encounter complex *Z,Z*-**1-INT$_2$** then emerges, wherein the alcohol hydrogen atom resides directly atop the alkene of 3,4-dihydro-2*H*-pyran (DHP) at a distance of 2.31 Å. Inherent to this intermediate and certainly linked to the cyclopropenium charge was a large degree of charge polarization across the N(3)−H···O−H hydrogen bond subassembly (NBO charges N = −0.671 e, H = 0.459 e, O = −0.795 e, H = 0.510 e), setting the stage for proton transfer to the β-carbon of the vinyl ether of DHP. Rate determining alcohol addition involving C−O bond formation coupled with proton transfer follows by transition state *Z,Z*-**1-TS** having a sizable Gibbs free energy activation barrier of 30.8 kcal mol^{-1} with respect to *Z,Z*-**1-INT$_2$**. In terms of the energetic span model and turnover frequency (TOF), *Z,Z*-**1-INT$_1$** corresponds to the TOF determining intermediate (TDI), while the TOF determining transition state (TDTS) was *Z,Z*-**1-TS**, thus resulting in an overall energy span of 34.6 kcal mol^{-1} (TON = 7.2×10^{-11}, TOF = 2.7×10^{-13} s^{-1}).[30] The defining metrics of first-order saddle point *Z,Z*-**1-TS** entailed an elongated C···O bond making distance of 2.72 Å, as well as, C···H and O···H proton transfer distances of 1.15 and 1.72 Å. Intermediate complex *Z,Z*-**1-INT$_3$** then forms, where after separation of the pyranylated product 2-methoxytetrahydropyran (MTP) and thiourea *Z,Z*-**1** liberates the catalyst for another reaction cycle providing an overall exergonic process.

Alternatively, pathway 2 (Brønsted acid catalysis) initiates from an *E,Z*-rotamer catalyst conformation *E,Z*-**1** that in the presence of methanol forms H-bond complex *E,Z*-**1-INT$_1$** featuring an S···H−O hydrogen bond measuring 2.64 Å (Scheme 2). Next, complex *E,Z*-**1-INT$_2$** follows in which the cyclopropenium N−H hydrogen is primed for protonation of

DOI: 10.1021/acs.joc.9b02682
J. Org. Chem. 2020, 85, 585−593

Scheme 2. Pathway 2: Brønsted Acid Catalysis by Charged Thiourea Conformer *E,Z*-1

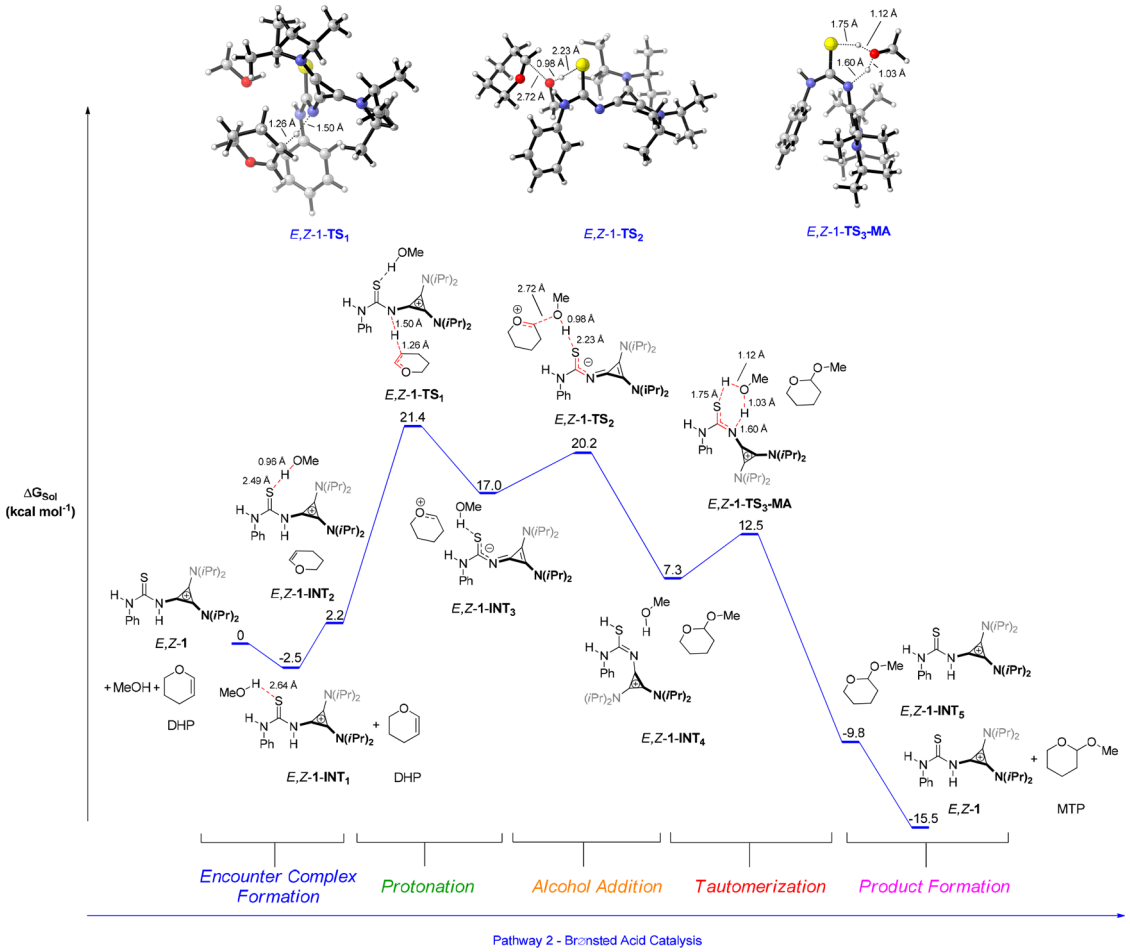

the vinyl ether alkene of DHP, while the alcohol acts as a bridging element bringing the catalyst and DHP in close proximity. Protonation transition state *E,Z*-**1-TS$_1$** then ensues with a Gibbs free energy activation barrier of 21.4 kcal mol^{-1} with respect to starting materials. Similarly, in terms of the energy span model, *E,Z*-**1-TS$_1$** was the TDTS and *E,Z*-**1-INT$_1$** was the TDI leading to an energy span of 23.9 kcal mol^{-1} for this cycle (TON = 8.3 × 10^{-4}, TOF = 1.7 × 10^{-5} s^{-1}).[30]

The defining features of this structure are proton-transfer distances of 1.50 and 1.26 Å with the alcohol component residing 4.52 Å from the vinyl ether α-carbon atom. Alternatively, protonation by the anilino nitrogen hydrogen N(4)−H was disfavored by 4.5 kcal mol^{-1} relative to transition state *E,Z*-**1-TS$_1$**, thus making this protonation process unlikely and further highlighting the significance of the cyclopropenium charge (see SI). Oxonium-thiourea anion ion pair *E,Z*-**1-INT$_3$** follows on the reaction pathway, residing 4.4 kcal mol^{-1} below transition state *E,Z*-**1-TS$_1$**. Next, alcohol addition *via* *E,Z*-**1-TS$_2$** displaying a C···O bond forming distance of 2.72 Å followed by proton transfer provides ion pair *E,Z*-**1-INT$_4$**. Thiol-to-nitrogen methanol assisted proton tautomerization by 6-membered cyclic transition state *E,Z*-**1-TS$_4$-MA** with a barrier of 12.5 kcal mol^{-1} then furnishes complex *E,Z*-**1-INT$_5$**. The key metrics of this transition state structure being S···H and N···H distances of 1.75 and 1.60 Å, as well as, corresponding O··H distances of 1.12 and 1.03 Å, respectively. Finally, this energetically favored pathway finishes with separation of the pyranylated product MTP and liberation of catalyst *E,Z*-**1** for another catalytic cycle. From these findings, based on the energetic span model, pathway 2 is energetically favored among the proposed mechanisms. It is important to note that exploration of pathway 2 via cyclopropenium nitrogen protonation was performed for all conformations of thiourea **1** as apparent in Figure 1; however, only a mechanism involving the *E,Z*-conformer was found to exist.

To corroborate these computed findings, we investigated potential catalyst−substrate interactions using ^{1}H NMR by sequentially adding substrate DHP to thiourea catalyst **1**·BF$_4^-$, resulting in no spectroscopic changes and by inference the lack of any interaction (Figure 4). Conversely, we have previously shown the sulfur of the catalyst engages in H-bonding with alcohols.[8a] From this evidence, we posit the thiourea catalyst plays a key bifunctional role[9] in these reactions by initially forming a more reactive metastable alcohol−catalyst complex (function 1) primed for proton transfer to DHP (function 2).

Next, the *anti*/*syn*-stereochemistry of alcohol addition to the alkene of DHP was investigated by reacting conformationally locked analogue 4-(*tert*-butyl)-3,4-dihydro-2*H*-pyran in methanol-d_4 in the presence of thiourea catalyst **1**·BF$_4^-$. Monitoring this reaction by ^{1}H NMR over a duration of 48 h revealed the formation of a diastereomeric mixture of pyranylated products with a kinetically controlled preference for *syn* product formation (*syn*/*anti* ratio of 70:30), consistent with a Brønsted acid mode of catalysis, vide supra (Scheme 3A). In contrast, a concerted H-bond-mediated reaction mechanism for alcohol addition proceeding through a pivotal intermediate displaying

DOI: 10.1021/acs.joc.9b02682
J. Org. Chem. 2020, 85, 585−593

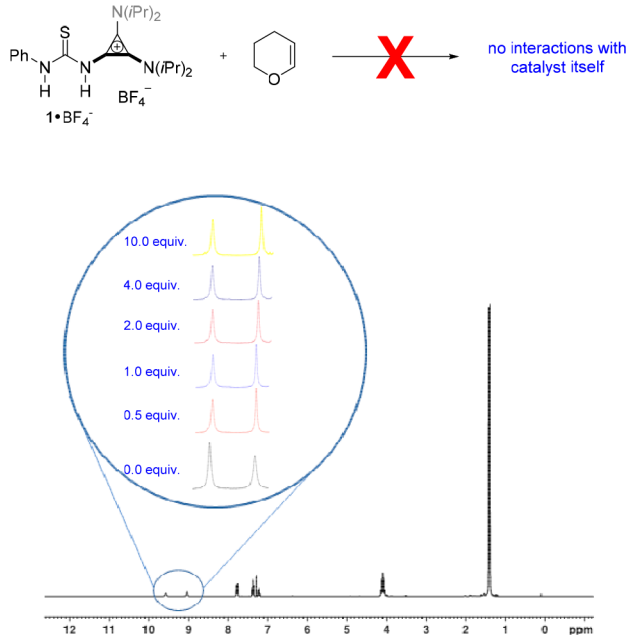

Figure 4. ^{1}H NMR spectra depicting no interactions between thiourea **1**·BF_4^- and DHP.

Scheme 3. Mechanistic Investigation of Alcohol Addition Using Deuterium-Labeled Alcohols: (A) Investigating the Stereochemistry of Addition Using Methanol-d_4 and 4-(*tert*-Butyl)-3,4-dihydro-2*H*-pyran; (B) Investigating the Stereochemistry of Addition Using Phenyl (O,1-$^2H_2$) Methanol and a Mixture of *Syn* and *Anti* Product Isomers (Methyl Adduct)

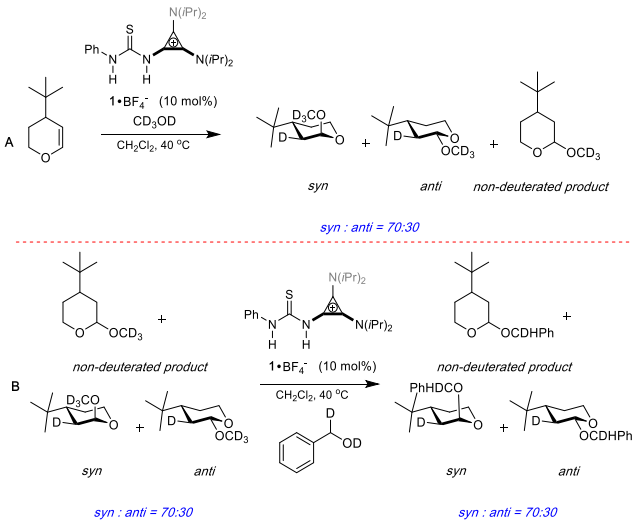

a ridged host–guest (catalyst–substrate) interaction allowing for nucleophilic attack from only one face would give rise to a single stereoisomer, thus opposing the likelihood of a concerted reaction mechanism under our employed conditions.

Subsequently, a series of control experiments using ethanol and benzyl alcohol were performed, wherein alkoxide exchange was observed (see the SI). Intrigued by the ability of thiourea catalyst **1**·BF_4^- to induce alkoxide exchange, we applied our reaction conditions to phenyl (O,1-$^2H_2$) methanol to distinguish between alkoxide exchange and epimerization (Scheme 3B).

From this experiment was observed a *syn*/*anti* product ratio of 70:30 mirroring that seen with methanol-d_4, which we ascribe to analogous mechanisms of alcohol addition. Based on this outcome, epimerization can be ruled out in favor of a catalyst-controlled stereoselective kinetic reaction scenario (see SI).

To gain further insight into the putative Brønsted acid mediated mechanism, ^{13}C KIE studies were pursued using Jacobsen's distortionless enhancement by a polarization transfer (DEPT) method[31] analyzing the product at low conversion at natural abundance (Figure 5). More specifically,

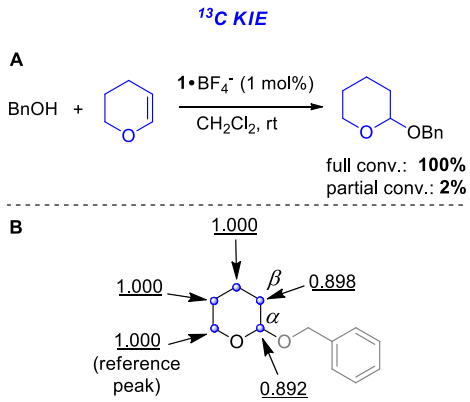

Figure 5. (A) ^{13}C kinetic isotope effect. (B) ^{13}C isotopic composition of THP protected alcohol from a reaction taken to 2% product conversion.

the DEPT-55 method was employed under pseudo-first-order conditions measuring KIEs at 2% product conversion. From this study, substantial inverse kinetic isotope effects were observed at the α- and β-carbons with values of 0.892 and 0.898, respectively, taking into account a 1.5% uncertainty in NMR integrations, thus, resulting in an uncertainty of 0.003[32] in the KIEs. These KIE findings are telling of two key features: (1) the observed large and inverse KIEs suggest that a multistep reaction involving a pre-equilibrium prior to the rate-determining step is plausible[33] and (2) the observed similar KIEs at the β- and α-carbons are indicative of $sp^2 \rightarrow sp^3$ rehybridization and negligible rehybridization, respectively at the rate-determining step. Though, this does not rule out other possible conclusions that can be drawn from these trends. Taken together, the experimental and computational findings support that thiourea-catalyzed (**1**) pyranylations is a stepwise Brønsted acid mechanism.

Having established charge-enhanced thiourea catalyst **1**·BF_4^- induced diastereoselection the use of 3,4,6-tri-*O*-benzyl-D-galactal (**2**) as a biorelevant 2-deoxysugar glycosyl donor equivalent[34] was investigated. In exploring this further application of our catalyst, **2** was reacted under standard conditions at reflux to afford 2-deoxygalactosylated product **3** in 84% yield with exclusive α-facial selectivity (Scheme 4). Inspired by this result, we sought to understand the origin of this selectivity by performing molecular mechanics searches.

Thus, utilizing the optimized structure of *E*,*Z*-1-**TS$_1$** as a template, *O*-benzyl functionality was appended and α- vs β-stereofacial alcohol addition considered, resulting in two representative transition state models (Figure 6). These models were then imported into the program MacroModel.[29]

DOI: 10.1021/acs.joc.9b02682
J. Org. Chem. 2020, 85, 585−593

Scheme 4. 2-Deoxygalactosylation of 3,4,6-Tri-*O*-benzyl-D-galactal Facilitated by Thiourea 1·BF$_4^-$

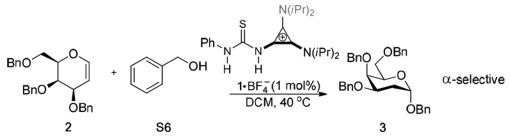

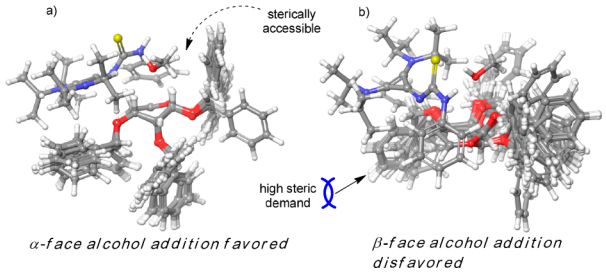

Figure 6. Comparison of α- vs β-stereofacial alcohol addition. (Superposition of conformers within 10 kJ mol^{-1} of the global minima.)

The internal coordinates of the atoms of the catalyst, alcohol and vinyl ether were frozen and Monte Carlo conformational searches (MCCS) with the OPLS3 force field[28] performed to generate an array of conformers for α- and β-stereofacial alcohol addition.

Visible from the superposition of the conformers for α-stereofacial alcohol addition was an open cavity allowing for more accessible alcohol addition (Figure 6, left-hand side), whereas, alcohol addition to the more sterically shielded β-face was impeded by the presence of bulky benzyl groups steering the catalyst away from the site of reactivity (Figure 6, right-hand side). While these simple molecular mechanics models offer a preliminary basis for understanding α- vs β-stereofacial alcohol addition a more thorough mechanistic investigation is required to unravel the fine details with respect to this transformation. That said, studies surrounding related aspects of glycosyl donor α- vs β-stereofacial selectivity and reactivity are currently underway in our laboratory.

■ CONCLUSION

In summary, we reported a computational and experimental mechanistic study of cationic thiourea-catalyzed pyranylations and the successful glycosylation of a 2-deoxy sugar. Arising from these studies was the importance of conformational dynamics, which is especially relevant in molecules with many degrees of freedom, wherein structural- and catalytic features are interdependent.[35] Further, a distinct feature of the catalytic reactivity examined in this report was "charge-enhanced acidity"[36] which is a timely concept gaining traction in the past decade for rational design of small molecule-based organocatalysts.[6c,8,37] The basis of this appeal stems from enhanced substrate activation relative to neutral catalysts, much like that found in more complex enzymatic counterparts. Further, the analysis discussed, herein, demonstrates judiciously designed organocatalysts having a charged moiety provide a general tool for improving catalytic reactivity.

■ EXPERIMENTAL SECTION

Materials and Methods. All materials were obtained from commercially available suppliers and used as received unless otherwise stated. The solvent employed in the reactions was dried using the following method: dichloromethane was distilled from CaH_2. All reactions were conducted in oven-dried round-bottom flasks under an inert atmosphere (N_2) and monitored by thin layer chromatography (TLC) using silica gel 60 F_{254} EMD Merck. NMR spectra were recorded on a Bruker DPX-300 spectrometer (^{1}H 300 MHz, ^{13}C 75.5 MHz) and Bruker Avance AV I 600 spectrometer (^{1}H 600 MHz) in $CDCl_3$. The observed chemical shifts are reported as δ-values (ppm) relative to tetramethylsilane (TMS). 1D NMR experiments were used to assist in rotamer identification. ^{13}C NMR KIE experiments were conducted to provide further support for the mechanistic hypothesis. **1**·BF$_4^-$,[8a] 4-(*tert*-butyl)-3,4-dihydro-2*H*-pyran,[38] and phenyl (O,1-$^2H_2$) methanol[39] were prepared according to literature procedures and the spectra match accordingly.

Low-Temperature NMR Experimental Acquisition. NMR spectra were recorded on a Bruker Avance AV I 600 spectrometer (^{1}H 600 MHz) in CD_2Cl_2. The observed chemical shifts are reported as δ values (ppm) relative to tetramethylsilane (TMS). The peaks of interest are denoted by red squares, as determined upon cooling of the sample. This protocol provides experimental evidence demonstrating the conformational orientation of thiourea **1**·BF$_4^-$, which was then compared with the computed results. The equations used to calculate the barrier to interconversion are shown below. The rate constant k_c at the coalescence temperature (T_c) was found using the difference in Hz ($\Delta\nu$, eq 1). The free activation energy ($\Delta G^{\ddagger}$) was determined using eq 2.

$$k_c = \frac{\pi\Delta\nu}{\sqrt{2}} \tag{1}$$

$$\Delta G^{\ddagger} = RT_c\left[22.96 + \ln\left(\frac{T_c}{\Delta\nu}\right)\right] \tag{2}$$

NMR Binding Studies. ^{1}H NMR titrations in $CDCl_3$ using catalyst **1**·BF$_4^-$ and DHP (up to 10.0 equiv) at room temperature revealed a lack of complex formation as seen from the presence of N−H hydrogen atoms belonging to thiourea catalyst **1**·BF$_4^-$ even after the solution was saturated with DHP.

Probing the Stereochemistry of Alcohol Addition. To probe the stereochemistry of alcohol addition, an experiment using methanol-d_4 was performed. This involved the use of a 10.0 mL round-bottom flask charged with thiourea **1**·BF$_4^-$ (115 mg, 10 mol %) to which methanol-d_4 (114 mg, 3.2 mmol) and 4-(*tert*-butyl)-3,4-dihydro-2*H*-pyran (340 mg, 2.4 mmol) were combined and subsequently diluted in dichloromethane (2.0 mL). The resulting solution was stirred at 40 °C while monitoring product formation with ^{1}H NMR spectroscopy over a period of 72 h (reaction completion). Next, all volatiles (dichloromethane and any residual methanol-d_4) were removed in vacuo, and the crude product was extracted with diethyl ether, concentrated, and analyzed with NMR spectroscopy.

Characterization Data for the Mixture of Nondeuterated and Deuterated Syn and anti Products (NMR Data Are Consistent with Literature).[7j] *Syn* isomer: ^{1}H NMR (300 MHz, $CDCl_3$, 25 °C) δ = 0.84 (s, 9H), 1.43−1.44 (m, 1H), 1.62 (d, J = 3.42 Hz; 1H), 1.66−1.68 (t, J = 3.39 Hz; 1H), 1.72−1.76 (d, J = 12.4 Hz; 1H), 3.62−3.68 (ddd, J = 11.1, 4.9, 1.6 Hz; 1H), 3.69−3.78 (td, 12.1, 2.3 Hz; 1H), 4.76−4.77 (d, J = 3.4 Hz; 1H); ^{13}C{^{1}H} NMR (75.5 MHz, $CDCl_3$, 25 °C): δ = 26.7, 26.8, 30.7−31.2 (t, J = 19.6 Hz), (nondeuterated: 31.3), 31.8, (nondeuterated: 38.7), 38.8, 60.0, 98.6.

Anti isomer: ^{1}H NMR (300 MHz, $CDCl_3$, 25 °C) δ = 0.86 (s, 9H), 1.03−1.06 (m, 1H), 1.19−1.23 (t, J = 6.99 Hz; 1H), 1.25−1.32 (m, 1H), 1.53 (m, 1H), 3.36−3.44 (m, 1H), 4.05−4.12 (m, 1H), 4.21−4.25 (d, J = 9.18 Hz; 1H); ^{13}C{^{1}H} NMR (75.5 MHz, $CDCl_3$, 25 °C): δ = 26.4, 27.1, 32.0, 32.4−32.9 (t, J = 18.5 Hz), (nondeuterated: 32.9), 44.6, 65.6, 103.6.

Experiments Investigating Alkoxide Exchange (NMR Data Are Consistent with Literature). A few key experiments were performed to test for the potential of alkoxide exchange. First, following a literature procedure[8a] 2-methoxytetrahydropyran (**S4**) was prepared using a 25.0 mL round-bottom flask charged with thiourea **1**·BF$_4^-$ (24 mg, 1 mol %) to which methanol (160 mg, 5.0 mmol) and 3,4-dihydro-2*H*-pyran (840 mg, 10 mmol) were combined and

DOI: 10.1021/acs.joc.9b02682
J. Org. Chem. 2020, 85, 585−593

subsequently diluted in dichloromethane (5.0 mL). The resulting solution was stirred at room temperature for 24 h. Thereafter, the solvent was removed and the resulting crude material was subjected to flash chromatography using a hexanes/ethyl acetate solvent system to yield **S4**.

*2-Methoxytetrahydropyran (**S4**):*[40] 0.53 g, 91%; clear oil; ^{1}H NMR (300 MHz, $CDCl_3$, 25 °C): δ = 1.49−1.90 (m, 6H), 3.41 (s, 3H), 3.49−3.56 (m, 1H), 3.83−3.90 (m, 1H), 4.51−4.53 (t, J = 2.97 Hz; 1H).

Next, to examine the potential for alkoxide exchange a 5.0 mL round-bottom flask was charged with thiourea **1**·BF_4^- (4 mg, 1 mol %), 2-methoxytetrahydropyran (**S4**, 100.0 mg, 0.86 mmol), and ethanol (52.0 mg, 1.1 mmol) and the resulting mixture diluted with dichloromethane (0.5 mL). This solution was allowed to stir for 72 h while monitoring reaction progress via NMR.

Experiments Investigating Epimerization. The reaction conditions were then applied to phenyl (O,1-$^2H_2$) methanol to distinguish between alkoxide exchange and epimerization. This involved the use of a 5.0 mL round-bottom flask charged with thiourea **1**·BF_4^- (49 mg, 10 mol %) to which phenyl (O,1-$^2H_2$) methanol (114 mg, 1.0 mmol) and the deuterated mixture of *syn* and *anti* product isomers (182 mg, 1.0 mmol) were combined and subsequently diluted in dichloromethane (0.75 mL). The resulting solution was stirred at 40 °C, while monitoring product formation with ^{1}H NMR spectroscopy over a period of 9 days. Next, dichloromethane was removed in vacuo, and the crude product was extracted with diethyl ether, concentrated, and analyzed with NMR spectroscopy.

Characterization Data for the Mixture of Nondeuterated and Deuterated Syn and Anti Products (Benzyl Adduct). Syn isomer: ^{1}H NMR (300 MHz, $CDCl_3$, 25 °C) δ = 0.87 (s, 9H), 1.47−1.49 (m, 1H), 1.68−1.71 (t, J = 3.51 Hz; 1H), 1.73−1.75 (t, J = 3.51 Hz; 1H), 1.77−1.83 (m, 1H), 3.68−3.74 (ddd, J = 11.0, 4.8, 1.7 Hz; 1H), 3.82−3.90 (td, 12.7, 2.3 Hz; 1H), 4.97−4.98 (d, J = 3.5 Hz; 1H), 7.37−7.40 (m, 5H); ^{13}C{^{1}H} NMR (75.5 MHz, $CDCl_3$, 25 °C): δ = 21.9, 26.8, 26.9, 30.7−31.2 (t, J = 19.8 Hz), (nondeuterated: 31.3), 31.9, (nondeuterated: 38.6), 38.7, 60.3, 96.6, 128.1, 128.3, 128.4, 128.5.

Anti isomer: ^{1}H NMR (300 MHz, $CDCl_3$, 25 °C) δ = 0.88 (s, 9H), 1.07−1.09 (m, 1H), 1.26−1.29 (overlapping signals; 1H), 1.31−1.36 (m, 1H), 1.58 (m, 1H), 3.40−3.48 (m, 1H), 4.10−4.16 (m, 1H), 4.43−4.46 (m; 1H), 7.28−7.36 (m, 5H); ^{13}C{^{1}H} NMR (75.5 MHz, $CDCl_3$, 25 °C): δ = 26.5, 27.1, 32.1, 32.6−33.0 (t, J = 20.4 Hz), (nondeuterated: 33.1), 44.7, 65.7, 101.5, 127.0, 127.5, 127.6, 127.8.

Procedure for ^{13}C KIE Experiments. Two independent reactions were conducted at either stoichiometric (1:1) or pseudo-first-order conditions to furnish the THP protected product at high conversion (100%) or low conversion (2%), respectively. The products were analyzed using Jacobsen's DEPT-55 technique.[31] Equation 3 was applied to calculate the KIEs.

$$\mathrm{KIE_{PTD}} = \frac{\ln(1 - F)}{\ln[(1 - F(R_{\mathrm{PDT}}/R_0))]} \tag{3}$$

High Conversion. To an oven-dried 10.0 mL round-bottom flask charged with thiourea **1**·BF_4^- (11 mg, 1 mol %); benzyl alcohol (2.3 mmol) and 3,4-dihydro-2H-pyran (2.3 mmol) were combined and subsequently diluted in dichloromethane (2.0 mL). The resulting solution was stirred at room temperature under an inert atmosphere for 3 h. After removal of the solvent, the crude material was triturated with diethyl ether (1 × 3.0 mL), and concentrated to yield the THP protected alcohol.

Low Conversion. To an oven-dried 10.0 mL round-bottom flask charged with thiourea **1**•BF_4^- (∼2 mg, 1 mol %); benzyl alcohol (0.37 mmol) and 3,4-dihydro-2H-pyran (18.5 mmol) were combined and subsequently diluted in dichloromethane (1.0 mL). The resulting solution was stirred at room temperature under an inert atmosphere for 3 h. After removal of the solvent, the crude material was subjected to flash chromatography using a hexanes/ethyl acetate (9:1) solvent system to yield the THP protected alcohol.

Procedure for the Thiourea-Catalyzed 2-Deoxygalactosylation (NMR Data Are Consistent with Literature).[41] In an oven-dried 10.0 mL round-bottom flask charged with thiourea **1**·BF_4^- (4.0 mg, 1 mol %) 3,4,6-tri-O-benzyl-D-galactal (0.400 mg, 0.960 mmol) (**2**) and benzyl alcohol (87 mg, 0.805 mmol) were combined and subsequently diluted in dichloromethane (1.5 mL). The resulting solution was stirred until near full consumption of **2** as determined by ^{1}H NMR spectroscopy analysis (∼12 h) at 40 °C under an inert atmosphere. Next, the crude material was subjected to flash column chromatography using hexanes/ethyl acetate (9:1) as a cosolvent system to furnish the title compound **3** as a clear and colorless oil (354 mg, 84%, α-anomer). ^{1}H NMR (300 MHz, $CDCl_3$, 25 °C) δ = 2.06−2.11 (dd, J = 12.7, 4.6 Hz; 1H), 2.25−2.35 (m, 1H), 3.58−3.69 (m, 2H), 3.99−4.06 (m, 3H), 4.45−4.73 (m, 7H), 4.96−5.00 (d, J = 11.6 Hz, 1H), 5.12−5.13 (d, J = 3.06 Hz; 1H), 7.28−7.39 (m, 20H).

■ ASSOCIATED CONTENT

Supporting Information

The Supporting Information is available free of charge at https://pubs.acs.org/doi/10.1021/acs.joc.9b02682.

Computational calculations, deuterated labeling studies, kinetic studies, and NMR spectra for all reported compounds (PDF)

■ AUTHOR INFORMATION

Corresponding Author

*E-mail: tdudding@brocku.ca.

ORCID

Barbara Herrera: 0000-0003-1911-4473

Travis Dudding: 0000-0002-2239-0818

Notes

The authors declare no competing financial interest.

■ ACKNOWLEDGMENTS

T.D. acknowledges financial support from the Natural Science and Engineering Research Council (NSERC) Discovery grant (2019-04205). I.S. acknowledges QEII-GSST for funding. M.G. acknowledges OGS for funding. The authors thank Razvan Simionescu for his aid in NMR experiments. Computations were carried out using the facilities at SHARCNET (Shared Hierarchical Academic Research Computing Network: www.sharcnet.ca) and Compute/Calcul Canada.

■ REFERENCES

(1) (a) Giacalone, F.; Gruttadauria, M.; Agrigento, P.; Noto, R. Low-Loading Asymmetric Organocatalysis. *Chem. Soc. Rev.* **2012**, *41*, 2406−2447. (b) Roberts, S. M., Poignant, G., Kozhevnikov, I., Xiao, J., Whittall, J., Pickett, T. E., Derouane, E. G., Eds. *Catalysis for Fine Chemical Synthesis, Vol. 1−5*; John Wiley & Sons, 2004. (c) van Leeuwen, P. W. M. N. *Homogeneous Catalysis: Understanding the Art*; Kluwer: Dordrecht, 2004.

(2) For reviews relating to the evolution of organocatalytic domains, see: (a) Auvil, T. J.; Schafer, A. G.; Mattson, A. E. Design Strategies for Enhanced Hydrogen-Bond Donor Catalysts. *Eur. J. Org. Chem.* **2014**, *2014*, 2633−2646. (b) Phipps, R. J.; Hamilton, G. L.; Toste, F. D. The Progression of Chiral Anions from Concepts to Applications in Asymmetric Catalysis. *Nat. Chem.* **2012**, *4*, 603−614. (c) Wende, R. C.; Schreiner, P. R. Evolution of Asymmetric Organocatalysis: Multi- and Retrocatalysis. *Green Chem.* **2012**, *14*, 1821−1849. (d) Doyle, A. G.; Jacobsen, E. N. Small-Molecule H-Bond Donors in Asymmetric Catalysis. *Chem. Rev.* **2007**, *107*, 5713−5743.

(3) For reviews pertaining to the attractive features of organocatalysis, see: (a) Alonso, D. A.; Baeza, A.; Chinchilla, R.; Gómez, C.; Guillena, G.; Pastor, I. M.; Ramón, D. J. Recent Advances in

DOI: 10.1021/acs.joc.9b02682
J. Org. Chem. 2020, 85, 585−593

Asymmetric Organocatalyzed Conjugate Additions to Nitroalkenes. *Molecules* **2017**, *22*, 895−946. (b) Qin, Y.; Zhu, L.; Luo, S. Organocatalysis in Inert C−H Bond Functionalization. *Chem. Rev.* **2017**, *117*, 9433−9520. (c) Alemań, J.; Cabrera, S. Applications of Asymmetric Organocatalysis in Medicinal Chemistry. *Chem. Soc. Rev.* **2013**, *42*, 774−793. (d) Bertelsen, S.; Jørgensen, K. A. Organocatalysis−After the Gold Rush. *Chem. Soc. Rev.* **2009**, *38*, 2178−2189. (e) MacMillan, D. W. C. The Advent and Development of Organocatalysis. *Nature* **2008**, *455*, 304−308. (f) Dalko, P. I.; Moisan, L. In the Golden Age of Organocatalysis. *Angew. Chem., Int. Ed.* **2004**, *43*, 5138−5175.

(4) Gensch, T.; Teders, M.; Glorius, F. Approach to Comparing the Functional Group Tolerance of Reactions. *J. Org. Chem.* **2017**, *82*, 9154−9159.

(5) For reviews on thiourea-based applications, see: (a) Held, F. E.; Tsogoeva, S. B. Asymmetric Cycloaddition Reactions Catalyzed by Bifunctional Thiourea and Squaramide Organocatalysts: Recent Advances. *Catal. Sci. Technol.* **2016**, *6*, 645−667. (b) Serdyuk, O. V.; Heckel, C. M.; Tsogoeva, S. B. Bifunctional Primary Amine-Thioureas in Asymmetric Organocatalysis. *Org. Biomol. Chem.* **2013**, *11*, 7051−7071. (c) Knowles, R. R.; Jacobsen, E. N. Attractive Noncovalent Interactions in Asymmetric Catalysis: Links between Enzymes and Small Molecule Catalysts. *Proc. Natl. Acad. Sci. U. S. A.* **2010**, *107*, 20678−20685. (d) Connon, S. J. Organocatalysis Mediated by (Thio)urea Derivatives. *Chem. - Eur. J.* **2006**, *12*, 5418−5427. (e) Takemoto, Y. Recognition and Activation by Ureas and Thioureas: Stereoselective Reactions using Ureas and Thioureas as Hydrogen-Bonding Donors. *Org. Biomol. Chem.* **2005**, *3*, 4299−4306. (f) Schreiner, P. R. Metal-Free Organocatalysis through Explicit Hydrogen Bonding Interactions. *Chem. Soc. Rev.* **2003**, *32*, 289−296.

(6) For examples of thiourea catalysts forming ion-pair complexes, see: (a) Kennedy, C. R.; Lehnherr, D.; Rajapaksa, N. S.; Ford, D. D.; Park, Y.; Jacobsen, E. N. Mechanism-Guided Development of a Highly Active Bis-thiourea Catalyst for Anion-Abstraction Catalysis. *J. Am. Chem. Soc.* **2016**, *138*, 13525−13528. (b) Mittal, N.; Lippert, K. M.; De, C. K.; Klauber, E. G.; Emge, T. J.; Schreiner, P. R.; Seidel, D. A Dual-Catalysis Anion-Binding Approach to the Kinetic Resolution of Amines: Insights into the Mechanism via a Combined Experimental and Computational Study. *J. Am. Chem. Soc.* **2015**, *137*, 5748−5758. (c) Berkessel, A.; Das, S.; Pekel, D.; Neudörfl, J. M. Anion-Binding Catalysis by Electron-Deficient Pyridinium Cations. *Angew. Chem., Int. Ed.* **2014**, *53*, 11660−11664. (d) Lin, S.; Jacobsen, E. N. Thiourea-Catalyzed Ring Opening of Episulfonium Ions with Indole Derivatives by means of Stabilizing, Non-Covalent Interactions. *Nat. Chem.* **2012**, *4*, 817−824. (e) Xu, H.; Zuend, S. J.; Woll, M. G.; Tao, Y.; Jacobsen, E. N. Asymmetric Cooperative Catalysis of Strong Brønsted Acid-Promoted Reactions using Chiral Ureas. *Science* **2010**, *327*, 986−990. (f) Reisman, S. E.; Doyle, A. G.; Jacobsen, E. N. Enantioselective Thiourea-Catalyzed Additions to Oxocarbenium Ions. *J. Am. Chem. Soc.* **2008**, *130*, 7198−7199. (g) Taylor, M. S.; Tokunaga, N.; Jacobsen, E. N. Enantioselective Thiourea-Catalyzed Acyl-Mannich Reactions of Isoquinolones. *Angew. Chem., Int. Ed.* **2005**, *44*, 6700−6704.

(7) For select examples of thiourea catalysts engaging in H-bonding interactions, see: (a) Yang, X.; Zhou, Y.-H.; Yang, H.; Wang, S.-S.; Ouyang, Q.; Luo, Q.-L.; Guo, Q.-X. Asymmetric Diels-Alder Reaction of 3-Vinylindoles and Nitroolefins Promoted by Multiple Hydrogen Bonds. *Org. Lett.* **2019**, *21*, 1161−1164. (b) Kennedy, C. R.; Guidera, J. A.; Jacobsen, E. N. Synergistic Ion-Binding Catalysis Demonstrated via an Enantioselective, Catalytic [2,3]-Wittig Rearrangement. *ACS Cent. Sci.* **2016**, *2*, 416−423. (c) Balmond, E. I.; Coe, D. M.; Galan, M. C.; McGarrigle, E. M. α-Selective Organocatalytic Synthesis of 2-Deoxygalactosides. *Angew. Chem., Int. Ed.* **2012**, *51*, 9152−9155. (d) Lippert, K. M.; Hof, K.; Gerbig, D.; Ley, D.; Hausmann, H.; Guenther, S.; Schreiner, P. R. Hydrogen-Bonding Thiourea Organocatalysts: The Privileged 3,5-Bis(trifluoromethyl)phenyl Group. *Eur. J. Org. Chem.* **2012**, *2012*, 5919−5927. (e) Kotke, M.; Schreiner, P. R. Generally Applicable Organocatalytic Tetrahydropyranylation of Hydroxy Functionalities with Very Low Catalyst Loading. *Synthesis* **2007**, *2007* (5), 779−790. (f) Yalalov, D. A.; Tsogoeva, S. B.; Schmatz, S. Chiral Thiourea-Based Bifunctional Organocatalysts in the Asymmetric Nitro-Michael Addition: A Joint Experimental-Theoretical Study. *Adv. Synth. Catal.* **2006**, *348*, 826−832. (g) Tsogoeva, S. B.; Wei, S. Highly Enantioselective Addition of Ketones to Nitroolefins Catalyzed by New Thiourea−Amine Bifunctional Organocatalysts. *Chem. Commun.* **2006**, 1451−1453. (h) Schreiner, P. R.; Wittkopp, A. H-Bonding Additives Act Like Lewis Acid Catalysts. *Org. Lett.* **2002**, *4*, 217−220. For reviews, see: (i) Nishikawa, Y. Recent Topics in Dual Hydrogen Bonding Catalysis. *Tetrahedron Lett.* **2018**, *59*, 216−223. For Brønsted acid type catalysis, see: (j) Madarász, A.; Dósa, Z.; Varga, S.; Soós, T.; Csámpai, A.; Pápai, I. Thiourea Derivatives as Brønsted Acid Organocatalysts. *ACS Catal.* **2016**, *6*, 4379−4387.

(8) For selected examples of electrostatically enhanced thiourea organocatalysts, see: (a) Smajlagic, I.; Durán, R.; Pilkington, M.; Dudding, T. Cyclopropenium Enhanced Thiourea Catalysis. *J. Org. Chem.* **2018**, *83*, 13973−13980. (b) Fan, Y.; Tiffner, M.; Schörgenhumer, J.; Robiette, R.; Waser, M.; Kass, S. R. Synthesis of Cyclic Organic Carbonates using Atmospheric Pressure CO_2 and Charge-Containing Thiourea Catalysts. *J. Org. Chem.* **2018**, *83*, 9991−10000. (c) Fan, Y.; Kass, S. R. Electrostatically Enhanced Thioureas. *Org. Lett.* **2016**, *18*, 188−191.

(9) For selected examples revealing thiocarbonyl Lewis base thiourea activity, see: (a) Park, Y.; Schindler, C. S.; Jacobsen, E. N. Enantioselective Aza-Sakurai Cyclizations: Dual Role of Thiourea as H-Bond Donor and Lewis Base. *J. Am. Chem. Soc.* **2016**, *138*, 14848−14851. (b) Tripathi, C. B.; Mukherjee, S. Lewis Base Catalysis by Thiourea: *N*-Bromosuccinimide-Mediated Oxidation of Alcohols. *J. Org. Chem.* **2012**, *77*, 1592−1598.

(10) For pertinent examples relating to (thio)urea conformations, see: (a) Luchini, G.; Ascough, D. M. H.; Alegre-Requena, J. V.; Gouverneur, V.; Paton, R. S. Data-Mining the Diaryl(thio)urea Conformational Landscape: Understanding the Contrasting Behaviour of Ureas and Thioureas with Quantum Chemistry. *Tetrahedron* **2019**, *75*, 697−702. (b) Supady, A.; Hecht, S.; Baldauf, C. About Underappreciated Yet Active Conformations of Thiourea Organocatalysts. *Org. Lett.* **2017**, *19*, 4199−4202. (c) Lam, C.-K.; Hau, S. C.-K.; Yau, C.-W.; Mak, T. C. W. Hydrogen-Bonded Anionic Host Lattices Constructed with Isocyanurate and Thiourea/Urea. *Cryst. Growth Des.* **2016**, *16*, 759−773. For reviews, see: (d) Crawford, J. M.; Sigman, M. S. Conformational Dynamics in Asymmetric Catalysis: Is Catalyst Flexibility a Design Element? *Synthesis* **2019**, *51*, 1021−1036.

(11) Cox, C.; Lectka, T. Solvent Effects on the Barrier to Rotation in Carbamates. *J. Org. Chem.* **1998**, *63*, 2426−2427.

(12) Rablen, P. R.; Miller, D. A.; Bullock, V. R.; Hutchinson, P. H.; Gorman, J. A. Solvent Effects on the Barrier to C−N Bond Rotation in *N,N*-Dimethylaminoacrylonitrile. *J. Am. Chem. Soc.* **1999**, *121*, 218−226.

(13) Cruz-Cabeza, A. J.; Bernstein, J. Conformational Polymorphism. *Chem. Rev.* **2014**, *114*, 2170−2191.

(14) Garric, J.; Léger, J.-M.; Grelard, A.; Ohkita, M.; Huc, I. Solid State and Solution Conformation of 2-Pyridinecarboxylic Acid Hydrazides: A New Structural Motif for Foldamers. *Tetrahedron Lett.* **2003**, *44*, 1421−1424.

(15) (a) Maskeri, M. A.; O'Connor, M. J.; Jaworski, A. A.; Davies, A. V.; Scheidt, K. A. A Cooperative Hydrogen Bond Donor−Brønsted Acid System for the Enantioselective Synthesis of Tetrahydropyrans. *Angew. Chem., Int. Ed.* **2018**, *57*, 17225−17229. (b) Krasnova, L.; Wong, C.-H. Understanding the Chemistry and Biology of Glycosylation with Glycan Synthesis. *Annu. Rev. Biochem.* **2016**, *85*, 599−630.

(16) Frisch, M. J.; Trucks, G. W.; Schlegel, H. B.; Scuseria, G. E.; Robb, M. A.; Cheeseman, J. R.; Scalmani, G.; Barone, V.; Mennucci, B.; Petersson, G. A.; Nakatsuji, H.; Caricato, M.; Li, X.; Hratchian, H. P.; Izmaylov, A. F.; Bloino, J.; Zhang, G.; Sonnenberg, J. L.; Hada, M.; Ehara, M.; Toyota, K.; Fukuda, R.; Hasegawa, J.; Ishida, M.; Nakajima, T.; Honda, Y.; Kitao, O.; Nakai, H.; Vreven, T.;

DOI: 10.1021/acs.joc.9b02682
J. Org. Chem. 2020, 85, 585−593

Montgomery, J. A., Jr.; Peralta, J. E.; Ogliaro, F.; Bearpark, M.; Heyd, J. J.; Brothers, E.; Kudin, K. N.; Staroverov, V. N.; Kobayashi, R.; Normand, J.; Raghavachari, K.; Rendell, A.; Burant, J. C.; Iyengar, S. S.; Tomasi, J.; Cossi, M.; Rega, N.; Millam, J. M.; Klene, M.; Knox, J.e.; Cross, J. B.; Bakken, V.; Adamo, C.; Jaramillo, J.; Gomperts, R.; Stratmann, R. E.; Yazyev, O.; Austin, A. J.; Cammi, A. R.; Pomelli, C.; Ochterski, J. W.; Martin, R. L.; Morokuma, K.; Zakrzewski, V. G.; Voth, G. A.; Salvador, P.; Dannenberg, J. J.; Dapprich, S.; Daniels, A. D.; Farkas, Ö.; Foresman, J. B.; Ortiz, J. V.; Cioslowski, J.; Fox, D. J. *Gaussian 09*, Revision D.02; Gaussian, Inc., Wallingford, CT, 2009.

(17) Chai, J.-D.; Head-Gordon, M. Long-Range Corrected Hybrid Density Functionals with Damped Atom−Atom Dispersion Corrections. *Phys. Chem. Chem. Phys.* **2008**, *10*, 6615−6620.

(18) Krishnan, R.; Binkley, J. S.; Seeger, R.; Pople, J. A. Self-Consistent Molecular Orbital Methods. XX. A Basis Set for Correlated Wave Functions. *J. Chem. Phys.* **1980**, *72*, 650−654.

(19) Scott, A. P.; Radom, L. Harmonic Vibrational Frequencies: An Evaluation of Hartree−Fock, Møller−Plesset, Quadratic Configuration Interaction, Density Functional Theory, and Semiempirical Scale Factors. *J. Phys. Chem.* **1996**, *100*, 16502−16513.

(20) Peng, C.; Ayala, P. Y.; Schlegel, H. B.; Frisch, M. J. Using Redundant Internal Coordinates to Optimize Equilibrium Geometries and Transition States. *J. Comput. Chem.* **1996**, *17*, 49−56.

(21) Hratchian, H. P.; Schlegel, H. B. Using Hessian Updating To Increase the Efficiency of a Hessian Based Predictor-Corrector Reaction Path Following Method. *J. Chem. Theory Comput.* **2005**, *1*, 61−69.

(22) Hratchian, H. P.; Schlegel, H. B. Accurate Reaction Paths using a Hessian Based Predictor-Corrector Integrator. *J. Chem. Phys.* **2004**, *120*, 9918−9924.

(23) Marenich, A. V.; Cramer, C. J.; Truhlar, D. G. Universal Solvation Model Based on Solute Electron Density and on a Continuum Model of the Solvent Defined by the Bulk Dielectric Constant and Atomic Surface Tensions. *J. Phys. Chem. B* **2009**, *113*, 6378−6396.

(24) Tomasi, J.; Mennucci, B.; Cammi, R. Quantum Mechanical Continuum Solvation Models. *Chem. Rev.* **2005**, *105*, 2999−3094.

(25) Legault, C.Y.. *CYLview*, version 1.0b; Universite de Sherbrooke, Quebec, Canada, 2009, http://www.cylview.org.

(26) Zhurko, G.; Zhurko, D. *ChemCraft*, version 1.8; http://www.chemcraftprog.com.

(27) Dennington, R.; Keith, T.; Millam, J. *GaussView*, version 5; Semichem, Inc., Shawnee Mission, 2009, .

(28) Storer, J. W.; Giesen, D. J.; Cramer, C. J.; Truhlar, D. G. Class IV Charge Models: A New Semiempirical Approach in Quantum Chemistry. *J. Comput.-Aided Mol. Des.* **1995**, *9*, 87−110.

(29) *Schrödinger Release 2019−2: MacroModel*; Schrödinger, LLC: New York, 2019.

(30) (a) Kozuch, S. A Refinement of Everyday Thinking: The Energetic Span Model for Kinetic Assessment of Catalytic Cycles. *WIREs: Comput. Mol. Sci.* **2012**, *2*, 795−815. (b) Kozuch, S.; Shaik, S. How to Conceptualize Catalytic Cycles? The Energetic Span Model. *Acc. Chem. Res.* **2011**, *44*, 101−110. (c) Uhe, A.; Kozuch, S.; Shaik, S. Automatic Analysis of Computed Catalytic Cycles. *J. Comput. Chem.* **2011**, *32*, 978−985.

(31) Kwan, E. E.; Park, Y.; Besser, H. A.; Anderson, T. L.; Jacobsen, E. N. Sensitive and Accurate ^{13}C Kinetic Isotope Effect Measurements Enabled by Polarization Transfer. *J. Am. Chem. Soc.* **2017**, *139*, 43−46.

(32) Singleton, D. A.; Thomas, A. A. High-Precision Simultaneous Determination of Multiple Small Kinetic Isotope Effects at Natural Abundance. *J. Am. Chem. Soc.* **1995**, *117*, 9357−9358.

(33) Laidler, K. J. *Chemical kinetics*, 3rd ed.; Harper & Row: New York, 1987.

(34) Daniel, P. T.; Koert, U.; Schuppan, J. Apoptolidin: Induktion von Apoptose durch einen Naturstoff. *Angew. Chem.* **2006**, *118*, 886−908; *Angew. Chem., Int. Ed.* **2006**, *45*, 872−893. (b) He, X.; Liu, H.-W. Mechanisms of Enzymatic CO Bond Cleavages in Deoxyhexose Biosynthesis. *Curr. Opin. Chem. Biol.* **2002**, *6*, 590−597. (c) Kirschning, A.; Bechthold, A. F.-W.; Rohr, J. Chemical and Biochemical Aspects of Deoxysugars and Deoxysugar Oligosaccharides. *Top. Curr. Chem.* **1997**, *188*, 1−84. (d) Sastry, M.; Patel, D. J. Solution Structure of the Mithramycin Dimer-DNA Complex. *Biochemistry* **1993**, *32*, 6588−6604.

(35) Metrano, A. J.; Abascal, N. C.; Mercado, B. Q.; Paulson, E. K.; Hurtley, A. E.; Miller, S. J. Diversity of Secondary Structure in Catalytic Peptides with β-Turn-Biased Sequences. *J. Am. Chem. Soc.* **2017**, *139*, 492−516.

(36) Samet, M.; Buhle, J.; Zhou, Y.; Kass, S. R. Charge-Enhanced Acidity and Catalyst Activation. *J. Am. Chem. Soc.* **2015**, *137*, 4678−4680.

(37) For reviews, see: (a) Bandar, J. S.; Lambert, T. H. Aminocyclopropenium Ions: Synthesis, Properties, and Applications. *Synthesis* **2013**, *45*, 2485−2498. For timely examples, see: (b) Dempsey, K.; Mir, R.; Smajlagic, I.; Dudding, T. Expanding the Repertoire of Cyclopropenium Ion Phase Transfer Catalysis: Benzylic Fluorination. *Tetrahedron* **2018**, *74*, 3507−3511. (c) Xu, C.; Loh, C. C. J. An Ultra-Low Thiourea Catalyzed Strain-Release Glycosylation and a Multicatalytic Diversification Strategy. *Nat. Commun.* **2018**, *9*, 4057−4069. (d) Mir, R.; Dudding, T. Phase-Transfer Catalyzed *O*-Silyl Ether Deprotection Mediated by a Cyclopropenium Cation. *J. Org. Chem.* **2017**, *82*, 709−714. (e) Fan, Y.; Kass, S. R. Enantioselective Friedel−Crafts Alkylation between Nitroalkenes and Indoles Catalyzed by Charge Activated Thiourea Organocatalysts. *J. Org. Chem.* **2017**, *82*, 13288−13296. (f) Belding, L.; Stoyanov, P.; Dudding, T. Phase-Transfer Catalysis via a Proton Sponge: A Bifunctional Role for Biscyclopropenimine. *J. Org. Chem.* **2016**, *81*, 553−558. (g) Mirabdolbaghi, R.; Dudding, T. Expanding the Forefront of Strong Organic Brønsted Acids: Proton-Catalyzed Hydroamination of Unactivated Alkenes and Activation of Au(I) for Alkyne Hydroamination. *Org. Lett.* **2015**, *17*, 1930−1933. (h) Nacsa, E. D.; Lambert, T. H. Higher-Order Cyclopropenimine Superbases: Direct Neutral Brønsted Base Catalyzed Michael Reactions with α-Aryl Esters. *J. Am. Chem. Soc.* **2015**, *137*, 10246−10253.

(38) (a) Brichacek, M. P.; Carlson, R. M. Dihydropyran as a Template for Lactone Synthesis. *Synth. Commun.* **2007**, *37*, 3541−3549. (b) Booth, H.; Dixon, J. M.; Khedhair, K. A.; Readshaw, S. A. Experimental Studies of the Anomeric Effect. Part III. Rotameric Preferences about the Exo-Cyclic C_2-X Bond in Equatorial and Axial 2-Methoxy- and 2-Methylamino-Tetrahydropyrans. *Tetrahedron* **1990**, *46*, 1625−1652.

(39) García-Muñoz, Á.; Ortega-Arizmendi, A. I.; García-Carrillo, M. A.; Díaz, E.; Gonzalez-Rivas, N.; Cuevas-Yañez, E. Direct, Metal-Free Synthesis of Benzyl Alcohols and Deuterated Benzyl Alcohols from *p*-Toluenesulfonylhydrazones Using Water as Solvent. *Synthesis* **2012**, *44*, 2237−2242.

(40) Ginzel, K.-D.; Steckhan, E.; Degner, D. Indirect Electrochemical α-Methoxylation of Aliphatic Ethers and Acetals - Reactivity and Regioselectivity of the Anodic Oxidation using tris(2,4-dibromophenyl)amine as Redox Catalyst. *Tetrahedron* **1987**, *43*, 5797−5805.

(41) Das, S.; Pekel, D.; Neudörfl, J.-M.; Berkessel, A. Organocatalytic Glycosylation by Using Electron-Deficient Pyridinium Salts. *Angew. Chem., Int. Ed.* **2015**, *54*, 12479−12483.

DOI: 10.1021/acs.joc.9b02682
J. Org. Chem. 2020, 85, 585−593

THE JOURNAL OF PHYSICAL CHEMISTRY A

Article

Cite This: J. Phys. Chem. A 2020, 124, 2−11

pubs.acs.org/JPCA

Theoretical Study of the Mechanism of Catalytic Enanteoselective N−H and O−H Insertion Reactions

Published as part of The Journal of Physical Chemistry virtual special issue "Paul Geerlings Festschrift".

Rocío Durán and Barbara Herrera*

Laboratorio de Química Teórica Computacional (QTC), Departamento de Química-Física, Facultad de Química y de Farmacia, Pontificia Universidad Católica de Chile, Av. Vicuña Mackenna,4860 Macul, Santiago, Chile

Supporting Information

ABSTRACT: Theoretical density functional theory (DFT) calculations were carried out to study bond insertion reactions using a copper(I)−Box-carbenoid as a bond activator. In order to understand the reaction mechanism where N−H and O−H bonds actively participate, the reaction force (RF) and activation strain model (ASM) were used. Results indicate that the first step of the reaction is barrierless for both bond insertions (N−H and O−H), and the second step of the insertion reaction in the phenol (O−H bond) is favored kinetically and thermodynamically with regard to the aniline substrate (N−H bond). The enantioselectivity is driven by the ligand of the catalyst by steric repulsion, favoring the formation of the *R* isomer. The analysis of the reaction force and ASM exhibited that the higher energy barrier in aniline is mainly due to a higher W_2 contribution together with repulsive interactions, which hinders the insertion process.

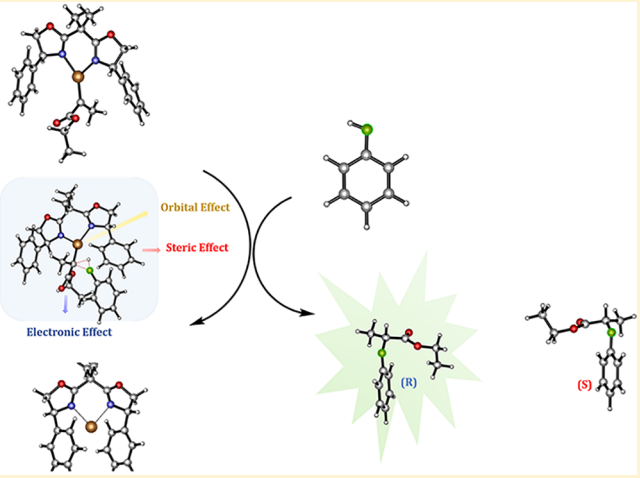

INTRODUCTION

Carbenoids are essential intermediates in organic synthesis.[1−3] Due to their dual electrophilic and nucleophilic nature, they participate in a broad range of chemical transformations.[4] Such is the case of the X−H bond insertion reactions (X = O, N), where carbenoids provide a direct and efficient route for the formation of C−X bonds.[3,5−7] Furthermore, although the metal atom in the carbenoid activates the X−H bond, it is in the adjacent carbon atom where direct interaction takes place. Thus, the metal complex that initiates the reaction is easily regenerated, which is why it is recognized as a catalytic process.[8]

Regarding the experimental works, most of them are based on the O−H insertion using copper carbenoids, with PhBox as a ligand.[9−12] This reaction is an efficient process, resulting in a high enantioselectivity and yield. It is well-known that in insertion reactions as well as aldolic additions,[13] aziridinations,[14,15] diels-alder reactions[16−19] the catalyst plays an important role into the activation of a desired atom and drives the stereoselectivity of a given system.[12,18,20]

The activation of the X−H bond needs an appropriate level of electrophilic character in the central carbon atom (C*), which can be achieved by choosing the right metal complex and substituents to form the carbenoid.[21−23] Previous experimental and computational works[8,11,23−26] have pointed out an insertion mechanism of the carbenoid at the X−H bond (see Figure 1), where initially a carbenoid intermediate is formed (c) from a diazocomposite (b) and a metal complex

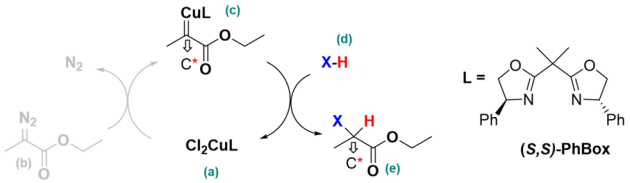

Figure 1. Proposed mechanism for the carbenoid insertion on heteroatom-hydrogen bond reaction. Adapted with permission from ref 11. Copyright 2012, American Chemical Society.

(a) and subsequently inserted into the X−H bond (d) in order to form a C*−X and a C*−X bond (e). In fact, there are previous results on the reaction mechanism of C−X insertions, giving accurate results regarding the nature of reactants and ligands.[14,27,28] However, whether the pathway between the formation of the intermediate carbenoid and the recovering of metal complex (bold black arrow on Figure 1) is concerted or occurs in a stepwise mechanism is an ongoing debate.

Received: July 30, 2019
Revised: December 5, 2019
Published: December 6, 2019

DOI: 10.1021/acs.jpca.9b07274
J. Phys. Chem. A 2020, 124, 2−11

In this work, we propose a density functional theory (DFT)[29−31] study of the mechanism of O−H and N−H insertion reactions; our interest is to discriminate if the reaction mechanism is concerted or stepwise and to determine the influence of the catalyst in the carbon activation and the enantioselectivity of the process. This study will be based on the concept of the reaction force (RF)[32−35] combined with the activation strain model (ASM)[36−39] and on electronic indexes such as noncovalent interactions (NCI).[40,41] For our goal, we have studied a model system with a copper(I) catalyst with PhBox as a chiral ligand to carry out the asymmetric insertion into the X−H bond. While a copper carbenoid provides a high enantioselectivity in these insertion reactions,[7,10,14,24,27,28,42] phenol and aniline are chosen as substrates in N−H and O−H bond activations due to their experimental importance.[25]

THEORETICAL METHODS

Reaction Force (RF). The reaction force concept was introduced by Toro-Labbé as the derivative of the potential energy $E(\xi)$ of the system with respect to the reaction coordinate (ξ).[32−35]

$$F(\xi) = -\left(\frac{\partial E(\xi)}{\partial \xi}\right) \tag{1}$$

For each elementary process, critical points partition the reaction force profile into three regions:[43−45] the reactant (R) region, the transition state (TS) region, and the products (P) region. Furthermore, areas under the reaction force profile define works associated with structural and electronic reordering, which are calculated as follows:

$$W_1 = -\int_{\xi_R}^{\xi_1} F(\xi) \qquad W_2 = -\int_{\xi_1}^{\xi_{TS}} F(\xi) \tag{2}$$

$$W_3 = -\int_{\xi_{TS}}^{\xi_2} F(\xi) \qquad W_4 = -\int_{\xi_2}^{\xi_P} F(\xi) \tag{3}$$

It has been demonstrated[46−49] that W_1 and W_4 involve mainly structural rearrangements, while the transition region, defined between ξ_1 and ξ_2 and associated with W_2 and W_3, is governed by bond breaking/forming processes accompanied by strong fluctuation in some electronic properties.

The analysis of the reaction force produced a rational partition of the activation energy, which can be written as the sum of W_1 and W_2.[33]

$$\Delta E^{\neq} = [E(\xi_{TS}) - E(\xi_R)] = W_1 + W_2 \tag{4}$$

A significant advantage of decomposing $\Delta E^{\neq}$ into this two components, is that it reveals how an external agent, such as a solvent or a catalyst, can affect the activation energy.

Activation Strain Model (ASM). This reactivity model based on the electronic density fragmentation was developed by Bickelhaupt et al.[36−39] with the aim of explaining differences in the activation energies of certain chemical reactions. ASM defines the total energy of a system as a sum of two contributions: distortion energy (ΔE_{strain}) and interaction energy (ΔE_{int}).

$$\Delta E(\xi) = \Delta E_{strain}(\xi) + \Delta E_{int}(\xi) \tag{5}$$

The first term (ΔE_{strain}) corresponds to the sum of the energy cost associated with the geometrical distortion of the each reactant along the reaction coordinate. The second, ΔE_{int}, quantifies the absorbed or release energy by the system when the distorted species interact at each point of the coordinate.

Politzer et al.[50] demonstrated that both RF and ASM allow the identification and quantification of the driving and retardant forces that govern the chemical reactions. With the use of these theoretical and computational tools, it is expected to advance in the understanding and characterization of the reaction mechanism under study.

The Energy Decomposition Analysis(EDA). The energy decomposition analysis method was independently developed by Morokuma[51] and Ziegler;[52] it is a powerful tool that connects the difference between elementary quantum mechanics and a simple conceptual interpretation of the nature of the chemical bond. Within this partition scheme, the energy reduction associated with the formation of a chemical bond is divided into three different terms.

This analysis extracts the interaction energy (ΔE_{int}) of an AB bond, which corresponds to the energy difference between the energy of the supermolecule (AB) and the energy of the isolated monomers A and B.

$$\Delta E_{int} = E_{AB} - E_A - E_B \tag{6}$$

As mentioned previously, the ΔE_{int} can be broken down into three physically significant components, which represent different steps toward the formation of a complex from its two fragments.

$$\Delta E_{int} = \Delta V_{elts} + \Delta E_{Pauli} + \Delta E_{orb} \tag{7}$$

The first term, ΔV_{elts}, is usually attractive and corresponds to the classical electrostatic interaction between the overlapping fragments with their frozen charge distribution (ρ_A and ρ_B) in the geometry of the complex. The second term, ΔV_{Pauli}, represents Pauli's repulsion energy and comprises the destabilizing interaction between occupied orbitals and is also responsible for the steric repulsion originated from Pauli's antisymmetry principle.

Finally, an empirical term ΔE_{disp} was adhered to the interaction energy of the effects of long-range dispersion, introduced by Grimme et al.[53,54] Thus, the interaction energy for A and B fragments is defined as

$$\Delta E_{int} = \Delta V_{elts} + \Delta E_{Pauli} + \Delta E_{orb} + \Delta E_{disp} \tag{8}$$

Noncovalent Interactions (NCI). The NCI[40,41] is a visualization index based on the electron density (ρ) and the reduced density gradient (RDG, s), which is defined as

$$s = \frac{1}{2(3\pi^2)^{1/3}} \frac{|\nabla \rho|}{\rho^{4/3}} \tag{9}$$

This index can be visualized in 2D and 3D plots. The 2D plot shows the reduced gradient (s) as a function of the electron density, ρ, oriented by the sign of λ (the second eigenvalue of the Hessian), while the 3D NCI plots correspond to the spatial visualization of the close contacts. A 3D NCI plot can be obtained for a system in order to rank interactions graphically along with the system.

COMPUTATIONAL DETAILS

All the calculations were carried out at the density functional theory (DFT) level of theory, using the hybrid-meta GGA M06-2X functional,[55] which accounts dispersion effects, along with the combination with the cc-pVDZ basis set for all nonmetallic atoms. Cu was described using the LANL2DZ

DOI: 10.1021/acs.jpca.9b07274
J. Phys. Chem. A 2020, 124, 2−11

quasirelativistic pseudopotential and basis set.[56−58] This functional was selected because it is highly recommended due to its satisfactory accuracy in thermochemistry, kinetics, and noncovalent interactions calculations.[55,59,60] Also, it is important to note that the M06-2X functional has been previously used in carbenoid systems, showing good results.[61−63] This functional was compared with high accuracy methods, such as DLPND-CCSD(T)[64] for both activation and reaction energies (see Supporting Information).

Minimum stationary points, reactants (R), intermediates (I), products (R), and transition states (TS), were verified by frequency calculations using analytic second derivatives.[65] TS structures were related to reactants and products using the intrinsic reaction coordinate (IRC).[66,67] The solvent effects were taken into account using the self-consistent reaction field (SCRF) method by applying the solvation model based on density (SMD)[68] using dichloromethane (ε = 8.93).

To understand the electronic behavior of the systems under study, atomic charges, molecular orbitals and molecular electrostatic potential (MEP) have been determined. Charges were described through Hirshfeld-I populations analysis and calculated using methods implemented in Multiwfn 3.5.[69] The choice of charge analysis is based on the accuracy with which Hirshfeld-I charges[70] reproduce dipole moments and geometrical changes. Hirshfeld-I charges also give a quantitatively correct picture of the MEP and therefore suitable for chemical interpretations.[71,72] The study of weak interactions was done through the noncovalent interaction (NCI)[40,41] by NCIPLOT 3.0[40,41,73,74] program.

All calculations were performed in Gaussian 09 (G09)[75] software package, and some TS were first optimized on Orca 3.0[76] software package and then reoptimized in G09. The energy decomposition analysis (EDA)[77−79] was calculated by the Amsterdan Density Functional (ADF) software,[80] using the M06-2X functional with double-ζ basis sets for all atoms without considering the solvent effects. Visualization and generation of molecular structures was performed with Chemcraft[81] graphical user interface software, and figures were generated with the CYLview[82] software.

■ RESULTS AND DISCUSSION

Copper Carbenoid Analysis. In order to reach the products, the copper carbenoid has to be stable and not allow dimerization reactions.[83,84] This stability is given by the electrophilic feature of the carbenoid central carbon (labeled as C* in Figure 2), which depends on the electronic contributions of the adjacent groups, the orbital, and steric contributions of the copper complex. In the direction to achieve the desired reactivity of the C*, we have combined a donor (CH_3) and acceptor group ($C_3H_6O_2$) bonded to the reactive atom. MEP, Hirshfeld atomic charges, and NBO analysis displayed at the Supporting Information, indicated that C* in our systems is an electrophilic atom.

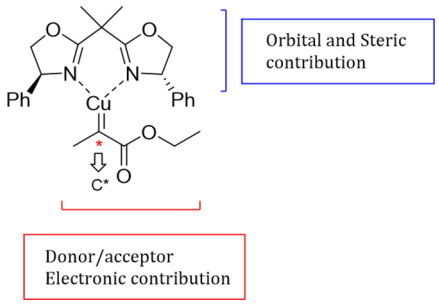

Figure 2. Representation of the copper carbenoid molecule.

Reaction Paths. The formation of C*−X and C*−H bonds in bond insertion reactions (Figure 3) was studied using aniline and phenol as substrates. The N−H and O−H bond activation by the carbenoid and subsequent bond insertion was found to proceed by two different routes depending on the substrate orientation and leading to optical isomers *S* and *R* in each case (see Figure 4). The *S* isomers are the products of a frontside attack of the substrate onto the C* atom, while a backside attack will yield an *R* isomer (see Figure 5).

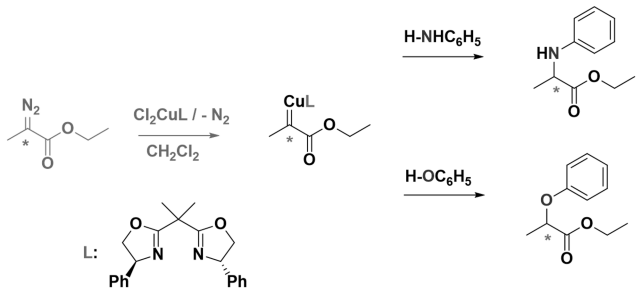

Figure 3. Carbenoid insertion reactions on X−H bond (X = N, O).

In order to analyze in detail the reactions, we are going to separate each step associated with the process. The first step of the reaction is a barrierless process that involves the nucleophilic attack of the substrate toward the carbenoid, forming a C*−X weak covalent bond, obtaining an ylide reactive complex (RC_X). The second step of the reaction includes the proton transfer from the substrate to the carbenoid center (C*) and the Cu−C* bond breaking, thus generating the product complex (PC_X). The reaction finishes with an *R* or *S* product depending on the orientation of the attack, coordinated to the copper complex are obtained. In a last step the product PC_X sepparates from the copper complex, forming a stationary point higher in energy.

Barrierless Process. The barrierless step corresponds to the C*−X bond formation and C*−Cu bond weakening processes. It is essential to study this step in detail since it gives rise to the enantioselectivity of the reaction. For each insertion (N−H and O−H) two barrierless processes were found, leading to two different RC_X reactant complex, each of which originates a specific optic isomer. The backside approach leads to the $RC_{X,R}$ species, while the $RC_{X,S}$ species is the product of the frontside approach. The interaction energy of each RC_X (ΔE_{RC}) was obtained from eq 10. The ΔE_{RC} for $RC_{X,R}$ was found to be greater than that for $RC_{X,S}$ in both bond insertions (N−H and O−H), being $RC_{X,R}$ more stable by 13.3 kcal/mol (N−H) and 9.70 kcal/mol (O−H) respectively.

$$\Delta E_{RC} = E_{carbenoid-substrate}(RC_X) - E_{carbenoid} - E_{substrate} \quad (10)$$

We have also calculated the strain percent present in each isomeric form, using

$$\%_{strain} = \frac{|\Delta E_{strain}|}{|\Delta E_{strain}| + |\Delta E_{int}|} \times 100 \quad (11)$$

To gain insights into the nature of these energies, we have decomposed ΔE_{RC} into ΔE_{int} and ΔE_{strain}. The decomposition

DOI: 10.1021/acs.jpca.9b07274
J. Phys. Chem. A 2020, 124, 2−11

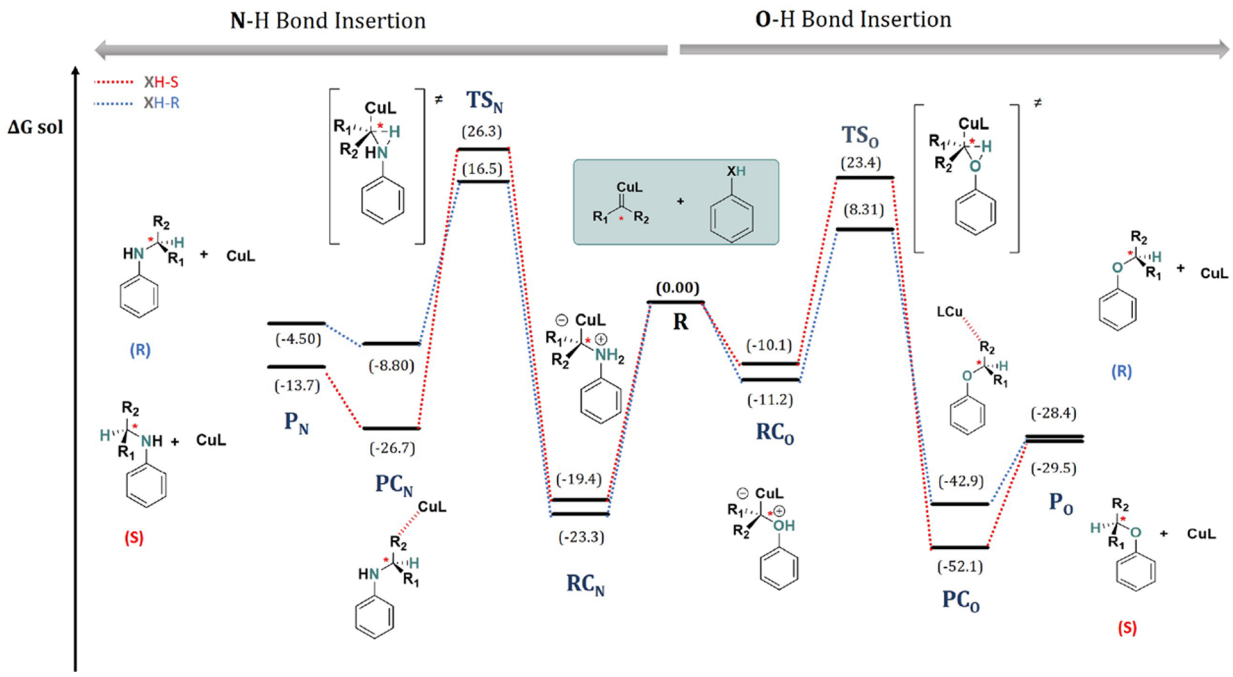

Figure 4. Calculated competitive pathways of the N−H (*R* and *S*) and O−H (*R* and *S*) insertions activated by copper carbenoid. The * notation corresponds to the electrophilic carbon (C*). $R_1 = CH_3$ and $R_2 = C_3H_6O_2$. The *S* product is represented in a red color path and the *R* product in blue. The energy corresponds to the Gibbs free energy ΔG^*_{sol} taking into account the effect of the dichloromethane solvent. All values are in kcal/mol.

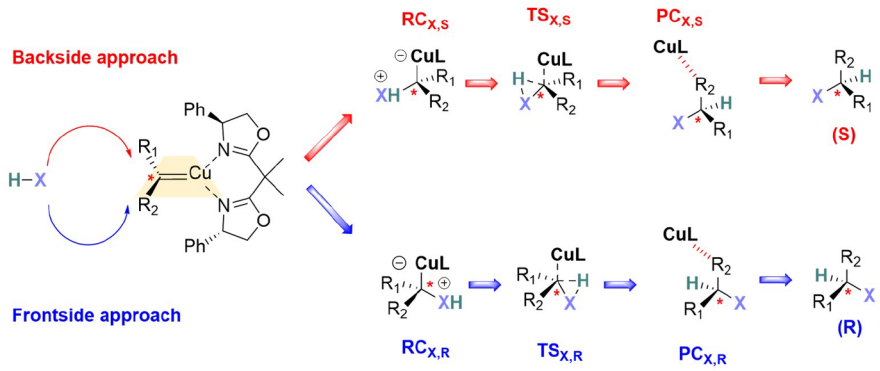

Figure 5. Proposed mechanism for the two substrate's approach orientations in the attack to the electrophilic carbenoid. The * notation corresponds to the electrophilic carbon (C*). $R_1 = CH_3$ and $R_2 = C_3H_6O_2$. X = NH, O.

Table 1. Reactant Complex Energy (ΔE_{RC}), Interaction Energy (ΔE_{int}), and Strain Energy (ΔE_{strain}) Calculated by ASM (All Values in kcal/mol)

	N−H		O−H	
	$RC_{N,R}$	$RC_{N,S}$	$RC_{O,R}$	$RC_{O,S}$
ΔE_{RC}	−27.6	−14.3	−20.3	−10.6
ΔE_{strain}	56.9 (40%)	103.2 (47%)	32.1 (38%)	73.8 (47%)
ΔE_{int}	−84.5 (60%)	−117.5 (53%)	−52.4 (62%)	−84.4 (53%)

energies are displayed in Table 1. The results indicate that for both enantiomers, the ΔE_{RC} is dominated by ΔE_{int} (60% (*R*) and 53% (*S*)) with respect to ΔE_{strain}. However, the lower stability of $RC_{X,S}$ is found to be due to the increase of ΔE_{strain}.

Figure 6 displays the RC_X structures corresponding to each approach for both insertions. As can be observed, both $RC_{N,S}$ and $RC_{O,S}$ present an important geometry loss with respect to the original carbenoid. The breaking of the Cu−C* bond, which can be inferred from the distances between these atoms (3.34 Å for aniline and 3.41 Å for phenol), leads to the shortening of the C*−X bond (resulting in distances of 1.46 Å for C*−N and 1.48 Å for C*−O). Hence, the breaking of the Cu−C* bond entails a loss of orbital contribution from the copper atom, which leads to a less stable specie.

The interaction and strain energies, and their contribution to the energy of the reactant complex (ΔE_{RC}) are shown in Table 1. As can be seen, ΔE_{int} is the major contributor in all cases, this being more evident in the case of the backside approach,

DOI: 10.1021/acs.jpca.9b07274
J. Phys. Chem. A 2020, 124, 2−11

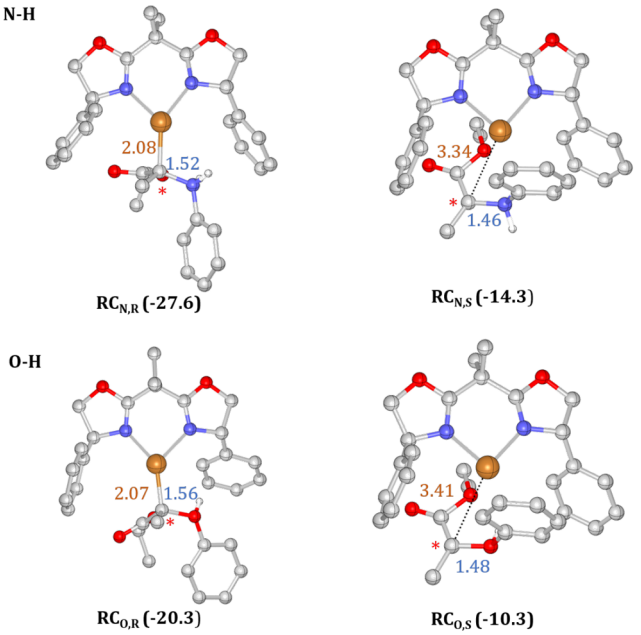

Figure 6. RC$_X$ structures to each X−H bond insertion with their respective enantiomers. The value in parentheses corresponds to the interaction energies on reactive complex (ΔE_{RC}). All values are in kcal/mol.

were it accounts for more tan 60% of ΔE_{RC}. Even more important is the fact that the negative (attractive) nature of ΔE_{int} is revealed, reaching its lowest value for RC$_{X,S}$ (−117.5 kcal mol). In order to inquire into what causes the changes in ΔE_{int}, RC$_X$ structures here analyzed on the basis of the energy decomposition analysis (EDA) implemented as developed by Ziegler et al.,[77−79] where $\Delta E_{int} = \Delta V_{elstat} + \Delta E_{Pauli} + \Delta E_{orb}$. The molecular partition that was used as fragment 1 corresponds to the carbenoid structure, and the substrate was labeled as fragment 2. Results from EDA (Figure 7) expose a higher percentage of Pauli repulsion between fragments (carbenoid and substrate) for the RC$_{X,S}$ formation: 3% higher for the N−H insertion and 2% higher for the O−H insertion. The increase in Pauli repulsion would account for the low contribution of interaction energy in these structures. The percentage of the Pauli repulsion was calculated using the eq 12.

$$\%_{Pauli} = \frac{|\Delta E_{Pauli}|}{|\Delta V_{elstat}| + |\Delta E_{Pauli}| + |\Delta E_{orb}|} \times 100 \quad (12)$$

To understand the nature of the Pauli repulsion, an analysis of noncovalent interactions by NCI index was carried out. The NCI analysis is displayed in Figure 7b, where the esential role of the chiral ligand (PhBOX) in the selectivity of the reaction is evident. It is known that steric effects are very important at the stereoselectivity of a reaction, and we consider that having quantitative proof on whether this effects are high confirms chemical intuition.

The frontal nucleophilic attack of the substrate to the carbenoid is mostly hindered by the steric effect (van der Waals repulsion), which is responsible for the higher Pauli repulsion of these systems, as opposed to the backside attack, which is favored by the conformation of the chiral ligand.

Enantioselectivity. The second step of both reactions involves only one energy barrier, which is the key to understand the enantioselectivity of each reaction. We have obtained barriers that indicated that the formation of the *R* isomer is favored for both N−H and O−H insertions (N−H, 39.8 (*R*) vs 45.7 kcal/mol (*S*); O−H, 19.5 (*R*) vs 33.5 kcal/mol (*S*)).

Noncovalent interactions (NCI) have been calculated with the aim to understand the nature in the enantioselectivity of the reactions. As said in the last section, we know that PhBox is the determinant in enantioselectivity; using this kind of plots, we can understand how this interaction takes place.

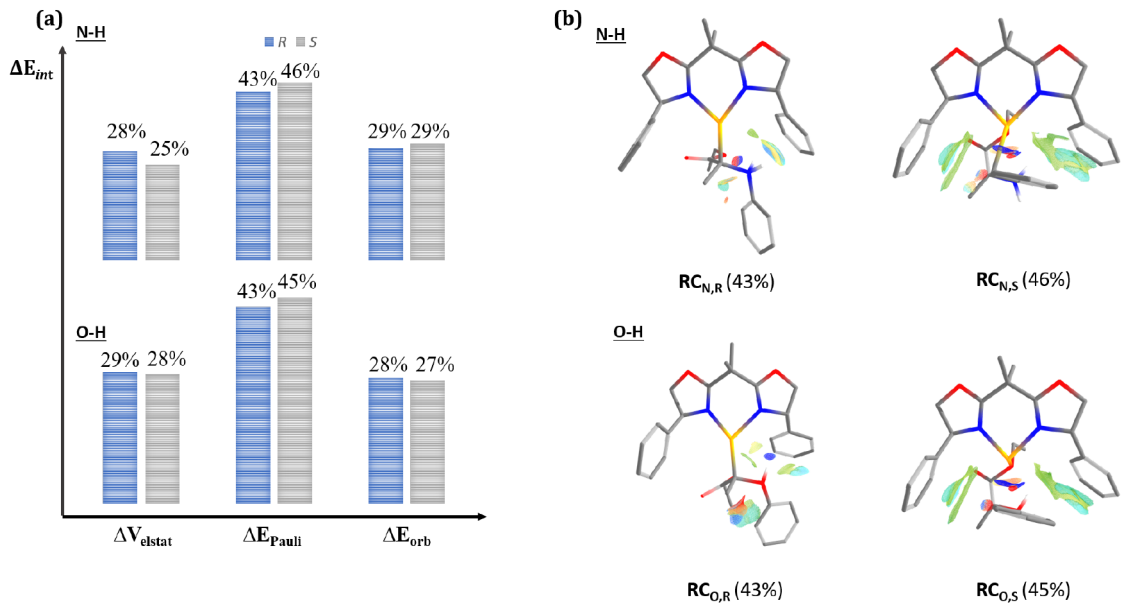

Figure 7. (a) EDA for interaction energy for RC structures in percentage of ΔE_{int}, the blue color corresponds to *R* enantiomers, while the gray color to *S* enantiomers (the dispersion is not displayed, due to values near zero). (b) 3D NCI plot of RC structures, in parentheses is ΔE_{Pauli} %. The red color isosurface corresponds to repulsive interactions, green to van der Waals interactions, and blue to attractive interactions.

DOI: 10.1021/acs.jpca.9b07274
J. Phys. Chem. A 2020, 124, 2−11

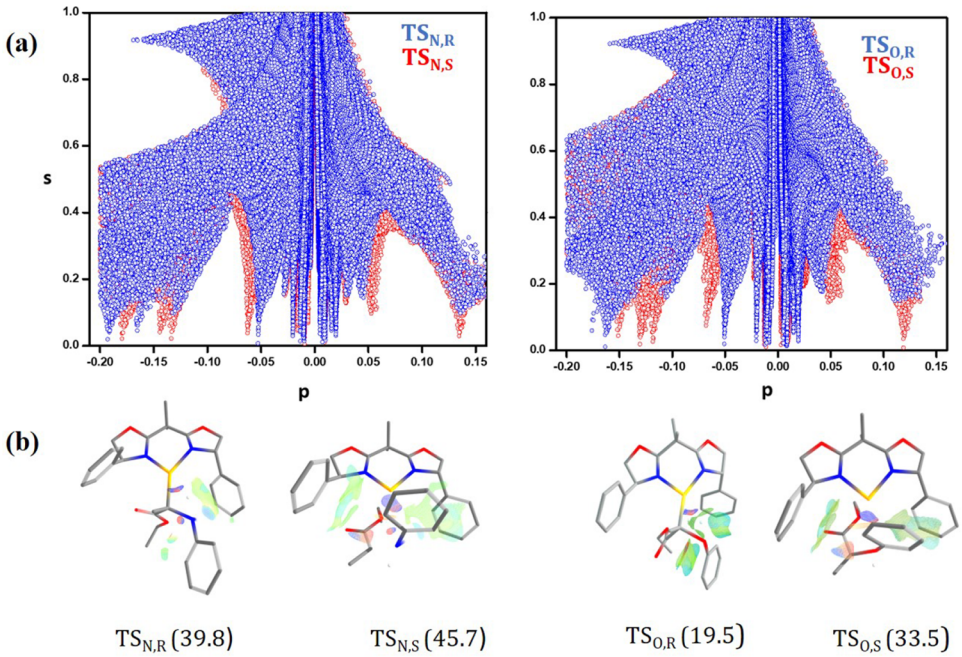

Figure 8. (a) 2D and (b) 3D NCI plots for the N−H and O−H bond insertions. For 2D plot the blue color corresponds to $TS_{X,R}$, and the red color corresponds to the $TS_{X,S}$ system. X corresponds to the heteroatom (X = N, O).

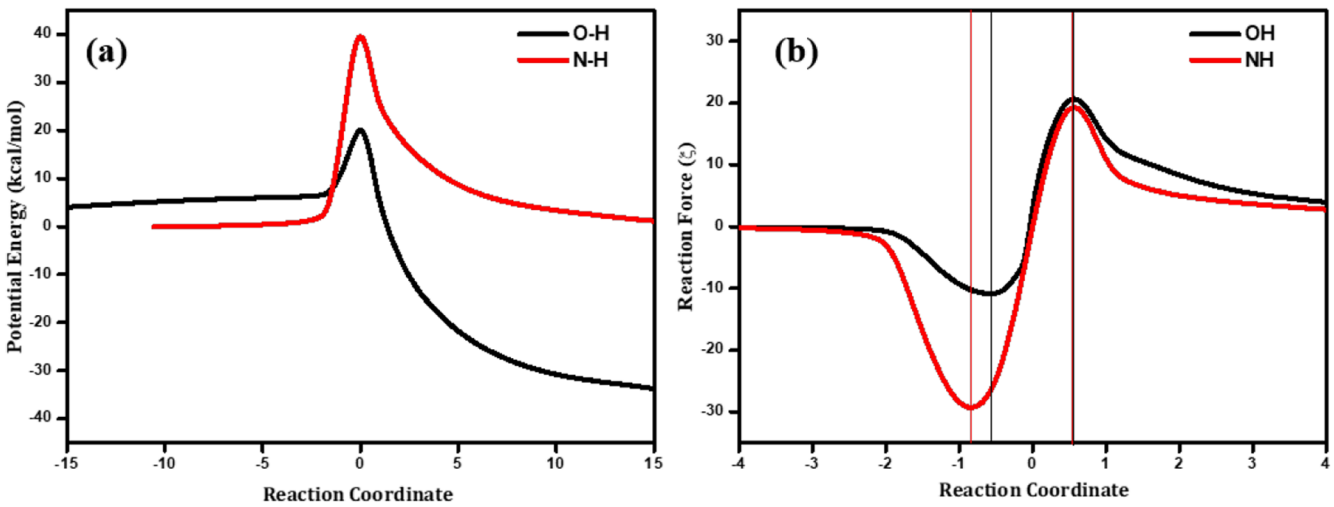

Figure 9. (a) Potential energy profile. (b) Reaction force profile. The red line represents the N−H insertion, while the black line is O−H insertion.

Table 2. Works W_1 and W_2 and their W_{strain} and W_{int} Contribution for Both Aniline (N−H) and Phenol (O−H) Reactions (All Values in kcal/mol)

N−H (39.2)				O−H (20.0)			
W_1 = 26.4 (66%)		W_2 = 12.8 (34%)		W_1 16.2 = (81%)		W_2 = 3.83 (19%)	
$W_{1\text{-strain}}$	$W_{1\text{-int}}$	$W_{2\text{-strain}}$	$W_{2\text{-int}}$	$W_{1\text{-strain}}$	$W_{1\text{-int}}$	$W_{2\text{-strain}}$	$W_{2\text{-int}}$
5.95 (23%)	20.4 (77%)	35.2 (61%)	−22.4 (39%)	−9.37 (27%)	25.5 (73%)	21.0 (55%)	−17.2 (45%)

NCI plots are shown for both transition states (*R* and *S*) in Figure 8. Strong repulsive interactions are observed between the PhBox and the substrate, leading to an energy increase in the barrier, where there are stronger interactions. This effect on the reaction barriers indicates that the step leading to the *R* systems is more likely to occur in both O−H and N−H.

Analysis of the Barriers from the Reaction Force (RF) and Activation Strain Model (ASM) Perspectives. Due to the relevance of the second step of the reaction leading to both *R* isomers, a detailed analysis to understand the physical meaning of the reaction barriers was performed on the basis of the reactions force and ASM. Figure 9 displays the potential energy and reaction force (RF) profiles for N−H (red line) and O−H (black line). ΔG^*_{sol} of the systems was calculated and showed that both reactions have a spontaneous behavior leading to the formation of thermodynamically stable products

DOI: 10.1021/acs.jpca.9b07274
J. Phys. Chem. A 2020, 124, 2−11

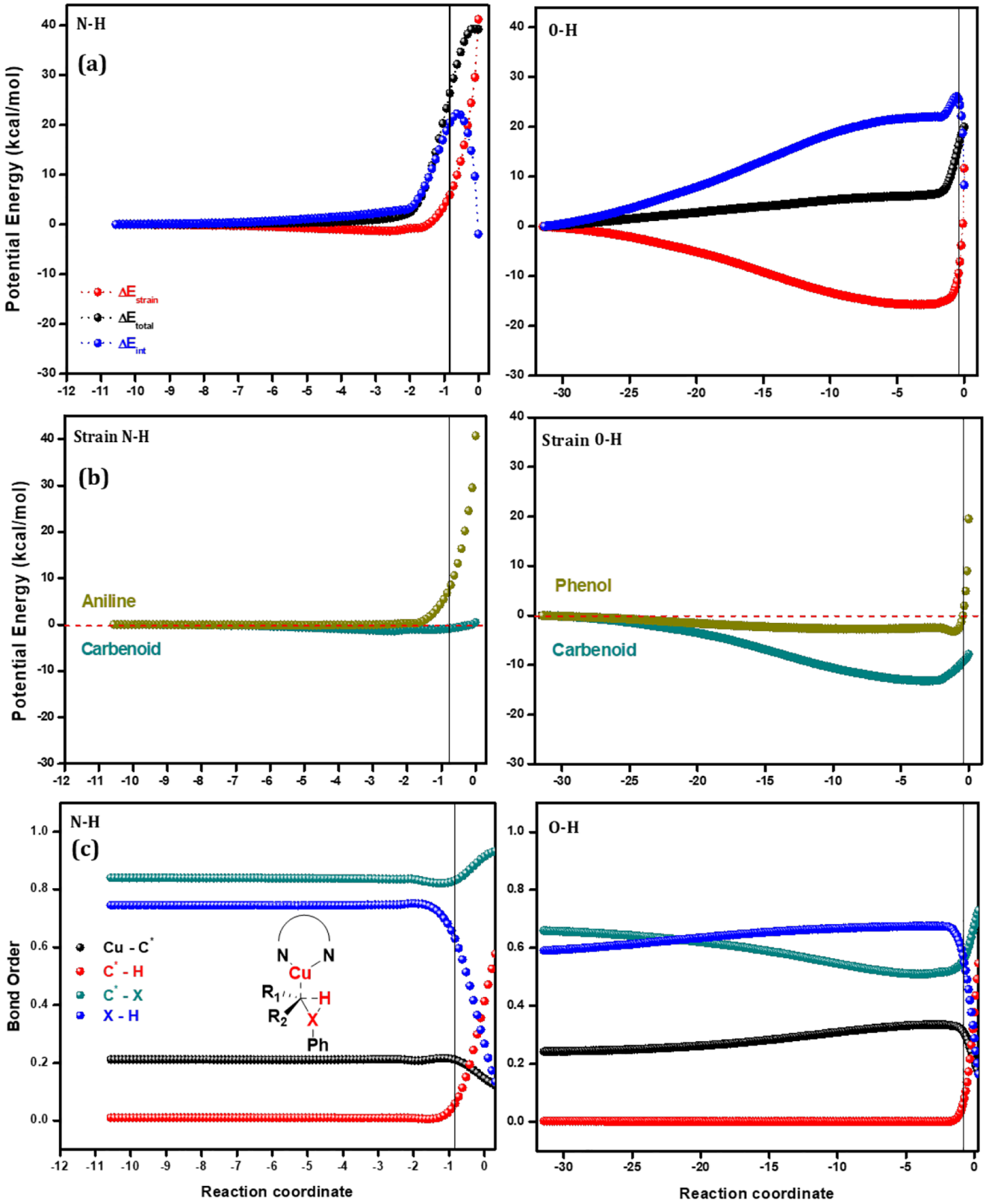

Figure 10. (a) Activation strain model profile, where ΔE_{total} is the total energy, ΔE_{int} is the interaction energy, and ΔE_{strain} is the strain energy. (b) Strain energy of both isolated fragments. (c) Bond order profile on participating bonds. All profiles are shown from reactants to transition state. All values are in kcal/mol.

(ΔG^{*}_{sol} = −8.8 and −42.9 kcal/mol for N−H and O−H respectively). Heights of the energy barriers indicate that the reaction is favored when the phenolic substrate is used ($\Delta G^{\neq}_{sol}$ = 15.5 kcal/mol vs 34.0 kcal/mol).

DOI: 10.1021/acs.jpca.9b07274
J. Phys. Chem. A 2020, 124, 2−11

The reaction force is shown in Figure 9b for both *R* isomer formations. In the reactants region, the negative value of the reaction force increases in the direction toward the progress of the reaction, which gives an account of the opposing forces (mainly geometric rearrangements) that must be overcome to in order to reach the transition state.

The reaction works are obtained from the RF profile, W_1 and W_2 being the most significant since they take into account the energetic contributions to the TS (shown in Table 2). In this case, a significant contribution of W_2 to the activation energy was found in aniline, in contrast to phenolic substrate (W_2 = 34% vs 19%). The difference in W_2 is due to the nucleophilic power of aniline in contrast to phenol. The oxygen atom contains one more electron pair than aniline, which provides the system electrons in a suitable geometric disposition which helps the phenolic system to reach the product.

The ASM along with the RF have been analyzed, in order to compare strain and interaction energies in terms of reaction works ($W_{1\text{-strain}}$, $W_{2\text{-strain}}$, $W_{1\text{-int}}$, and $W_{2\text{-int}}$). Notably, over 70% of W_1 is due to steric repulsion between the phenyl group of the ligand and the substrate, while W_2 is dominated by the geometric distortion of the substrate. In this case, aniline has a more significant structural deformation, resulting in a 6% increase of the activation energy.

The activation strain model (ASM) profile was studied (see Figure 10a). The blue line corresponds to the interaction energy ΔE_{int}, which is the sum of all the energetic effects that result from combining and mixing the charge distributions of the fragments. The red line corresponds to the strain energy ΔE_{strain}, identified as the geometric distortion between isolated fragments. The black line represents the total energy. From a qualitative perspective, the ASM shows that the reactant region is dominated by a positive interaction energy due to Pauli repulsion, generating a destabilization of the system. This trend takes place in both insertion reactions, but is more evident for the O−H reaction since it is accompanied of a high stabilizing strain energy (ΔE_{strain}), which is associated with the structural rearrangement taking place.

Figure 10b shows the reactants' contribution of strain energy for both insertion reactions, where the stabilizing strain energy at O−H has a significant contribution to the decreasing of the activation energy, mainly involving geometric deformation of the carbenoid (dark cyan line). This result can be associated with the bond order analysis (see Figure 10c), where at the reactants region essential changes in the bond order profile appear, mainly involving the Cu−C* bond strengthening process, which releases energy and thus contributes to the stabilization of the carbenoid (primarily in the strain energy of the carbenoid). In addition, the O−H bond is also stabilized, producing a slight stabilization of the phenol (dark yellow line). Conversely, in the N−H reaction, the primary bonds are kept constant, so the bonds are not stabilized in that region, allowing the strain energy to be next to zero in the reactant region (both for the carbenoid and for the aniline).

Finally, the last step of the reactions corresponds to the breaking of the interaction present in PC_X to obtain the product and the copper complex separately. The energetic cost associated with this process is 4.30 and 14.5 kcal/mol for N−H and O−H, respectively; this energy is used to break the noncovalent interactions between copper and oxygen from the ethyl formate.

CONCLUSIONS

At the M06-2X/cc-pVDZ level of theory, we have studied the backside and frontside binding of the substrate to the copper carbenoid in order to insert a N−H or O−H bond. The first step of both insertion reactions (N−H and O−H) was found to be barrierless, leading to the formation of RC_X intermediates.

The second step favors the TS associated with the backside approach, due to the lower steric repulsions, which indicate the regioselectivity of the reaction. Lower steric interactions are decisive on the formation of the *R* isomer, generated by the backside approach.

The interaction and strain energy contributions to the activation energy for the backside mechanism were obtained through ASM analysis. While for the O−H reaction a counterbalance between the repulsive interaction energy and the stabilized strain (negative strain) was reported, the aniline presents a great contribution of repulsive interaction energy in the reactant region (W_1). At the same time, the greatest W_2 contribution corresponds to the destabilizing strain energy, which is higher for N−H. Both effects resulted in a lower energy barrier for the phenolic substrate.

The insertion reaction on the O−H bond using copper(I) carbenoid was favored energetically. However, when the heteroatom oxygen was exchanged for nitrogen, the insertion reaction was no longer favored, which indicates that for the N−H bond insertion the carbenoid should be modified, either by changing the metal or the substituents to increase the electrophilic character of the carbon.

ASSOCIATED CONTENT

Supporting Information

The Supporting Information is available free of charge at https://pubs.acs.org/doi/10.1021/acs.jpca.9b07274.

> Benchmarking quantum chemical methods, including a table of reaction energies; copper carbenoid reactivity, including figures of the molecular electrostatic potential of copper carbenoid, NBOs, and Cu carbenoid structureand a table of Hirshfeld-I atomic charges; Cartesian coordinates of R, TS, and P of the systems studied (PDF)

AUTHOR INFORMATION

Corresponding Author

*E-mail: bherrera@uc.cl.

ORCID

Barbara Herrera: 0000-0003-1911-4473

Notes

The authors declare no competing financial interest.

ACKNOWLEDGMENTS

The authors thank FONDECYT Grants No. 1170837 for the financial support. EDA computations were carried out using facilities at SHARCNET (Shared Hierarchical Academic Research Computing Network: www.sharcnet.ca). R. Durán acknowledges VRI-PUC and ELAP fellowships, and Cesar Barrales-Martínez and Alessandra Missad for the fruitful discussions and the organization of the manuscript. The authors want to thank Alejandro Toro-Labbé for the support and advice.

DOI: 10.1021/acs.jpca.9b07274
J. Phys. Chem. A 2020, 124, 2−11

REFERENCES

(1) Ye, T.; McKervey, M. A. Organic Synthesis with α-Diazo Carbonyl Compounds. *Chem. Rev.* **1994**, *94*, 1091−1160.

(2) Wee, A. H. Rhodium(II)-Catalyzed Reaction of Diazocompounds in the Service of Organic Synthesis of Natural and Non-Natural Products. *Curr. Org. Synth.* **2006**, *3*, 499−555.

(3) Ford, A.; Miel, H.; Ring, A.; Slattery, C. N.; Maguire, A. R.; McKervey, M. A. Modern Organic Synthesis with α-Diazocarbonyl Compounds. *Chem. Rev.* **2015**, *115*, 9981−10080.

(4) Dalko, P. I. *Enantioselective Organocatalysis*; Wiley-VCH Verlag GmbH & Co. KGaA: Weinheim, Germany, 2007; pp 1−17.

(5) Goldsmith, D. Modern Catalytic Methods for Organic Synthesis with Diazo Compounds: From Cyclopropanes to Ylides (Doyle, Michael P.; McKervey, M. Anthony; Ye, Tao). *J. Chem. Educ.* **1999**, *76*, 1191.

(6) Zhang, Z.; Wang, J. Recent studies on the reactions of α-diazocarbonyl compounds. *Tetrahedron* **2008**, *64*, 6577−6605.

(7) Song, X.-G.; Ren, Y.-Y.; Zhu, S.-F.; Zhou, Q.-L. Enantioselective Copper-Catalyzed Intramolecular NH Bond Insertion: Synthesis of Chiral 2-Carboxytetrahydroquinolines. *Adv. Synth. Catal.* **2016**, *358*, 2366−2370.

(8) Davies, H. M. L.; Beckwith, R. E. J. Catalytic enantioselective C-H activation by means of metal-carbenoid-induced C-H insertion. *Chem. Rev.* **2003**, *103*, 2861−2903.

(9) Maier, T. C.; Fu, G. C. Catalytic Enantioselective O - H Insertion Reactions. *J. Am. Chem. Soc.* **2006**, *128*, 4594−4595.

(10) Le Maux, P.; Carrié, D.; Jéhan, P.; Simonneaux, G. Asymmetric O−H insertion reaction of carbenoids catalyzed by chiral bicyclo bisoxazoline copper(I) and (II) complexes. *Tetrahedron* **2016**, *72*, 4671−4675.

(11) Zhu, S. F.; Zhou, Q. L. Transition-metal-catalyzed enantioselective heteroatom-hydrogen bond insertion reactions. *Acc. Chem. Res.* **2012**, *45*, 1365−1377.

(12) Jiménez-Osés, G.; Vispe, E.; Roldán, M.; Rodríguez-Rodríguez, S.; López-Ram-de Viu, P.; Salvatella, L.; Mayoral, J. A.; Fraile, J. M. Stereochemical Outcome of Copper-Catalyzed C−H Insertion Reactions. An Experimental and Theoretical Study. *J. Org. Chem.* **2013**, *78*, 5851−5857.

(13) Johnson, J. S.; Evans, D. A. Chiral bis(oxazoline) copper(II) complexes: Versatile catalysts for enantioselective cycloaddition, aldol, Michael, and carbonyl ene reactions. *Acc. Chem. Res.* **2000**, *33*, 325−335.

(14) Meng, Q.; Wang, F.; Li, M. Bisoxazoline−copper(I)-catalyzed aziridination of diazoacetate with imines — A DFT study. *Can. J. Chem.* **2010**, *88*, 981−990.

(15) Müller, P.; Fruit, C. Enantioselective Catalytic Aziridinations and Asymmetric Nitrene Insertions into C-H Bonds. *Chem. Rev.* **2003**, *103*, 2905−2920.

(16) Evans, D. A.; Barnes, D. M.; Johnson, J. S.; Lectka, T.; von Matt, P.; Miller, S. J.; Murry, J. A.; Norcross, R. D.; Shaughnessy, E. A.; Campos, K. R. Bis(oxazoline) and Bis(oxazolinyl)pyridine Copper Complexes as Enantioselective DielsAlder Catalysts: Reaction Scope and Synthetic Applications. *J. Am. Chem. Soc.* **1999**, *121*, 7582−7594.

(17) DeChancie, J.; Acevedo, O.; Evanseck, J. D. Density Functional Theory Determination of an Axial Gateway To Explain the Rate and Endo Selectivity Enhancement of DielsAlder Reactions by Bis-(oxazoline)-Cu(II). *J. Am. Chem. Soc.* **2004**, *126*, 6043−6047.

(18) Desimoni, G.; Faita, G.; Jørgensen, K. A. C2 -Symmetric Chiral Bis(Oxazoline) Ligands in Asymmetric Catalysis. *Chem. Rev.* **2006**, *106*, 3561−3651.

(19) Deeth, R. J.; Fey, N. A Molecular Mechanics Study of Copper(II)-Catalyzed Asymmetric DielsAlder Reactions. *Organometallics* **2004**, *23*, 1042−1054.

(20) Slattery, C. N.; Ford, A.; Maguire, A. R. Catalytic asymmetric C−H insertion reactions of α-diazocarbonyl compounds. *Tetrahedron* **2010**, *66*, 6681−6705.

(21) Davies, H. M. L.; Hansen, T.; Churchill, M. R. Catalytic Asymmetric CH Activation of Alkanes and Tetrahydrofuran. *J. Am. Chem. Soc.* **2000**, *122*, 3063−3070.

(22) Davies, H. M. Catalytic asymmetric C-H activation of sp3 hybridized C-H bonds by means of carbenoid C-H insertions: applications in organic synthesis. *J. Mol. Catal. A: Chem.* **2002**, *189*, 125−135.

(23) Davies, H. M. L.; Manning, J. R. Catalytic C-H functionalization by metal carbenoid and nitrenoid insertion. *Nature* **2008**, *451*, 417−24.

(24) Pereira, A.; Champouret, Y.; Martín, C.; Álvarez, E.; Etienne, M.; Belderraín, T. R.; Pérez, P. J. Copper-Carbene Intermediates in the Copper-Catalyzed Functionalization of O-H Bonds. *Chem. - Eur. J.* **2015**, *21*, 9769−9775.

(25) Liu, Y.; Luo, Z.; Zhang, J. Z.; Xia, F. DFT Calculations on the Mechanism of Transition-Metal-Catalyzed Reaction of Diazo Compounds with Phenols: O−H Insertion versus C−H Insertion. *J. Phys. Chem. A* **2016**, *120*, 6485−6492.

(26) Liu, Y.; Yu, Z.; Luo, Z.; Zhang, J. Z.; Liu, L.; Xia, F. Mechanistic Investigation of Aromatic C(sp 2)−H and Alkyl C(sp 3)−H Bond Insertion by Gold Carbenes. *J. Phys. Chem. A* **2016**, *120*, 1925−1932.

(27) Ariafard, A.; Zarkoob, F.; Batebi, H.; Stranger, R.; Yates, B. F. DFT Studies on the Carboxylation of the C−H Bond of Heteroarenes by Copper(I) Complexes. *Organometallics* **2011**, *30*, 6218−6224.

(28) Wang, F.; Meng, Q.; Li, M. Density functional studies on copper-catalysed asymmetric aziridination of diazoacetate with imines. *Mol. Simul.* **2010**, *36*, 15−25.

(29) Parr, R. G.; Yang, W. *Density-Functional Theory of Atoms and Molecules*; Oxford University Press: New York, 1989.

(30) Kohn, W.; Becke, A. D.; Parr, R. G. Density Functional Theory of Electronic Structure. *J. Phys. Chem.* **1996**, *100*, 12974−12980.

(31) Geerlings, P.; De Proft, F.; Langenaeker, W. Conceptual Density Functional Theory. *Chem. Rev.* **2003**, *103*, 1793−1874.

(32) Toro-Labbé, A. Characterization of Chemical Reactions from the Profiles of Energy, Chemical Potential, and Hardness. *J. Phys. Chem. A* **1999**, *103*, 4398−4403.

(33) Toro-Labbé, A.; Gutiérrez-Oliva, S.; Concha, M. C.; Murray, J. S.; Politzer, P. Analysis of two intramolecular proton transfer processes in terms of the reaction force. *J. Chem. Phys.* **2004**, *121*, 4570−4576.

(34) Herrera, B.; Toro-Labbe, A. The role of the reaction force to characterize local specific interactions that activate the intramolecular proton transfers in DNA basis. *J. Chem. Phys.* **2004**, *121*, 7096−7102.

(35) Politzer, P.; Toro-Labbé, A.; Gutiérrez-Oliva, S.; Herrera, B.; Jaque, P.; Concha, M. C.; Murray, J. S. The reaction force: Three key points along an intrinsic reaction coordinate. *Proc. - Indian Acad. Sci., Chem. Sci.* **2005**, *117*, 467−472.

(36) van Zeist, W.-J.; Koers, A. H.; Wolters, L. P.; Bickelhaupt, F. M. Reaction Coordinates and the Transition-Vector Approximation to the IRC. *J. Chem. Theory Comput.* **2008**, *4*, 920−928.

(37) van Zeist, W.-J.; Bickelhaupt, F. M. The activation strain model of chemical reactivity. *Org. Biomol. Chem.* **2010**, *8*, 3118.

(38) Wolters, L. P.; Bickelhaupt, F. M. The activation strain model and molecular orbital theory. *Wiley Interdiscip. Rev. Comput. Mol. Sci.* **2015**, *5*, 324−343.

(39) Kubelka, J.; Bickelhaupt, F. M. Activation Strain Analysis of S N 2 Reactions at C, N, O, and F Centers. *J. Phys. Chem. A* **2017**, *121*, 885−891.

(40) Otero-de-la Roza, A.; Johnson, E. R.; Contreras-García, J. Revealing non-covalent interactions in solids: NCI plots revisited. *Phys. Chem. Chem. Phys.* **2012**, *14*, 12165.

(41) Boto, R. A.; Contreras-García, J.; Tierny, J.; Piquemal, J.-P. Interpretation of the reduced density gradient. *Mol. Phys.* **2016**, *114*, 1406−1414.

(42) Liang, Y.; Zhou, H.; Yu, Z. X. Why is copper(I) complex more competent than dirhodium(II) complex in catalytic asymmetric O-H insertion reactions? A computational study of the metal carbenoid O-H insertion into water. *J. Am. Chem. Soc.* **2009**, *131*, 17783−17785.

(43) Gutiérrez-Oliva, S.; Herrera, B.; Toro-Labbé, A.; Chermette, H. On the Mechanism of Hydrogen Transfer in the HSCH(O)(S)CHOH and HSNO SNOH Reactions. *J. Phys. Chem. A* **2005**, *109*, 1748−1751.

DOI: 10.1021/acs.jpca.9b07274
J. Phys. Chem. A 2020, 124, 2−11

(44) Rincón, E.; Jaque, P.; Toro-Labbé, A. Reaction Force Analysis of the Effect of Mg(II) on the 1,3 Intramolecular Hydrogen Transfer in Thymine. *J. Phys. Chem. A* **2006**, *110*, 9478−9485.
(45) Herrera, B.; Toro-Labbé, A. The Role of Reaction Force and Chemical Potential in Characterizing the Mechanism of Double Proton Transfer in the AdenineUracil Complex. *J. Phys. Chem. A* **2007**, *111*, 5921−5926.
(46) Burda, J. V.; Toro-Labbé, A.; Gutiérrez-Oliva, S.; Murray, J. S.; Politzer, P. Reaction Force Decomposition of Activation Barriers To Elucidate Solvent Effects. *J. Phys. Chem. A* **2007**, *111*, 2455−2457.
(47) Toro-Labbé, A.; Gutiérrez-Oliva, S.; Murray, J. S.; Politzer, P. The reaction force and the transition region of a reaction. *J. Mol. Model.* **2009**, *15*, 707−710.
(48) Ortega, D. E.; Cortés-Arriagada, D.; Toro-Labbé, A. Mechanistic details of ethylene polymerization reaction using methallyl nickel (ii) catalysts. *Phys. Chem. Chem. Phys.* **2018**, *20*, 22915−22925.
(49) Barrales-Martínez, C.; Cortés-Arriagada, D.; Gutiérrez-Oliva, S. Molecular hydrogen formation in the interstellar medium: the role of polycyclic aromatic hydrocarbons analysed by the reaction force and activation strain model. *Mon. Not. R. Astron. Soc.* **2018**, *481*, 3052−3062.
(50) Politzer, P.; Murray, J. S.; Yepes, D.; Jaque, P. Driving and retarding forces in a chemical reaction. *J. Mol. Model.* **2014**, *20*, 2351.
(51) Morokuma, K. Molecular Orbital Studies of Hydrogen Bonds. III. C = O···H−O Hydrogen Bond in H 2 CO···H2O and H2CO···2H2O. *J. Chem. Phys.* **1971**, *55*, 1236−1244.
(52) Ziegler, T.; Rauk, A. On the calculation of bonding energies by the Hartree Fock Slater method. *Theor. Chim. Acta* **1977**, *46*, 1−10.
(53) Grimme, S.; Antony, J.; Ehrlich, S.; Krieg, H. A consistent and accurate ab initio parametrization of density functional dispersion correction (DFT-D) for the 94 elements H-Pu. *J. Chem. Phys.* **2010**, *132*, 154104.
(54) Grimme, S.; Ehrlich, S.; Goerigk, L. Effect of the damping function in dispersion corrected density functional theory. *J. Comput. Chem.* **2011**, *32*, 1456−1465.
(55) Mardirossian, N.; Head-Gordon, M. How Accurate Are the Minnesota Density Functionals for Noncovalent Interactions, Isomerization Energies, Thermochemistry, and Barrier Heights Involving Molecules Composed of Main-Group Elements? *J. Chem. Theory Comput.* **2016**, *12*, 4303−4325.
(56) Hay, P. J.; Wadt, W. R. Ab initio effective core potentials for molecular calculations. Potentials for K to Au including the outermost core orbitals. *J. Chem. Phys.* **1985**, *82*, 299−310.
(57) Wadt, W. R.; Hay, P. J. Ab initio effective core potentials for molecular calculations. Potentials for main group elements Na to Bi. *J. Chem. Phys.* **1985**, *82*, 284−298.
(58) Hay, P. J.; Wadt, W. R. Ab initio effective core potentials for molecular calculations. Potentials for the transition metal atoms Sc to Hg. *J. Chem. Phys.* **1985**, *82*, 270−283.
(59) Mardirossian, N.; Head-Gordon, M. Characterizing and Understanding the Remarkably Slow Basis Set Convergence of Several Minnesota Density Functionals for Intermolecular Interaction Energies. *J. Chem. Theory Comput.* **2013**, *9*, 4453−4461.
(60) Goerigk, L. Treating London-Dispersion Effects with the Latest Minnesota Density Functionals: Problems and Possible Solutions. *J. Phys. Chem. Lett.* **2015**, *6*, 3891−3896.
(61) Ramachandran, B.; Kharidehal, P.; Pratt, L. M.; Voit, S.; Okeke, F. N.; Ewan, M. Computational Strategies for Reactions of Aggregated and Solvated Organolithium Carbenoids. *J. Phys. Chem. A* **2010**, *114*, 8423−8433.
(62) Pratt, L. M.; Mai, B. K.; Ramachandran, B. R. Carbenoid Alkene Insertion Reactions of Oxiranyllithiums. *J. Org. Chem.* **2012**, *77*, 8605−8614.
(63) Pons, A.; Tognetti, V.; Joubert, L.; Poisson, T.; Pannecoucke, X.; Charette, A. B.; Jubault, P. Catalytic Enantioselective Cyclopropanation of α-Fluoroacrylates: An Experimental and Theoretical Study. *ACS Catal.* **2019**, *9*, 2594−2598.
(64) Riplinger, C.; Neese, F. An efficient and near linear scaling pair natural orbital based local coupled cluster method. *J. Chem. Phys.* **2013**, *138*, 034106.
(65) Scott, A. P.; Radom, L. Harmonic Vibrational Frequencies: An Evaluation of HartreeFock, MøllerPlesset, Quadratic Configuration Interaction, Density Functional Theory, and Semiempirical Scale Factors. *J. Phys. Chem.* **1996**, *100*, 16502−16513.
(66) Hratchian, H. P.; Schlegel, H. B. Accurate reaction paths using a Hessian based predictor−corrector integrator. *J. Chem. Phys.* **2004**, *120*, 9918−9924.
(67) Hratchian, H. P.; Schlegel, H. B. Using Hessian Updating To Increase the Efficiency of a Hessian Based Predictor-Corrector Reaction Path Following Method. *J. Chem. Theory Comput.* **2005**, *1*, 61−69.
(68) Marenich, A. V.; Cramer, C. J.; Truhlar, D. G. Universal Solvation Model Based on Solute Electron Density and on a Continuum Model of the Solvent Defined by the Bulk Dielectric Constant and Atomic Surface Tensions. *J. Phys. Chem. B* **2009**, *113*, 6378−6396.
(69) Lu, T.; Chen, F. Multiwfn: A multifunctional wavefunction analyzer. *J. Comput. Chem.* **2012**, *33*, 580−592.
(70) Bultinck, P.; Van Alsenoy, C.; Ayers, P. W.; Carbó-Dorca, R. Critical analysis and extension of the Hirshfeld atoms in molecules. *J. Chem. Phys.* **2007**, *126*, 144111.
(71) Van Damme, S.; Bultinck, P.; Fias, S. Electrostatic Potentials from Self-Consistent Hirshfeld Atomic Charges. *J. Chem. Theory Comput.* **2009**, *5*, 334−340.
(72) Verstraelen, T.; Pauwels, E.; De Proft, F.; Van Speybroeck, V.; Geerlings, P.; Waroquier, M. Assessment of Atomic Charge Models for Gas-Phase Computations on Polypeptides. *J. Chem. Theory Comput.* **2012**, *8*, 661−676.
(73) Contreras-Garcia, J.; Johnson, E. R.; Keinan, S.; Chaudret, R.; Piquemal, J.-P.; Beratan, D. N.; Yang, W. NCIPLOT: A Program for Plotting Noncovalent Interaction Regions. *J. Chem. Theory Comput.* **2011**, *7*, 625−632.
(74) Chaudret, R.; de Courcy, B.; Contreras-García, J.; Gloaguen, E.; Zehnacker-Rentien, A.; Mons, M.; Piquemal, J.-P. Unraveling non-covalent interactions within flexible biomolecules: from electron density topology to gas phase spectroscopy. *Phys. Chem. Chem. Phys.* **2014**, *16*, 9876.
(75) Frisch, M.; Trucks, G.; Schlegel, H. B.; Scuseria, G.; Robb, M.; Cheeseman, J.; Scalmani, G.; Barone, V.; Mennucci, B.; Petersson, G.; et al. *Gaussian 09*, revision A02; Gaussian Inc.: Wallingford, CT, 2009.
(76) Neese, F. The ORCA program system. *Wiley Interdiscip. Rev. Comput. Mol. Sci.* **2012**, *2*, 73−78.
(77) Ziegler, T.; Rauk, A. On the calculation of bonding energies by the Hartree Fock Slater method. *Theor. Chim. Acta* **1977**, *46*, 1−10.
(78) Ziegler, T.; Rauk, A. Carbon monoxide, carbon monosulfide, molecular nitrogen, phosphorus trifluoride, and methyl isocyanide as σ donors and π acceptors. A theoretical study by the Hartree-Fock-Slater transition-state method. *Inorg. Chem.* **1979**, *18*, 1755−1759.
(79) Ziegler, T.; Rauk, A. A theoretical study of the ethylene-metal bond in complexes between copper(1+), silver(1+), gold(1+), platinum(0) or platinum(2+) and ethylene, based on the Hartree-Fock-Slater transition-state method. *Inorg. Chem.* **1979**, *18*, 1558−1565.
(80) SCM. *ADF*; Theoretical Chemistry, Vrije Universiteit: Amsterdam, The Netherlands, 2014; http://www.scm.com.
(81) Zhurko, G.; Zhurko, D. *ChemCraft*, Version 1.8, 2017; http://www.chemcraftprog.com.
(82) Legault, C. *CYLview*, Version 1.0b, 2009; http://www.cylview.org.
(83) Boche, G.; Lohrenz, J. C. W. The Electrophilic Nature of Carbenoids, Nitrenoids, and Oxenoids. *Chem. Rev.* **2001**, *101*, 697−756.
(84) Davies, H. M.; Antoulinakis, E. G. Recent progress in asymmetric intermolecular CH activation by rhodium carbenoid intermediates. *J. Organomet. Chem.* **2001**, *617−618*, 47−55.

DOI: 10.1021/acs.jpca.9b07274
J. Phys. Chem. A 2020, 124, 2−11

ACS OMEGA

Article

Cite This: ACS Omega 2019, 4, 19452−19461

http://pubs.acs.org/journal/acsodf

Reaction Mechanism of Li and Mg Carbenoid Cyclopropanations: Metal-π and σ Interactions

Daniel Villablanca,[†] Rocio Durán,[†] Al Mokhtar Lamsabhi,[*,‡,§] and Barbara Herrera[*,†]

[†]Laboratorio de Química Teórica Computacional (QTC), Facultad de Química, Pontificia Universidad Católica de Chile, Santiago 7820436, Región Metropolitana, Chile

[‡]Departamento de Química, Facultad de Ciencias, Módulo 13 and [§]Institute for Advanced Research in Chemical Sciences (IAdChem), Universidad Autónoma de Madrid, Madrid 28049, Spain

Supporting Information

ABSTRACT: The mechanism of the reaction of lithium and magnesium carbenoids with ethylene to give cyclopropane has been explained in detail in all the steps at the G4 level of theory. We explored the lithium and magnesium interaction toward $\pi_{C=C}$ and σ_{C-C} bonds in the reactants and the products. We have also investigated the reaction path by means of the force profile formalism in order to highlight the electronic and the structural rearrangements along the potential energy surface of the cyclopropanation. The results indicate that all of the reactions are stepwise, exoenergetic, with low barriers. All our findings were confirmed by dynamic simulations for chlorometal carbenoids. Furthermore, from the intrinsic reaction coordinate procedure, we were able to find out the intermediates that can take place when the reaction is descending from the transition state to the products or reactants. The reaction force analysis at B3LYP/6-311G(d,p) indicates that the energy barriers are mostly due to structural rearrangements which are produced by the approach of the carbenoid to ethylene. Quantum theory of atoms in molecules and electron localization function analyses indicate that products, reactants, and intermediates form complexes stabilized by attractive forces between Li/Mg and single/double bonds.

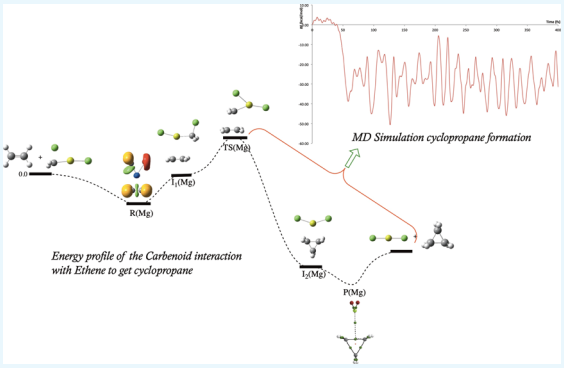

INTRODUCTION

In molecular synthesis, there are many possible pathways that can connect the reactants and products. Hence, the proposed mechanisms usually involve different types of intermediates. Rather often, a wise combination of imagination and experimental pieces of evidence may suggest molecular structures that are rather far from chemical intuition. In chemical textbooks, the possible intermediates in a chemical reaction are classified into four groups: cations, anions, radicals, and carbenes. In particular, carbenes have been proved to be systems with unique reactivities,[1−6] although normally under extreme conditions due to their high reactivity. Closely related to carbenes are the so-called carbenoids, a term used for the first time by Closs and Moss in the early sixties[7,8] to designate any system having the characteristics of a carbene or able to produce carbenes, in other words, systems that may react as carbenes even though they are not free divalent carbon species.[9] Carbenoids have been shown to be particularly useful in cyclopropanation reactions,[10−12] in organic synthesis, and as catalysis intermediates.[13−17]

Recovering the way to gain cyclopropane derivatives may be considered as a springboard to attain many valuable compounds, including natural products and biologically active species.[18−21] Understanding their chemistry becomes mandatory before exploring the paths to reach them. In gas phase and precisely by computational methods, the study of reactivity in chemistry has largely showed its validity to understand complex systems.

The main aim of the present paper is to explore the simplest way to reach cyclopropane within reactants as lithium and magnesium carbenoids. Why do we choose these reactants? The main reason for this choice, besides the ones cited above, is to be able to apply the highest level of theory such as the G4 theory and describe adequately the stationary points. The second reason is to try to offer a novel point of view on the interaction of lithium and magnesium with double and single covalent bonds. Hence our survey on cyclopropanation reactions, involving carbenoids with a metalated carbon atom, such as an alkyl lithium or alkyl magnesium $R_2C(X)M$ (M = Li, Mg; X = F, Cl, Br), is to get a new picture of the insertion of CH_2 to ethylene.

The second goal of our work is to explore the reactivity toward ethene as a simple model for more complex systems.[22−25] The reaction mechanism of cyclopropanation

Received: September 6, 2019
Accepted: October 28, 2019
Published: November 8, 2019

reactions involving carbenoid systems vary depending on the carbon bonded to the metal and the metal itself. It can be either a single-step reaction, concerted, or a stepwise mechanism. Actually, cyclopropanation reactions involving iodomethyl zinc iodide carbenoids seems to proceed by a concerted mechanism.[13,26] Other studies reported on lithium carbenoids have shown that the concerted pathway was always favored over a stepwise or carbometallation mechanism that exclusively occurs with lithium aggregates.[27−29] All these analyses were based on the use of low-level theoretical methods, and no detailed exploration of the reaction mechanism was done. On this sense, our main aim in this study is to use specific mechanism analysis formalisms, such as the reaction force and the reaction electronic flux,[30,31] to unambiguously recover the nature of the mechanism involved. This analysis will be combined with other reactivity descriptors to gain further insights on the intrinsic changes that occur when ethene is transformed to cyclopropane by the action of lithium and magnesium carbenoids, including halogen atoms (F, Cl, and Br) as leaving groups.

THEORETICAL FRAMEWORK

The theoretical descriptors are used for the analysis of the reaction mechanisms; energetic and electronic properties of carbenoid cyclopropanation reaction are defined in the following paragraphs:

Reaction Force. To characterize reaction mechanisms, the evaluation of energy is the most important task that gives information about the reaction energy (ΔE°) and the height of the reaction barrier ($\Delta E^\ddagger$).

The reaction force is the first derivative of the reaction energy over the reaction coordinate and is defined as[30−35]

$$F(\xi) = -\left(\frac{\mathrm{d}E}{\mathrm{d}\xi}\right) \tag{1}$$

In a single step potential, this function presents two critical points, a minimum ξ_1 and a maximum ξ_2. These points delimit three zones: the reactant zone (from ξ_R to ξ_1) where the structural rearrangements occur, the transition-state zone (from ξ_1 to ξ_2) where all of the electronic rearrangements take place and the product zone defined from ξ_2 to ξ_P where structural relaxation of the system occurs to lead to products. From these partitions, it is possible to get the works associated with structural and electronic phenomena.[36]

Electronic Chemical Potential. From conceptual density functional theory, various response functions or local and global reactivity descriptors can be defined.[37,38] One of the most important properties is the electronic chemical potential or the escaping tendency of electrons from an equilibrium state. It has been associated with the negative of electronegativity defined by Mulliken. For an N electron system, chemical potential is defined as[37,38]

$$\mu = \left(\frac{\partial E}{\partial N}\right)_{v(\vec{r})} = -\chi \tag{2}$$

Owing to the discontinuity of the energy along the number of particles, the finite difference approximation can be used to get an analytic expression of μ in terms of the ionization energy I and the electron affinity A. Also within Koopman's theorem, this index can be expressed in term of the frontier orbital of highest occupied molecular orbital (HOMO) and lowest unoccupied molecular orbital (LUMO), $\varepsilon_{\mathrm{HOMO}}$ and $\varepsilon_{\mathrm{LUMO}}$.[38]

$$\mu = -\frac{I + A}{2} \approx \frac{\varepsilon_{\mathrm{LUMO}} + \varepsilon_{\mathrm{HOMO}}}{2} \tag{3}$$

Reaction Electronic Flux. The relation between electron flux and the gradient of the chemical potential is used to define the reaction electronic flux.[32,35,39,40] This index measures the electronic reorganization in a chemical reaction and is defined as

$$J(\xi) = -\left(\frac{\mathrm{d}\mu}{\mathrm{d}\xi}\right) \tag{4}$$

In analogy with thermodynamics, this property can be associated with the spontaneity of the electronic processes. When $J(\xi)$ is positive, it may point out to a spontaneous reorganization of the electron cloud, indicating bond forming or strengthening, and when it is negative, the electronic changes are then nonspontaneous meaning bond breaking or weakening.[31,41]

RESULTS AND DISCUSSION

Lithium and magnesium are known by their ability to donate their valence electrons when interacting with new species. Its electronic charge in a molecule where they are inserted usually approaches unity for lithium and two for magnesium. This makes the adjacent atoms chemically more reactive. The lithium carbenoid inserts easily CH_2 into a double bond in ethene or ethylene, leading a rupture of π bond substituted by two new σ bonds.

In order to analyze in detail the mechanism of the cyclopropane formation, that is, the energetic, structural, and electronic profiles of this transformation, a series of G4 calculations of the reactants, products, and transition states connecting them have been carried out. The calculations have been achieved considering different halogen atoms as substituents in order to counteract the electropositive effect of the alkaline metal and consequently explore their effect on electronic distribution in this reaction. Our research was additionally extended to consider the magnesium-containing carbenoids in order to explore the differences that could exist between alkaline and alkaline-earth metals.

The first step to have a complete picture of the reaction mechanism is to explore the nature and strength of the interactions between the reactants. The optimized structures show that the most stable configuration corresponds to the metal interacting with the double bond of ethylene with interatomic distances between the metal and the double bond of about 2.3 and 2.5 Å for lithium and magnesium, respectively (see Figure S1). As far as the nature of the interaction is concerned, the electron localization function (ELF) shows the existence of a trisynaptic basin (M, C, C) (M = Li, Mg) associated with the polarization of the C═C double bond toward the metal center (see Figure 1). This is consistent with the presence of a bond critical point(BCP) between the metal and the π cloud of the C═C bond, with an electronic density about 0.016 a.u.

The dissociation energy, D_e, of an AB system is defined as the difference between the energy global system, AB, and the sum of the energies of the two fragments, A and B, when all of them are in their equilibrium conformation. However, additional information on the nature and strength of the interaction can be achieved by evaluating the interaction energy (E_{int}), defined as the difference between the energy of the global system AB and the sum of the energies of the two

DOI: 10.1021/acsomega.9b02905
ACS Omega 2019, 4, 19452−19461

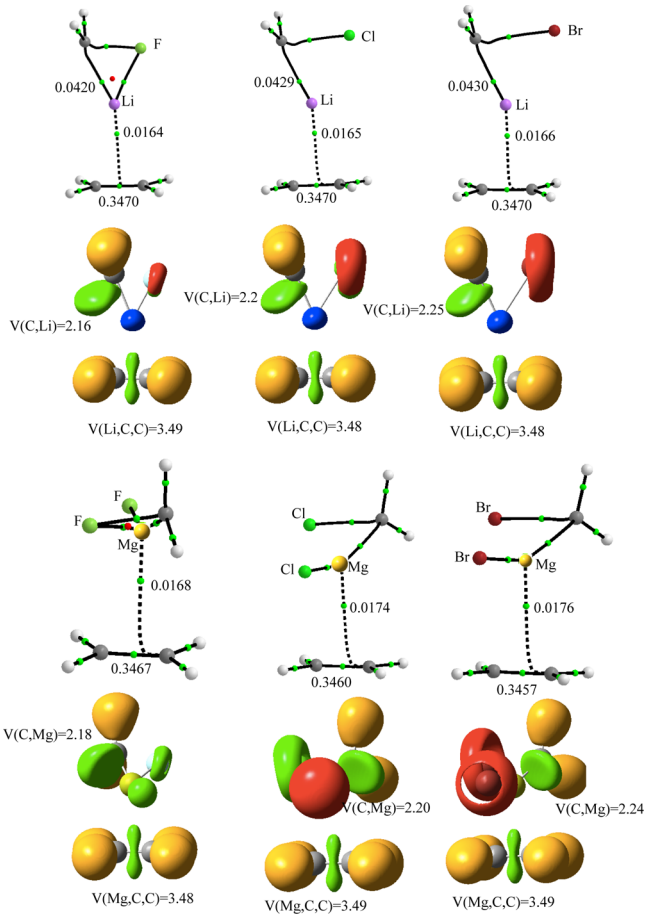

Figure 1. AIM and ELF population analysis on the reactants highlighting the most important points. The electronic density in the BCP is in a.u. while the electronic charge in the mentioned basin is in e. (Li: purple, Mg: yellow, Cl: green, C: gray, Br: red, F: light green, H: white).

fragments, A and B, when they retain the structure they had in the global system. It is obvious, as illustrated in Scheme 1, that

Scheme 1. Thermodynamic Cycle for the Formation of the Reactants for $MgCH_2X_2$ and $LiCH_2X$ (Li: Purple, Mg: Yellow, X: Green, C: Gray, H: White)

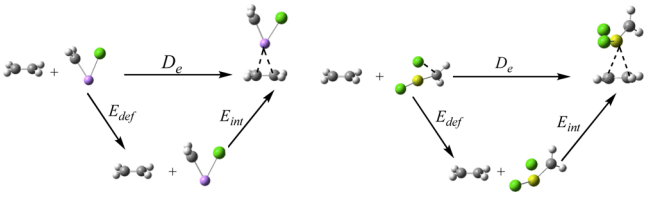

D_e can be decomposed in two terms: the interaction energy, E_{int}, and the deformation energy (E_{def}), defined as the energy necessary to distort the structure of the subunits A and B from their equilibrium geometry to their forms in the complex. The results for both sets of compounds are reported in Table 1.

The dissociation energies indicate a typical lithium and magnesium bonds toward a π-system which was already highlighted by Ammal et al. for C_2H_4−LiX (X = H, F)[42] complexes and by Li et al. for C_2H_4−MgX_2 (X = H, F) ones.[43] The dissociation energies found for the halocarbon are found to be slightly smaller to the ones reported previously by

Table 1. Energies, in Terms of Enthalpy at 298 K, Calculated at G4 Level of Theory for the Complexation of Halogen-Methyl Lithium and Magnesium with Ethylene[a]

	E_{def} (carbenoid)	E_{def} (ethene)	E_{int}	D_e
$LiFCH_2$	0.0	−0.1	−7.7	−7.8, −8.35[b]
$LiClCH_2$	−0.1	−0.1	−8.5	−8.7
$LiBrCH_2$	−0.1	−0.1	−8.9	−9.1
MgF_2CH_2	2.1	−0.1	−11.9	−9.7, −12.57[c]
$MgCl_2CH_2$	2.9	−0.1	−13.6	−10.8
$MgBr_2CH_2$	3.0	−0.1	−14.1	−11.2

[a](Values are in kcal/mol). [b]Value taken form ref 42 for C_2H_2−LiF interaction obtained at the MP4/6-311++G(d,p)//MP2/6-311++G(d,p) level including BSSE correction. [c]Value taken form ref 43 C_2H_2−MgF_2 interaction obtained at the CCSD(T)/aug-cc-pVTZ//MP2/aug-cc-pVTZ level including BSSE correction.

Ammal et al.[42] and Li et al.,[43] respectively. In the case of Mg, the difference is larger, being the G4 estimates systematically smaller.

We have found that for these systems the deformation energy is negligibly small for Li-containing carbenoids, independent of the nature of the leaving group (F, Cl, Br). Conversely, the same deformation energies are not negligible for the Mg-containing analogues, being up to 21% of the total interaction energy.

The second-order natural bond orbital (NBO) perturbation analysis shows that the interaction between the carbenoid and ethylene involves the bonding π_{C-C} orbital of the former and the σ^*_{C-M} (M = Li, Mg) antibonding orbital of the carbenoid, with a perturbation energy being of the order of 8.0 kcal/mol (see Figure 2). The partial population of this antibonding

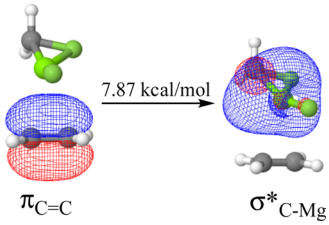

Figure 2. Electronic donation deduced from the NBO molecular orbital interactions between $\pi_{C=C}$ of ethylene and the anti-bonding σ^* of magnesium chloromethane Mg−C bond.

orbital predicted by the NBO method is consistent with the lengthening observed for the C−M (M = Li, Mg) bonds on going from the isolated carbenoid to the complex between the carbenoid and ethylene (Figure S1). It should be mentioned that although this effect is weaker for Li- than for Mg-containing systems, it raises the question of why the deformation energy is negligibly small for Li systems, whereas for Mg ones it is not.

A more detailed exploration of the ethylene-M-carbenoid adducts (M = Li, Mg) clearly shows that as mentioned above, the M−CH_2 and the M−X (X = F, Cl, Br) of the carbenoid become longer with respect to the separated systems, whereas the X−CH_2 distance becomes shorter for the Li-containing systems; this effect is almost inexistent for Mg-containing ones (see Figure S1). This means that for Li the formation of the complex with ethylene implies X−CH_2 bond shortening that counterbalance the effect of the Li−CH_2 and the Li−X bond lengthening, whereas this effect is practically inexistent for Mg.

DOI: 10.1021/acsomega.9b02905
ACS Omega 2019, 4, 19452−19461

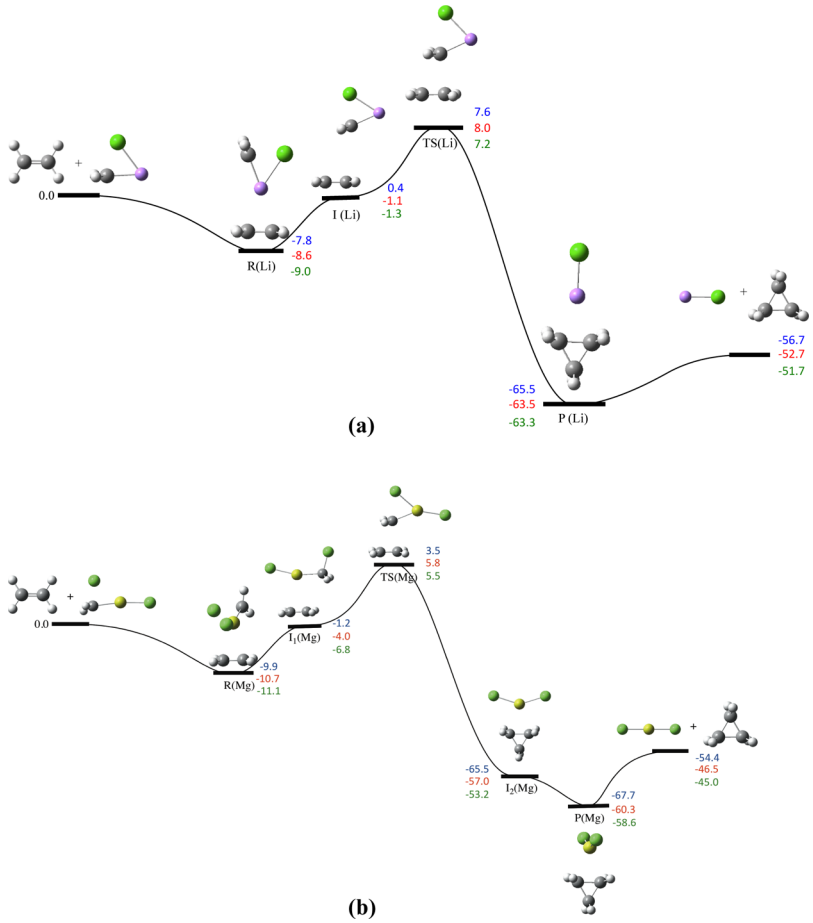

Figure 3. Energy profiles of the formation of cyclopropane from the action of metal halocarbenoid on ethylene. (a) Li-halocarbenoid. (b) Mg-halocarbenoid relative energies obtained at the G4 level of theory are in kcal/mol. Color codes are as follows: blue: fluorine, red: chlorine, and green: bromine. Relative energies obtained at the G4 level of theory are in kcal/mol (Li: purple, Mg: yellow, Cl: green, C: gray, H: white).

By contrast, in the later the perturbation induced by the interaction is translated into a deformation of the carbenoid structure. The angle $XMgCH_2$ is reduced from 169° in the isolated reactant to 136° in the chlorine complex. Therefore, the complexation affects the bonds of lithium complexes while in the magnesium systems changes the angle between atoms.

To get in the mechanism of the formation of cyclopropane it is reliable to present the reactants as the interaction between the metal and the double bond of ethylene as reported above. However, from this interaction a first accommodation of the fragments where methylene group needs to get closer to π bond is mandatory. This raises a fundamental question: how do the isolate reactants (Li/Mg halo-carbenoids and ethylene) evolve to products? To answer this question the first step is to find out the transition states that connect reactants and products followed by a detailed description of the different stationary points of potential energy surface of the reaction. Our calculation at the G4 level of theory suggests a transition-state structure where methylene is nearby the π bond of ethene. Its activation energy is about 8.0 and 5.8 kcal/mol above the entrance channel if we take, as example, chlorine derivative in lithium and magnesium reactions, respectively.

To get a detailed picture of the process, an intrinsic reaction coordinate (IRC) calculation was carried out in order to find out the minima in both directions following the reaction coordinate. The results are reported in Figure 3. The most important finding was that in the reaction pathways an intermediate [I(Li)/I_1(Mg)] takes place in the reverse direction. This means that the interaction between reactants can go through the minimum previously proposed in the literature[42,43] [R(Li)/R(Mg)] then, by a structural reorganization attains the intermediate I(Li)/I_1(Mg) to reach the transition state. In the forward direction, the lithium mechanism progresses directly to product while the magnesium reaction goes through an intermediate, namely, [I_2(Mg)], before reaching the product (see Figure 3b). It is worth noting that all our tries to find transition states between the intermediates and the reactants or products were unsuccessful. It is quite intuitive because the subtle structural differences between these species suggest the rearrangement between them to be barrierless.

At this stage, based on the IRC calculation we can conclude that the mechanism of the cyclopropane formation is not concerted, but it is a two-step process. The formation of the two new C−C bonds initially corresponds to the formation of an intermediate I(Li)/I_1(Mg), where the first C−C bond begins its assembly to reach the TS(Li)/TS(Mg), which in turn is followed by a formation of second C−C bond leading to the final product P(Li). In the case of magnesium, the second step goes through an intermediary I_2(Mg), which collapses directly to the product by a simple accommodation of MgX_2 on the cyclopropane ring (see Figure 3).

This description is totally coherent with the results of the noncovalent interaction (NCI) plots and the quantum theory

DOI: 10.1021/acsomega.9b02905
ACS Omega 2019, 4, 19452−19461

of atoms in molecules (QTAIM) analysis. If we focus on the lithium mechanism (see Figure 4), the NCI analysis of the intermediate shows an attractive region (Figure 4a) between the carbon of the $LiClCH_2$ system and one of the carbon atoms of the ethylene molecule. Consistently, the QTAIM presents a BCP between both carbon atoms (Figure 4b), whereas the energy density in the region (Figure 4c) also indicates a bonding interaction.

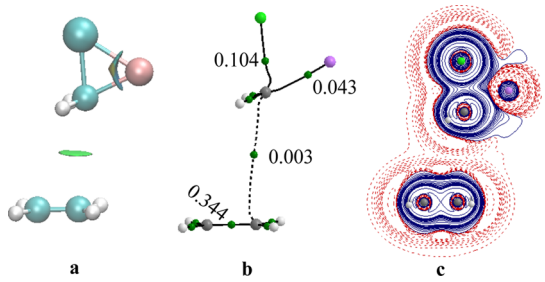

Figure 4. (a) NCI analysis of the intermediary I(Li) of the chlorine derivative. (b,c) QTAIM analysis of the electronic density and the energy density respectively of the same compound. (Li: pink, C: light blue, H: white).

To validate our assumption, a molecular dynamics propagation of the nuclei from the transition state was done by means of the atom-centered density matrix propagation (ADMP).[44−46] The main objective is to localize the points that the interaction of halocarbenoid with ethene overpasses in its travel from the reactants to products.

Over the 20 explored trajectories in each case we selected the ones which can describe roughly the mechanism in both reactions. In Figure 5 represents the evolution in both directions [reverse (a) and forward (b)] of the chlorocarbenoid Mg mechanism from the transition state to reactants and products, respectively. The chloro-lithium mechanism is reported in the Supporting Information (Figure S2). The first conspicuous result from dynamics is the existence of the intermediate I_1(Mg)/I(Li) as one of minima of the mechanism pathway. It appears in the range between 50 and 100 fs with a HOMO orbital involving the lone pair of carbon and the π orbital of the ethene double bond (see Figure 5a). The mechanism elapses then through this, confirming the IRC calculations. In the forward direction, we can deduce that the cyclopropane begins its formation at approximately 50 fs. The intermediate I_2(Mg) appears at about 100 fs to get transformed to P(Mg) at about 150 fs. The energy of the mechanism expressed by the dynamics potential energy follows the same trends as in the static calculation. Both potential energy

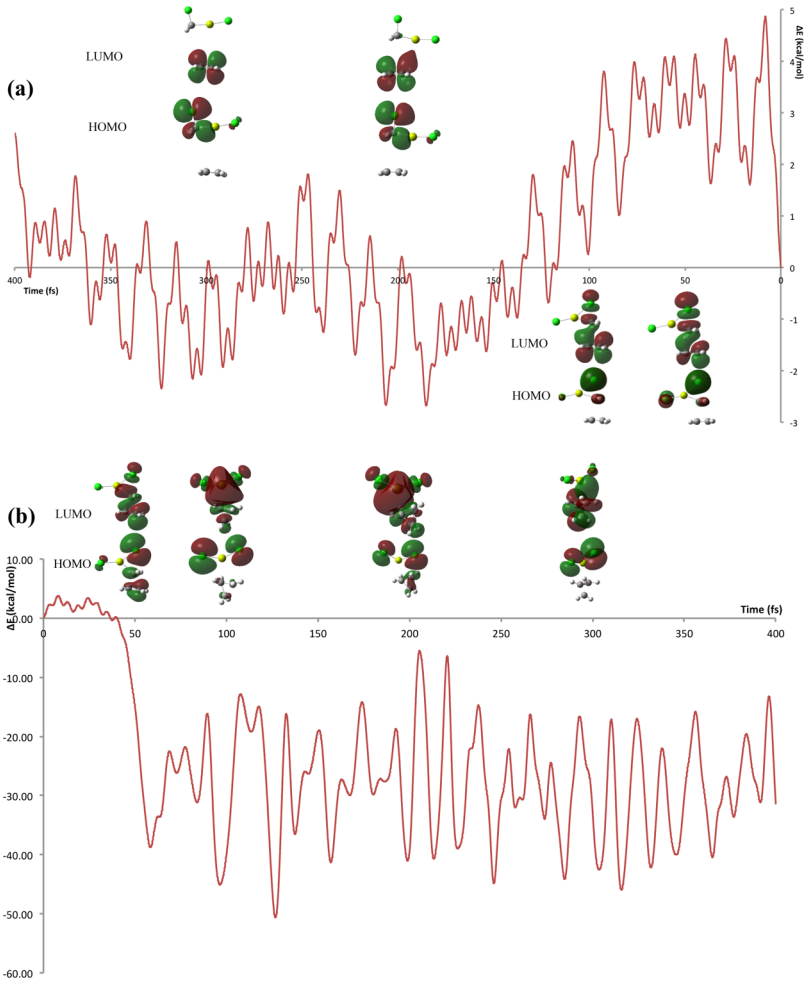

Figure 5. Relative potential energy (in kcal/mol) of the Mg-halocarbenoid mechanism to reactants (a) and to product (b) during ADMP simulation of 400 fs. The structure of some selected points is reported by their HOMO and LUMO orbitals.

DOI: 10.1021/acsomega.9b02905
ACS Omega 2019, 4, 19452−19461

Table 2. Relative Energies, Barriers, and the Works Associated to the Reaction Zones Defined by the Reaction Force Obtained by IRC Calculations (*) at B3LYP/6-311G(d,p)

	$\Delta E°$ (kcal/mol)	$\Delta E^{\ddagger}$* (kcal/mol)	W_1 (kcal/mol)	W_2 (kcal/mol)	W_3 (kcal/mol)	W_4 (kcal/mol)
Li−F	−64.96	6.18	4.23 (68.45%)	1.95 (31.55%)	−33.74	−37.40
Li−Cl	−66.11	4.70	3.25 (69.15%)	1.45 (30.85%)	−33.41	−37.40
Li−Br	−63.20	4.97	3.47 (69.82%)	1.50 (30.18%)	−33.78	−34.39
Mg−F	−58.80	4.21	3.01 (71.49%)	1.20 (28.51%)	−31.22	−31.73
Mg−Cl	−50.19	8.75	7.26 (82.97%)	1.48 (17.03%)	−28.11	−30.73
Mg−Br	−46.12	9.30	8.02 (86.23%)	1.31 (13.77%)	−28.53	−28.66

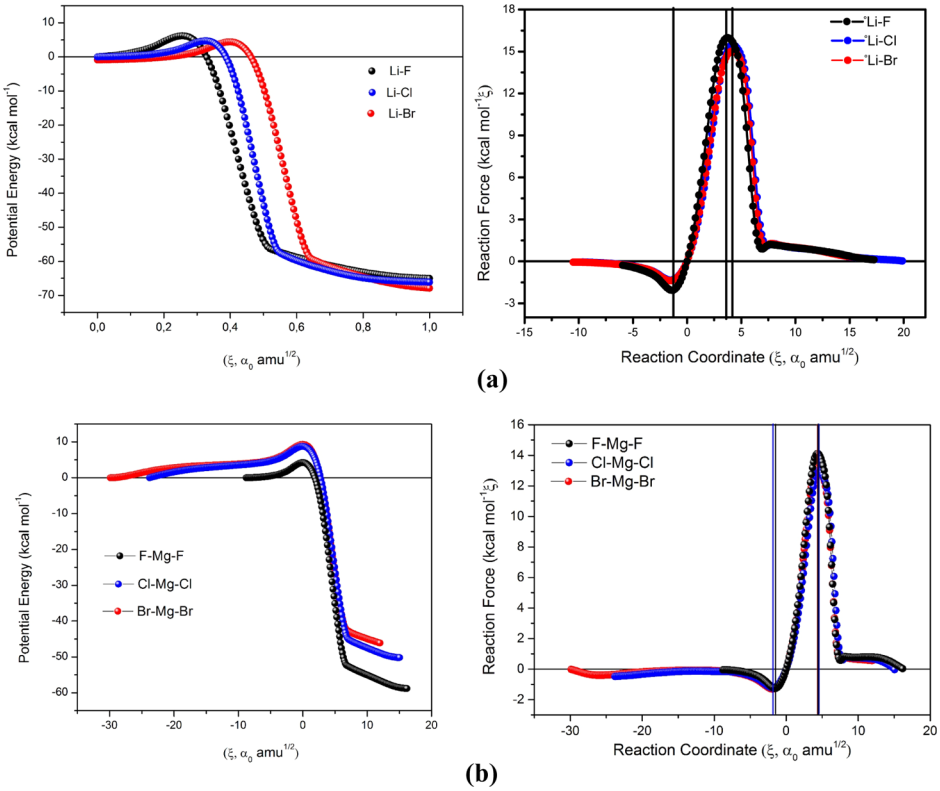

Figure 6. Reaction energies and force along the IRC in kcal/mol for Li (a) and Mg (b) carbenoids, black: F, blue: Cl and red: Br.

surfaces (Figures 3 and 5), indicate that although the carbenoid reactions follow a stepwise energy, they are extremely favorable, thus with an endoenergetic reaction and low barriers leading to products. These results confirm that the reactions need a small activation, and might be the reason why carbenoid reactions are performed at low temperatures.[27]

To understand the structural and electronic contributions to the reaction energy profile, we have determined the reaction force and their associated works that are shown in Table 2 and Figure 6. Because the progress of the reaction profile could not overpass the intermediates in both reactions (Li and Mg), the following analysis will be exclusively focused on the region achieved by the IRC calculation. Therefore, the relative energies and barriers are calculated from now on at this level of theory, taking as reference the intermediates I(Li)/I(Mg). It is to note that the trends with the calculation at the G4-level of theory reported in Figure 3 are conserved.

The first conspicuous conclusion from the energy profile is that the primary structural reorganization at the transition state oscillates in the range 4.3−8.0 kcal/mol. In fact, focusing on this step and going deeper on the force profile analysis, we can shed some light on more aspects. Hence, by evaluating the energy and the force profile, the structural reorganization with respect to the electronic reorganization presents about 70% of the activation energy in lithium carbenoids at the determinant step of the reaction. This analysis is reinforced when the works corresponding to each zone of the reaction profile are evaluated. As it can be appreciated in the Table 2 which can be confirmed by the values reported in Figure 3, the reaction is highly exothermic. The halogen electronegativity affects slightly the global activation barriers if the reactant [R(Li)] is taken as reference see Figure 3. However, if we analyze the profile from I(Li) to the products, we can notice that fluorine derivative is the less reactive species in the lithium carbenoid reaction, whereas in the Mg counterparts it appears the most reactive. In the former the energy barrier accounts for the highest activation energy in the lithium set (about 6.2 kcal/mol) while in the latter it accounts for the smallest barrier in the Mg set (about 4.2 kcal/mol). Chlorine and bromine derivatives in the lithium reaction present similar reactivity whereas in the Mg homologues chlorine is slightly more reactive than the bromine derivative. The electronic rearrangement in global trending is similar in all of the reactions considered. The work W_2 which reflects these changes oscillates around 2 kcal/mol. However, if we compare its participation in the activation energy, we found that the

DOI: 10.1021/acsomega.9b02905
ACS Omega 2019, 4, 19452−19461

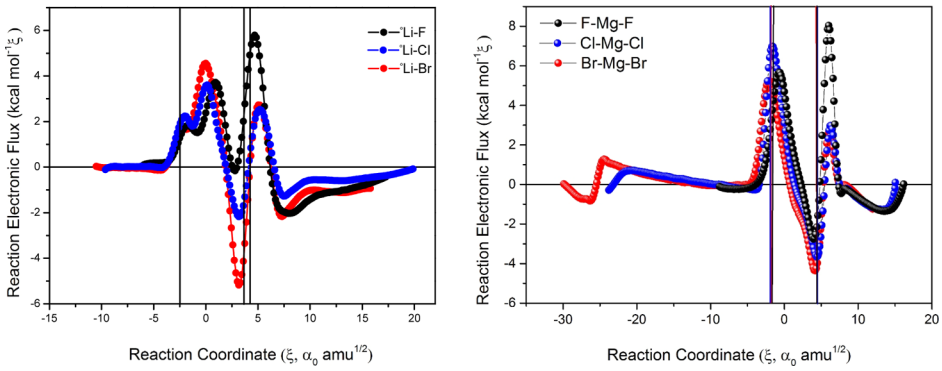

Figure 7. Reaction electronic flux in lithium and magnesium carbenoids X = F (black), Cl (blue), Br (red).

electronic rearrangement is about 30% in all of the cases with exception of Mg−Cl and Mg−Br that present values of 17 and 13%. This result can be understood by the electronegative capability of the atoms under scrutiny.

With respect to the third and fourth step of the mechanism, W_3 and W_4 indicate that the electronic rearrangement is slightly higher than the structural relaxation in the formation of the product. These last works might be associated with the bond breaking and the formation of the cyclopropane, and the following formation of the complex between the halide salt and the cyclopropane.

We have so far obtained the energies and the contributions to the main step of the cyclopropanation reactions. However, it is necessary to understand the electronic rearrangements during both reactions and the nature of the reactive intermediaries.

For the electronic analysis, we have used the REF formalism over the IRCs calculations from I(Li) to P(Li) on lithium and from I_1(Mg) to I_2(Mg) on magnesium carbenoids. The plots of the reaction electronic flux are shown in Figure 6, using the geometries given by the IRC calculations. For all of the systems, this index starts at the reactant zone, indicating that the electronic phenomena are coupled to the structural rearrangements. Most of the changes are concentrated at the transition state. For both Li−X and Mg−X profiles, some electronic activity at the product zone was observed which might be associated with the rotation of the cyclopropane to attain the product. The sign of the flux in this region indicates a spontaneous reaction step, which might be representing bond strengthening/formation. In other words, it could denote the interactions that appears between the metal (Li, Mg) and cyclopropane at the product or intermediary I_2(Mg) in the case of magnesium.

With alkyl magnesium carbenoids, all of the systems present changes condensed at the same points of the IRC, indicating a spontaneous rearrangement, followed by a nonspontaneous change that might be associated with the detachment of the CH_2 group in order to form the cyclopropane. With lithium, we found mild changes that follow the same trend; this might be attributed to the electronic nature of the alkyl lithium carbenoid, and analyzing the charges of the systems, the CH_2 radical has less electronic charge (∼0.8|e|) in contrast to their magnesium counterparts (∼1.0|e|).

Having explored all of the stationary structures of the potential energy surface of the lithium and magnesium carbenoids, it appears necessary to close our study by a discussion of the complexation in products. In other words, lithium and magnesium bonds with cyclopropane are of a great relevance to be analyzed. In fact, in the cyclopropane the interaction is provided by σ_{C-C} to the metal which is underlined by a great electronic donation from the σ_{C-C} orbital to the empty antibonding orbital σ^*_{M-X} (see Figure 7). The second-order perturbation analysis in the NBO population quantifies this donation by approximately 2.3 kcal/mol for lithium, whereas for magnesium it is about 1.6 kcal/mol for each Mg−X bond in the case of chlorine derivatives.

It is worth to mention that the interaction between the metal and cyclopropane has been also explored by QTAIM and ELF techniques. The presence of a BCP and trisynaptic basin in the interaction region is a great proof of that (see Figure 8). The

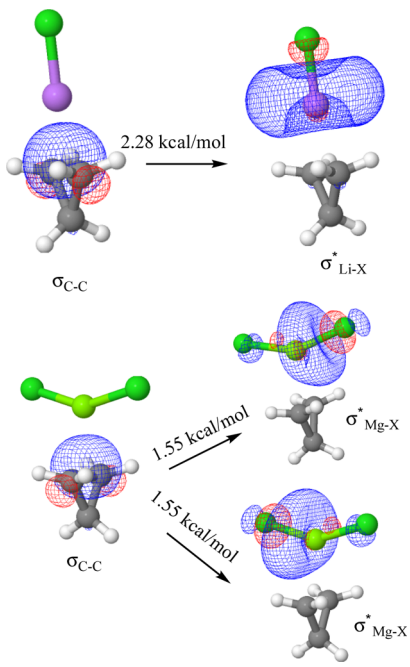

Figure 8. Electronic donation deduced from second-order NBO perturbation analysis in the orbital interactions between cyclopropane and LiCl and $MgCl_2$.

effect of halogen substitution is noticeable in the lithium bonding because the electronic density in the BCP between the metal and cyclopropane increases when moving from the most electronegative halogen (F) to the least electronegative one (Br). It is clear that the nature of halogen plays an important role in the interaction. In fact, the high electronegativity of the halogen apparently disfavors the complexation of lithium to the cyclopropane. These results can be ratified if

DOI: 10.1021/acsomega.9b02905
ACS Omega 2019, 4, 19452−19461

the binding energies involved are analyzed in each case. In fact, the binding energies of LiX and cyclopropane are about 8.8, 10.9, and 11.6 kcal/mol for F, Cl, and Br, respectively. In the case of magnesium complexation even with two halogen atoms attached to the metal, the perturbation to get a complex appears minimal. The electronic densities of the bond critical points and the binding energies of each association can demonstrate it (Figure 9).

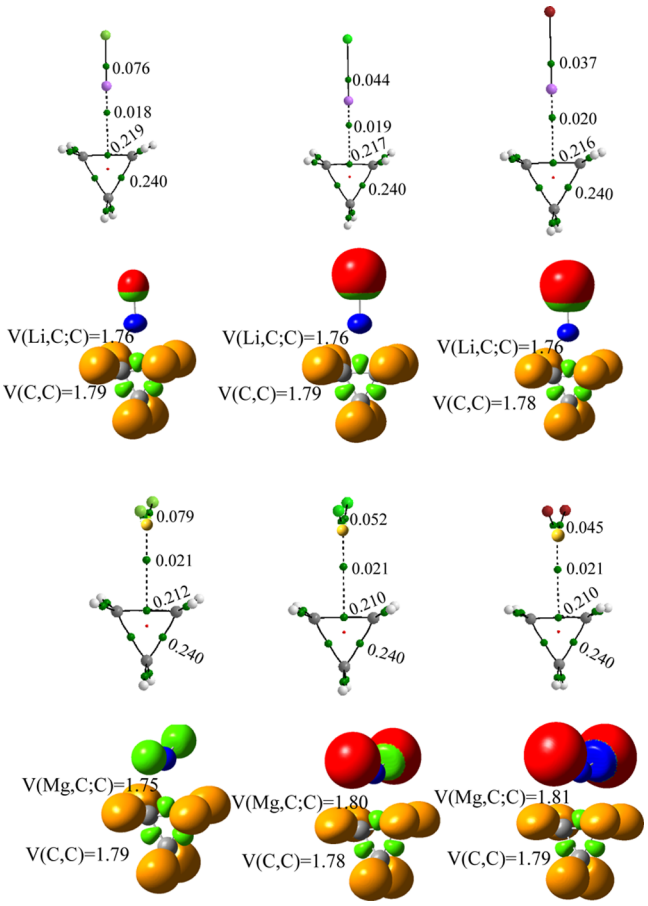

Figure 9. AIM and ELF population analysis on the products highlighting the most important points. The electronic density in the BCP are in a.u. while the electronic charge in the mentioned basin are in *e*. (Li: purple, Mg: yellow, X: green, C: gray, H: white).

CONCLUSIONS

In this study, we have presented the cyclopropanation reactions on magnesium and lithium carbenoids substituted with halogens (F, Cl, Br) with ethylene at the G4 theory level. We found that all of the Li and Mg reactions are stepwise with intermediaries that are basically in between the transition states and do not differ in more than 4 kcal/mol from the reactants and products. Our findings suggest a new mechanism of the cyclopropanations by Li and Mg carbenoid.

The Li and Mg reactants are formed by an electrostatic interaction of the π bond with the electron-deficient metal coming from the carbenoid. These results were confirmed by QTAIM, ELF, and NBO analysis.

The inspection of the works given by the reaction force at the determinant step indicated that the structural work defines the barrier height, being the highest at Mg carbenoids and associated with the transposition of the methyl group and rearrangement of the carbenoid in order to get the transition state.

The REF analysis pointed out that the electronic rearrangements occur mostly at the TS zone where all of the bond forming and breaking take place and are characterized by a spontaneous flux at the beginning of the TS zone and a nonspontaneous by the end of the same zone. At the products zone, there is some electronic activity related to the rearrangement of the cyclopropane in order to give a complex with the halide salt I(Li) and I_2(Mg). The QTAIM, ELF, and NBO analysis indicated that an electrostatic interaction between the cyclopropane and the halide lithium and halide magnesium salt is formed.

COMPUTATIONAL DETAILS

The optimization of the stationary points of the complexes under study was achieved at the G4-theory level, using a composite technique based on B3LYP-optimized geometries that provides final total energies at an effective CCSD(T,full)/G3LargeXP + HF limit level.[47] The connection between reactants and products was established by applying the IRC procedure at the B3LYP/6-311G(d,p)[48,49] level of theory, taking into account more than 180 points far from the transition state in each direction. In order to test our assumptions, dynamic simulation was done for some selected systems. ADMP molecular dynamics[44−46] was chosen with simulation time of 400 femtosecond and an initial kinetic energy about 6.3 kcal/mol. The selection of the velocities and momentums along the transition-state coordinate is done randomly.

All of the calculations have been carried out by means of Gaussian 09 series of programs.[50] The electronic population analysis was done by the QTAIM,[51,52] by using the AIMall program,[53] NBO,[54−56] and the ELF[57−59] using TopMOD suite of programs.[60] To highlight the weak interaction, we used the NCI method proposed by Contreras-García et al.[61]

ASSOCIATED CONTENT

Supporting Information

The Supporting Information is available free of charge on the ACS Publications website at DOI: 10.1021/acsomega.9b02905.

Geometries; lithium carbenoid dynamics; QTAIM calculations for lithium; and Cartesian coordinates of R, TS, and P of lithium and magnesium carbenoids (PDF)

AUTHOR INFORMATION

Corresponding Authors

*E-mail: mokhtar.lamsabhi@uam.es (A.M.L.).
*E-mail: bherrera@uc.cl (B.H.).

ORCID

Al Mokhtar Lamsabhi: 0000-0002-1509-2513
Barbara Herrera: 0000-0003-1911-4473

Notes

The authors declare no competing financial interest.

ACKNOWLEDGMENTS

This work has been partially supported by the FONDECYT REGULAR 1170837 (BH) DGI projects no. CTQ2015-63997-C2, A generous allocation of computing time at the

DOI: 10.1021/acsomega.9b02905
ACS Omega 2019, 4, 19452−19461

Centro de Computación Científica of the UAM is also acknowledged (A.M.L.).

REFERENCES

(1) Hudnall, T. W.; Moerdyk, J. P.; Bielawski, C. W. Ammonia N-H activation by a N,N′-diamidocarbene. *Chem. Commun.* **2010**, *46*, 4288−4290.
(2) Frey, G. D.; Lavallo, V.; Donnadieu, B.; Schoeller, W. W.; Bertrand, G. Facile splitting of hydrogen and ammonia by nucleophilic activation at a single carbon center. *Science* **2007**, *316*, 439−441.
(3) Back, O.; Kuchenbeiser, G.; Donnadieu, B.; Bertrand, G. Nonmetal-Mediated Fragmentation of P4: Isolation of P1and P2Bis(carbene) Adducts. *Angew. Chem., Int. Ed.* **2009**, *48*, 5530−5533.
(4) Frey, G. D.; Masuda, J. D.; Donnadieu, B.; Bertrand, G. Activation of Si-H, B-H, and P-H Bonds at a Single Nonmetal Center. *Angew. Chem., Int. Ed.* **2010**, *49*, 9444−9447.
(5) Lavigne, F.; Maerten, E.; Alcaraz, G.; Branchadell, V.; Saffon-Merceron, N.; Baceiredo, A. Activation of CO2 and SO2 by Boryl(phosphino)carbenes. *Angew. Chem., Int. Ed.* **2012**, *51*, 2489−2491.
(6) Schmidt, D.; Berthel, J. H. J.; Pietsch, S.; Radius, U. C-N Bond Cleavage and Ring Expansion of N-Heterocyclic Carbenes using Hydrosilanes. *Angew. Chem., Int. Ed.* **2012**, *51*, 8881−8885.
(7) Closs, G. L.; Moss, R. A. Carbenoid Formation of Arylcyclopropanes from Olefins, Benzal Bromides, and Organolithium Compounds and from Photolysis of Aryldiazomethanes. *J. Am. Chem. Soc.* **1964**, *86*, 4042−4053.
(8) Closs, G. L.; Closs, L. E. Stereospezifische Bildung von Cyclopropanen durch Umsetzung von Diphenyldibrommethan mit Methyllithium und Olefinen. *Angew. Chem.* **1962**, *74*, 431.
(9) Gessner, V. H. Stability and reactivity control of carbenoids: recent advances and perspectives. *Chem. Commun.* **2016**, *52*, 12011−12023.
(10) Meng, F.; Xu, X.; Liu, X.; Zhang, S.; Lu, X. Theoretical studies of samarium carbenoid promoted cyclopropanation reaction with allylic alcohol on the reaction pathways. *J. Mol. Struct.* **2008**, *858*, 66−71.
(11) Feng, R.; Zou, J.-J.; Zhang, X.; Wang, L.; Zhao, H. Theoretical study on cyclopropanation of endo-dicyclopentadiene with zinc carbenoids: effects of solvent and (ICH2)2Zn. *J. Org. Chem.* **2012**, *77*, 10065−10072.
(12) Huang, G.; Xie, K.; Lee, D.; Xia, Y. Reactivity of Alkynyl Metal Carbenoids: DFT Study on the Pt-Catalyzed Cyclopropanation of Propargyl Ester Containing 1,3-Diynes. *Org. Lett.* **2012**, *14*, 3850−3853.
(13) Simmons, H. E.; Smith, R. D. A new synthesis of cyclopropanes from olefins. *J. Am. Chem. Soc.* **1958**, *80*, 5323−5324.
(14) Goh, S. H.; Closs, L. E.; Closs, G. L. Carbenoid decomposition of aryldiazomethanes with lithium and zinc halides. Synthesis of arylcyclopropanes. *J. Org. Chem.* **1969**, *34*, 25−31.
(15) Li, Z.; Parr, B. T.; Davies, H. M. L. Highly Stereoselective C-C Bond Formation by Rhodium-Catalyzed Tandem Ylide Formation/[2,3]-Sigmatropic Rearrangement between Donor/Acceptor Carbenoids and Chiral Allylic Alcohols. *J. Am. Chem. Soc.* **2012**, *134*, 10942−10946.
(16) Miura, T.; Funakoshi, Y.; Murakami, M. Intramolecular Dearomatizing [3 + 2] Annulation of α-Imino Carbenoids with Aryl Rings Furnishing 3,4-Fused Indole Skeletons. *J. Am. Chem. Soc.* **2014**, *136*, 2272−2275.
(17) Torres, Ò.; Parella, T.; Solà, M.; Roglans, A.; Pla-Quintana, A. Enantioselective Rhodium(I) Donor Carbenoid-Mediated Cascade Triggered by a Base-Free Decomposition of Arylsulfonyl Hydrazones. *Chem.—Eur. J.* **2015**, *21*, 16240−16245.
(18) de Meijere, A.; Kozhushkov, S. I. The Chemistry of Highly Strained Oligospirocyclopropane Systems†. *Chem. Rev.* **2000**, *100*, 93−142.
(19) Faust, R. Fascinating Natural and Artificial Cyclopropane Architectures. *Angew. Chem., Int. Ed.* **2001**, *40*, 2251−2253.
(20) Wessjohann, L. A.; Brandt, W.; Thiemann, T. Biosynthesis and Metabolism of Cyclopropane Rings in Natural Compounds. *Chem. Rev.* **2003**, *103*, 1625−1648.
(21) Gnad, F.; Reiser, O. Synthesis and Applications of β-Aminocarboxylic Acids Containing a Cyclopropane Ring. *Chem. Rev.* **2003**, *103*, 1603−1624.
(22) Pratt, L. M.; Nguỹên, N. V. Structure, Bonding, and Solvation of Lithium Vinylcarbenoids. *J. Org. Chem.* **2005**, *70*, 2294−2298.
(23) Saitoh, H.; Ishida, N.; Satoh, T. Synthesis of conjugated enynes by assembly of three components, ketones, chloromethyl p-tolyl sulfoxide, and acetylenes, with the magnesium carbenoid 1,2-CC insertion as the key reaction. *Tetrahedron Lett.* **2010**, *51*, 633−637.
(24) Watanabe, H.; Ogata, S.; Satoh, T. A method for the synthesis of cyclopropanes by regiospecific and regioselective magnesium carbenoid 1,3-CH insertion as the key reactions. *Tetrahedron* **2010**, *66*, 5675−5686.
(25) Kashiwamura, G.; Kimura, T.; Satoh, T. A novel one-pot synthesis of cyclopropanols based on the reaction of magnesium carbenoids with lithium enolate of ketones. *Tetrahedron Lett.* **2013**, *54*, 2533−2535.
(26) Simmons, H. E.; Smith, R. D. A New Synthesis of Cyclopropanes1. *J. Am. Chem. Soc.* **1959**, *81*, 4256−4264.
(27) Wang, B.; Deng, C. Theoretical studies of carbenes and carbenoids. 5. Intramolecular reactions of cyclopropylcarbene. *Tetrahedron* **1988**, *44*, 7355−7362.
(28) Hermann, H.; Lohrenz, J. C. W.; Kühn, A.; Boche, G. The Influence of the Leaving Group X (X=F, Cl, Br, I, OH) on the Carbenoid Nature of the Carbenoids LiCH 2 X and XZnCH 2 X-A Theoretical Study. *Tetrahedron* **2000**, *56*, 4109−4115.
(29) Wang, Y.-G.; Sun, C.-J.; Deng, C.-H. A theoretical study of C2H3OLi. *J. Mol. Struct.* **1998**, *429*, 207−216.
(30) Toro-Labbé, A.; Gutiérrez-Oliva, S.; Murray, J. S.; Politzer, P. The reaction force and the transition region of a reaction. *J. Mol. Model.* **2009**, *15*, 707−710.
(31) Herrera, B.; Toro-Labbé, A. The Role of Reaction Force and Chemical Potential in Characterizing the Mechanism of Double Proton Transfer in the Adenine−Uracil Complex. *J. Phys. Chem. A* **2007**, *111*, 5921−5926.
(32) Herrera, B.; Toro-Labbé, A. Theoretical Study of the HXNY → XNYH (X,Y = O,S) Intramolecular Proton Transfer Reactions. *J. Phys. Chem. A* **2004**, *108*, 1830−1836.
(33) Toro-Labbé, A.; Gutiérrez-Oliva, S.; Concha, M. C.; Murray, J. S.; Politzer, P. Analysis of two intramolecular proton transfer processes in terms of the reaction force. *J. Chem. Phys.* **2004**, *121*, 4570.
(34) Politzer, P.; Burda, J. V.; Concha, M. C.; Lane, P.; Murray, J. S. Analysis of the Reaction Force for a Gas Phase SN2 Process: CH3Cl + H2O → CH3OH + HCl†. *J. Phys. Chem. A* **2006**, *110*, 756−761.
(35) Herrera, B. Study of ring influence and electronic response to proton transfer reactions. Reaction electronic flux analysis. *J. Mol. Model.* **2011**, *17*, 1051−1060.
(36) Toro-Labbé, A. Characterization of Chemical Reactions from the Profiles of Energy, Chemical Potential, and Hardness. *J. Phys. Chem. A* **1999**, *103*, 4398−4403.
(37) Geerlings, P.; De Proft, F.; Langenaeker, W. Conceptual Density Functional Theory. *Chem. Rev.* **2003**, *103*, 1793−1874.
(38) Parr, R. G.; Yang, W. *Density Functional Theory of Atoms and Molecules*; Oxford University Press: New York, 1989.
(39) Echegaray, E.; Toro-Labbé, A. Reaction Electronic Flux: A New Concept To Get Insights into Reaction Mechanisms. Study of Model Symmetric Nucleophilic Substitutions. *J. Phys. Chem. A* **2008**, *112*, 11801−11807.
(40) Cerón, M. L.; Echegaray, E.; Gutiérrez-Oliva, S.; Herrera, B.; Toro-Labbé, A. The reaction electronic flux in chemical reactions. *Sci. China: Chem.* **2011**, *54*, 1982−1988.
(41) Morell, C.; Tognetti, V.; Bignon, E.; Dumont, E.; Hernandez-Haro, N.; Herrera, B.; Grand, A.; Gutiérrez-Oliva, S.; Joubert, L.;

DOI: 10.1021/acsomega.9b02905
ACS Omega 2019, 4, 19452−19461

Toro-Labbé, A.; Chermette, H. Insights into the chemical meanings of the reaction electronic flux. *Theor. Chem. Acc.* **2015**, *134*, 133.
(42) Ammal, S. S. C.; Venuvanalingam, P.; Pal, S. Lithium bonding interaction in H2CY···LiF (Y=O,S) complexes: A theoretical probe. *J. Chem. Phys.* **1997**, *107*, 4329−4336.
(43) Li, S.-Y.; Wu, D.; Li, Y.; Yu, D.; Liu, J.-Y.; Li, Z.-R. Insight into structural and π-magnesium bonding characteristics of the X2Mg···Y (X = H, F; Y = C2H2, C2H4and C6H6) complexes. *RSC Adv.* **2016**, *6*, 102754−102761.
(44) Iyengar, S. S.; Schlegel, H. B.; Millam, J. M.; Voth, G.; Scuseria, G. E.; Frisch, M. J. Ab initio molecular dynamics: Propagating the density matrix with Gaussian orbitals. II. Generalizations based on mass-weighting, idempotency, energy conservation and choice of initial conditions. *J. Chem. Phys.* **2001**, *115*, 10291−10302.
(45) Schlegel, H. B.; Iyengar, S. S.; Li, X.; Millam, J. M.; Voth, G. A.; Scuseria, G. E.; Frisch, M. J. Ab initio molecular dynamics: Propagating the density matrix with Gaussian orbitals. III. Comparison with Born-Oppenheimer dynamics. *J. Chem. Phys.* **2002**, *117*, 8694−8704.
(46) Schlegel, H. B.; Millam, J. M.; Iyengar, S. S.; Voth, G. A.; Daniels, A. D.; Scuseria, G. E.; Frisch, M. J. Ab initiomolecular dynamics: Propagating the density matrix with Gaussian orbitals. *J. Chem. Phys.* **2001**, *114*, 9758−9763.
(47) Curtiss, L. A.; Redfern, P. C.; Raghavachari, K. Gaussian-4 theory. *J. Chem. Phys.* **2007**, *126*, 084108−084112.
(48) Lee, C.; Yang, W.; Parr, R. G. Development of the Colle-Salvetti correlation-energy formula into a functional of the electron density. *Phys. Rev. B: Condens. Matter Mater. Phys.* **1988**, *37*, 785−789.
(49) Becke, A. D. Density-functional thermochemistry. III. The role of exact exchange. *J. Chem. Phys.* **1993**, *98*, 5648−5652.
(50) Frisch, M. J.; Trucks, G. W.; Schlegel, H. B.; Scuseria, G. E.; Frisch, H.; Trucks, M. J.; Schlegel, G. W.; Scuseria, H. B.; Robb, G. E.; Cheeseman, M. A.; Scalmani, J. R.; Barone, G.; Mennucci, V.; Petersson, B.; Nakatsuji, G. A.; Caricato, H.; Li, M.; Hratchian, X.; Izmaylov, H. P.; Bloino, A. F.; Zheng, J.; Sonnenberg, G.; Hada, J. L.; Ehara, M.; Toyota, M.; Fukuda, K.; Hasegawa, R.; Ishida, J.; Nakajima, M.; Honda, T.; Kitao, Y.; Nakai, O.; Vreven, H.; Montgomery, T. J.; Peralta, J. A.; Ogliaro, J. E.; Bearpark, F.; Heyd, M.; Brothers, J. J.; Kudin, E.; Staroverov, K. N.; Kobayashi, V. N.; Normand, R.; Raghavachari, J.; Rendell, K.; Burant, A.; Iyengar, J. C.; Tomasi, S. S.; Cossi, J.; Rega, M.; Millam, N.; Klene, J. M.; Knox, M.; Cross, J. E.; Bakken, J. B.; Adamo, V.; Jaramillo, C.; Gomperts, J.; Stratmann, R.; Yazyev, R. E.; Austin, O.; Cammi, A. J.; Pomelli, R.; Ochterski, C.; Martin, J. W.; Morokuma, R. L.; Zakrzewski, K.; Voth, V. G.; Salvador, G. A.; Dannenberg, P.; Dapprich, J. J.; Daniels, S.; Farkas, A. D.; Foresman, Ö.; Ortiz, J. B.; Cioslowski, J. V.; Fox, J. *Gaussian 09*, Revision E01; Gaussian Inc: Wallingford, CT, 2017.
(51) Bader, R. F. W. *Atoms in Molecules*; Clarendon Press: U. K., 1990.
(52) Matta, C. F.; Boyd, R. J. *The Quantum Theory of Atoms in Molecules: From Solid State to DNA and Drug Design*; Wiley-VCH Verlag: Weinheim (Germany), 2007; p 567.
(53) Keith, T. A. AIMAll: Overland Park http://aim.tkgristmill.com 17.11.14, 2018.
(54) Reed, A. E.; Curtiss, L. A.; Weinhold, F. Intermolecular interactions from a natural bond orbital, donor-acceptor viewpoint. *Chem. Rev.* **1988**, *88*, 899−926.
(55) Weinhold, F.; Landis, C. R. *Valency and Bonding: A Natural Bond Orbital Donor-Acceptor Perspective*; Cambridge University Press: Cambridge (KU), 2005; p 749.
(56) Glendening, E. D.; Badenhoop, J. K.; Reed, A. E.; Carpenter, J. E.; Bohmann, J. A.; Morales, C. M.; Landis, C. R.; Weinhold, F. NBO, 6.0; Theoretical Chemistry Institute, University of Wisconsin: Madison, WI http://nbo6.chem.wisc.edu/, 2013.
(57) Savin, A.; Becke, A. D.; Flad, J.; Nesper, R.; Preuss, H.; von Schnering, H. G. A new look at electron localization. *Angew. Chem., Int. Ed. Engl.* **1991**, *30*, 409−412.
(58) Silvi, B.; Savin, A. Classification of chemical bonds based on topological analysis of electron localization functions. *Nature* **1994**, *371*, 683−686.
(59) Savin, A.; Nesper, R.; Wengert, S.; Fässler, T. F. ELF: The Electron Localization Function. *Angew. Chem., Int. Ed. Engl.* **1997**, *36*, 1808−1832.
(60) Silvi, B. TopMod; The TopMod. http://www.lct.jussieu.fr/pagesperso/silvi/topmod.html, GNU: 2010.
(61) Contreras-García, J.; Johnson, E. R.; Keinan, S.; Chaudret, R.; Piquemal, J.-P.; Beratan, D. N.; Yang, W. NCIPLOT: A Program for Plotting Noncovalent Interaction Regions. *J. Chem. Theory Comput.* **2011**, *7*, 625−632.

DOI: 10.1021/acsomega.9b02905
ACS Omega 2019, 4, 19452−19461

PCCP

PAPER

View Article Online
View Journal | View Issue

Cite this: *Phys. Chem. Chem. Phys.*, 2019, **21**, 10163

Theoretical study of C-arylations with aryl halides to determine the reaction mechanism, the effect of substituents and heteroatoms†

Rocío Durán,[a] Nicolás Núñez-Navarro,[bc] Flavia C. Zacconi[bd] and Barbara Herrera *[a]

Received 19th December 2018,
Accepted 18th April 2019

DOI: 10.1039/c8cp07752e

rsc.li/pccp

Carbon arylations are very important in the pharmaceutical industry. New synthesis routes are often studied with the objective of trying to insert new bonds and substituents into an organic framework. Ullman reactions have been very useful in this context. In light of this, a wB97XD/6-311g set of Ullman-like reactions among substituted amide arylations with iodoaniline were theoretically studied in order to understand their intrinsic reactivity and their reaction mechanisms. The studied systems included unsubstituted (C), sulphur (S), synthesized by the authors in a previous experimental work. In this study, amino (NH) and butyloxycarbonyl (NBoc) amides were added. IRC calculations on catalyzed species showed that the catalyst lowers the reaction barrier, and changes the reactivity in order to lower the nitrogen charge. The reaction mechanism proceeds by binding the CuI catalyst and *N*,*N*-dimethylethylenediamine (DMEN) to the N lactam, in a barrierless reaction, thereby activating the nitrogen to bond with the aryl iodine through a nucleophilic substitution, and thus recovering the catalyst.

1. Introduction

Carbon arylations are very interesting reactions in the pharmaceutical industry given that they are the starting materials for several families of drugs. The synthetic routes for their production have been studied in order to increase their yields and minimize the reaction times, thereby reducing the costs[1] of synthesis.

With the development of new compounds, it is fundamentally important that the C–N bond is examined in terms of its relation to the synthesis of new drugs.[2] A lot of work has been done to create these bioactive molecules, and one of the most popular reactions is the Ullmann reaction.[3] This reaction consists of coupling aryl halides by using copper as a catalyst. This product is then used as a starting material for the production of the desired drug through further biological assays.[1] The reaction was first performed by Fritz Ullmann in 1901. Ullmann allowed for the coupling of two 1-bromo-2-nitrobenzene units through the formation of a C–C bond using copper as a catalyst.[3]

A few years later, Irma Goldberg developed a new reaction in accordance with Ullmann's procedures and was able to couple potassium 2-aminobenzoate with 4-bromobenzene. The halogen substitution was done with the nitrogen atom in the C–Br bond, thereby producing a new C–N bond.[5] This allowed for the synthesis of several new compounds and enhanced the importance of C–N bond production.

Over the years the original reactions were subsequently modified to improve the yields and synthesis conditions.

Recently, Núñez-Navarro *et al.*[4] have synthesized 4-C, 4-O and 4-S lactams with an aromatic amide substituent by using a microwave-assisted modified Ullmann reaction (Fig. 1). The overall aim being to obtain new antineoplastic drugs.[2]

Núñez-Navarro *et al.*[4] reported that there are changes to the yield and the conditions depending on the halogen atom, and lactam heteroatom (Y). When the synthesis methodologies were

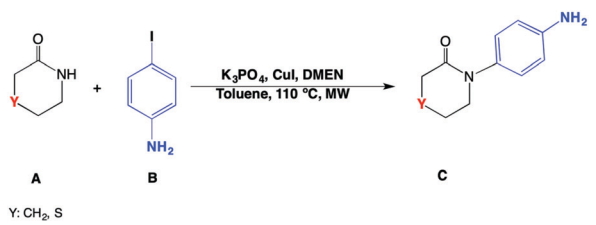

Fig. 1 Different lactams synthesized by using a recently modified Ullmann reaction.[1]

[a] QTC, Facultad de Quimica y de Farmacia, Pontificia Universidad Católica de Chile, Av, Vicuña Mackenna 4860, Macul, Santiago, Chile. E-mail: bherrera@uc.cl
[b] Departamento de Química Orgánica, Facultad de Química y de Farmacia, Pontificia Universidad Católica de Chile, Av. Vicuña Mackenna 4860, Macul, Santiago, Chile
[c] Departamento Ingeniería Química y Bioprocesos, Escuela de Ingeniería, Pontificia Universidad Católica de Chile, Av, Vicuña Mackenna 4860, Macul, Santiago, Chile
[d] Institute for Biological and Medical Engineering, Schools of Engineering, Medicine and Biological Sciences, Pontificia Universidad Católica de Chile, Santiago, Chile

† Electronic supplementary information (ESI) available. See DOI: 10.1039/c8cp07752e

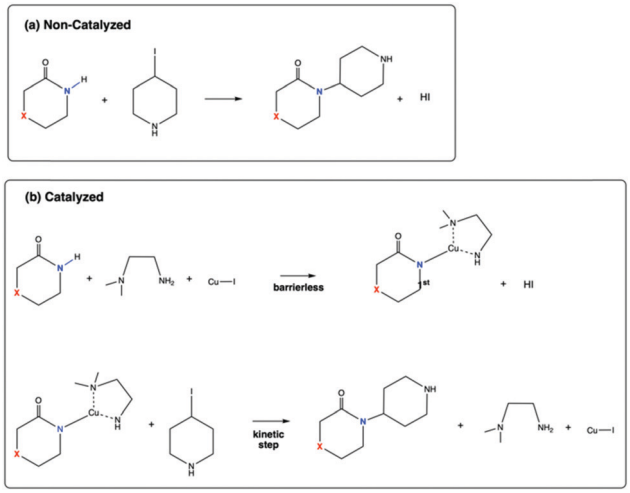

Fig. 2 Reactions under study, where X = C, S, NBoc, NH. (a) Non-catalyzed reaction, where the aryl iodine is inserted into the lactam in a single step, and (b) catalyzed reaction, this last reaction occurs in two steps. First a process without a barrier, and second, the 4-aryliodine insertion into the first reaction product.

changed (Fig. 2), it can be seen that most of the reactions were performed by using CuI as a catalyst, a bidentate ligand (*N*,*N*-dimethyl-ethylenediamine, *N*,*N*′-dimethyl-ethylenediamine) and microwave reactor for two hours. The results reported indicated different behaviors for the substituted lactams, indicating that the S substituted ring used the methodology with the mildest conditions and the best yield in the set of reactions. The differences in the reactivity of the synthesis were determined by further steps. However, many questions remain unanswered during the experimental work. In order to understand how the structural differences, lead to differences in reactivity in the chosen system, a reaction mechanism, and subsequent synthesis methodology[2] was determined.

In order to explain and predict the possible products, there are four proposed experimental mechanisms for the Ullmann type reactions. The first proposed mechanism, Single Electron Transfer (SET), involves radical intermediates and redox Cu(I)/Cu(II) couples. The second considers a metathesis reaction through a Cu coordination to the halogen atom with the aryl halide producing the four-membered cyclic transition state. The aromatic nucleophilic substitution is the third accepted mechanism in which the Cu(I) produces a π-coordinating intermediate with the aryl halide to induce a more electrophilic position for the corresponding substitution. The last mechanism is the oxidative addition-reductive elimination cycle *via* direct oxidation with Cu(III) intermediates.[1,3–9]

Several theoretical studies have been done to analyze and determine the reaction mechanisms. These studies have shown the importance of Cu–aryl ligand stabilization, the intermediates generated *via* caged radicals and the SET mechanism by using DFT calculations.[3,10,11] The use of carbonate as a partially soluble base was used to increase conversion and decrease the side product[5] and the possible actions of carbonate and phosphate ions acting as bidentate ligands in the catalytic cycle monitored by FTIR and DFT thermodynamic studies.[12,13]

With the aim of further understanding the experimental mechanism and to move towards a more rational synthesis of C–N bonded systems using the Ullman reaction, the four systems were studied. Two have already been reported in a previous work (X = C and S),[1] and two were considered as good candidates for the presented synthesis paths, where X = NH_2 and the *N-tert*-butyloxycarbonyl (NBoc) groups. This study was done by using a model reaction as shown in Fig. 2. In order to do this work, these reactions were studied taking into consideration the isolated reactants and the reactants along with the use of copper catalyst. The aim was to assess the influence of the CuI system on the reaction mechanism and the changes in reactivity of the molecules involved. The reactivities of the isolated systems and the catalyzed reactants were compared. Their reactions were then plotted along the intrinsic reaction coordinate (IRC) to determine the reaction mechanism by exploring the reaction energy profile of this reaction. It was important to understand and predict the possible paths in which the reactions might undergo, especially the last two substituents that were not being tested in the laboratory.

The reactivity indexes in the framework of conceptual Density Functional Theory (DFT) were analyzed to help understand the chemical reactivity of any given system. Reactivity indexes such as chemical potential (μ), hardness (η), and electrophilicity index (ω), are in particular, good descriptors to understand intrinsic chemical reactivity, indicating the global and local susceptibility of a molecule that might participate in a chemical reaction. In addition to this, a total of eight reactions on the intrinsic reaction coordinate (IRC) were studied to understand the reaction mechanism using the same model. This was done in order to test whether the reaction force framework helps to indicate the overall reactivity. Concerning the role of the catalyst, the substitution and understanding of how the activation works is very important when analyzing the reactions.

In this paper, Section 1 will outline the theoretical tools on which we have based our analysis. Section 2 will include theoretical details of this study. Section 4 will be devoted to the Results and discussion of this work, and finally, Section 5, is the Conclusion.

2. Theoretical framework

The theoretical description of a chemical system is a powerful tool to describe and understand the reaction mechanism of a reaction or the intrinsic reactivity. In this context, conceptual DFT was used, which includes concepts based on empirical descriptions such as electronegativity, chemical potential, hardness and electrophilicity. These are based on the complete theoretical description of the molecular density, an experimental observable.

2.1. Electronic chemical potential

The electronic chemical potential indicates the escaping tendency of electrons from an electronic cloud. In an analogy with the thermodynamic chemical potential, the tendency of electrons going from sites of high chemical potential to low chemical

potential is associated with the negative of the electronegative defined by Mulliken.[14]

$$\mu = \left(\frac{\partial E}{\partial N}\right)_{v(\vec{r})} \tag{1}$$

Given the discontinuity of the energy with respect to the number of electrons, this index is quantified by the finite difference approximation and the Koopmans theorem,[15,16] giving:

$$\mu \approx \frac{I + A}{2} \approx \frac{\varepsilon_{\mathrm{LUMO}} + \varepsilon_{\mathrm{HOMO}}}{2} \tag{2}$$

where the chemical potential is associated to the ionization potential and the electron affinity, and to the energies of the LUMO and HOMO molecular orbitals.

2.2. Chemical hardness

This index indicates the resistance to deformation of an electronic cloud. It is defined by the derivative of the chemical potential with respect to the number of electrons at a constant external potential.[17]

$$\eta = \left(\frac{\partial \mu}{\partial N}\right)_{v(\vec{r})} = \left(\frac{\partial^2 E}{\partial N^2}\right)_{v(\vec{r})} \tag{3}$$

The same as for chemical potential, in order to quantify this index, the finite difference approximation and the Koopmans theorem was used.[14–16]

$$\eta \approx I - A \approx \varepsilon_{\mathrm{LUMO}} - \varepsilon_{\mathrm{HOMO}} \tag{4}$$

In relation to the above defined chemical potential and hardness, Parr *et al.*, proposed the electrophilicity index. This, is defined as the stabilization of energy that a system acquires when it is saturated by external electrons.[18]

$$\omega = \frac{\mu^2}{2\eta} \tag{5}$$

2.3. Reaction force

Firstly, to characterize reaction mechanisms, it is necessary to follow the reaction along a reaction coordinate and monitor the systems properties at each point along it. The most important property is the energy. This gives information about the reaction energy (ΔE°) and the height of the reaction barrier ($\Delta E^{\neq}$), thereby reaching the thermodynamic and the kinetic reaction with few transformations.

When derivating the reaction energy, this leads to the Hellman–Feynman reaction force. This is a global property that helps to give useful information about the chemical events that are taking place in any given reaction.[19–26]

$$F(\xi) = -\frac{\partial E}{\partial \xi} \tag{6}$$

In a single step potential, this index presents two critical points. First, a minimum ξ_1 that defines the reactant zone, (from ξ_R to ξ_1) where the structural rearrangements occur. Second, the maximum of the reaction force, ξ_2. From ξ_1 to this last point is defined as the transition state zone, where all the electronic rearrangements take place. From ξ_2 to ξ_P, it is defined as the product zone where structural relaxation of the system occurs in order to form the products. This concept defines a rational partition of the reaction coordinate, thus indicating the activation or de-deactivation of chemical properties. The critical point of the reaction force defines how the reaction works. This can be associated with structural (W_1 and W_4) and electronic (W_2 and W_3) rearrangements. All these properties can be obtained using the work expressions on references given by Toro–Labbé.[20,27]

2.4. Reaction electronic flux

The reaction electronic flux comes from the gradient of the chemical potential. It indicates the electronic reorganization in a chemical reaction and is defined as:[24,28]

$$J(\xi) = -\frac{\partial \mu}{\partial \xi} \tag{7}$$

Given the analogy with thermodynamics, this property can be associated with the spontaneity of the electronic processes. When $J(\xi)$ is positive, it may highlight a spontaneous reorganization of the electron cloud, indicating bond forming or strengthening. When it is negative, the electronic changes are then non-spontaneous, meaning bond breaking or weakening.[28,29]

2.5 Non-covalent interactions (NCI)

The non-covalent interaction (NCI)[30–32] is a visualization index based on the electron density (ρ) and the reduced density gradient (RDG, s), and it is defined as:

$$s = \frac{1}{2(3\pi^2)^{1/3}} \frac{|\nabla \rho|}{\rho^{4/3}} \tag{8}$$

The main importance of this index is that helps to understand the stability of the system, based on the counterbalance between attractive interactions and steric repulsions.

This index can be obtained as a function of the electron density (ρ), oriented by the sign of λ_2 (the second eigenvalue of the Hessian). Values of $\rho > 0.01$ a.u. and $\lambda_2 < 0$ correspond to strong stabilizing interactions, whereas values $\rho > 0.01$ a.u. and $\lambda_2 < 0$ are identified as strong destabilizing interactions, finally at very low-density values and is assigned to much weaker interactions. Weaker interactions are defined at $\rho > 0.01$ a.u. and $\lambda_2 \sim 0$.

A 3D NCI plots can be obtained for a system in order to rank interactions, where repulsive interactions are colored in red, while electrostatic or stabilizing interactions are in blue, and delocalized weak interactions are plotted in green.

3. Computational details

All the calculations were performed considering non-catalyzed (Fig. 2a) and catalyzed (Fig. 2b) reactions using CuI and *N*,*N*-dimethyl-ethylenediamine (DMEN), on four different substituted lactams. The calculations were performed using DFT/wB97XD/6-311G(d,p)[33] as a basis set for light atoms and LanL2DZ[34–36] to treat iodine atoms at Gaussian 09.[37] All stationary states were

confirmed by vibrational frequencies. Intrinsic Reaction Coordinate (IRC)[38] calculations were also performed on the complete set of reactions.

Chemical potential (μ), hardness (η)[16] and electrophilicity index (ω),[18,39] were calculated using HOMO and LUMO energies. Electrostatic potential,[40] population analysis *via* NBO[41] using the routines available in Gaussian 09,[37] and non-covalent interactions (NCI) using NCIplot[42] calculations, were also performed.

4. Results and discussion

4.1. Electronic chemical potential

Table 1 lists the chemical potential of all the species studied. The electronic chemical potential is shown to be lower with the inclusion of the catalyst in the molecular structure of the lactam. It is about 0.5–1.0 eV from the isolated reactant that being NBoc, and the system that changes the most upon the use of a catalyst with NH being the species less changed.

This index indicates the escaping tendency of electrons from sites of high chemical potential to low chemical potential. Thus, by plotting the chemical potential among all the lactams in contrast to the aryl iodine, we can have an idea of the direction of the electronic transfer. In Fig. 3, the lactams are plotted against the aryl Iodine. Here it can be seen that the electronic transfer goes from sites of high μ to low μ, but in most of the systems it goes from the lactam to the aryl iodine. This being therefore an indicator of a possible nucleophilic attack on the lactam nitrogen by the aryl iodine. It is interesting to note that mostly all the systems have a larger chemical potential than the aryl Iodine. The NBoc system is the only one that when used with the catalyst, it changes its chemical potential, reversing the direction of the electronic motion.

Table 1 Chemical potential (μ), hardness (η), and electrophilicity index in (ω) the studied systems. All energies are represented in eV

System	μ (eV)	η (eV)	ω (eV)
Non-catalyzed			
C	−3.1	11.4	0.3
S	−3.2	11.5	0.4
NH	−3.5	11.2	0.6
NBoc	−3.0	11.2	0.4
Catalyzed			
C	−2.4	8.6	0.3
S	−2.5	8.6	0.4
NH	−2.4	8.6	0.3
NBoc	−2.5	8.6	0.4
4-Iodoaniline	−3.2	5.0	1.1

4.2. Chemical hardness

Chemical hardness indicates the tendency of deformation of an electronic cloud, and is a good index to indicate the reactivity of a system. In Table 1, it is noted that the system becomes more reactive upon the use of the catalyst. The hardness changes dramatically around 2 eV in all of the systems. According to Pearson's definition,[43,44] the harder systems are less able to react, in contrast to softer systems.[31] It is interesting to note that without the catalyst, the order of reactivity is NH $\approx$ NBoc $>$ C $>$ S. Using a catalyst, the reactivities differ slightly and there is not a preference for a determined system. Nonetheless, it can only be concluded that the use of the catalyst enhances the reactivity of the lactams. Intrinsic reactivity is not the only factor which indicates if the reaction will be favorable. Other factors must be included, such as the electrophilicity index and the analysis of the reaction coordinate in order to understand the reaction mechanism and other structural and electronic systems.

4.3. Electrophilicity index

In order to understand more the ability of accepting and receiving electrons, the electrophilicity index values given in Table 1 were analyzed. This index indicates the tendency to accept electrons in an equilibrium system, which along with μ and η, is a descriptor of the nature or the intrinsic reactivity of a given system. The electrophilicity index of all the non-catalyzed and the catalyzed reactions were plotted, using ω of 4-iodoaniline as a reference in Fig. 3(c). In this plot, the difference between the reacting systems was noted. The iodoaniline being the most electrophilic system, and as the chemical intuition indicates, it should react with a nucleophile, represented by the lactams in this study, which are all less electrophilic than 4-iodoaniline.

Upon the use of a catalyst, the lactams presented lower electrophilicity values than the non-catalyzed systems. The gap between the reactants was enlarged, indicating that the use of bidentate copper iodine, contributes to the overall nucleophilic tendencies.

4.4. Electrostatic potential

In order to understand the local reactivity and the differences between the systems studied, the electrostatic potential was determined, and it is shown in Fig. 4. This gave the most

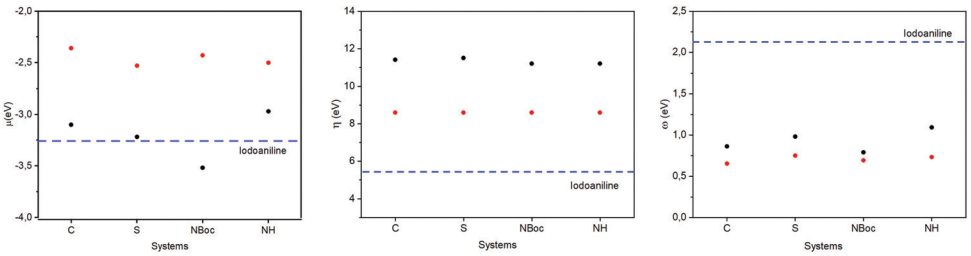

Fig. 3 Electronic chemical potential (a) chemical hardness (b) and electrophilicity index (c) at the non-catalyzed (black dots) and the catalyzed (red dots) in terms of the 4-iodoaniline chemical potential (dashed blue line). All values are in eV.

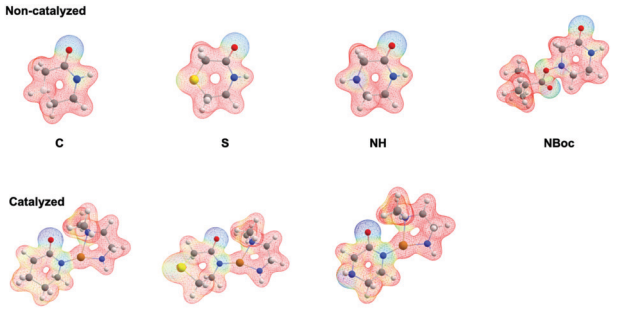

Fig. 4 Changes to the electrostatic potential among non-catalyzed and catalyzed systems. Blue indicates zones of high electrostatic potential; red zones indicate low potential.

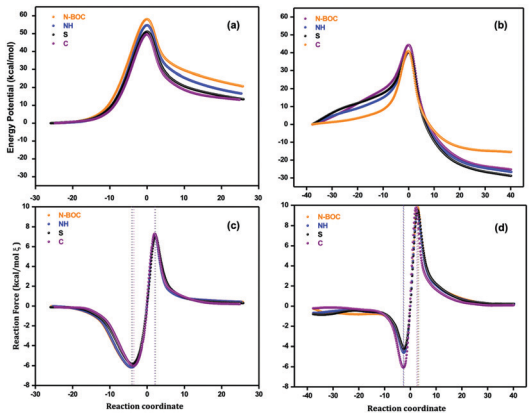

Fig. 5 Energy profiles of (a) non-catalyzed and (b) catalyzed reactions. Reaction force (c) non catalyzed; (d) catalyzed along the IRC for the coupling of C (purple), S (black), NBoc (orange) and NH (blue) lactams and iodoaniline. All values are shown in kcal mol^{-1}.

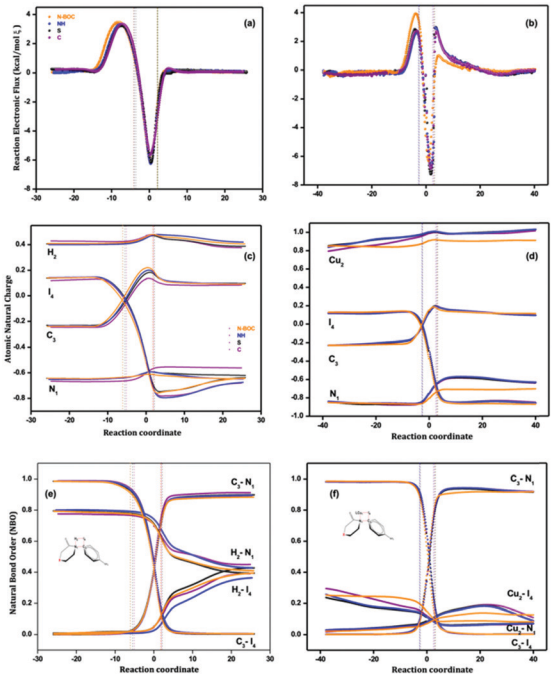

Fig. 6 Reaction electronic flux (a) non-catalyzed; (b) catalyzed, atomic charges at the reaction zone (c) non-catalyzed; (d) catalyzed, and natural bond orders (e) non-catalyzed; (f) catalyzed, along the IRC for the coupling of C (purple), S (black), NBoc (orange) and NH (blue) lactams and iodoaniline. All values are shown in kcal mol^{-1}.

preferred sites of electronic accumulation/depletion in a given system. The most negative sites are plotted in blue, while the red zones indicate low electrostatic potential or electron depletion.

It is known that the nucleophilic ability of these lactam systems is given by the ring nitrogen, which should react when it is confronted with the aryl iodine system. As the Fig. 5 shows, there is neutral zone at the nitrogen atom (yellow) on the isolated lactam. As it is shown, using the catalyst the reactive aryl nitrogen gets activated along the use of a catalyst, showing more negative electrostatic potential, making the N of the lactam activated to act as a nucleophilic site on the molecule. When observing the reactivity at the non-catalyzed systems, C and S are the molecules with higher MEP. On catalyzed systems, S and N lactams are more reactive, in agreement with our results at experimental level.

4.5. Reaction energies

The reaction energies in Fig. 5(a and b) were plotted to elucidate the mechanism of the C–N coupling of the four lactams (S, NBoc, NH). For the non-catalyzed reaction (Fig. 6a), the energetic analysis indicates that all the reactions are concerted and exergonic, and their reaction energies are listed in Table 2. The reaction mechanism proceeds by a concerted transition state that represents an aromatic nucleophilic substitution, with the nitrogen of the lactam substituting the iodine in order to form the coupling products, thus confirming the experimental evidence of the reaction mechanism.[2] The most favorable reaction was with the unsubstituted lactam. This was very closely followed by S lactam, which was the most successful reaction in terms of the experimental conditions and yield, with a barrier of 49.6 kcal mol^{-1}, and NBoc, that enhanced the barrier by 8.4 kcal mol^{-1}.

With regard to the reactivity differences of the four lactams, it is important to emphasize that experimentally the *S*-lactam was the most reactive of the series, and this IRC calculation does not show a large difference in the unsubstituted system. By way of contrast, the catalyzed reaction proceeds by a first barrierless process where the catalyst Cu–I and DMEN occurs. There is then a second kinetic step, whereby a nucleophilic substitution occurs between the lactam and the aryl iodine system. In Fig. 6b, the reaction energies show a drastic change on all the energies by which all the reactions are endoenergetic and the barriers lower by 30%. The order in which the systems react is S $<$ NBoc $<$ C $<$ N, agreeing with experimental results. The effect of the catalyst implies a lowering of the barrier and the reaction energies as a consequence of what has been discussed throughout this section. In summary, each lactam is softer and less electrophilic.

The reaction force on the four systems has also been calculated, as shown in Fig. 5c and d. As has been discussed, all the couplings are presenting the same reaction mechanism, showing the same critical points.

The work associated with the reaction profiles, coming from the reaction force plots, are shown in Table 2. As the table

Table 2 Reaction barriers, reaction energies, and works associated with the activation of the reactions. All values are given in kcal mol^{-1}

System	$\Delta E^{\neq}$	ΔE°	W_1	W_2
Non-catalyzed				
C	49.7	13.2	34.0 (68%)	15.7 (32%)
S	51.0	13.4	34.9 (68%)	16.1 (32%)
NH	54.6	16.6	35.9 (66%)	18.7 (34%)
NBoc	58.0	20.6	39.9 (69%)	18.1 (31%)
Catalyzed				
C	44.3	−25.3	36.7 (83%)	7.60 (17%)
S	40.0	−26.7	32.5 (83%)	7.50 (17%)
NH	40.3	−28.9	33.2 (82%)	7.08 (18%)
NBoc	40.8	−15.5	30.6 (75%)	10.2 (25%)

indicates, the structural work determines the reaction barriers. However, they differ in extension in the catalyzed reactions, where the structural rearrangement is around 80% of the barrier. On the other hand, the electronic work in order to achieve the TS in the catalyzed reactions, is half the electronic work associated to the non-catalyzed barriers. This indicates that the electronic influence of the copper catalyst is favoring the nucleophilicity of the lactam, thus lowering the barrier.

4.6. Reaction electronic flux

The reaction electronic flux along the reaction coordinate for both non-catalyzed and catalyzed systems as shown in Fig. 7(a and b) has been calculated. As can be seen, at the non-catalyzed reactions, the reaction starts with a spontaneous reaction electronic flux that peaks at the reactants zone, indicating a strengthening or the formation of a bond. At the TS zone, the reaction electronic flux shows negative values indicating breaking or weakening of the bond. Furthermore, it is zero at the products zone, indicating an equilibrium of the electronic cloud. On the other hand, the catalyzed system has quite a similar behavior, but narrower around the TS zone. It shows a narrower positive flux, a non-spontaneous electronic rearrangement along the TS zone and it finishes at the transition state zone with a spontaneous flux.

4.7. Electronic population analysis

In order to understand these changes, especially local reactivity, the atomic charges (Fig. 6c and d) and the bond orders (Fig. 6e and f) have been plotted. As can be seen at the atomic charges, they change around the transition state with the exception of carbon and nitrogen of the non-catalyzed system, which can indicate the spontaneous change of the flux at this stage of the reaction. Interestingly, when going from the non-catalyzed to the catalyzed system, the copper–aryl-ligand triad acts by lowering the nitrogen charge. It becomes more nucleophilic and more reactive towards iodoaniline, thereby favoring the reaction.

When analyzing the NBO populations displayed in Fig. 6(e and f), it was noted that the mechanism of the nucleophilic substitution is concerted with a 4-member TS on the non-catalyzed reactions, where N and C are very close together and demonstrates a hydrogen bond with iodine. On the other hand, the catalyzed reaction shows there is a 4-member TS which involves an attractive interaction of the copper and the ligand towards the iodine and the N and C that will form the N–C bond and the condensation product. From the population analysis, at the TS zone almost all the bonds changed to give the final product the non-catalyzed reaction. Only the HI bond was weakly formed and weakly bonded at the products zone, as shown by the NBO populations. With the catalyzed systems, the bond orders changed only along a narrow TS zone, moreover in a synchronized way. After this addition, the reaction products recovered a weakly Cu–I complex as a product, dissociating from the reaction products at the product zone.

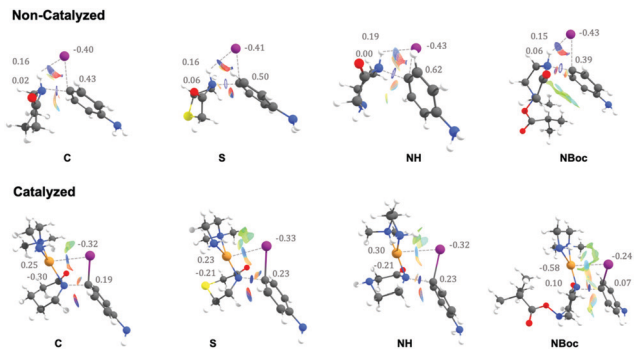

Fig. 7 Non-covalent interactions (NCI) plots on the eight transition states. Red indicates steric repulsions, blue electrostatic and green, van der Waals interactions.

4.8. Non-covalent interactions

Fig. 7 displays the non-covalent interactions (NCI) of the series of eight transition states. First, it can be seen that all of them represent a nucleophilic substitution, whether they are catalyzed or not. The differences were seen by the electronic indexes and by this interaction analysis. For the non-catalyzed reaction, the NCI[29] index and the atomic distances show that the N–C bond is weakly formed at the TS. In addition, the interactions between the rings are mostly repulsive (red basins), indicating that the systems have to overcome this repulsion in order to form the products, contributing to high barriers. With the catalyzed reactions, there are more attractive interactions such as electrostatic (blue) especially with copper and iodine, and with carbon and nitrogen. They are close enough to create an attractive interaction to form the bond, indicating that the Cu–aryl ligand addition assists the system with increasing the electrostatic interactions. In addition, the van der Waals interactions which favor the NH and NBoc systems, lower the barrier thereby allowing all the reactions to occur in the presence of a catalyst.

5. Conclusions

Ullman-like reactions of DFT/wB97XD/6-311g and LanL2DZ for heavy atoms such as iodine substituted lactam arylations with 4-iodobenzene have been studied. The objective was to examine the intrinsic reactivity of previously studied unsubstituted (C), sulphur (S) along with amino (NH) and *t*-Butyloxycarbonyl (NBoc) systems. This was done in order to predict their behavior, and to analyze their reaction mechanism with and without the

use of a copper catalyst, and then to be able to apply this knowledge to the design of the synthesis of new arylations.

Intrinsic global reactivity using μ, η and ω, have been studied. This indicated that when adding the catalysts, all the lactams become more reactive, they increase the electron transfer, decrease the hardness and make the systems more nucleophilic. The catalyst makes no difference on reactivity among all the substituted systems. However, S and NH substituted lactams behave as good candidates for synthesis.

When analyzing the electrostatic potential, it has been observed that the nitrogen reactivity towards an electrophile is increased when using the catalyst. The copper complex binds itself to the nitrogen, enhancing its negative charge, thus augmenting its electrostatic potential specially at S and NH systems.

IRC calculations were also performed showing that the reaction mechanism proceeds by a concerted nucleophilic aromatic substitution, where the lowest energies and barriers are presented at S and NH amides. The use of the catalyst lowers the energy and barriers in all systems, reflected by a lower electronic activation work. This activation is produced by the decrease of the lactam nitrogen charge. The higher electrostatic and van der Waals interactions were induced by the copper catalyst at the transition state.

Conflicts of interest

There are no conflicts to declare.

Acknowledgements

BH thanks FONDECYT 1170837. FZ is grateful to FONDECYT 1181408. NN-N and RD are thankful to Pontificia Universidad Católica de Chile for the Beca VRI-UC (2017) and NN-N also thanks CONICYT-PCHA/Doctorado Nacional/2018-21181735. We also want to thank Ruth A Clyndes for the English version of this manuscript, and the referees for their kind advice.

References

1 E. A. Lewis, M. D. Marcinkowski, C. J. Murphy, M. L. Liriano, A. J. Therrien, A. Pronschinske and E. C. H. Sykes, *Chem. Commun.*, 2017, **53**, 7816–7819.
2 N. Núñez-Navarro, G. Segovia, R. Burgos, C. Lagos, N. Fuentes-Ibacache, M. Faúndez and F. Zacconi, *J. Braz. Chem. Soc.*, 2016, **28**, 203–207.
3 C. Sambiagio, S. P. Marsden, A. J. Blacker and P. C. McGowan, *Chem. Soc. Rev.*, 2014, **43**, 3525–3550.
4 G. Clavé, C. Garel, C. Poullain, B.-L. Renard, T. K. Olszewski, B. Lange, M. Shutcha, M.-P. Faucon and C. Grison, *RSC Adv.*, 2016, **6**, 59550–59564.
5 L. M. Huffman and S. S. Stahl, *J. Am. Chem. Soc.*, 2008, **130**, 9196–9197.
6 X. H. Zhang, F. L. Zhang and Z. Y. Geng, *J. Chem. Sci.*, 2010, **122**, 363–369.
7 E. Sperotto, G. P. M. van Klink, G. van Koten and J. G. de Vries, *Dalton Trans.*, 2010, **39**, 10338–10351.
8 K. K. Gurjar and R. K. Sharma, *ChemCatChem*, 2017, **9**, 862–869.
9 S. M. Soria-Castro, D. M. Andrada, D. A. Caminos, J. E. Argüello, M. Robert and A. B. Peñéñory, *J. Org. Chem.*, 2017, **82**, 11464–11473.
10 E. A. Lewis, M. D. Marcinkowski, C. J. Murphy, M. L. Liriano, A. J. Therrien, A. Pronschinske and E. C. H. Sykes, *Chem. Soc. Rev.*, 2017, **53**, 7816–7819.
11 S. M. Soria-Castro, D. M. Andrada, D. A. Caminos, J. E. Argüello, M. Robert and A. B. Peñéñory, *J. Org. Chem.*, 2017, **82**, 11464–11473.
12 G. O. Jones, P. Liu, K. N. Houk and S. L. Buchwald, *J. Am. Chem. Soc.*, 2010, **132**, 6205–6213.
13 G. J. Sherborne, S. Adomeit, R. Menzel, J. Rabeah, A. Brückner, M. R. Fielding, C. E. Willans and B. N. Nguyen, *Chem. Sci.*, 2017, **8**, 7203–7210.
14 R. G. Parr and W. Yang, *Density Functional Theory of Atoms and Molecules*, Oxford University Press, New York, 1989.
15 C. K. Jorgensen, Electronegativy, in *Structure and Bonding: chemical hardness*, ed. K. D. Sen, Berly, Germany, 1987.
16 P. Geerlings, F. De Proft and W. Langenaeker, *Chem. Rev.*, 2003, **103**, 1793.
17 R. G. Parr and R. G. Pearson, *J. Am. Chem. Soc.*, 1983, **105**, 7512–7516.
18 R. G. Parr and W. Yang, *J. Am. Chem. Soc.*, 1984, **106**, 4049–4050.
19 A. Toro-Labbé, S. Gutiérrez-Oliva, M. C. Concha, J. S. Murray and P. Politzer, *J. Chem. Phys.*, 2004, **121**, 4570.
20 B. Herrera and A. Toro-Labbé, *J. Chem. Phys.*, 2004, **121**, 7096–7102.
21 P. Politzer, A. Toro-Labbé, S. Gutiérrez-Oliva, B. Herrera, P. Jaque, M. C. Concha and J. S. Murray, *J. Chem. Sci.*, 2005, **117**, 467–472.
22 S. Gutiérrez-Oliva, B. Herrera, A. Toro-Labbé and H. Chermette, *J. Phys. Chem. A*, 2005, **109**, 1748–1751.
23 P. Politzer, J. V. Burda, M. C. Concha, P. Lane and J. S. Murray, *J. Phys. Chem. A*, 2006, **110**, 756–761.
24 B. Herrera and A. Toro-Labbé, *J. Phys. Chem. A*, 2007, **111**, 5921–5926.
25 A. Toro-Labbé, S. Gutiérrez-Oliva, J. S. Murray and P. Politzer, *J. Mol. Model.*, 2009, **15**, 707–710.
26 B. Herrera, *J. Mol. Model.*, 2011, **17**, 1051–1060.
27 A. Toro-Labbé, *J. Phys. Chem. A*, 1999, **103**, 4398–4403.
28 M. L. Cerón, E. Echegaray, S. Gutierrez-Oliva and B. Herrera, *Sci. China: Chem.*, 2011, **54**, 1982.
29 C. Morell, V. Tognetti, E. Bignon, E. Dumont, N. Hernandez-Haro, B. Herrera, A. Grand, S. Gutiérrez-Oliva, L. Joubert, A. Toro-Labbé and H. Chermette, *Theor. Chem. Acc.*, 2015, **134**, 133.
30 R. A. Boto, J. Contreras-García, J. Tierny and J.-P. Piquemal, *Mol. Phys.*, 2015, **114**, 1406–1414.
31 J. Contreras-García, E. R. Johnson, S. Keinan, R. Chaudret, J.-P. Piquemal, D. N. Beratan and W. Yang, *J. Chem. Theory Comput.*, 2011, **7**, 625–632.
32 E. R. Johnson, S. Keinan, P. Mori-Sánchez, J. Contreras-García, A. J. Cohen and W. Yang, *J. Am. Chem. Soc.*, 2010, **132**, 6498–6506.

33 J.-D. Chai and M. Head-Gordon, *Phys. Chem. Chem. Phys.*, 2008, **10**, 6615–6620.
34 P. J. Hay and W. R. Wadt, *J. Chem. Phys.*, 1998, **82**, 299–310.
35 W. R. Wadt and P. J. Hay, *J. Chem. Phys.*, 1998, **82**, 284–298.
36 P. J. Hay and W. R. Wadt, *J. Chem. Phys.*, 1998, **82**, 270–283.
37 M. J. Frisch, G. W. Trucks, H. B. Schlegel, G. E. Scuseria, H. Frisch, M. J. Trucks, G. W. Schlegel, H. B. Scuseria, G. E. Robb, M. A. Cheeseman, J. R. Scalmani, G. Barone, V. Mennucci, B. Petersson, G. A. Nakatsuji, H. Caricato, M. Li, X. Hratchian, H. P. Izmaylov, A. F. Bloino, J. Zheng, G. Sonnenberg, J. L. Hada, M. Ehara, M. Toyota, K. Fukuda, R. Hasegawa, J. Ishida, M. Nakajima, T. Honda, Y. Kitao, O. Nakai, H. Vreven, T. J. Montgomery, J. A. Peralta, J. E. Ogliaro, F. Bearpark, M. Heyd, J. J. Brothers, E. Kudin, K. N. Staroverov, V. N. Kobayashi, R. Normand, J. Raghavachari, K. Rendell, A. Burant, J. C. Iyengar, S. S. Tomasi, J. Cossi, M. Rega, N. Millam, J. M. Klene, M. Knox, J. E. Cross, J. B. Bakken, V. Adamo, C. Jaramillo, J. Gomperts, R. Stratmann, R. E. Yazyev, O. Austin, A. J. Cammi, R. Pomelli, C. Ochterski, J. W. Martin, R. L. Morokuma, K. Zakrzewski, V. G. Voth, G. A. Salvador, P. Dannenberg, J. J. Dapprich, S. Daniels, A. D. Farkas, Ö. Foresman, J. B. Ortiz, J. V. Cioslowski and J. Fox, *Gaussian 09*, Gaussian Inc., Wallingford, CT, 1st edn, 2009.
38 K. Fukui, *J. Phys. Chem.*, 1970, **74**, 4161–4163.
39 R. G. Parr, L. Szentpaly and S. Liu, *J. Am. Chem. Soc.*, 1999, **121**, 1922–1924.
40 P. Politzer and J. S. Murray, *Theor. Chem. Acc.*, 2002, **108**, 134–142.
41 G. Knizia, *J. Chem. Theory Comput.*, 2013, **9**, 4834–4843.
42 J. Contreras-García, E. R. Johnson, S. Keinan, R. Chaudret, J.-P. Piquemal, D. N. Beratan and W. Yang, *J. Chem. Theory Comput.*, 2011, **7**, 625–632.
43 R. G. Pearson, *Science*, 1966, **151**, 172–177.
44 R. G. Pearson, *Hard and Soft Acid and Bases*, Dowden, Hutchinson and Ross, Stroudsberg, USA, 1973.

JOC The Journal of Organic Chemistry
Article
Cite This: J. Org. Chem. 2018, 83, 13973−13980
pubs.acs.org/joc

Cyclopropenium Enhanced Thiourea Catalysis

Ivor Smajlagic, Rocio Durán, Melanie Pilkington, and Travis Dudding*

Brock University, 1812 Sir Isaac Brock Way, St. Catharines, Ontario L2S 3A1, Canada

Supporting Information

ABSTRACT: An integral part of modern organocatalysis is the development and application of thiourea catalysts. Here, as part of our program aimed at developing cyclopropenium catalysts, the synthesis of a thiourea-cyclopropenium organocatalyst with both cationic hydrogen-bond donor and electrostatic character is reported. The utility of the this thiourea organocatalyst is showcased in pyranylation reactions employing phenols, primary, secondary, and tertiary alcohols under operationally simple and mild reaction conditions for a broad substrate scope. The addition of benzoic acid as a co-catalyst facilitating cooperative Brønsted acid catalysis was found to be valuable for reactions involving phenols and higher substituted alcohols. Mechanistic investigations, including kinetic and ^{1}H NMR binding studies in conjunction with density function theory calculations, are described that collectively support a Brønsted acid mode of catalysis.

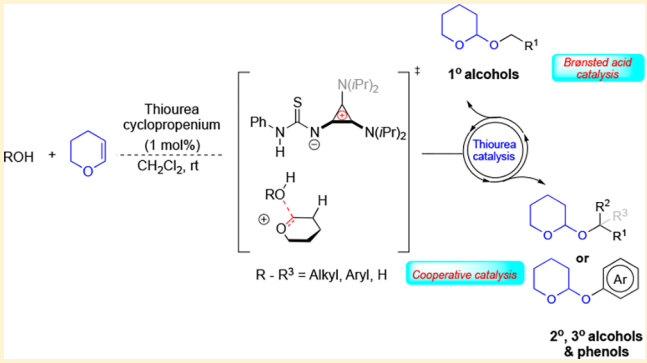

INTRODUCTION

Organocatalyzed processes offering broad chemical scope, chemo-, regio-, and/or stereoselectivity and rapid reaction rates are a major theme of modern-day catalysis.[1,2] On this front, small-molecule hydrogen-bond (H-bond) donors, such as (thio)urea organocatalysts, hold a prominent status owing to their ability to access various modes of H-bond electrophilic activation, in conjunction with other noncovalent interactions (e.g., electrostatic interactions,[3] $\pi-\pi$,[4] cation−π,[5] hydrophobic,[6] and van der Waals forces[7]). Linked to this privileged role, however, has been differing views of their function as organocatalysts. For instance, early perceptions held (thio)urea *Z,Z*-conformations[8] enabling dual H-bond donor activation were vital for promoting catalysis, while in more recent times, the salient catalytic role of other (thio)urea rotomers (e.g., *E,Z* and *Z,E*-conformations) has emerged.

Despite this complexity, (thio)urea-mediated LUMO-lowering activation,[9] ion-pair catalysis,[3a,10] dual H-bond donor/Lewis base catalysis,[11] Brønsted acid catalysis,[8c] and cooperative catalysis[12] among others have been reported. Electrostatically enhanced thiourea catalysis[13] is another recent addition, allowing for enhanced reaction rates, much like that available using well-established cationic H-bond donors, such as amidinium,[14] ammonium,[15] guanidinium,[16] pyridinium,[17] and quinolinium ions.[18]

Given this basis and our established interest in the chemistry of cyclopropenium systems, we sought to develop the cyclopropenium augmented thiourea (**1**) (Figure 1A). Motivating this enterprise was the premise that **1** would exhibit both cationic H-bond donor (*domain A*) and electrostatically enhanced character due to the presence of the cyclopropenium ring (*domain B*), in addition to a Lewis basic sulfur atom that could serve as a H-bond acceptor (*domainC*). A view supported by computed natural bond order (NBO) charges and the electrostatic potential (ESP) surface of envisioned **1** (*Z,Z*-conformer), with positively charged N−H

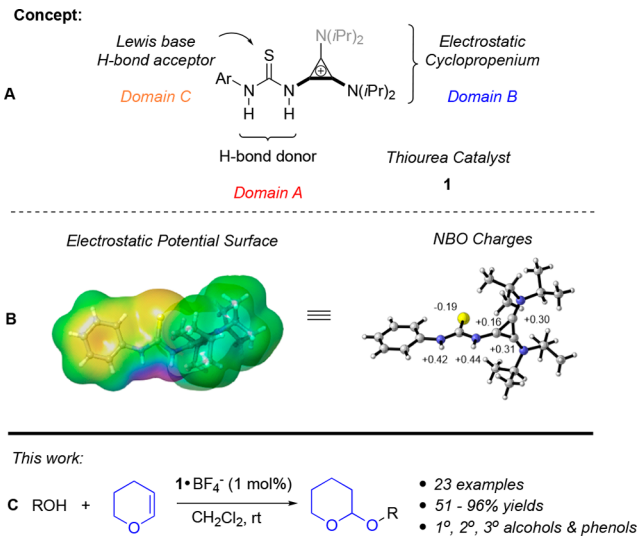

Figure 1. (A) Cyclopropenium as a new charged domain for thiourea catalysts. (B) ESP surface with isodensity value 0.0001 au (left-hand side) and computed NBO charges of select atoms of thiourea **1** at the B3LYP/6-31G+(d,p) level of theory (right-hand side). (C) General conditions for the pyranylation of alcohols and phenols using thiourea catalyst **1**·BF_4^-.

Received: September 7, 2018
Published: October 23, 2018

DOI: 10.1021/acs.joc.8b02321
J. Org. Chem. 2018, 83, 13973−13980

hydrogens and cyclopropenium ring carbon atoms (Figure 1B). Exploring this concept further, we report herein the first cyclopropenium thiourea and its application as a Brønsted acid catalyst for the synthetically important pyranylation of alcohols and phenols (Figure 1C).

■ RESULTS AND DISCUSSION

At the outset of this study, the synthesis of our envisioned thiourea was investigated, ultimately leading to a short preparative route involving the treatment of phenyl isothiocyanate with 2,3-bis(diisopropylamino)cyclopropenimine in CH_2Cl_2 affording **1**·BF_4^- in 44% isolated yield (see SI). Subsequent, X-ray diffraction studies on a single crystal of **1**·BF_4^- revealed several interesting features, viz., a *Z*,*Z*-conformation and short intermolecular contacts between the thiourea N−H hydrogen atoms and BF_4^- counterion such that N(4)−H(4)···F(1) = 2.312 Å and N(3)−H(3)···F(2) = 2.003 Å (Figure 2a). Furthermore, the phenyl and thiourea groups

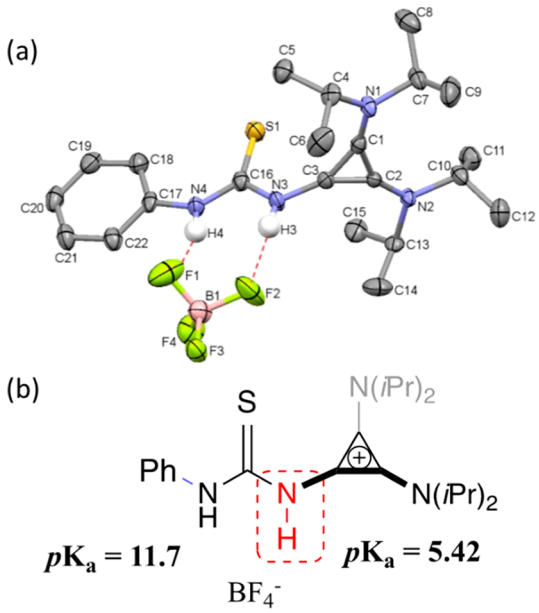

Figure 2. (a) Thermal ellipsoid plot of the molecular structure of **1**·BF_4^- with appropriate labeling scheme. Thermal ellipsoids are plotted at 50%. Only selected H atoms are shown. Short N−H···F contacts are shown as red dashed lines. (b) Two-dimensional representation of **1**·BF_4^- highlighting the computed pK_a values in DMSO.

were coplanar ($\theta_{C(16)-N(4)-C(17)-C(22)}$ = 174.4(4)°), consistent with extended π-conjugation, while in contrast, the orthogonal ($\theta_{C(16)-N(3)-C(3)-C(1)}$ = 87.7(5)°) alignment of the cyclopropenium ring and the thiourea functionality was indicative of poor π-conjugation. Supporting this bonding scenario was a slight lengthening (~0.03 Å) of the N(3)−C(16) bond distance when compared to the N(4)−C(16) distance of 1.352(4) Å. Meanwhile, the computed acidity of the N(3)−H(3) group (pK_a = 5.42 in DMSO) was considerably greater than the N(4)−H(4) group (pK_a = 11.7 in DMSO), presumably as a result of the electrostatically enhanced H-bond donor capacity conferred by the adjacent positively charged cyclopropenium moiety (Figure 2b, see SI for details).

Having insight into the structural and physical properties of thiourea **1**·BF_4^-, we next explored its use as a catalyst for the pyranylation of alcohols (**2**) with dihydropyran (DHP) (**3**). Initial efforts to facilitate the pyranylation of alcohols consisted of using benzyl alcohol (**2a**) and **3** as substrates in dilute conditions (0.5 mM in alcohol and 1.0 mM in dihydropyran), which led to poor conversion rates even after 12 h (Table 1,

Table 1. Optimization of Reaction Conditions

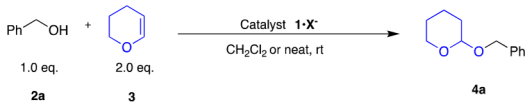

entry	catalyst	loading (mol %)	conversion[d] 1 h	6 h	12 h
1	**1**·BF_4^-[a]	1	3%	6%	11%
2	**1**·BF_4^-[a]	10	13%	20%	28%
3	**1**·BF_4^-[b]	1	35%	100%	100%
4	**1**·BF_4^-[b]	10	24%	100%	100%
5	**1**·BF_4^-[c]	1	28%	100%	100%
6	**1**·BF_4^-[c]	10	30%	100%	100%
7	**1**·Cl^-[b]	1	0%	0%	0%
8	**1**·Cl^-[b]	10	28%	50%	100%

[a]Reactions were performed at room temperature using the following conditions: 0.5 mmol **2a**, 1.0 mmol **3** and 1.0 mL DCM. [b]0.5 mmol **2a**, 1.0 mmol **3** and 0.5 mL DCM. [c]1.0 mmol **2a**, 2.0 mmol **3** under neat conditions. [d]Conversion was determined via ^{1}H NMR spectroscopic analysis of the crude reaction mixtures. This involved monitoring the disappearance of the signal at 6.37 ppm for (**3**) and appearance of the signal at 4.51 ppm for the THP protected product (**4a**).

entries 1 and 2). A phenomenon presumably resulting from the lack of interactions between the substrates and the catalyst, which speaks to the molecularity of the reaction. To circumvent this issue, we subjected the substrates of interest and catalyst to different reaction conditions that were more optimal involving low catalyst loading (1 mol %) and more concentrated reaction conditions (1.0 mM in alcohol and 2.0 mM in dihydropyran), affording full conversion of **4a** in 3 h (Table 1, entry 3). Furthermore, these conditions were then applied using reported electrostatically enhanced thiourea, 1-methyl-3-(3-phenylthioureido)pyridinium iodide[13] (1 mol %), which resulted in no conversion after 6 h. Next, the use of solvent-free conditions and a 1:2 reagent stoichiometry provided a similar reaction outcome, though a slightly longer reaction time was required (Table 1, entry 5). Notably, there was a 3-fold rate acceleration in comparison to Schreiner's reported thiourea pyranylation of **2a** under the same solvent-free reaction conditions.[19] Also, apparent from the optimization studies was the observation of catalyst inhibition in the presence of a chloride counterion (Table 1, entries 7 and 8), attributed to tight anion binding in solution[3a,10] as supported by a downfield shift of the N−H hydrogen atoms of thiourea **1**·Cl^- vs **1**·BF_4^- (^{1}H NMR ($CDCl_3$) $\Delta\delta NH_4$ = 2.59 ppm and $\Delta\delta NH_3$ = 2.84 ppm), (see SI).

With the optimal conditions identified, **1**·BF_4^- was applied to the reaction of various alkyl- and aryl-substituted primary alcohols (Table 2). For example, functionalized benzyl alcohols (**2a**−**g**) provided high yields in short reaction times, for example, *p*-methyl-substituted **2b** provided a 93% yield of product **4b** in 4 h. Likewise, methylene acetal protected substrate **2c** afforded the pyranyl product **4c** in 90% yield after 3 h, while the electron-rich *p*-methoxy- and 3,5-dimethoxy-substituted benzyl alcohols (**2d** and **2e**) provided products **4d** and **4e** in high yields after slightly longer reaction times.

DOI: 10.1021/acs.joc.8b02321
J. Org. Chem. 2018, 83, 13973−13980

Table 2. Pyranylation of Primary Alcohols

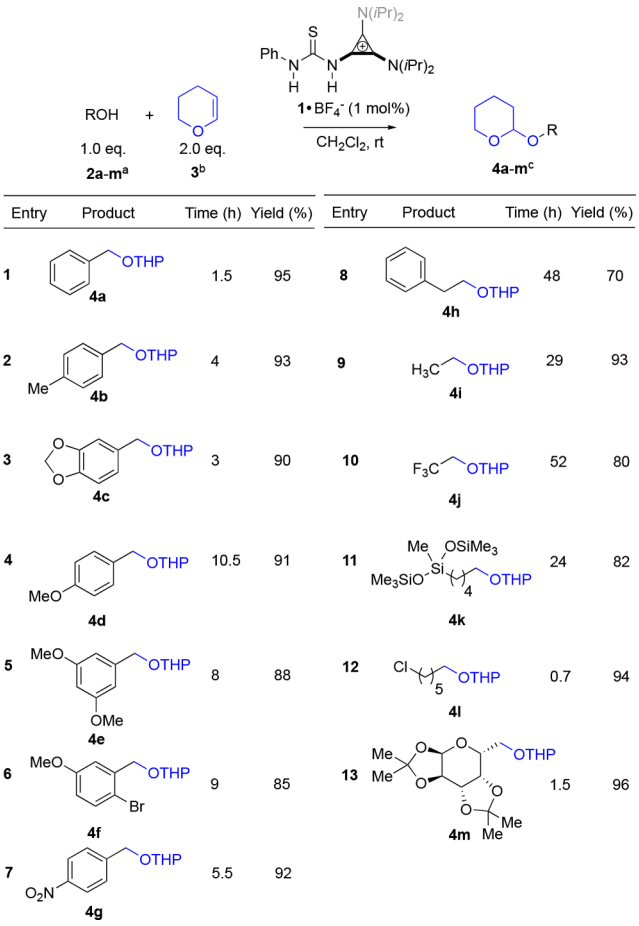

[a]5.0 mmol of respective alcohols. [b]10.0 mmol 3,4-dihydro-2*H*-pyran. [c]The reaction was performed in 5.0 mL DCM at room temperature under an inert atmosphere. The yields provided are reported as isolated yields after flash chromatography. There was no conversion witnessed in the absence of **1**·BF_4^-.

Furthermore, compound **2f** with an inductively withdrawing *m*-methoxy group and sterically demanding *o*-bromo substituent afforded the pyranyl product **4f** in 85% yield. Benzyl alcohol substrate **2g** bearing an electron-deficient *p*-nitro group afforded product **4g** in 92% yield after 5.5 h. The reaction of 3-phenyl-1-propanol (**2h**), furnished product **4h** in 70% yield after 48 h. In the case of the latter, the attenuated reactivity compared to benzyl alcohols may be ascribed to the loss of noncovalent interactions that include π−π-(aryl−aryl) stacking phenomena that subsequently impart transition-state stabilization, though this does not rule out other possible modes of action that may account for this observed reactivity. Similarly, ethanol (**2i**) and electron-poor trifluoroethanol (**2j**) reacted sluggishly, albeit, in high isolated yields. Conversely, primary alcohols bearing extended functionalized aliphatic side chains (**2k** and **2l**) afforded the desired products (Table 2, entries 11 and 12, **4k** and **4l**) in good to excellent yields. Extending our catalytic methodology to sugar analogues, we reacted substrate **2m** that furnished the pyranyl product **4m** in 96% yield after 1.5 h.

The reaction of secondary alcohols was then probed using α-methyl benzyl alcohol (**5a**) as the substrate together with **3** under our optimized conditions (vide supra), which raised immediate concerns as product **8a** was produced in a low yield after 24 h. Nevertheless, the addition of benzoic acid (**7**) as a co-catalyst (10 mol %) remedied this lack of reactivity as conferred by a 93% yield of the sterically congested pyranyl product **8a** after 5.5 h (Table 3). Employing these modified

Table 3. Pyranylation of Higher Substituted Alcohols and Phenols

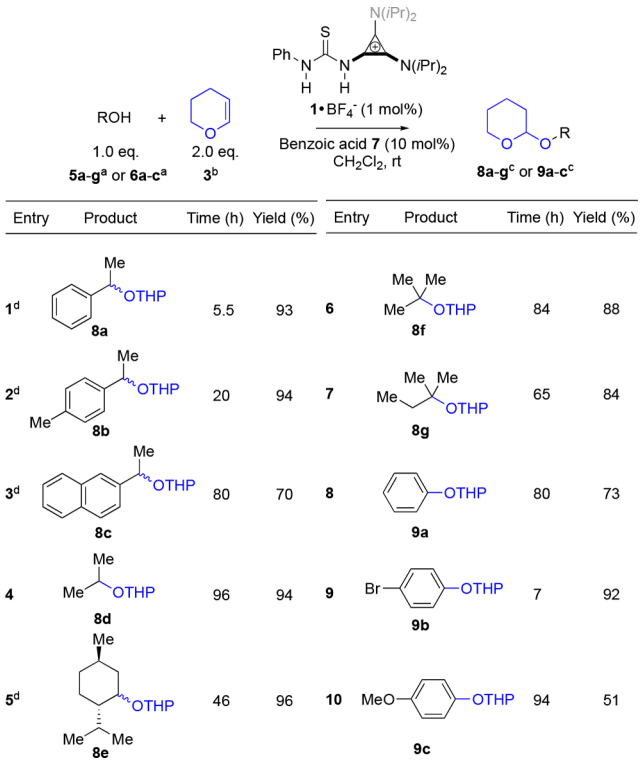

[a]5.0 mmol of respective alcohols or phenols (ROH). [b]10.0 mmol 3,4-dihydro-2*H*-pyran. [c]The reaction was performed in 5.0 mL DCM at room temperature under an inert atmosphere. The yields provided are reported as isolated yields after flash chromatography. There was no conversion witnessed in the absence of **1**·BF_4^- with or without benzoic acid. [d]The diastereomeric ratio (dr) of compounds **8a**−**c** and **8e** is 1:1.

conditions, α-methyl benzyl/naphthyl alcohols were also reacted with **3** to afford products **8b** and **8c** in good to excellent yields. The use of sterically hindered aliphatic substrates such as isopropanol and menthol likewise afforded products **8d** and **8e** in high yields. The extension of our methodology to the reactions of tertiary alcohols also resulted in good yields of the desired products >80%. Finally, the reactivity of phenols was explored using substrates **6a**−**c**, all of which gave the desired pyranyl products (Table 3, entries 8−10, **9a**−**c**) in moderate to excellent yields.

To probe the mechanism of these reactions, a solution of catalyst **1**·BF_4^- (1 equiv) was monitored by ^{1}H NMR as aliquots of benzyl alcohol (1−10 equiv) were added. This experiment resulted in a pronounced downfield shift of the alcohol O−H signal that we attribute to the presence of a hydrogen-bonding interaction between the thiocarbonyl sulfur atom and the alcohol, which based on DFT calculations was computed be a favorable process (ΔE_{int} = −21.5 kcal/mol) linked to $S_{LP} \rightarrow \sigma_{(O-H)}^*$ donor−acceptor interactions (E_{NBO} = 4.94 kcal/mol) (see SI). The conspicuous lack of a change in the thiourea N−H signal, though unexpected, suggests the

DOI: 10.1021/acs.joc.8b02321
J. Org. Chem. 2018, 83, 13973−13980

presence of weak or nonexistent interactions between the alcohol oxygen atom and the thiourea N−H hydrogens. Further kinetic studies revealed a first-order dependency with respect to both alcohol and dihydropyran (see SI for details). Lastly, we performed additional ^{1}H NMR titration experiments to better understand the role of the co-catalyst (**7**) in the reactions of phenols, secondary and tertiary alcohols. Upon titration of **7** (1−2 equiv), we observed that the thiourea N−H signals were participating in rapid proton exchange events with benzoic acid on the NMR time scale, thus providing evidence for the formation of a thiourea-benzoic acid complex as further supported by variable-temperature NMR studies (see SI for details). This is consistent with previous reports of Brønsted acids enhancing the catalytic activity of thioureas through a concept formally referred to as cooperative catalysis.[12]

Based on the above findings, the putative catalytic cycle for thiourea **1** pyranylation of primary alcohols is offered in Figure 3. A pre-equilibrium establishing metastable catalyst-substrate

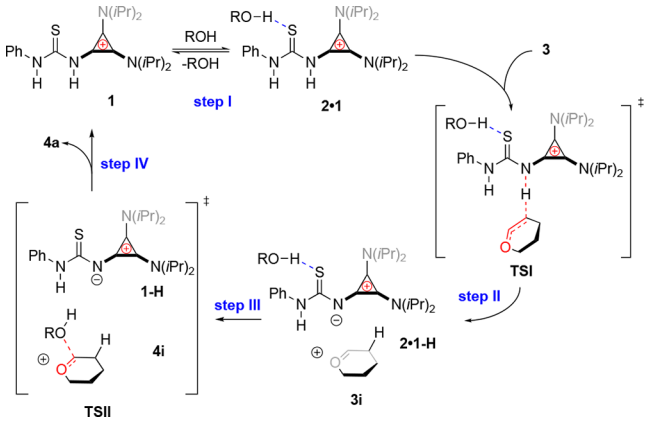

Figure 3. Mechanistic proposal for the thiourea-catalyzed (**1**) pyranylation of primary alcohols.

H-bond complex **2·1** (step I) initiates the cycle. Subsequent reaction of dihydropyran (**3**) via proton-transfer transition state **TS1** (step II) then provides oxocarbenium intermediate **3i** and **2·1-H**, corresponding to a tight or loose ion pair (solvent-separated vs solvent-shared). Addition of alcohol then results in the formation of transient oxonium species **4i** by transition state **TSII** (step III). Deprotonation of the latter by in situ derived thiourea conjugate base **1-H** then provides the pyranyl product **4a** concomitant with regeneration of catalyst **1** (step IV). As for the role of the co-catalyst in these reactions, efforts to clarify its function and more generally the reactivity in these thiourea catalyzed processes are still ongoing in our laboratory.

■ CONCLUSION

In summary, a unique thiourea-cyclopropenium organocatalyst with dual cationic H-bond donor and electrostatic character has been reported. As a proof-of-principle application, the utility of this thiourea was demonstrated in synthetically relevant pyranylation transformations using various substrates, including challenging tertiary alcohols and phenols. Salient features of this reactivity comprise simplicity, mild reaction conditions, high product yields, and cooperative Brønsted acid catalysis. Mechanistic investigations that include kinetic and ^{1}H NMR binding studies in conjunction with DFT calculations collectively support a Brønsted acid mode of catalysis. In a broader sense, we anticipate that this novel thiourea catalyst and related H-bond donors will find a wide range of future applications. Current efforts in our lab are underway in this respect.

■ EXPERIMENTAL SECTION

Computational Methodology. All the density functional theory (DFT) calculations were performed in the Gaussian 16 program.[20] The hybrid B3LYP[21−23] functional and the dispersion energy corrections by D3[24] version of Grimme's dispersion with the original D3 damping function were used. All the electronic properties were obtained with the 6-311+G(d,2p) basis sets. The solvent effects were taken into account using the self-consistent reaction field (SCRF) method grounded from the solvation model based on density (SMD).[25] The pK_a calculation was performed using equation pK_a = $\Delta G^*_{aq}/2.303\,RT$, where ΔG^*_{aq} was calculated directly from the aqueous Gibbs free energies of the acid and conjugate base in dimethyl sulfoxide (DMSO ε = 46.7), using the solvation corrections to construct the solute cavity made by Peng L. et al.[26] The interaction energy (E_{int}) was calculated using the B3LYP/6-311+G(d,2p) level of theory in chloroform ($CHCl_3$, ε = 4.81) (SMD model) using the following equation: $E_{int} = E_{alcohol\text{-}thiourea} - E_{alcohol} - E_{thiourea}$, which corresponds to the difference between the total energy of the supermolecular system (i.e., alcohol-thiourea) and the total energy of its fragments (i.e., alcohol and thiourea isolated). This property is used to determine the stability of an interaction. A negative value indicates that the molecular system is more energetically stable with respect to the isolated fragments, and thus the interaction is favorable. Conversely, if E_{int} is positive, it indicates that the isolated fragments are more stable than in the supermolecule, and therefore the interaction does not favor an increase in stability. Visualization and generation of molecular structures were performed with Chemcraft[27] graphical user interface software.

Materials and Methods. All materials were obtained from commercially available suppliers and used as received unless otherwise stated. The solvents employed in the reactions were all dried using the following methods: dichloromethane and acetonitrile were distilled from CaH_2, and tetrahydrofuran was distilled from sodium/benzophenone. All reactions were conducted in oven-dried round-bottom flasks under an inert atmosphere (N_2) and monitored by thin-layer chromatography (TLC) using silica gel 60 F254 EMD Merck while visualized with a hand-held UV lamp. Flash column chromatography was performed over Silicycle ultrapure silica gel (230−400 mesh). NMR spectra were recorded on a Bruker DPX-300 spectrometer (^{1}H 300 MHz, ^{13}C 75.5 MHz, ^{19}F 292.4 MHz, ^{11}B 96.3 MHz) and Bruker Avance AV I 600 spectrometer (^{1}H 600 MHz) in $CDCl_3$. The observed chemical shifts are reported as δ-values (ppm) relative to tetramethylsilane (TMS). Mass spectra were obtained on an MSI/Kratos concept IS mass spectrometer. Tetrachlorocyclopropene[28,29] (**S1**), 1,2:3,4-di-*O*-isopropylidene-α-D-galactopyranose,[30] and 1-methyl-3-(3-phenylthioureido)pyridinium iodide[13] were prepared according to literature procedures and the spectra match accordingly.

*Chloro[Bis(diisopropylamino)]cyclopropenium (**S2**)·BF_4^-.*[31] To a stirred solution of tetrachlorocyclopropene (**S1**) (1.0 g, 5.62 mmol, 1.00 equiv) in DCM (12.0 mL) at 0 °C was added diisopropylamine (4.0 mL, 28.1 mmol, 5.00 equiv) dropwise. The solution stirred for 6 h while gradually warming to room temperature. Next, $NaBF_4$ (0.80 g, 7.31 mmol, 1.30 equiv) was added in one portion, and the resulting mixture stirred overnight. The solution was then extracted with water (5 × 35.0 mL), dried over $MgSO_4$, and concentrated in vacuo to afford an orange solid. The crude material was then dissolved in DCM (5.0 mL), purified with diethyl ether (Et_2O) ((15.0 mL washes), 3×), and dried under high vacuum to obtain a white powder (1.51g, 76%). ^{1}H NMR (300 MHz, $CDCl_3$, 25 °C): δ = 1.41−1.43 (d, J = 6.78 Hz; 24H), 3.81−3.94 (m, 2H), 4.01−4.21 (m, 2H).

*2,3-Bis(diisopropylamino)cyclopropenimine (**S3**)·BF_4^-.* Ammonia gas (excess) was vigorously bubbled through a solution of (**S2**) (1.51 g, 4.21 mmol, 1.00 equiv) in DCM (16.0 mL) at 0 °C for 1 h. The

DOI: 10.1021/acs.joc.8b02321
J. Org. Chem. 2018, 83, 13973−13980

solution was maintained at a temperature of ∼0 °C for the entire duration. After 15 min, a white precipitate began to crash out indicating product formation. After completion of the reaction, as observed by TLC, the salt was filtered off, and the filtrate collected. The filtrate was then concentrated and washed with diethyl ether to further purify (**S3**) (3 × 10.0 mL washed) affording a beige solid (1.36 g, 95%). Mp: 142−144 °C; ^{1}H NMR (300 MHz, $CDCl_3$, 25 °C): δ = 1.30−1.32 (d, J = 6.78 Hz; 24 H), 3.71−3.84 (m, 4 H), 6.08 (s, 2H); $^{13}C\{^1H\}$ NMR (75.5 MHz, $CDCl_3$, 25 °C): δ = 22.3, 50.8, 113.9, 114.7; ^{19}F NMR (292.4 MHz, $CDCl_3$, 25 °C) δ = −151.7; ^{11}B NMR (96.3 MHz, $CDCl_3$, 25 °C) δ = −1.0; HRMS (FAB) m/z: $[M - BF_4]^+$ calcd for $C_{15}H_{30}N_3^+$, 252.2434; found: 252.2435.

2,3-Bis(diisopropylamino)cyclopropenimine (S4).[32] Compound (**S3**) (1.36 g, 4.01 mmol, 1.00 equiv) was dissolved in DCM (15.00 mL), and the resulting solution was washed with 3 M NaOH (3 × 80.0 equiv), dried over $MgSO_4$, and concentrated in vacuo affording an off-white solid (0.86 g, 80−85%). ^{1}H NMR (300 MHz, $CDCl_3$, 25 °C): δ = 1.16−1.18 (d, J = 6.60 Hz; 24 H), 3.53−3.67 (m, 4 H).

N-(2,3-Bis(diisopropylamino)cyclopropenium)-N′-phenyl-thiourea (1)·Cl⁻. A solution of phenyl isothiocyanate (**S5**) (0.92 g, 6.82 mmol, 2.0 equiv) in DCM (3.00 mL) was added dropwise to a solution of (**S4**) (0.86 g, 3.41 mmol, 1.0 equiv) in DCM (6.00 mL) at room temperature. After 1 h, the reaction was extracted with 3 M HCl until disappearance of **S4**, as visualized via TLC. The combined organic layers were dried over $MgSO_4$ and concentrated. The resulting residue was then washed with diethyl ether (3 × 15.0 mL) to afford a yellow solid (0.71 g, 49%). Mp: 159−161 °C; ^{1}H NMR (300 MHz, $CDCl_3$, 25 °C): δ = 1.42−1.44 (d, J = 6.63 Hz; 24 H), 4.14−4.18 (m, 4 H), 7.16−7.20 (t, J = 7.32 Hz; 1H), 7.33−7.38 (t, J = 7.62 Hz; 2H), 7.86−7.89 (d, J = 7.92 Hz; 2H), 11.8 (s, 1H), 12.1 (s, 1H); $^{13}C\{^1H\}$ NMR (75.5 MHz, $CDCl_3$, 25 °C): δ = 22.1, 51.6, 107.4, 123.1, 125.0−125.5 (d, J = 32.4 Hz), 128.4, 138.7, 178.8; HRMS (FAB) m/z: $[M - Cl]^+$ calcd for $C_{22}H_{35}N_4S^+$, 387.2566; found: 387.2570.

N-(2,3-Bis(diisopropylamino)cyclopropeniminyl)-N′-phenyl-thione (S6). Thiourea **1**·Cl⁻ (0.71 g, 1.67 mmol) was dissolved in DCM (10.00 mL) and washed with saturated bicarbonate (1 × 30.0 mL), dried over $MgSO_4$, and solvent evaporated resulting in a chartreuse solid (0.62 g, 96%). Mp: 165−167 °C; ^{1}H NMR (300 MHz, $CDCl_3$, 25 °C): δ = 1.34−1.36 (d, J = 6.60 Hz; 24H), 4.01- 4.10 (m, 4H), 6.91−6.95 (t, J = 7.2 Hz; 1H), 7.20−7.25 (t, J = 7.50 Hz; 2H), 7.56−7.59 (d, J = 7.8 Hz; 2H), 7.69 (s, 1H); $^{13}C\{^1H\}$ NMR (75.5 MHz, $CDCl_3$, 25 °C): δ = 22.0, 50.4, 119.5, 121.5−121.6 (d, J = 6.27 Hz), 124.0, 128.4, 141.0, 178.5; HRMS (EI) m/z: $[M + H]^+$ calcd for $C_{22}H_{34}N_4S$, 386.2504; found: 386.2495.

N-(2,3-Bis(diisopropylamino)cyclopropenium)-N′-phenyl-thiourea (1)·BF₄⁻. Compound **S6** (0.62 g, 1.60 mmol) was dissolved in DCM (10.00 mL) and washed with a 3 M solution of 50% $HBF_{4(aq)}$ (1 × 30.0 mL), dried over $MgSO_4$, and concentrated in vacuo to afford a viscous green oil. The oil was then triturated with diethyl ether (1 × 15.0 mL) to furnish thiourea **1**·BF_4^- as a lime-green solid (0.71 g, 93%). Mp: 121−123 °C; ^{1}H NMR (300 MHz, $CDCl_3$, 25 °C): δ = 1.38−1.40 (d, J = 6.60 Hz; 24H), 4.02−4.15 (m, 4H), 7.18−7.23 (t, J = 7.50 Hz; 1H), 7.34−7.40 (t, J = 7.50 Hz; 2H), 7.75−7.78 (d, J = 8.1 Hz; 2H), 8.96 (s, 1H), 9.51 (s, 1H); $^{13}C\{^1H\}$ NMR (75.5 MHz, $CDCl_3$, 25 °C): δ = 21.8, 51.9, 106.1, 123.5, 126.1−126.4 (d, J = 23.2 Hz), 128.6, 138.2, 178.0; ^{19}F NMR (292.4 MHz, $CDCl_3$, 25 °C) δ = −149.2; ^{11}B NMR (96.3 MHz, $CDCl_3$, 25 °C) δ = −0.8.

Representative Procedure for the Thiourea-Catalyzed Pyranylation of Primary Alcohols. To an oven-dried 25.0 mL round-bottom flask charged with thiourea **1**·BF_4^- (24 mg, 1 mol %), primary alcohols (5.0 mmol) and 3,4-dihydro-2*H*-pyran (10.0 mmol) were combined and subsequently diluted in dichloromethane (5.0 mL). The resulting solution was stirred at room temperature under an inert atmosphere. Reaction progress was monitored via TLC. After removal of the solvent, the crude material was subjected to flash chromatography using a hexanes/ethyl acetate solvent system to yield the THP protected alcohol.

Characterization Data of the Products (4a−m). NMR Data Are Consistent with the Literature. *2-(Benzyloxy)-tetrahydropyran (4a).*[33] (0.91 g, 95%), clear oil. ^{1}H NMR (300 MHz, $CDCl_3$, 25 °C): δ = 1.53−2.00 (m, 6H), 3.56−3.63 (m, 1H), 3.94−4.02 (m, 1H), 4.53−4.58 (d, J = 12.1 Hz; 1H), 4.75−4.78 (t, J = 3.48 Hz; 1H), 4.83−4.87 (d, J = 12.1 Hz; 1H), 7.29−7.44 (m, 5H).

2-(4-Methylbenzyloxy)tetrahydropyran (4b).[34] (0.92 g, 89%), clear oil. ^{1}H NMR (300 MHz, $CDCl_3$, 25 °C): δ = 1.52−1.96 (m, 6H), 2.37 (s, 3H), 3.54−3.61 (m, 1H), 3.92−4.00 (m, 1H), 4.48−4.51 (d, J = 11.8 Hz; 1H), 4.71−4.74 (t, J = 3.51 Hz; 1H), 4.76−4.80 (d, J = 11.8 Hz; 1H), 7.17−7.20 (d, J = 7.89 Hz; 2H), 7.28−7.30 (d, J = 7.95 Hz; 2H).

5-(Tetrahydro-2H-pyran-2-yloxy)methylbenzo[d][1,3]dioxole (4c).[35] (1.06 g, 90%), clear oil. ^{1}H NMR (300 MHz, $CDCl_3$, 25 °C): δ = 1.49−1.92 (m, 6H), 3.53−3.60 (m, 1H), 3.88−3.97 (m, 1H), 4.40−4.44 (d, J = 11.7 Hz; 1H), 4.68−4.72 (overlapping signals, 2H), 5.96 (s, 2H), 6.77−6.82 (m, 2H), 6.85−6.90 (m, 1H).

2-(4-Methoxybenzyloxy)tetrahydropyran (4d).[36] (1.01 g, 91%), clear oil. ^{1}H NMR (300 MHz, $CDCl_3$, 25 °C): δ = 1.49−1.95 (m, 6H), 3.53−3.60 (m, 1H), 3.83 (s, 3H), 3.91−3.99 (m, 1H), 4.44−4.48 (d, J = 11.6 Hz; 1H), 4.70−4.72 (t, J = 3.54 Hz; 1H), 4.72−4.76 (d, J = 15.8 Hz; 1H), 6.88−6.93 (d, J = 11.6 Hz; 2H), 7.30−7.33 (d, J = 8.64 Hz; 2H).

2-(3,5-Dimethoxybenzyloxy)tetrahydropyran (4e). (1.11 g, 88%), clear oil. ^{1}H NMR (300 MHz, $CDCl_3$, 25 °C): δ = 1.53−1.97 (m, 6H), 3.53−3.60 (m, 1H), 3.81 (s, 6H), 3.89−3.98 (m, 1H), 4.46−4.50 (d, J = 12.3 Hz; 1H), 4.71−4.73 (t, J = 3.60 Hz; 1H), 4.73−4.77 (d, J = 15.3 Hz; 1H), 6.40−6.41 (t, J = 2.22 Hz; 1H), 6.55−6.56 (d, J = 2.20 Hz; 2H); $^{13}C\{^1H\}$ NMR (75.5 MHz, $CDCl_3$, 25 °C): δ = 19.4, 25.5, 30.6, 55.3, 62.2, 68.7, 97.7, 99.5, 105.5, 140.7, 160.8; HRMS (EI) m/z: $[M + H]^+$ calcd for $C_{14}H_{20}O_4$, 252.1362; found: 252.1358.

2-(2-Bromo-5-methoxybenzyloxy)tetrahydropyran (4f).[37] (1.28 g, 85%), clear oil. ^{1}H NMR (300 MHz, $CDCl_3$, 25 °C): δ = 1.52−2.00 (m, 6H), 3.56−3.63 (m, 1H), 3.82 (s, 3H), 3.91−4.00 (m, 1H), 4.54−4.58 (d, J = 13.5 Hz; 1H), 4.78−4.81 (t, J = 3.45 Hz; 1H), 4.80−4.83 (d, J = 9.10 Hz; 1H), 6.70−6.74 (dd, J = 8.7, 3.09 Hz; 1H), 7.12−7.13 (d, J = 3.09 Hz; 1H), 7.42−7.45 (d, J = 8.7 Hz; 1H).

2-(4-Nitrobenzyloxy)tetrahydropyran (4g).[35] (1.09 g, 92%), clear oil. ^{1}H NMR (300 MHz, $CDCl_3$, 25 °C): δ = 1.54−1.97 (m, 6H), 3.54−3.61 (m, 1H), 3.86−3.94 (m, 1H), 4.60−4.64 (d, J = 13.5 Hz; 1H), 4.74−4.76 (t, J = 3.45 Hz; 1H), 4.88−4.92 (d, J = 13.5 Hz; 1H), 7.53−7.56 (d, J = 8.67 Hz; 2H), 8.20−8.23 (d, J = 8.70 Hz; 2H).

2-(2-Phenylethoxy)tetrahydropyran (4h).[38] (0.72 g, 70%), clear oil. ^{1}H NMR (300 MHz, $CDCl_3$, 25 °C): δ = 1.47−1.90 (m, 6H), 2.92−2.96 (t, J = 7.26 Hz; 2H), 3.44−3.51 (m, 1H), 3.60−3.68 (dd, J = 16.9, 7.17 Hz; 1H), 3.75−3.82 (m, 1H), 3.94−4.02 (dd, J = 17.0, 7.35 Hz; 1H), 4.61−4.63 (t, J = 2.88 Hz; 1H), 7.19−7.34 (m, 5H).

2-Ethoxytetrahydropyran (4i). (0.60 g, 93%), clear oil. ^{1}H NMR (300 MHz, $CDCl_3$, 25 °C): δ = 1.20−1.25 (t, J = 7.11 Hz; 3H), 1.47−1.87 (m, 6H), 3.41−3.53 (overlapping signals, 2H), 3.75−3.91 (overlapping signals, 2H), 4.57−4.60 (t, J = 2.76 Hz; 1H); $^{13}C\{^1H\}$ NMR (75.5 MHz, $CDCl_3$, 25 °C): δ = 15.2, 19.8, 25.5, 30.8, 62.4−62.8 (d, J = 31.7 Hz), 98.7; HRMS (EI) m/z: $[M + H]^+$ calcd for $C_7H_{14}O_2$, 130.0994; found: 130.0985.

2-(2,2,2-Trifluoroethoxy)tetrahydropyran (4j).[39] (0.74 g, 80%), clear oil. ^{1}H NMR (300 MHz, $CDCl_3$, 25 °C): δ = 1.55−1.93 (m, 6H), 3.51−3.61 (m, 1H), 3.80−3.81 (m, 1H), 3.84−3.96 (dq, J = 8.70 Hz; 1H), 3.99−4.10 (dq, J = 12.3 Hz; 1H), 4.76−4.78 (t, J = 3.15 Hz; 1H).

2-(5-(1,1,1,3,5,5,5-Heptamethyltrisiloxan-3-yl)-pentoxy)-tetrahydropyran (4k). (1.61 g, 82%), clear oil. ^{1}H NMR (300 MHz, $CDCl_3$, 25 °C): δ = 0.011 (s, 3H), 0.100 (s, 18H), 0.457−0.509 (m, 2H), 1.35−1.44 (m, 4H), 1.51−1.96 (m, 8H), 3.36−3.44 (m, 1H), 3.48−3.55 (m, 1H), 3.71−3.80 (m, 1H), 3.85−3.95 (m, 1H), 4.58−4.61 (t, J = 4.29 Hz; 1H); $^{13}C\{^1H\}$ NMR (75.5 MHz, $CDCl_3$, 25 °C): δ = −0.303, 1.84, 17.6, 19.7, 23.0, 25.5, 29.5−29.8 (d, J = 18.4 Hz), 30.8, 62.3, 67.6, 98.8; HRMS (EI) m/z: $[M + H]^+$ calcd for $C_{17}H_{40}O_4Si_3$, 392.2234; found: 392.2224.

6-(Chloro-hexyloxy)tetrahydropyran (4l).[40] (1.04 g, 94%), clear oil. ^{1}H NMR (300 MHz, $CDCl_3$, 25 °C): δ = 1.33−1.65 (m, 10 H), 1.66−1.89 (m, 4H), 3.34−3.41 (m, 1H), 3.45−3.54 (m, 3H), 3.69−3.77 (m, 1H), 3.81−3.89 (m, 1H), 4.55−4.57 (t, J = 2.52 Hz; 1H).

DOI: 10.1021/acs.joc.8b02321
J. Org. Chem. 2018, 83, 13973−13980

2,2,7,7-Tetramethyl-5-(((tetrahydro-2H-pyran-2-yl)oxy)methyl)-tetrahydro-3aH-bis([1,3]dioxolo)[4,5-b:4′,5′-d]pyran (**4m**).[41] (1.63 g, 96%), clear oil. ^{1}H NMR (300 MHz, $CDCl_3$, 25 °C): δ = 1.25 (s, 3H), 1.26 (s, 3H), 1.36 (s, 3H), 1.46 (s, 3H), 1.51−1.85 (m, 6H), 3.38−3.45 (m, 1H), 3.52−3.66 (m, 1H), 3.69−3.85 (m, 2H), 3.91−3.97 (m, 1H), 4.16−4.19 (dd, J = 1.53, 7.95 Hz; 1H), 4.20−4.23 (m, 1H), 4.50−4.60 (m, 2H), 5.43−5.47 (t, J = 6.24 Hz; 1H).

Representative Procedure for the Thiourea-Catalyzed Pyranylation of Higher Substituted Alcohols and Phenols. To an oven-dried 25.0 mL round-bottom flask charged with thiourea **1**·BF_4^- (24 mg, 1 mol %) and benzoic acid (61.0 mg, 10 mol %), alcohols or phenols (5.0 mmol) and 3,4-dihydro-2*H*-pyran (10.0 mmol) were combined and subsequently diluted in dichloromethane (5.0 mL). The resulting solution was stirred at room temperature under an inert atmosphere. Reaction progress was monitored via TLC. After removal of the solvent, the crude material was subjected to flash chromatography using a hexanes/ethyl acetate solvent system to yield the THP protected product.

Characterization Data of the Products (8a−g and 9a−c). NMR. Data Are Consistent with the Literature. *2-(1-Phenylethoxy)-tetrahydropyran* (**8a**).[42] (0.96 g, 93%), clear oil. ^{1}H NMR (300 MHz, $CDCl_3$, 25 °C): 1:1 diastereomeric mixture δ = 1.49−1.99 (overlapping signals, 18H), 3.40−3.47 (m, 1H), 3.50−3.57 (m, 1H), 3.71−3.79 (m, 1H), 3.97−4.05 (m, 1H), 4.45−4.48 (t, J = 3.21 Hz; 1H), 4.86−4.91 (m, 1H), 4.92−4.97 (overlapping signals, 2H), 7.26−7.48 (m, 10H).

2-(4-Methylphenylethoxy)-tetrahydropyran (**8b**). (1.04 g, 94%), clear oil. ^{1}H NMR (300 MHz, $CDCl_3$, 25 °C): 1:1 diastereomeric mixture δ = 1.45−1.94 (overlapping signals, 18H), 2.38 (s, 6H), 3.38−3.46 (m, 1H), 3.47−3.54 (m, 1H), 3.69−3.77 (m, 1H), 3.95−4.02 (m, 1H), 4.41−4.43 (m, 1H), 4.80−4.85 (m, 1H), 4.86−4.92 (overlapping signals, 2H), 7.16−7.34 (m, 8H).; ^{13}C{^{1}H} NMR (75.5 MHz, $CDCl_3$, 25 °C): δ = 19.2, 19.9, 21.1, 21.9, 24.3, 25.5 (d, J = 1.81 Hz), 30.9, 61.9, 62.8, 72.9−73.0 (d, J = 11.9 Hz), 96.0−96.1 (d, J = 8.83 Hz), 126.0, 126.4, 128.9, 129.1, 136.5, 137.0, 140.6, 141.5.; HRMS (EI) m/z: [M + H]$^+$ calcd for $C_{14}H_{20}O_2$, 220.1463; found: 220.1457.

2-(1-Napthalenylethoxy)-tetrahydropyran (**8c**). (0.90 g, 70%), clear oil. ^{1}H NMR (300 MHz, $CDCl_3$, 25 °C): 1:1 diastereomeric mixture δ = 1.49−2.02 (overlapping signals, 18H), 3.42−3.49 (m, 1H), 3.53−3.60 (m, 1H), 3.74−3.82 (m, 1H), 4.03−4.11 (m, 1H), 4.51−4.54 (t, J = 3.42 Hz; 1H), 5.02−5.04 (m, 1H), 5.07−5.18 (overlapping signals, 2H), 7.49−7.66 (m, 6H), 7.84−7.93 (m, 8H).; ^{13}C{^{1}H} NMR (75.5 MHz, $CDCl_3$, 25 °C): δ = 19.4, 19.9, 22.2, 24.3, 25.6 (d, J = 3.40 Hz), 30.9−40.0 (d, J = 3.85 Hz), 62.1, 62.8, 73.4, 96.1, 96.5, 124.4 (d, J = 1.96 Hz), 124.8, 125.5−125.6 (d, J = 4.53 Hz), 125.8−125.9 (d, J = 8.91 Hz), 126.1, 127.7−127.8 (d, J = 5.06 Hz), 127.9−128.0 (d, J = 6.95 Hz), 128.1, 128.4, 132.8, 133.1, 133.3−133.4 (d, J = 6.57 Hz), 141.1, 142.1.; HRMS (EI) m/z: [M + H]$^+$ calcd for $C_{17}H_{20}O_2$, 256.1463; found: 256.1458.

2-Isopropoxytetrahydropyran (**8d**).[43] (0.69 g, 96%), clear oil. ^{1}H NMR (300 MHz, $CDCl_3$, 25 °C): δ = 1.05−1.07 (d, J = 6.12 Hz; 3H), 1.15−1.17 (d, J = 6.30 Hz; 3H), 1.44−1.55 (m, 4H), 1.57−1.68 (m, 1H), 1.71−1.83 (m, 1H), 3.38−3.45 (m, 1H), 3.80−3.92 (overlapping signals, 2H), 4.58−4.61 (t, J = 3.75 Hz; 1H).

2-(2-Isopropyl-5-methylcyclohexyloxy)-tetrahydropyran (**8e**). (1.13 g, 94%), clear oil. ^{1}H NMR (300 MHz, $CDCl_3$, 25 °C): 1:1 diastereomeric mixture δ = 0.769−1.09 (overlapping signals, 24H), 1.20−1.46 (m, 4H), 1.50−1.90 (overlapping signals, 16H), 2.06−2.20 (m, 3H), 2.32−2.42 (m, 1H), 3.28−3.37 (td, 10.6, 4.38, Hz; 1H), 3.45−3.53 (m, 3H), 3.86−4.02 (m, 2H), 4.59−4.62 (m, 1H), 4.80−4.82 (t, J = 3.51 Hz; 1H).; ^{13}C{^{1}H} NMR (75.5 MHz, $CDCl_3$, 25 °C): δ = 15.6, 16.3, 19.7, 20.3, 21.2 (d, J = 3.55 Hz), 22.2, 22.4, 23.0, 23.3, 25.2, 25.5, 25.6 (d, J = 2.34 Hz), 31.2, 31.3, 31.4, 31.8, 34.4, 34.6, 40.1, 43.6, 48.2, 48.9, 62.4, 63.0, 74.1, 79.9, 94.4, 101.3.; HRMS (EI) m/z: [M + H]$^+$ calcd for $C_{15}H_{28}O_2$, 240.2089; found: 240.2085.

2-tert-Butyloxy-tetrahydropyran (**8f**).[35] (0.70 g, 88%), clear oil. ^{1}H NMR (300 MHz, $CDCl_3$, 25 °C): δ = 1.26 (s, 9H), 1.47−1.53 (m, 4H), 1.63−1.70 (m, 1H), 1.81−1.91 (m, 1H), 3.42−3.50 (m, 1H), 3.94−4.00 (m, 1H), 4.73−4.75 (t, J = 3.18 Hz; 1H).

2-(1,1-Dimethyl-propoxy)-tetrahydropyran (**8g**).[44] (0.72 g, 84%), clear oil. ^{1}H NMR (300 MHz, $CDCl_3$, 25 °C): δ = 0.863−0.913 (t, J = 7.44 Hz; 3H), 1.18−1.20 (d, J = 4.38 Hz; 6H), 1.46−1.60 (m, 6H), 1.62−1.68 (m, 1H), 1.81−1.88 (m, 1H), 3.41−3.48 (m, 1H), 3.93−4.00 (m, 1H), 4.71−4.73 (t, J = 3.09 Hz; 1H).

2-Phenoxytetrahydropyran (**9a**).[44] (0.65 g, 73%), clear oil. ^{1}H NMR (300 MHz, $CDCl_3$, 25 °C): δ = 1.59−1.81 (m, 3H), 1.88−1.93 (m, 2H), 2.01−2.13 (m, 1H), 3.60−3.68 (m, 1H), 3.92−4.00 (m, 1H), 5.45−5.47 (t, J = 3.27 Hz; 1H), 6.99−7.05 (m, 1H) 7.08−7.11 (m, 2H), 7.28−7.35 (m, 2H).

2-(4-Bromophenoxy)-tetrahydropyran (**9b**).[44] (1.18 g, 92%), clear oil. ^{1}H NMR (300 MHz, $CDCl_3$, 25 °C): δ = 1.58−1.77 (m, 3H), 1.85−190 (m, 2H), 1.92−2.10 (m, 1H), 3.58−3.65 (m, 1H), 3.85−3.93 (m, 1H), 5.38−5.40 (t, J = 3.18 Hz; 1H), 6.93−6.99 (m, 2H), 7.38−7.40 (m, 2H).

2-(4-Methoxyphenoxy)-tetrahydropyran (**9c**).[44] (0.53 g, 51%), clear oil. ^{1}H NMR (300 MHz, $CDCl_3$, 25 °C): δ = 1.58−1.78 (m, 3H), 1.85−1.90 (m, 2H), 1.97−2.10 (m, 1H), 3.58−3.65 (m, 1H), 3.80 (s, 3H), 3.93−4.01 (m, 1H), 5.31−5.33 (t, J = 3.33 Hz; 1H), 6.82−6.88 (m, 2H), 7.00−7.05 (m, 2H).

■ ASSOCIATED CONTENT

Supporting Information

The Supporting Information is available free of charge on the ACS Publications website at DOI: 10.1021/acs.joc.8b02321.

Crystallographic data (CIF)

Computational calculations and X-ray crystallographic analysis for **1**·BF_4^- as well as optimization studies and NMR spectra for all reported compounds (PDF)

■ AUTHOR INFORMATION

Corresponding Author

*E-mail: tdudding@brocku.ca.

ORCID

Melanie Pilkington: 0000-0002-9274-8512

Travis Dudding: 0000-0002-2239-0818

Notes

The authors declare no competing financial interest.

■ ACKNOWLEDGMENTS

T.D. acknowledges financial support from the Natural Science and Engineering Research Council (NSERC) Discovery grant (2014-04410). Computations were carried out using facilities at SHARCNET (Shared Hierarchical Academic Research Computing Network: www.sharcnet.ca) and Compute/Calcul Canada. T.D. also acknowledges the Zelisko group for donation of compound **2k**.

■ REFERENCES

(1) For timely reviews of organocatalysis, see: (a) Auvil, T. J.; Schafer, A. G.; Mattson, A. E. Design Strategies for Enhanced Hydrogen-Bond Donor Catalysts. *Eur. J. Org. Chem.* **2014**, *2014*, 2633−2646. (b) Doyle, A. G.; Phipps, R. J.; Hamilton, G. L.; Toste, F. D. The Progression of Chiral Anions from Concepts to Applications in Assymetric Catalysis. *Nat. Chem.* **2012**, *4*, 603−614. (c) Giacalone, F.; Gruttadauria, M.; Agrigento, P.; Noto, R. Low-Loading Asymmetric Organocatalysis. *Chem. Soc. Rev.* **2012**, *41*, 2406−2447. (d) Wende, R. C.; Schreiner, P. R. Evolution of Asymmetric Organocatalysis: Multi- and Retrocatalysis. *Green Chem.* **2012**, *14*, 1821−1849. (e) Doyle, A. G.; Jacobsen, E. N. Small-Molecule H-Bond Donors in Asymmetric Catalysis. *Chem. Rev.* **2007**, *107*, 5713−5743.

(2) For reviews revealing the attractive features of organocatalysis, see: (a) Alonso, D. A.; Baeza, A.; Chinchilla, R.; Gómez, C.; Guillena, G.; Pastor, I. M.; Ramón, D. J. Recent Advances in Asymmetric

DOI: 10.1021/acs.joc.8b02321
J. Org. Chem. 2018, 83, 13973−13980

Organocatalyzed Conjugate Additions to Nitroalkenes. *Molecules* **2017**, *22*, 895−945. (b) Qin, Y.; Zhu, L.; Luo, S. Organocatalysis in Inert C-H Bond Functionalization. *Chem. Rev.* **2017**, *117*, 9433−9520. (c) Alemań, J.; Cabrera, S. Applications of Asymmetric Organocatalysis in Medicinal Chemistry. *Chem. Soc. Rev.* **2013**, *42*, 774−793. (d) Bertelsen, S.; Jørgensen, K. A. Organocatalysis − After the Gold Rush. *Chem. Soc. Rev.* **2009**, *38*, 2178−2189. (e) MacMillan, D. W. The Advent and Development of Organocatalysis. *Nature* **2008**, *455*, 304−308. (f) Dalko, P. I.; Moisan, L. In the Golden Age of Organocatalysis. *Angew. Chem., Int. Ed.* **2004**, *43*, 5138−5175.

(3) (a) Brak, K.; Jacobsen, E. N. Asymmetric Ion-Pairing Catalysis. *Angew. Chem., Int. Ed.* **2013**, *52*, 534−561. (b) Israelachvili, J. *Intermolecular and Surface Forces*, 2nd ed.; Academic Press: London, 1991.

(4) (a) Neel, A. J.; Hilton, M. J.; Sigman, M. S.; Toste, F. D. Exploiting Non-Covalent π Interactions for Catalyst Design. *Nature* **2017**, *543*, 637−646. (b) Grimme, S. Do Special Noncovalent π-π Stacking Interations Really Exist? *Angew. Chem., Int. Ed.* **2008**, *47*, 3430−3434. (c) Meyer, E. A.; Castellano, R. K.; Diederich, F. Interactions with Aromatic Rings in Chemical and Biological Recognition. *Angew. Chem., Int. Ed.* **2003**, *42*, 1210−1250.

(5) (a) Kennedy, C. R.; Lin, S.; Jacobsen, E. N. The Cation-π Interaction in Small-Molecule Catalysis. *Angew. Chem., Int. Ed.* **2016**, *55*, 12596−12624. (b) Ma, J. C.; Dougherty, D. A. The Cation-π Interaction. *Chem. Rev.* **1997**, *97*, 1303−1324.

(6) Tanford, C. *The Hydrophobic Effect*, 2nd ed.; Wiley: New York, 1980.

(7) (a) Wagner, J. P.; Schreiner, P. R. *Angew. Chem., Int. Ed.* **2015**, *54*, 12274−12296. (b) Stone, A. J. *The Theory of Intermolecular Forces*; Oxford University Press: New York, 1996.

(8) For pertinent examples relating to (thio)urea conformations, see: (a) Supady, A.; Hecht, S.; Baldauf, C. About Underappreciated Yet Active Conformations of Thiourea Organocatalysts. *Org. Lett.* **2017**, *19*, 4199−4202. (b) Lam, C.-K.; Hau, S. C-K.; Yau, C.-W.; Mak, T. C. W. Hydrogen-Bonded Anionic Host Lattices Constructed with Isocyanurate and Thiourea/Urea. *Cryst. Growth Des.* **2016**, *16*, 759−773. (c) Madarász, A.; Dósa, Z.; Varga, S.; Soós, T.; Csámpai, A.; Pápai, I. Thiourea Derivatives as Brønsted Acid Organocatalysts. *ACS Catal.* **2016**, *6*, 4379−4387.

(9) Siau, W. Y.; Wang, J. Asymmetric Organocatalytic Reactions by Bifunctional Amine-Thioureas. *Catal. Sci. Technol.* **2011**, *1*, 1298−1310.

(10) For examples of thiourea catalysts forming ion pair complexes, see: (a) Kennedy, C. R.; Lehnherr, D.; Rajapaksa, N. S.; Ford, D. D.; Park, Y.; Jacobsen, E. N. Mechanism-Guided Development of a Highly Active Bis-thiourea Catalyst for Anion-Abstraction Catalysis. *J. Am. Chem. Soc.* **2016**, *138*, 13525−13528. (b) Mittal, N.; Lippert, K. M.; De, C. K.; Klauber, E. G.; Emge, T. J.; Schreiner, P. R.; Seidel, D. A Dual-Catalysis Anion-Binding Approach to the Kinetic Resolution of Amines: Insights into the Mechanism via a Combined Experimental and Computational Study. *J. Am. Chem. Soc.* **2015**, *137*, 5748−5758. (c) Berkessel, A.; Das, S.; Pekel, D.; Neudörfl, J. M. Anion-Binding Catalysis by Electron-Deficinet Pyridinium Cations. *Angew. Chem., Int. Ed.* **2014**, *53*, 11660−11664. (d) Lin, S.; Jacobsen, E. N. Thiourea-Catalyzed Ring Opening of Episulfonium Ions with Indole Derivatives by means of Stabilizing, Non-Covalent Interactions. *Nat. Chem.* **2012**, *4*, 817−824. (e) Xu, H.; Zuend, S. J.; Woll, M. G.; Tao, Y.; Jacobsen, E. N. Asymmetric Cooperative Catalysis of Strong Brønsted Acid-Promoted Reactions using Chiral Ureas. *Science* **2010**, *327*, 986−990. (f) Reisman, S. E.; Doyle, A. G.; Jacobsen, E. N. Enantioselective Thiourea-Catalyzed Additions to Oxocarbenium Ions. *J. Am. Chem. Soc.* **2008**, *130*, 7198−7199. (g) Taylor, M. S.; Tokunaga, N.; Jacobsen, E. N. Enantioselective Thiourea-Catalyzed Acyl-Mannich Reactions of Isoquinolones. *Angew. Chem., Int. Ed.* **2005**, *44*, 6700−6704.

(11) Park, Y.; Schindler, C. S.; Jacobsen, E. N. Enantioselective Aza-Sakurai Cyclizations: Dual Role of Thiourea as H-Bond Donor and Lewis Base. *J. Am. Chem. Soc.* **2016**, *138*, 14848−14851.

(12) For reviews and select examples relating to cooperative catalysis, see: reviews: (a) Hong, L.; Sun, W.; Yang, D.; Li, G.; Wang, R. Additive Effects on Asymmetric Catalysis. *Chem. Rev.* **2016**, *116*, 4006−4123. (b) Zhang, Z. G.; Schreiner, P. R. (Thio)Urea Organocatalysis − What can be learnt from Anion Recognition? *Chem. Soc. Rev.* **2009**, *38*, 1187−1198. Examples: (b) Xu, H.; Zuend, S. J.; Woll, M. G.; Tao, Y.; Jacobsen, E. N. Asymmetric Cooperative Catalysis of Strong Brønsted Acid-Promoted Reactions using Chiral Ureas. *Science* **2010**, *327*, 986−990. (c) Uraguchi, D.; Ueki, Y.; Ooi, T. Chiral Organic Ion Pair Catalysts Assembled Through a Hydrogen-Bonding Network. *Science* **2009**, *326*, 120−123. (c) Weil, T.; Kotke, M.; Kleiner, C. M.; Schreiner, P. R. Cooperative Brønsted Acid-Type Organocatalysis: Alcoholysis of Styrene Oxides. *Org. Lett.* **2008**, *10*, 1513−1516.

(13) (a) Fan, Y.; Kass, S. R. Electrostatically Enhanced Thioureas. *Org. Lett.* **2016**, *18*, 188−191. (b) Fan, Y.; Tiffner, M.; Schörgenhumer, J.; Robiette, R.; Waser, M.; Kass, S. R. Synthesis of Cyclic Organic Carbonates using Atmospheric Pressure CO_2 and Charge-Containing Thiourea Catalysts. *J. Org. Chem.* **2018**, *83*, 9991−10000.

(14) (a) Akalay, D.; Dürner, G.; Bats, J. W.; Bolte, M.; Göbel, M. W. Synthesis of C_2-Symmetric Bisamidines: A New type of Chiral Metal-Free Lewis Acid Analogue Interacting with Carbonyl Groups. *J. Org. Chem.* **2007**, *72*, 5618−5624. (b) Schuster, T.; Kurz, M.; Göbel, M. W. *J.* Catalysis of a Diels-Alder Reaction by Amidinium Ions. *J. Org. Chem.* **2000**, *65*, 1697−1701.

(15) Huang, J.; Corey, E. J. A New Chiral Catalyst for the Enantioselective Strecker Synthesis of α-Amino Acids. *Org. Lett.* **2004**, *6*, 5027−5029.

(16) (a) Selig, P. Guanidine Organocatalysis. *Synthesis* **2013**, *45*, 703−718. (b) Uyeda, C.; Jacobsen, E. N. Transition-State Charge Stabilization through Multiple Non-Covalent Interactions in the Guanidinium-Catalyzed Enantioselective Claisen Rearrangement. *J. Am. Chem. Soc.* **2011**, *133*, 5062−5075. (c) Leow, D.; Tan, C.-H. Catalytic Reactions of Chiral Guanidines and Guanidinium Salts. *Synlett* **2010**, *2010*, 1589−1605. (d) Uyeda, C.; Jacobsen, E. N. Enantioselective Claisen Rearrangements with a Hydrogen-Bond Donor Catalyst. *J. Am. Chem. Soc.* **2008**, *130*, 9228−9229. (e) Terada, M.; Ube, H.; Yaguchi, Y. Axially Chiral Guanidine as Enantioselective Base Catalyst for 1,4-Addition Reaction of 1,3-Dicarbonyl Compounds with Conjugated Nitroalkenes. *J. Am. Chem. Soc.* **2006**, *128*, 1454−1455. (f) Terada, M.; Nakano, M.; Ube, H. Axially Chiral Guanidine as Highly Active and Enantioselective Catalyst for Electrophilic Amination of Unsymmetrically Substituted 1,3-Dicarbonyl Compounds. *J. Am. Chem. Soc.* **2006**, *128*, 16044−16045. (g) Corey, E. J.; Grogan, M. J. Enantioselective Synthesis of α-Amino Nitriles from *N*-Benzhydryl Imines and HCN with a Chiral Bicyclic Guanidine as Catalyst. *Org. Lett.* **1999**, *1*, 157−160.

(17) (a) Takenaka, N.; Chen, J.; Captain, B.; Sarangthem, R. S.; Chandrakumar, A. Helical Chiral 2-Aminopyridinium Ions: A New Class of Hydrogen Bond Donor Catalysts. *J. Am. Chem. Soc.* **2010**, *132*, 4536−4537. (b) Takenaka, N.; Sarangthem, R. S.; Seerla, S. K. 2-Aminopyridinium Ions Activate Nitroalkenes through Hydrogen Bonding. *Org. Lett.* **2007**, *9*, 2819−2822.

(18) (a) Singh, A.; Johnston, J. N. A Diastero- and Enantioselective Synthesis of α-Substituted *syn*-α,β-Diamino Acids. *J. Am. Chem. Soc.* **2008**, *130*, 5866−5867. (b) Ganesh, M.; Seidel, D. Catalytic Enantioselective Additions of Indoles to Nitroalkenes. *J. Am. Chem. Soc.* **2008**, *130*, 16464−16465. (c) Singh, A.; Yoder, R. A.; Shen, B.; Johnston, J. N. Chiral Proton Catalysis: Enantioselective Brønsted Acid Catalyzed Additions of Nitroacetic Acid Derivatives as Glycine Equivalents. *J. Am. Chem. Soc.* **2007**, *129*, 3466−3467. (d) Nugent, B. M.; Yoder, R. A.; Johnston, J. N. Chiral Proton Catalysis: A Catalytic Enantioselective Direct Aza-Henry Reaction. *J. Am. Chem. Soc.* **2004**, *126*, 3418−3419.

(19) Kotke, M.; Schreiner, P. R. Generally Applicable Organocatalytic Tetrahydropyranylation of Hydroxy Functionalities with Very Low Catalyst Loading. *Synthesis* **2007**, *2007*, 779−790.

DOI: 10.1021/acs.joc.8b02321
J. Org. Chem. 2018, 83, 13973−13980

(20) Frisch, M. J.; Trucks, G. W.; Schlegel, H. B.; Scuseria, G. E.; Robb, M. A.; Cheeseman, J. R.; Scalmani, G.; Barone, V.; Petersson, G. A.; Nakatsuji, H.; Li, X.; Caricato, M.; Marenich, A. V.; Bloino, J.; Janesko, B. G.; Gomperts, R.; Mennucci, B.; Hratchian, H. P.; Ortiz, J. V.; Izmaylov, A. F.; Sonnenberg, J. L.; Williams-Young, D.; Ding, F.; Lipparini, F.; Egidi, F.; Goings, J.; Peng, B.; Petrone, A.; Henderson, T.; Ranasinghe, D.; Zakrzewski, V. G.; Gao, J.; Rega, N.; Zheng, G.; Liang, W.; Hada, M.; Ehara, M.; Toyota, K.; Fukuda, R.; Hasegawa, J.; Ishida, M.; Nakajima, T.; Honda, Y.; Kitao, O.; Nakai, H.; Vreven, T.; Throssell, K.; Montgomery, J. A., Jr.; Peralta, J. E.; Ogliaro, F.; Bearpark, M. J.; Heyd, J. J.; Brothers, E. N.; Kudin, K. N.; Staroverov, V. N.; Keith, T. A.; Kobayashi, R.; Normand, J.; Raghavachari, K.; Rendell, A. P.; Burant, J. C.; Iyengar, S. S.; Tomasi, J.; Cossi, M.; Millam, J. M.; Klene, M.; Adamo, C.; Cammi, R.; Ochterski, J. W.; Martin, R. L.; Morokuma, K.; Farkas, O.; Foresman, J. B.; Fox, D. J. *Gaussian 16*, Revision B.01; Gaussian, Inc., Wallingford, CT, 2016.

(21) Becke, A. D. Density-Functional Thermocehmistry. III. The Role of Exact Exchange. *J. Chem. Phys.* **1993**, *98*, 5648−5652.

(22) Stephens, P. J.; Devlin, F. J.; Chabalowski, C. F.; Frisch, M. J. Ab Initio Calculation of Vibrational Absorption and Circular Dichroism Spectra using Density Functional Force Fields. *J. Phys. Chem.* **1994**, *98*, 11623−11627.

(23) Lee, C.; Yang, W.; Parr, R. G. Development of the Colle-Salvetti Correlation-Energy Formula into a Functional of the Electron Density. *Phys. Rev. B: Condens. Matter Mater. Phys.* **1988**, *37*, 785−789.

(24) Grimme, S.; Antony, J.; Ehrlich, S.; Krieg, H. A Consistent and Accurate ab Initio Parametrization of Density Functional Dispersion Correction (DFT-D) for the 94 Elements H-Pu. *J. Chem. Phys.* **2010**, *132*, 154104−154119.

(25) Marenich, A. V.; Cramer, C. J.; Truhlar, D. G. Universal Solvation Model Based on Solute Electron Density and on a Continuum Model of the Solvent Defined by the Bulk Dielectric Constant and Atomic Surface Tensions. *J. Phys. Chem. B* **2009**, *113*, 6378−6396.

(26) Lian, P.; Johnston, R. C.; Parks, J. M.; Smith, J. C. Quantum Chemical Calculation of pkas of Environmentally Relevant Functional Groups: Carboxylic Acids, Amines and Thiols in Aqueous Solution. *J. Phys. Chem. A* **2018**, *122*, 4366−4374.

(27) Zhurko, G.; Zhurko, D. *ChemCraft*, Version 1.8 http://www.chemcraftprog.com.

(28) Tobey, S. W.; West, R. Tetrachlorocyclopropene and Hexachlorocyclopropane from Pentachlorocyclopropane. *Tetrahedron Lett.* **1963**, *4*, 1179−1182.

(29) Tobey, S. W.; West, R. Pentachlorocyclopropane. *J. Am. Chem. Soc.* **1966**, *88*, 2478.

(30) Sennari, G.; Hirose, T.; Iwatsuki, M.; Ōmura, S.; Sunazuka, T. A concise Total Synthesis of Puberulic Acid, a Potent Antimalarial Agent. *Chem. Commun.* **2014**, *50*, 8715−8718.

(31) Lavallo, V.; Ishida, Y.; Donnadieu, B.; Bertrand, G. Isolation of Cyclopropenylidene-Lithium Adducts: The Weiss-Yoshida Reagent. *Angew. Chem., Int. Ed.* **2006**, *45*, 6652−6655.

(32) Nacsa, E. D.; Lambert, T. H. Higher-Order Cyclopropenimine Superbases: Direct Neutral Brønsted Base Catalyzed Michael Reactions with α-Aryl Esters. *J. Am. Chem. Soc.* **2015**, *137*, 10246−10253.

(33) Das, S.; Pekel, D.; Neudörfl, J. M.; Berkessel, A. Organocatalytic Glycosylation by Using Electron-Deficient Pyridinium Salts. *Angew. Chem., Int. Ed.* **2015**, *54*, 12479−12483.

(34) Kayastha, A. K.; Hotha, S. Versatile Gold Catalyzed Transglycosidation at Ambient Temperature. *Chem. Commun.* **2012**, *48*, 7161−7163.

(35) Kumar, B.; Aga, M. A.; Mukherjee, D.; Chimni, S. S.; Taneja, S. C. Allyl Tetrahydropyranyl Ether: A Versatile Alcohol/Thiol Protecting Reagent. *Tetrahedron Lett.* **2009**, *50*, 6236−6240.

(36) Hajipour, A. R.; Nasresfahani, Z. Mild and Efficient Chemoselective Tetrahydropyranylation of Alcohols using Brønsted Acidic Ionic Liquid as Catalyst under Solvent-Free Conditions. *Synth. Commun.* **2012**, *42*, 1995−2006.

(37) Speicher, A.; Groh, M.; Hennrich, M.; Huynh, A. M. Synthesis of Macrocyclic Bis(bibenzyl) Compounds Derived from Perrottetine E. *Eur. J. Org. Chem.* **2010**, *2010*, 6760−6778.

(38) González-Calderón, D.; González- González, C.; Fuentes-Benítez, A.; Cuevas-Yáñez, E.; Corona-Becerril, D.; González-Romero, C. Cerium(IV) Sulfate Tetrahydrate: A Catalytic and Highly Chemoselective Deprotection of THP, MOM and BOM Ethers. *Tetrahedron Lett.* **2013**, *54*, 7164−7166.

(39) Casson, S.; Kocieński, P. Palladium(0)-Catalyzed Hydrostannylation of 1-Alkoxy-1-alkyenes: A Synthesis of α-Alkoxyalkenylstannanes and their Transmetallation to α-Alkoxyalkenyllithiums. *Synthesis* **1993**, *1993*, 1133−1140.

(40) Zheng, W. W.; Hsieh, Y. H.; Chiu, Y. C.; Cai, S. J.; Cheng, C. L.; Chen, C. Organic Functionalization of Ultradispersed Nanodiamond: Synthesis and Applications. *J. Mater. Chem.* **2009**, *19*, 8432−8441.

(41) Khan, A. T.; Ghosh, S.; Choudhury, L. H. A Highly Efficient Synthetic Protocol for Tetrahydropyranylation/Depyranylation of Alcohols and Phenols. *Eur. J. Org. Chem.* **2005**, *2005*, 4891−4896.

(42) Poon, P. S.; Banerjee, A. K.; Bedoya, L.; Laya, M. S.; Cabrera, E. V.; Albornoz, K. M. Dowex 50WX4−100: An Efficient Catalyst for the Tetrahydropyranylation of Alcohols. *Synth. Commun.* **2009**, *39*, 3369−3377.

(43) Schmalisch, S.; Mahrwald, R. Organocatalyzed Direct Glycosylation of Unprotected and Unactivated Carbohydrates. *Org. Lett.* **2013**, *15*, 5854−5857.

(44) Mahato, S.; Chatterjee, R.; Ghosal, N. C.; Majee, A. Zwitterionic Imidazolium Salt: An Efficient Organocatalyst for Tetrahydropyranylation of Alcohols. *Synth. Commun.* **2017**, *47*, 1905−1915.

DOI: 10.1021/acs.joc.8b02321
J. Org. Chem. 2018, 83, 13973−13980

PCCP

PAPER

View Article Online
View Journal | View Issue

Check for updates

Cite this: *Phys. Chem. Chem. Phys.*, 2017, **19**, 14512

Study of antiradical mechanisms with dihydroxybenzenes using reaction force and reaction electronic flux†

Cristina Ortega-Moo,[a]* Rocio Durán,[b] Bárbara Herrera,[b] Soledad Gutiérrez-Oliva,[b] Alejandro Toro-Labbé[bc] and Rubicelia Vargas[a]*

Received 27th February 2017,
Accepted 8th May 2017

DOI: 10.1039/c7cp01304c

rsc.li/pccp

Phenolic compounds represent an important category of antioxidants because they help inhibit the oxidation process of organic compounds, while also acting as antiradicals in many biological processes. In this work, we analyze the transfer mechanisms for a set of catechols and resorcinols of a single electron, proton and hydrogen, with the radical peroxyl (•OOH) and with different electron withdrawing and donating groups as substituents. By using the M05-2X exchange correlation functional within the Density Functional Theory framework combined with the 6-311++G(d,p) basis set, we were able to compute the Gibbs free energies for all mechanisms and compounds. According to the thermodynamic results, the hydrogen atom transfer mechanism was the most favorable. Therefore, this mechanism with substituents $-CH_3$ and $-COH$ in catechol and resorcinol was analyzed, using the reaction force and reaction electronic flux to characterize the structural and electronic changes that take place during the reaction. Our results show that electron donating groups favor electronic changes along the reaction path, increasing the spontaneity of the hydrogen atom transfer mechanism.

1 Introduction

Since isolation of the first phenol, the chemistry of phenolic compounds and their derivatives has attracted attention, due to a wide variety of applications for example in the food industry, cosmetics and medicine.[1,2] Phenol derivatives may be formed from simple structures, which have at least one aromatic ring with one or more hydroxyl groups or they may even form more complex structures such as polymers, *e.g.* phenolic acids and tannins.[1,3]

Phenolic compounds constitute an important category of antioxidants with high reactivity, acting either as electron donors or by losing hydrogen atoms to become radical oxygen species with unpaired electrons, such as peroxyl radicals (•OOR).[4,5] These two kinds of processes resulting in radicals are crucial intermediates involved in a variety of biological and industrial processes, and these promote inhibition of the oxidation process of organic compounds.[1,6]

Catechol (1,2-dihydroxybenzene) and resorcinol (1,3-dihydroxybenzene) are compounds with an aromatic ring and two hydroxyl groups, which differ in terms of the position of the OH groups (Fig. 1). There are many studies about both dihydroxybenzenes although catechol and its derivatives are better known, since they are involved in several oxidation processes in plant and animal cells.[1,7,8] In the literature, there is also experimental data showing the effectiveness of resorcinol and its derivatives as good antioxidants; however the mechanisms directing the action of this dihydroxybenzene are still being deliberated.[9–12]

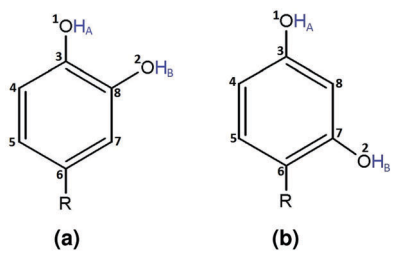

Fig. 1 Chemical structure of (a) *ortho*-dihydroxybenzene (catechol) and (b) *meta*-dihydroxybenzene (resorcinol).

[a] *Departamento de Química, División de Ciencias Básicas e Ingenierías, Universidad Autónoma Metropolitana-Iztapalapa, San Rafael Atlixco 186, Col. Vicentina, Iztapalapa, A.P. 55-534, 09340, Ciudad de México, Mexico. E-mail: ruvf@xanum.uam.mx*

[b] *Nucleus Millennium Chemical Processes and Catalysis (CPC), Laboratorio de Química Teórica Computacional (QTC), Departamento de Química Física, Facultad de Química, Pontificia Universidad Católica de Chile, Av. Vicuña Mackenna 4860, 76220436, Casilla 306, Correo 22, Santiago, Chile*

[c] *Freiburg Institute for Advanced Studies (FRIAS), Albert-Ludwig Universität Freiburg, Germany*

† Electronic supplementary information (ESI) available. See DOI: 10.1039/c7cp01304c

Three mechanisms are accepted in the literature as being involved in the antiradical activity of phenolic compounds;[8,13,14] the first is the single-electron transfer (SET) of phenol (PhOH) to a radical, for example $^{\bullet}$OOH, resulting in a radical cation ($PhOH^{\bullet+}$) and a peroxyl anion ($^{-}$OOH):

$$PhOH + {}^{\bullet}OOH \rightarrow PhOH^{\bullet+} + {}^{-}OOH. \quad (1)$$

The second mechanism is the proton transfer (PT), where a proton is transferred from the hydroxyl groups of the phenol, producing an anion molecule (PhO^{-}) and a radical cation ($^{+\bullet}$HOOH):

$$PhOH + {}^{\bullet}OOH \rightarrow PhO^{-} + {}^{+\bullet}HOOH. \quad (2)$$

The third mechanism is the hydrogen-atom transfer (HAT), which occurs when a hydrogen atom from the hydroxyl group of the phenol is transferred, resulting in the formation of a radical ($PhO^{\bullet}$) and hydrogen peroxide (H_2O_2).

$$PhOH + {}^{\bullet}OOH \rightarrow PhO^{\bullet} + H_2O_2. \quad (3)$$

The literature also presents a number of theoretical and experimental studies on a variety of phenolic compounds and derivatives, which primarily analyze antioxidant activity under SET, PT and HAT mechanisms.[6–8,15,16] The antioxidant capacity of a phenolic compound can be determined by assessing the relative stability of the species produced in the reaction.[17]

In particular, the HAT of phenolic compounds towards radicals has been one of the processes most studied for determining antioxidant activity. These studies are generally limited to a thermodynamic and kinetic analysis, providing information on the energy of reaction and activation.[5,8,18] However, they do not provide information about the reaction mechanism, *i.e.*, the structural and electronic factors that drive the reaction evolving from reactants to the formation of desired products.[18]

Over the years, we have developed theoretical tools that can help in the analysis of a chemical reaction mechanism, they are the reaction force and reaction electronic flux. The reaction force defines a framework to identify regions along the reaction coordinate where different mechanisms, associated with structural or electronic effects, can be driving the reaction. On the other hand, the reaction force provides a rational partition of the reaction and activation energies in terms of specific reaction works that unveil the physical nature, structural or electronic, of these energies. Otherwise, the reaction electronic flux (REF) characterizes the electronic activity that takes place during the reaction, it accounts for bond strengthening/formation and bond weakening/breaking processes.[19,20] These quantities have been used for a wide variety of reactions,[18–24] in order to obtain interesting insights into the chemical events that drive a reaction, consistent with experimental and theoretical data, such as the transition state theory.[25,26]

In this article, we studied the mechanisms of SET, PT and HAT with the radical peroxyl ($^{\bullet}$OOH) for a set of catechols and resorcinols, which have different electron withdrawing and electron donating groups, as substituents (Fig. 1). Likewise, we used the reaction force and reaction electronic flux indices for the HAT mechanism to analyze the structural and electronic changes, along the reaction coordinate.

2 Computational details

Two conformers of catechol and four of resorcinol were selected to determine the most stable structure in *ortho* and *meta* dihydroxybenzene (Fig. 2). For each conformer –R was substituted by: –H, $-CH_3$, $-CH_2CH_3$, $-CH_2CH_2CH_3$, $-CH{=}CH_2$, $-CH{=}CHCOOH$, $-CO(CH_2)_4CH_3$, –COOH, –COH groups; these substituents were selected according to their own electron withdrawing and electron donating properties.

In order to determine the thermodynamic feasibility of ET, PT and HAT mechanisms proposed on eqn (1)–(3), Gibbs free energy was calculated at 298 K:

$$\Delta G^{\circ}_{\text{reaction}} = \left[\sum\left(G_{\text{products}}\right) - \sum\left(G_{\text{reagents}}\right)\right]. \quad (4)$$

DFT was used to fully determine mechanisms in the Gaussian09 program.[27] The hybrid *meta*-GGA M05-2X exchange correlation functional[28] was used in all the calculations in combination of the 6-311++G(d,p) basis sets[29] with the SMD implicit model,[30] using water as a solvent. The M05-2X exchange correlation functional was chosen because of its good performance for predicting thermodynamics and kinetics in main group elements, together with an improvement in non-covalent interactions, necessary for the proper description of transition states (TS).[31,32] All reactions were followed along the intrinsic reaction coordinate (IRC) and stationary points. Likewise, transition state structures were fully optimized, and verified by harmonic frequency calculations. Analysis of electron population was performed using the NBO 6.0 program[33] also implemented in Gaussian09.

3 Theoretical background

3.1 Reaction force analysis (RFA)

The reactivity of a chemical system and the interaction with other molecules to produce new chemical systems can be interpreted with its potential energy along a reaction coordinate. The Hellmann–Feynman reaction force is defined as the negative

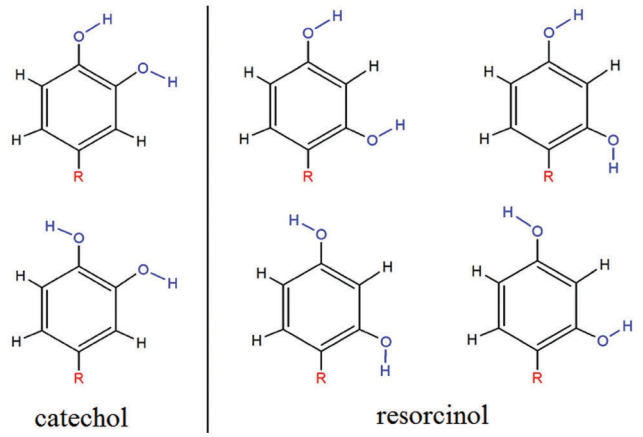

R=-H, $-CH_3$, $-CH_2CH_3$, $-CH_2CH_2CH_3$, $-CH{=}CH_2$, $-CH{=}CHCOOH$, $-CO(CH_2)_4CH_3$, -COOH, -COH.

Fig. 2 Conformers of dihydroxybenzenes.

derivative of the potential energy $E(\xi)$, with respect to the reaction coordinate:[19,20]

$$F(\xi) = -\frac{\mathrm{d}E(\xi)}{\mathrm{d}\xi}. \quad (5)$$

The reaction force results in a rational partition of the energy profile, which helps to identify different regions along the reaction where different reaction mechanisms might be operating.[19,20]

For a single step reaction in which the reactants are separated from the product by an energy barrier, the reaction force profile presents two critical points, a minimum before the transition state structure at ξ_1 and a maximum after the TS at ξ_2. These critical points allow us to define three reaction regions in which structural and/or electronic effects drive the reaction. The regions between $[\xi_R \rightarrow \xi_1]$ and $[\xi_2 \rightarrow \xi_P]$, where R and P refer to reactants and products, respectively, involve mainly structural rearrangements, whereas in region $[\xi_1 \rightarrow \xi_2]$, the electronic activity dominates leading to bond breaking and bond formation. The works associated with each type of reorganization can be obtained as follows:[20,34]

$$\begin{aligned} W_1 &= -\int_{\xi_R}^{\xi_1} F(\xi)\mathrm{d}\xi > 0, \quad W_2 = -\int_{\xi_1}^{\xi_{TS}} F(\xi)\mathrm{d}\xi > 0, \\ W_3 &= -\int_{\xi_{TS}}^{\xi_2} F(\xi)\mathrm{d}\xi < 0, \quad W_4 = -\int_{\xi_2}^{\xi_P} F(\xi)\mathrm{d}\xi < 0. \end{aligned} \quad (6)$$

As W_1 and W_4 are defined within the reactant and product regions, respectively, they are more associated with structural effects. In contrast to this, W_2 and W_3 are defined within the transition state region, which mostly accounts for electronic effects.

Thus, the reaction and activation energies can be written as:

$$\Delta E^\circ = [E(\xi_P) - E(\xi_R)] = W_1 + W_2 + W_3 + W_4, \quad (7)$$

$$\Delta E^{\neq} = [E(\xi_{TS}) - E(\xi_R)] = W_1 + W_2. \quad (8)$$

This rational partition enables us to obtain the reaction energy (ΔE°) and the barrier ($\Delta E^{\neq}$) in terms of structural and electronic energies. In summary, RFA provides a rigorous way to produce a division in the reaction coordinate to unveil the physical nature of the reaction and activation energies in terms of the predominance of structural or electronic effects.

3.2 Reaction electronic flux (REF)

Similarly, we obtained response functions from the Spin Polarized-Density Functional Theory (DFT-SP) to study the chemical reactivity of molecules by means of transfer processes related to electronic charge. This presupposes an expansion of the second-order Taylor series of energy as a function of the number of electrons at fixed values of the external potential (v) and spin number (N_s):[24,35]

$$\Delta E_{v,N_s} = \mu_N \Delta N + \frac{1}{2}\eta_{NN}\Delta N^2, \quad (9)$$

where μ_N is the chemical potential within DFT-SP. In this scheme, μ_N is defined in terms of the frontier orbitals as:[36]

$$\mu_N \cong \frac{1}{2}\left(\frac{\varepsilon_H^\alpha + \varepsilon_H^\beta}{2} + \frac{\varepsilon_L^\alpha + \varepsilon_L^\beta}{2}\right), \quad (10)$$

where only in the closed-shell case of $\varepsilon_H^\alpha = \varepsilon_H^\beta$ and $\varepsilon_L^\alpha = \varepsilon_L^\beta$, α and β stand for the spin state. From the chemical potential of eqn (10), the REF can be defined as the negative of the derivative for chemical potential along the reaction coordinate:

$$J(\xi) = -\frac{\mathrm{d}\mu_N}{\mathrm{d}\xi}. \quad (11)$$

Changes in REF are associated with spontaneity in reorganization of electronic density; a positive REF is associated with spontaneous changes in electronic density that are related to bond formation or strengthening processes, whereas negative REF values indicate that non-spontaneous changes in electronic density are taking place driven by bond breaking or weakening processes.[18]

4 Results

4.1 Thermodynamic analysis

We conducted a thermodynamic analysis of the optimized structures of catechol and resorcinol conformers, as shown in Fig. 2. The energy differences between catechol and resorcinol conformers with different substituents are less than 2.0 kcal mol^{-1}. In a previous paper, it was observed with the B3LYP method that the solvent (water) was not relevant to the selection of different conformers of dihydroxybenzenes, therefore, all the conformers of catechol and resorcinol were considered in the thermodynamic study.[11]

To analyze the SET, PT and HAT mechanisms with the radical $^\bullet$OOH, we estimated ΔG° with eqn (4). In particular, we evaluated ΔG° for the HAT and PT mechanisms for atoms H_A and H_B (Fig. 1). Fig. 3 displays the average values of ΔG° for catechol and resorcinol conformers. The thermodynamically favorable reaction corresponds to the HAT processes. For this mechanism, $\Delta G^\circ < 0$ for all catechol derivatives. In the case of resorcinol compounds, those with alkyl substituents have a negative ΔG° value, while for substituents –CH=CHCOOH, –COOH, –CO$(CH_2)_4CH_3$ and –COH, ΔG° reaches positive values of about 10 kcal mol^{-1}. In all cases, the transfer of an electron has values of approximately 30 kcal mol^{-1}, and the least favorable reactions are the proton transfer reactions, which have ΔG° values of about 50 kcal mol^{-1}. Dihydroxybenzenes in particular constitute compounds with a lower ΔG° value in the HAT mechanism, where substituents have electron donating properties (–CH_3, –CH_2CH_3 and –$CH_2CH_2H_3$). Electron withdrawing groups (–COH, –COOH and –CO$(CH_2)_4CH_3$) however cause the value of ΔG° to increase, this concurs with the experimental results.[1,37] Dihydroxybenzenes with electron donating groups have low acidity constant values compared to bare diphenol;[1,38] therefore, these have greater capacity to transfer a hydrogen as these compounds tend to stabilize the phenoxyl radical. Constrastingly, dihydroxybenzenes with electron withdrawing groups have a higher acidity constant in contrast to diphenol without substituents, therefore these compounds are less susceptible to oxidation by hydrogen transfer, as they tend to stabilize the diphenol form.[6]

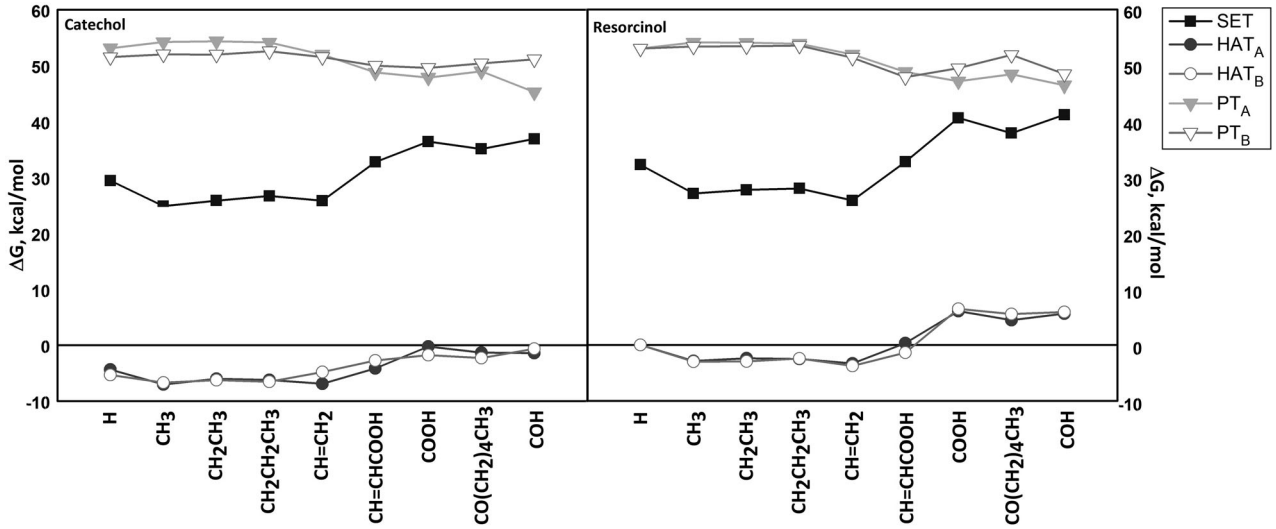

Fig. 3 Average values of Gibbs free energy for the SET, PT and HAT mechanisms with the catechol and resorcinol conformers at 298 K with the M05-2X/6-311g++(d,p) level, using the SMD solvation model to simulate the water as a solvent.

4.2 Electrostatic analysis

Fig. 4 displays the electrostatic potential for analyzing the substituent effect in catechol and resorcinol, together with two substituted analogs with electron withdrawing and with electron donating groups (–COH and –CH_3, respectively). In this figure, we see that the negative charges (blue surface) are located mainly on the oxygen atoms of the hydroxyl groups and on the compounds with the –COH substituent. The distribution of positive charge (red surface) occurs mainly in the aromatic ring, systems substituted with –COH present a large red surface, compared to the –CH_3 substituted systems. This indicates that the substitution of aliphatic groups stabilizes the aromatic ring with respect to the –COH group, mainly due to the inductive donating effect of methyl groups. On the other hand, the electrostatic potential helps to identify the susceptibility to hydrogen atom transfer of a site. Thus for both, catechol and resorcinol, the hydrogen transfer is favored in regions where the electrostatic potential has mostly negative values, *i.e.*, the hydroxyl groups.

4.3 Energy profile and reaction force

According to thermodynamic results for Gibbs free energy, we selected the HAT mechanism (eqn (3)) for the purpose of analyzing the structural and electronic changes involved in this process. In Fig. 5, the structures of the transition states for catechol and resorcinol reacting with the •OOH radical are displayed (all resulting structures are presented in the ESI†). In all cases, the angle between [$O_{diphenol}$–H–$O_{radical}$] is 162.50°, the distance of [$O_{diphenol}$–H] is 1.10 Å and the distance between [$O_{radical}$–H] is 1.30 Å.

With the geometries of transition states at hand, we obtained the path of minimum energy linking transition states with reactants and products through the IRC procedure. Energy and reaction force profiles are displayed in Fig. 6. In the case of catechol, we see that the substitution of any of the three substituents (–H, –CH_3 and –COH) involves exergonic reactions, favoring the HAT with the –CH_3 group as a substituent (Fig. 6a). In resorcinol reactions, the process is endergonic, except for the compound with the substituent group –CH_3 (Fig. 6c).

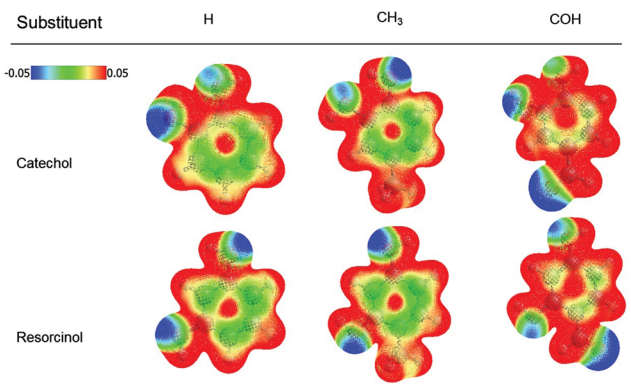

Fig. 4 Surface of electrostatic potential (SEP) catechol and resorcinol with –H, –CH_3 and –COH substituents, with an isovalue of 0.027.

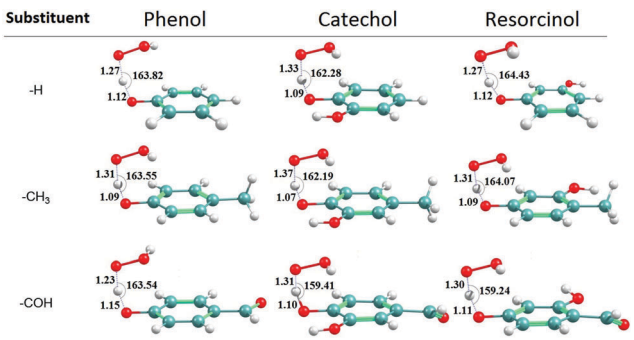

Fig. 5 Structures of the transition state for phenol, catechol and resorcinol with –CH_3, –H, –COH as substituents. The values of bond lengths in angstroms (Å) and angles in degrees (°).

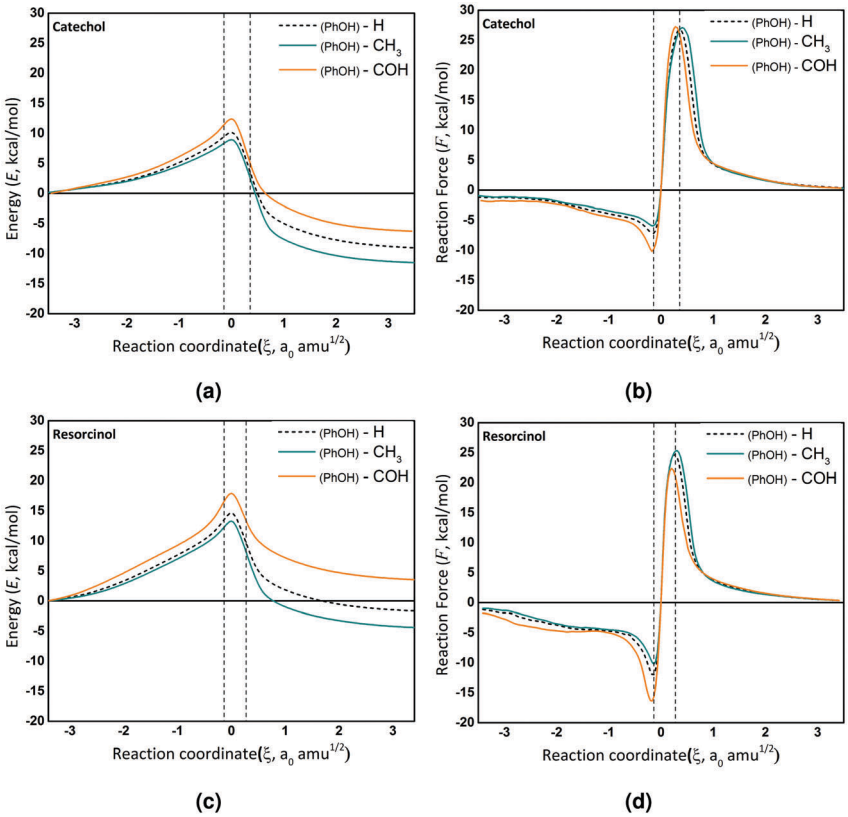

Fig. 6 Energy and reaction force profiles in kcal mol^{-1} for catechol (a and b) and resorcinol (c and d) with substituents: $-CH_3$, −H and −COH.

From the energy profiles, we observed that for all compounds where either catechol or resorcinol was substituted, the order of energy in the region of the products and the transition states was $-CH_3 < -H < -COH$.

The RFA defines three reaction regions that are indicated through vertical dashed lines in Fig. 6. It can be observed that in both cases (catechol and resorcinol reactions) the $-CH_3$ substituted systems present the lower activation energy and lead to the most stable products. Numerical values of reaction and activation energies as well as reaction works used in eqn (7) and (8) to define ΔE° and $\Delta E^{\neq}$ are quoted in Table 1, it can be observed that reactions with $-CH_3$ substitution are thermodynamically and kinetically favored.

The differences observed in the activation energies are mainly due to the fact that the substituents in an aromatic system strongly influence its reactivity. Donor activating groups, as is the case of $-CH_3$ (donor by inductive effect), increase reactivity, these mainly affect the reaction kinetics by stabilizing the transition state through the electron delocalization in the ring. Contrastingly, −COH is an electron acceptor deactivating group by the resonance effect, it decreases the reactivity due to the destabilization of the transition state caused by the positive charge that the substituent induces on the ring. This behavior is reflected in the reaction works shown in Table 1.

In all cases the structural contributions (W_1 and W_4) are larger than their electronic counterparts (W_2 and W_3); meaning that the HAT mechanism is preferably driven by structural rearrangements. In summary, reaction and activation energies indicate that thermodynamically as well as kinetically the most favorable scenario for hydrogen transfer to radicals occurs with $-CH_3$ substituted systems and not with the −COH group

Table 1 Reaction works (W_R), reaction energy (ΔE°) and activation energy ($\Delta E^{\neq}$) associated with the HAT process for catechol and resorcinol with $-CH_3$, −H and −COH substituents. In parentheses the percentages of contribution of the works between W_1–W_2 and W_3–W_4. All values are expressed in kcal mol^{-1}

Moiety	Substituent	W_1	W_2	W_3	W_4	ΔE°	$\Delta E^{\neq}$
Catechol	$-CH_3$	8.33 (93%)	0.60 (7%)	−7.64 (37%)	−12.82 (63%)	−11.54	8.93
	−H	9.47 (93%)	0.67 (7%)	−6.55 (34%)	−12.64 (66%)	−9.05	10.14
	−COH	11.14 (90%)	1.22 (10%)	−5.09 (27%)	−13.52 (73%)	−6.25	12.36
Resorcinol	$-CH_3$	12.28 (93%)	0.98 (7%)	−5.99 (34%)	−11.66 (66%)	−4.39	13.25
	−H	13.54 (92%)	1.07 (8%)	−4.92 (30%)	−11.33 (70%)	−1.65	14.61
	−COH	16.06 (90%)	1.81 (10%)	−3.05 (21%)	−11.26 (79%)	3.55	17.87

as it would be expected, this trend is observed for reactions with both catechol and resorcinol.

4.4 Spin densities

In order to explain why W_3 is larger than W_2 (Table 1), in Fig. 7 we have plotted spin density at the critical points of the reaction force for the catechol and resorcinol systems without substituent. The changes observed are mainly due to the electronic transfer from the oxygen (O^9) of the peroxyl radical ($^{\bullet}O^9O^{10}H$) towards the aromatic ring. The reaction work W_2 ($\xi_1 - \xi_{TS}$) explains the spin transfer of 0.06e from O^9 of the radical to O^6 of the phenol. While W_3 ($\xi_{TS} - \xi_2$) is mainly associated with a spin density of about 0.10e distributed in the aromatic rings of catechol and resorcinol. Therefore, the electronic changes that predominate in W_3 correspond to a higher distribution of spin density in the aromatic ring.

4.5 Reaction electronic flux and electronic population analysis

For a detailed analysis of the reaction electronic flux, in Fig. 8 we present its behavior for catechol and resorcinol. We first note that the trend followed by the REF is similar for catechol and resorcinol with different substituents. The REF initiates exhibiting an equilibrium trend until leaving the reactant region where a positive peak starts to develop reaching a maximum within the transition state region. This means that most electronic activity takes place inside the transition state region. Positive values of the REF indicates that bond strengthening/forming processes drive the reaction. In particular this peak may be attributed to the prevalence of the OH bond forming process to produce hydrogen peroxide. Then, entering the product region a negative peak indicates that bond weakening processes drive the reaction in this region. The low intensity negative peak should be associated with the achievement of the OH breaking as well as other bond weakening taking place within the aromatic rings. Finally the REF attains a zero regime indicating that the electronic activity ceases and the reaction gets terminated.

Small differences observed in terms of the catechol and resorcinol systems are associated with the intensity of the electronic flux, which in the case of the resorcinol system is 10 kcal mol$^{-1}\cdot\xi$ more intense. The $-CH_3$ substituent donates electrons to the ring by the sigma bond $C^{\delta+}(CH_3)$–$C^{\delta-}$(ring), generating delocalization in the aromatic ring (which can be observed in the SEP analysis shown in Fig. 4). Note that this activating group is directed from the *ortho* and *para* positions, which is why the largest electronic effect occurs for resorcinol because the O–H group (participant in the hydrogen transfer) is in the *para* position with respect to the $-CH_3$ substituent.

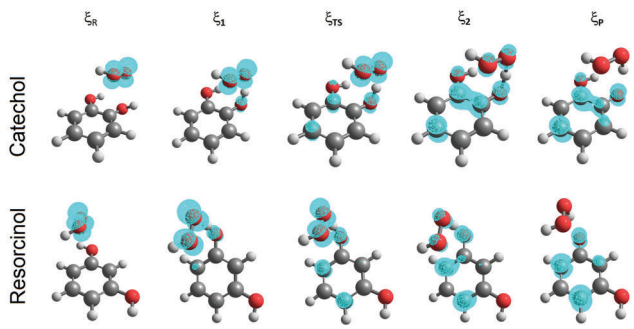

Fig. 7 Spin density calculated at the M05-2X/6-311++G(d,p) level.

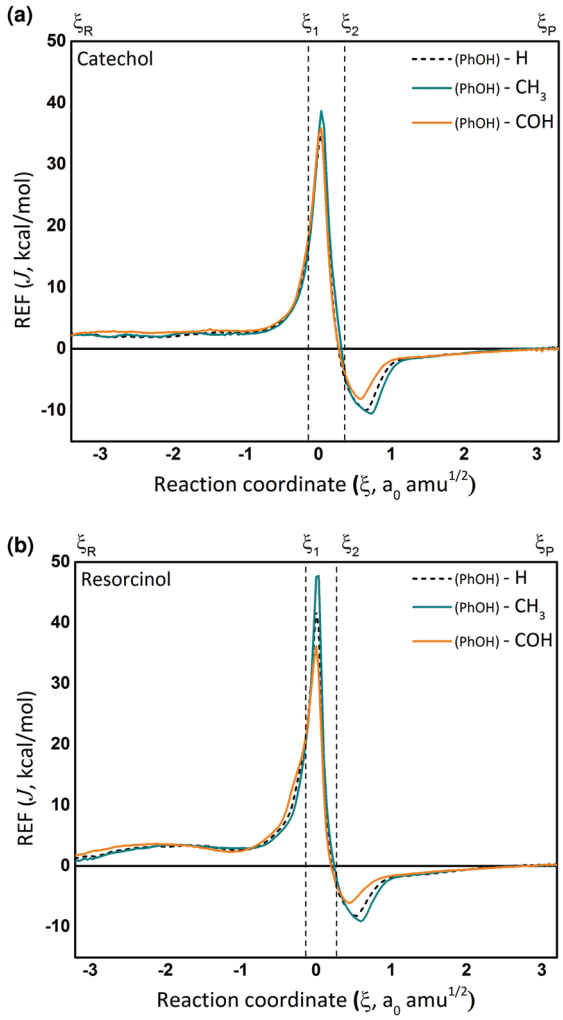

Fig. 8 Reaction electronic flux (REF, $J(\xi)$) profiles for (a) catechol and (b) resorcinol with $-CH_3$, $-H$ and $-COH$ substituents.

In order to complement REF analysis, bond orders were obtained from the Natural Bond Orbital (NBO) analysis (displayed in Fig. 9), to identify the main electronic activity taking place during the reaction evidenced by the REF. Notably, all the reactions with the different substituents showed similar trends, with no major differences. This is why bare catechol and resorcinol profiles were taken as representative for further analysis. We first note that most electronic activity is concentrated within the transition state region, as predicted by the REF profiles.

The REF profile and bond order analysis show consistently that all reactions begin with an equilibrium condition in the electron density from ξ_R to ξ_1, this then gives way at the transition state region to spontaneous changes in electron density, mainly associated with O_9–H_7 bond formation and C_3–O_6 bond strengthening.

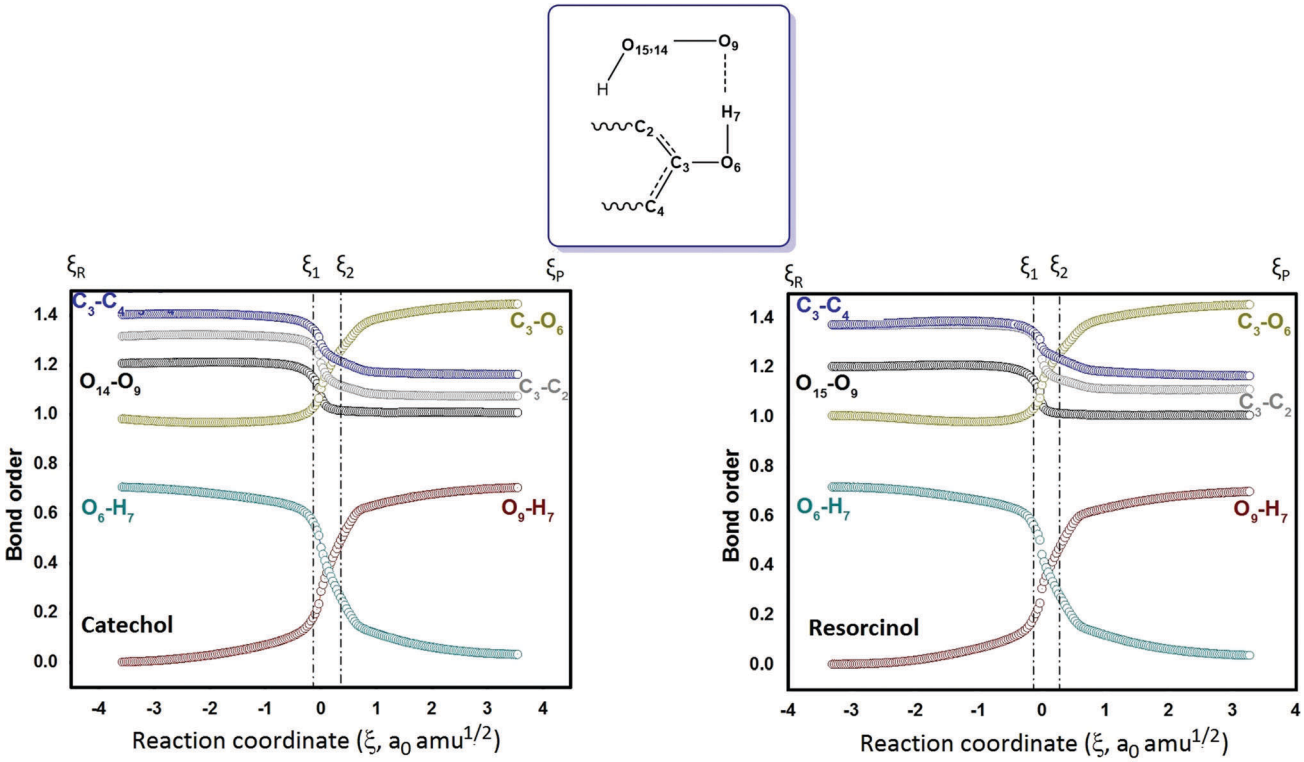

Fig. 9 Natural bond orbital analysis for catechol and resorcinol as function of reaction coordinate. Bond lengths C_3–C_4 (blue), C_3–C_2 (gray), C_3–O_6 (brown), O_6–H_7 (light blue) and O_9–H_7 (red), in particular the bond lengths in black for O_{14}–O_9 (catechol) and O_{15}–O_9 (resorcinol).

However, in the product region the non-spontaneous electron density rearrangements are mainly due to O_6–H_7 bond breaking and C_3–C_2 and C_3–C_4 bond weakening that pertain to the aromatic ring. The reactions end when the REF ceases to change giving rise to an equilibrium regime for all the electronic properties.

5 Conclusions

In this work, we have compared the activity of substituted catechols and resorcinols, acting as antiradicals or antioxidants against the $^{\bullet}$OOH radicals, using a variety of computational chemistry tools. According to the ΔG° values, the thermodynamically favorable mechanism resulted in the transfer of a hydrogen atom. Then we have analyzed this mechanism in detail, using the reaction force analysis and the reaction electronic flux. We were able to unveil the structural and electronic effects that predominate during the HAT mechanism. The RFA permitted to unveil the physical nature of all activation energies, it was found to be mostly structural, however electronic effects played key roles within the transition state regions where most electronic activity takes place. On the other hand, although the structural works (W_1 and W_4) show a greater contribution with respect to the works associated with electronic changes, it has been shown that the electronic changes have an important contribution in the HAT mechanism since W_3 is related to a greater distribution of the density of spin in the aromatic ring. The $-CH_3$ group decreases activation and reaction energies, in contrast to the –COH group that increases both energies with respect to the unsubstituted systems. All data collected in this work indicate that the HAT mechanism is favored in catechol and resorcinol substituted with the $-CH_3$ group, this is explained by the distribution of the extra negative charge supplied to the aromatic ring by the electron donor $-CH_3$ group.

Acknowledgements

We thank the Laboratorio de Supercómputo y Visualización en Paralelo at the Universidad Autónoma Metropolitana-Iztapalapa for access to their computer facilities. The authors thank the Nucleus Millenium no. 120082 "Chemical Processes and Catalysis" and the FONDECYT Grants no. 1141098. R. D. acknowledges the VRI-PUC fellowship. This project also has been supported by CONACYT, México, through project 154784, and scholarship 371984.

References

1 Z. Rappoport, *The Chemistry of Phenols*, Wiley, England, 2003.
2 M. C. Foti, *J. Pharm. Pharmacol.*, 2007, **59**, 1673–1685.
3 C. M. Galanakis, V. Goulas, S. Tsakona, G. A. Manganaris and V. Gekas, *Int. J. Food Prop.*, 2013, **16**, 382–396.
4 D. Prakash, S. Suri, G. Upadhyay and B. N. Singh, *Int. J. Food Sci. Nutr.*, 2007, **58**, 18–28.
5 A. Galano, L. Muñoz-Rugeles, J. R. Alvarez-Idaboy, J. L. Bao and D. G. Truhlar, *J. Phys. Chem. A*, 2016, **120**, 4634–4642.

6 G. Brigati, M. Lucarini, V. Mugnaini and G. F. Pedulli, *J. Org. Chem.*, 2002, **67**, 4828–4832.
7 S. A. Ordoudi, M. Z. Tsimidou, A. P. Vafiadis and E. G. Bakalbassis, *J. Agric. Food Chem.*, 2006, **54**, 5763–5768.
8 A. Galano, G. Mazzone, R. Alvarez-Diduk, T. Marino, J. R. Alvarez-Idaboy and N. Russo, *Annu. Rev. Food Sci. Technol.*, 2016, **7**, 335–352.
9 R. B. Durairaj, *Resorcinol derivatives*, Springer Berlin Heidelberg, Berlin, Heidelberg, 2005, pp. 37–116.
10 E. Alvarez-Parrilla, L. A. de la Rosa, J. Rodrigo-García, R. Escobedo-González, G. Mercado-Mercado, E. Moyers-Montoya, A. Vázquez-Flores and G. A. González-Aguilar, *Food Chem.*, 2007, **101**, 1346–1356.
11 C. Ortega-Moo, J. Garza and R. Vargas, *Theor. Chem. Acc.*, 2016, **135**, 177.
12 N. Robledo-O'Ryan, M. J. Matos, S. Vazquez-Rodriguez, L. Santana, E. Uriarte, M. Moncada-Basualto, F. Mura, M. Lapier, J. D. Maya and C. Olea-Azar, *Bioorg. Med. Chem.*, 2017, **25**, 621–632.
13 A. Galano, R. Álvarez-Diduk, M. T. Ramírez-Silva, G. Alarcón-Ángeles and A. Rojas-Hernández, *Chem. Phys.*, 2009, **363**, 13–23.
14 G. Litwinienko and K. U. Ingold, *Acc. Chem. Res.*, 2007, **40**, 222–230.
15 A. Martínez, A. Galano and R. Vargas, *J. Phys. Chem. B*, 2011, **115**, 12591–12598.
16 R. Apak, M. Ozyurek, K. Guclu and E. Capanoglu, *J. Agric. Food Chem.*, 2016, **64**, 997–1027.
17 M. Leopoldini, T. Marino, N. Russo and M. Toscano, *J. Phys. Chem. A*, 2004, **108**, 4916–4922.
18 M. L. Cerón, E. Echegaray, S. Gutiérrez-Oliva, B. Herrera and A. Toro-Labbé, *Sci. China: Chem.*, 2011, **54**, 1982–1988.
19 A. Toro-Labbé, *J. Phys. Chem. A*, 1999, **103**, 4398–4403.
20 P. Jaque and A. Toro-Labbé, *J. Phys. Chem. A*, 2000, **104**, 995–1003.
21 R. Durán, E. Vöhringer-Martinez, A. Toro-Labbé and B. Herrera, *J. Mol. Model.*, 2016, **22**, 1–10.
22 N. Villegas-Escobar, S. Gutiérrez-Oliva and A. Toro-Labbé, *J. Phys. Chem. C*, 2015, **119**, 26598–26604.
23 D. E. Ortega, S. Gutiérrez-Oliva, D. J. Tantillo and A. Toro-Labbé, *Phys. Chem. Chem. Phys.*, 2015, **17**, 9771–9779.
24 D. Cortés-Arriagada, S. Gutiérrez-Oliva, B. Herrera, K. Soto and A. Toro-Labbé, *J. Chem. Phys.*, 2014, **141**, 134701.
25 S. Giri, E. Echegaray, P. W. Ayers, A. S. Nunez, F. Lund and A. Toro-Labbé, *J. Phys. Chem. A*, 2012, **116**, 10015–10026.
26 D. Guzmán-Angel, R. Inostroza-Rivera, S. Gutiérrez-Oliva, B. Herrera and A. Toro-Labbé, *Theor. Chem. Acc.*, 2016, **135**, 37.
27 M. J. Frisch, G. W. Trucks, H. B. Schlegel, G. E. Scuseria, M. A. Robb, J. R. Cheeseman, G. Scalmani, V. Barone, B. Mennucci, G. A. Petersson, H. Nakatsuji, M. Caricato, X. Li, H. P. Hratchian, A. F. Izmaylov, J. Bloino, G. Zheng, J. L. Sonnenberg, M. Hada, M. Ehara, K. Toyota, R. Fukuda, J. Hasegawa, M. Ishida, T. Nakajima, Y. Honda, O. Kitao, H. Nakai, T. Vreven, J. A. Montgomery, Jr., J. E. Peralta, F. Ogliaro, M. Bearpark, J. J. Heyd, E. Brothers, K. N. Kudin, V. N. Staroverov, R. Kobayashi, J. Normand, K. Raghavachari, A. Rendell, J. C. Burant, S. S. Iyengar, J. Tomasi, M. Cossi, N. Rega, J. M. Millam, M. Klene, J. E. Knox, J. B. Cross, V. Bakken, C. Adamo, J. Jaramillo, R. Gomperts, R. E. Stratmann, O. Yazyev, A. J. Austin, R. Cammi, C. Pomelli, J. W. Ochterski, R. L. Martin, K. Morokuma, V. G. Zakrzewski, G. A. Voth, P. Salvador, J. J. Dannenberg, S. Dapprich, A. D. Daniels, Ö. Farkas, J. B. Foresman, J. V. Ortiz, J. Cioslowski and D. J. Fox, *Gaussian 09 Revision A.1*, Gaussian Inc., Wallingford, CT, 2009.
28 Y. Zhao, N. E. Schultz and D. G. Truhlar, *J. Chem. Theory Comput.*, 2006, **2**, 364–382.
29 R. Krishnan, J. S. Binkley, R. Seeger and J. A. Pople, *J. Chem. Phys.*, 1980, **72**, 650–654.
30 A. V. Marenich, C. J. Cramer and D. G. Truhlar, *J. Phys. Chem. B*, 2009, **113**, 6378–6396.
31 R. Valero, R. Costa, I. de P. R. Moreira, D. G. Truhlar and F. Illas, *J. Chem. Phys.*, 2008, **128**, 114103.
32 Y. Zhao and D. G. Truhlar, *Theor. Chem. Acc.*, 2008, **120**, 215–241.
33 E. D. Glendening, J. K. Badenhoop, A. E. Reed, J. E. Carpenter, J. A. Bohmann, C. M. Morales, C. R. Landis and F. Weinhold, *NBO 6.0*, Weinhold, Theoretical Chemistry Institute, University of Wisconsin, Madison, 2013.
34 S. Gutiérrez-Oliva, B. Herrera, A. Toro-Labbé and H. Chermette, *J. Phys. Chem. A*, 2005, **109**, 1748–1751.
35 R. Vargas, A. Cedillo, J. Garza and M. Galván, in *Reactivity criteria in spin-polarized density functional theory*, ed. K. D. Sen, World Scientific, Singapore, 2002, pp. 936–965.
36 M. Galván, A. Vela and J. L. Gázquez, *J. Phys. Chem.*, 1988, **92**, 6470–6474.
37 M. Krogsgaard, V. Nue and H. Birkedal, *Chem. – Eur. J.*, 2016, **22**, 844–857.
38 M. D. Liptak, K. C. Gross, P. G. Seybold, S. Feldgus and G. C. Shields, *J. Am. Chem. Soc.*, 2002, **124**, 6421–6427.

THE JOURNAL OF PHYSICAL CHEMISTRY C

Article

pubs.acs.org/JPCC

Why Low Valent Lead(II) Hydride Complex Would be a Better Catalyst for CO_2 Activation than Its 14 Group Analogues?

Nery Villegas-Escobar,[†] Daniela E. Ortega,[†] Diego Cortés-Arriagada,[‡] Rocío Durán,[†] Diana Yepes,[§] Soledad Gutiérrez-Oliva,[†] and Alejandro Toro-Labbé*[,†,∥]

[†]Nucleus Millennium Chemical Processes and Catalysis (CPC), Laboratorio de Química Teórica Computacional (QTC), Facultad de Química, Pontificia Universidad Católica de Chile, Casilla 306, Correo 22, Santiago, Chile

[‡]Programa Institucional de Fomento a la Investigación, Desarrollo e Innovación, Universidad Tecnológica Metropolitana, Ignacio Valdivieso 2409, P.O. Box 8940577, San Joaquín, Santiago, Chile

[§]Departamento de Ciencias Químicas, Facultad de Ciencias Exactas, Universidad Andres Bello, Avenida República 275, Santiago, Chile

[∥]Freibourg Institute for Advanced Studies (FRIAS), Albert-Ludwigs-Universität Freiburg, Albertstrasse 19, D-79104 Freiburg, Germany

Supporting Information

ABSTRACT: A low valent $Pb^{(II)}$ hydride complex with NacNac ligand (NacNac = $[ArNC(Me)CHC(Me)NAr]^-$, with Ar = 2,6−$iPr_2C_6H_3$) is predicted to be the best catalyst for CO_2 activation compared to its $Ge^{(II)}$ and $Sn^{(II)}$ analogues, which have been experimentally reported (Jana, A., et al. *J. Am. Chem. Soc.* **2009**, 131, 1288;Jana, A. et al. *Angew. Chem. Int. Ed.* **2009**, 48, 1106). The CO_2 activation mechanism mediated by $Ge^{(II)}$, $Sn^{(II)}$ and $Pb^{(II)}$ catalysts was studied in toluene using density functional theory calculations. The results show that the activation can be carried out through two reaction pathways, giving rise to two different conformers which have been computationally predicted for the first time. In all the cases, the activation process was thermodynamically favored, in addition, the $Pb^{(II)}$ catalyst exhibited the lowest activation energy, compared with $Ge^{(II)}$, $Sn^{(II)}$, and even $Si^{(II)}$. Thus, it was found that, going down in group 14, the reactivity of the NacNac based complexes toward CO_2 activation increases considerably. This result is due to the increase of the acidic character of the metal as the metal size increases causing a more polar $^{\delta+}$**M**−$H^{\delta-}$ bond, which allows an easier channel for the hydride transfer reaction. Interestingly, a linear dependence between activation energies and the polarity of the **M**−H bond was found. Additionally, a detailed characterization of possible interconversions between the products of activation helps to explain the X-ray structures obtained to date. Most importantly, it was found that the direct interconversion of the products obtained after the addition of CO_2 from each reaction pathway is not possible, and can be reached by means of subsequent C−O and M−O bond torsions. Our calculations suggest that the CO_2 activation catalyzed by $Pb^{(II)}$−NacNac hydride complex would be both thermodynamically and kinetically viable. The reactivity trend found in this work contributes to the growing development of CO_2 activation by transition metal-free catalysts.

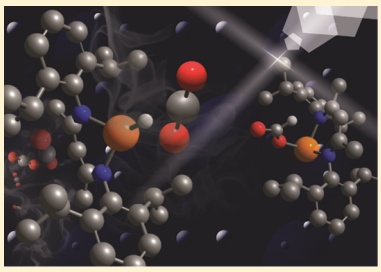

1. INTRODUCTION

Massive CO_2 production has been linked to a deep atmospheric impact, whose origins are coming from natural and anthropogenic sources.[1] It is well-known that CO_2 is largely responsible for greenhouse gases, causing "global warming". In this regard, the United States Environmental Protection Agency (US-EPA) reported that carbon dioxide was responsible for the 82% of the greenhouse gas emissions, with an equivalent to 6.673 million metric tons of CO_2.[2] Although a portion of CO_2 concentrations can be removed naturally by plants via the carbon cycle,[3,4] additional tools should be developed to reduce such concentrations by means of techniques that allow the control and transformation of the pollutant gases. This problem has caught the attention of specialists to make unflagging efforts to reduce the CO_2 concentrations from the atmosphere.

Nowadays, several chemical methods have been developed for the CO_2 transformation, but only a few of them have been industrially used.[5,6] One of the most widely implemented is the urea synthesis, which utilizes CO_2 in its main process.[5−7] Synthesis of poly and cyclic carbonates is another recent industrialized process, which uses the reaction of CO_2 with epoxides in the presence of a catalyst.[8,9] In a minor scale, CO_2 has been also used as feedstock for organic synthesis, such as carboxylations of C−H bonds[10,11] and N−H bonds.[11]

Furthermore, some recent advances in CO_2 fixation have reported the use of N-heterocyclic carbenes (NHCs) to form imidazolium carboxylates.[12,13] In this sense, improvements in

Received: January 10, 2017
Revised: May 15, 2017
Published: May 16, 2017

DOI: 10.1021/acs.jpcc.7b00278
J. Phys. Chem. C 2017, 121, 12127−12135

reducing CO_2 have been achieved with transition metal (TMs) NHC complexes.[14,15] Strategies mentioned above exhibit good results in fixation and activation of CO_2 under mild reaction conditions.[16−19] Moreover, other recent leading synthetic methodology in CO_2 fixation is easily accomplished by means of using TM through incorporation of this gas into complexes containing M−C bonds.[20−24]

Recently, Jana and co-workers have reported the CO_2 reduction by using stable low-valent $Ge^{(II)}$[25] and $Sn^{(II)}$[26] hydrides coordinated to *N*-arylisopropyl-*β*-diketiminate [also known as NacNac ligand (NacNac = [ArNC(Me)CHC(Me)-NAr]$^-$ with Ar = 2,6−iPr$_2$C$_6$H$_3$)] (see complexes **1** and **2** in Scheme 1). On the other hand, efforts to obtain the low valent

Scheme 1. CO_2 Activation by the Main Group $Ge^{(II)}$ (1), $Sn^{(II)}$ (2), and $Pb^{(II)}$ (3) Based Catalyst[a]

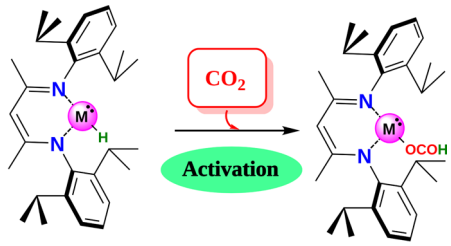

M=Ge(II), **1**; Sn(II), **2**; Pb(II), **3**

[a]CO_2 insertion in the **M**−H bond is schematized in color-code.

silicon(II) hydride derivative have been made but without success.[27] Unfortunately, the synthesis strategies for Ge and Sn analogues do not apply for silicon, most probably due to its high reactivity. The synthesis of **1** and **2** is carried out from the corresponding germanium(II) and tin(II) chlorides, NacNac-GeCl and NacNacSnCl, respectively. The reaction is carried out by exchange of the chloride by the hydride through a Cl/H metathesis reaction. For $Si^{(II)}$ the NacNacSiCl derivative is not accessible. Likewise, although lead *β*-diketiminate halide,[28,29] aryloxide,[30] amido,[31] anilido,[31] alkoxide,[29,32,33] alkyl,[34] and phosphanide[32] among other complexes have been synthesized, no evidence for a hydride lead complex has been obtained to date. Moreover, CO_2 activation has been observed for tin and lead NacNac alkoxides, in which the dependence of the reaction rate and reversibility of the reaction is sensible upon minor changes in the alkoxide unit.[33,35]

The high impact of using main group (MG) low-valent complexes comes from the fact that they can react either through the lone pair of electrons on the metal center, in a carbene-like behavior[36−40] and/or by a hydride transfer reaction, allowing a high effectiveness toward the activation of small molecules.[25,26,39] The latter is important because the activation of small molecules is a key step in most of the catalytic cycles, and this has been an exclusive feature for TM catalyst. In this regard, MG elements have emerged as alternative compounds of the traditional TMs complexes.[39,41] Most of the TM based catalysts are expensive and soluble in the reaction medium (homogeneous catalysis), even with low recovery. Otherwise, MG based complexes are cheaper and "greener" than TMs,[37,39,41,42] therefore they have become good candidates for a new branch of catalytic applications. Surprisingly, several complexes containing low valent MG elements react at room temperature without using any cocatalyst.[25,26,43]

Takagi and Sakaki[44] have performed a density functional theory (DFT) investigation to predict the catalytic cycle of **1** with $(CH_3)_2CO$, Ph_2CO and CF_3PhCO ketones, comparing the results with the organometallic catalyst $(PPh_3)_2RhH$. They found that ketones easily react with **1** to afford the corresponding $Ge^{(II)}$ alkoxide. Also, a catalytic cycle for CO_2 activation was proposed, in which SiF_3H was used as a hydride-source to restore the catalyst. However, to the best of our knowledge, no further theoretical studies for CO_2 activation using **1** have been reported; and no exploration using it with heavier elements of the group have neither been attempted. Moreover, further analysis are necessary for a deeper understanding of the catalytic activity and applicability of MG based complexes in chemical reactions.

In this contribution, the use of MG catalysts (**1**−**3**) in the activation of CO_2 was explored by means of quantum chemistry calculations. A full analysis of the reaction products was carried out with the aim of explaining accessible conformational isomers that can be formed after activation. All the analyses serve as proof that system **3** would perform better than the already synthesized complexes **1** and **2**.

2. COMPUTATIONAL DETAILS

All the calculations were carried out at the DFT level using the hybrid meta-GGA M06-2X functional.[45] This method was selected because it is highly recommended for main group computations in order to obtain accuracy in both kinetic and thermochemistry as well as to correctly describe noncovalent interactions.[45−47] Ge, Sn, and Pb were treated with the LANL2DZ basis sets and quasi-relativistic effective core potentials;[48] C, H, N, and O atoms were treated with the 6-31G(d,p) basis sets.[49,50] For comparison purposes, the activation of CO_2 was computed using the larger 6-311+G(d,p) basis set for the above-mentioned atoms by performing single point calculations on the optimized structures obtained with the 6-31G(d,p) basis. Stationary points and transition states (TS) were verified by frequency calculations using analytic second derivatives.[51] The Berni Synchronous Transit-Guided Quasi-Newton (STQN) algorithm was used for searching the TS geometries.[52,53] TS structures were connected with reactants and products using the intrinsic reaction coordinate methodology (IRC)[54−56] in mass-weighted Cartesian coordinates, using a step size of 0.100 amu$^{1/2}$ bohr. To take into account solvent effects (toluene with a electric constant of 2.3741), single point computations were carried out on the optimized gas-phase geometries via the Polarizable Continuum Model (PCM).[57] The reason for doing so is because optimization of the TS structures using PCM encountered convergence problems when Sn and Pb were used. All computations were performed in the Gaussian 09 software package.[58] Wave function analyses were performed in the Multiwfn analyzer.[59] The reported charges correspond to the natural atomic charges (NBO).[60]

3. RESULTS AND DISCUSSION

In a first stage, the interaction of CO_2 with each of the catalysts is expected to be charge-controlled, forming the reactant complex (**R**); then orbital-controlled interactions will rule the second step, i.e., the activation of CO_2 by the MG-complex. There are two ways in which CO_2 approaches the catalyst, giving rise to different TS structures and products (Figure 1). The first reaction path is obtained when the CO_2 molecule

DOI: 10.1021/acs.jpcc.7b00278
J. Phys. Chem. C 2017, 121, 12127−12135

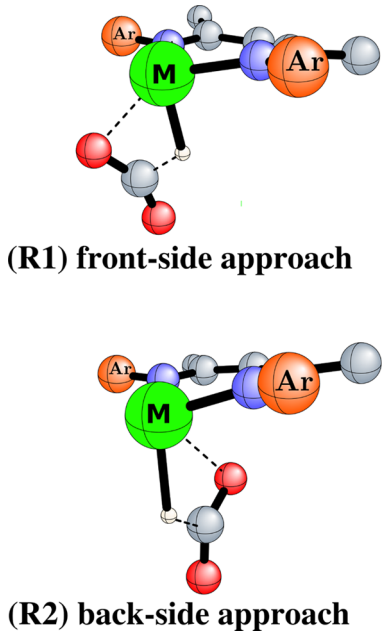

Figure 1. Two approaches of CO_2 to the **1**−**3** MG-complexes. Hydrogen atoms attached to carbons and **Ar** = 2,6-iPr$_2$C$_6$H$_3$ are omitted from the molecular representations. Oxygens in red, nitrogens in blue, carbons in gray, and hydride in white.

frontally approaches the **M**−H bond in the complex (the front-side approach); the second reaction path arises from the backward approach of CO_2, this is the back-side approach. In Figure 1, the front-side and back-side approaches are labeled as reactions **R1** and **R2**, respectively. In both cases, the reaction mechanism does not change significantly, although different conformational stereoisomers are obtained as final products. Note in Figure 1 that the hydride complexes exhibit an *endo* conformation where the metal center and the hydride are below the NCCCN plane and the **M**−H bond is roughly perpendicular to the same plane. The latter is in agreement with related alkoxide complexes with nonbulky alkyl substituents. On the other hand, bulky ligands are observed to adopt an *exo* conformation.[34,61]

In the isolated CO_2 molecule, the carbon atom behaves as an electron deficient center with a charge (Q) of +1.06|*e*|, while the atomic charge per oxygen atom is −0.53|*e*|. In complexes **1**−**3**, the hydrogen atom bonded to the metal center behaves as a hydride; it appears negatively charged, −0.32|*e*| (**1**), −0.40|*e*| (**2**), and −0.41|*e*| (**3**), due to its higher electronegative character compared to Ge, Sn, and Pb [2.20 (H), 2.01 (Ge), 1.96 (Sn), and 1.87 (Pb) in the Pauling scale].[62,63] The increase of the negative charge on the hydride atom correlates well with the respective charge depletion for the metal center, + 0.83|*e*| (Ge), + 1.00|*e*| (Sn), and +1.02|*e*| (Pb), as their electronegativities decrease. An important result arises here, which will serve as a proof to establish the reactivity trend in group 14 NacNac catalysts. The difference between the metal atomic charge and that on the hydride atom ($\Delta Q_{M-H} = |Q_M - Q_H|$) serves as indicator of the polarity of the **M**−H bond. The larger the value of ΔQ_{M-H}, the larger is the **M**−H bond polarity. The values obtained for ΔQ_{M-H} are 1.15|*e*|, +1.40|*e*|, and +1.43|*e*| for complexes **1**, **2**, and **3**, respectively. These values will be discussed in section 3.2. On the other hand, two electrostatic interactions would drive the CO_2 approach to the **M**−H fragment; these are the C···H and O···**M** interactions. The molecular electrostatic potential depicted in Figure 2 characterizes these specific interactions. Additionally, the H···O and **M**···C interactions are electrostatically destabilizing, and consequently, the **M**−COOH product is not allowed.

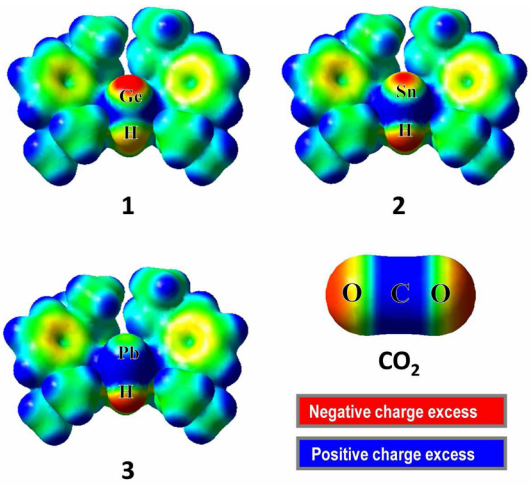

Figure 2. Molecular electrostatic potential of complexes **1**−**3** and CO_2. The molecular orientation is the same as that in Figure 3.

On the other hand, frontier molecular orbitals were examined to rationalize the orbital-controlled interaction between the reactants. Figure 3 depicts the densities for the highest occupied (HOMO) and lowest unoccupied molecular orbitals (LUMO) of CO_2 molecule and complexes **1**−**3**. As observed, the HOMO is localized on the metal center and the hydride atom, with contributions of 56% (systems **1** and **2**) and 6% (**3**) from the metal and of up to 20% from the 1*s* orbital of the hydride. These results indicate that when the CO_2 molecule is close enough to the **M**−H bond, the 1*s* orbital of H will interact with the LUMO orbital of CO_2, which is mainly centered on the carbon atom (62%) with $2p_y$ and $3p_y$ atomic orbitals contributing the most.

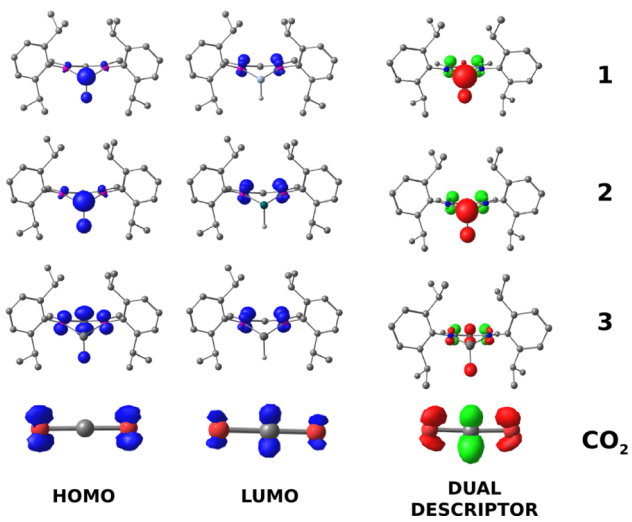

Figure 3. HOMO and LUMO densities and dual descriptor computed for the complexes **1**−**3** and CO_2 molecule. For dual descriptor, nucleophilic and electrophilic zones are represented in red and green, respectively. Hydrogen atoms attached to carbons were omitted from molecular representations.

DOI: 10.1021/acs.jpcc.7b00278
J. Phys. Chem. C 2017, 121, 12127−12135

Table 1. Interaction Energy of the Reactant Complex ($E_R = E_{(C\ CO_2)R} - (E_C + E_{CO_2})$), Activation ($\Delta E^{\ddagger} = E_{(C\ CO_2)TS} - (E_C + E_{CO_2})$), Reverse Activation ($\Delta E_r^{\ddagger} = E_{(C\ CO_2)TS} - E_{(C\ CO_2)P}$), and Reaction Energy ($\Delta E^{\circ} = E_{(C\ CO_2)P} - (E_C + E_{CO_2})$); $E_{(C\ CO_2)R}$, $E_{(C\ CO_2)TS}$, and $E_{(C\ CO_2)P}$ Correspond to the Energy of the Complex-CO_2 System in the Reactant Complex, Transition State, and Product, Respectively[a]

reaction	E_R	$\Delta E^{\ddagger}$	$\Delta G^{\ddagger}$ (%$T\Delta S^{\ddagger}$)	$\Delta E_r^{\ddagger}$	ΔE°	ΔG°	k (s^{-1})
(1 + CO_2)@R1	0.4	14.8 (14.0)	24.8 (41)	35.7	−20.9 (−19.8)	−12.2	4.1×10^{-6}
(1 + CO_2)@R2	−2.9	13.3 (10.8)	24.6 (50)	34.9	−21.6 (−21.0)	−11.1	5.8×10^{-6}
(2 + CO_2)@R1	−3.5	8.6 (6.7)	19.3 (58)	33.5	−24.0 (−25.0)	−13.4	4.4×10^{-2}
(2 + CO_2)@R2	−4.0	8.7 (6.3)	19.2 (57)	33.3	−24.7 (−25.1)	−14.5	5.2×10^{-2}
(3 + CO_2)@R1	−3.3	3.8 (2.1)	13.6 (74)	29.0	−25.3 (−25.7)	−13.2	6.7×10^{2}
(3 + CO_2)@R2	−3.2	4.4 (2.2)	15.7 (76)	28.5	−24.9 (−24.7)	−14.8	1.9×10^{1}
(Si*+ CO_2)@R1	0.0	21.2 (20.8)	32.5(33)	42.4	−21.2 (−17.5)	−9.3	9.3×10^{-12}
(Si*+ CO_2)@R2	−0.1	20.0 (18.0)	28.0(27)	39.4	−19.4 (−20.0)	−11.4	1.9×10^{-8}

[a] E_C and E_{CO_2} are energies of the isolated complex and CO_2, respectively. $\Delta E^{\ddagger}$ and ΔE° were also computed using the 6-311+G(d,p) basis set (in parentheses). Direct Gibbs free energies ($\Delta G^{\ddagger}$) along with the percentage of the entropic contribution of activation (%$T\Delta S^{\ddagger}$) is also reported. Rate constants (k) were estimated according to transition state theory at standard ambient temperature (298.15 K), assuming a first order (unimolecular) reaction (note that reactions are bimolecular). Values reported in toluene (gas phase energies are given in the Supporting Information). All energies are referenced to the isolated reactants, given in kcal mol^{-1} and corrected with zero point energies.

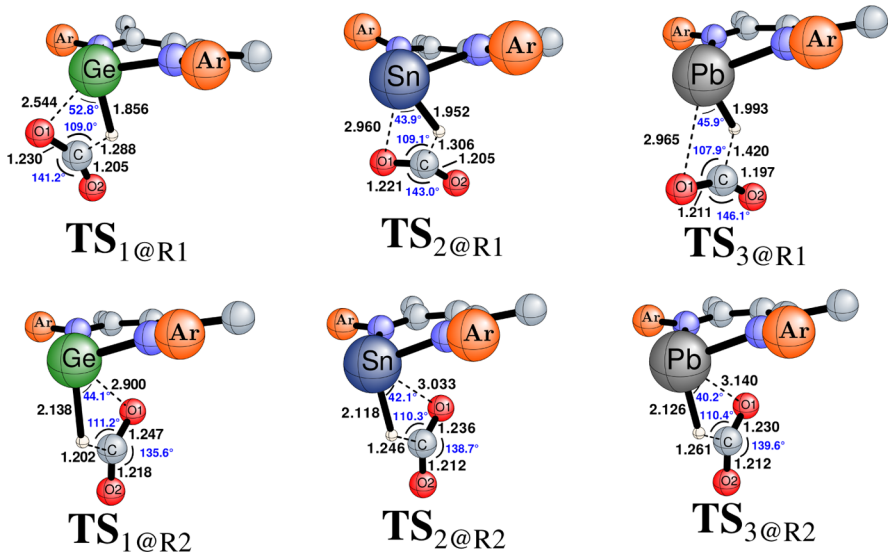

Figure 4. Transition state structures for both front- and back-side approaches (**R1** and **R2**), respectively. Hydrogens attached to carbons and **Ar** = 2,6-$iPr_2C_6H_3$ are omitted from the molecular representations. Bond distances and angles are in (Å) and degrees (deg), respectively.

In addition, the dual descriptor[64,65] was computed to characterize the reactivity of the systems **1**−**3**, which allows to rationalize the reactivity in terms of the simultaneous knowledge of nucleophilic and electrophilic sites within a molecule.[66−71] Dual descriptor of complexes **1**−**3** and CO_2 are shown in Figure 3; nucleophilic and electrophilic sites are represented in red and green, respectively. Hydride is characterized as a high nucleophilic site, while the nucleophilic character of the metal center progressively dissapears from Ge to Pb. The reaction is initiated by the nucleophilic attack of the hydride to the carbon atom of CO_2. Once the reactant complex is formed, the reaction mechanism involves the following main chemical events: (i) breaking of the σ**M**−H bond and (ii) formation of a C−H bond; coordination of CO_2 takes place through formation of a **M**−O bond.

3.1. The Reactant Complex. As noted above, the reaction mechanism starts with the electrostatic interaction between the CO_2 molecule and the MG-complex, giving rise to the reactive complex **R**. For all the systems, the distance between the hydride and the carbon atom of CO_2 (**M**−H···CO_2) is ∼2.5 Å, with weak interaction energies ranging from −4.0 to 0.4 kcal mol^{-1} (Table 1). Reaction of **1** with CO_2 through the front-side approach, (1 + CO_2)@R1, shows the weakest interaction energy of the studied complexes possibly due to the low positive charge in Ge compared to Sn and Pb, which decreases the electrostatic interacton with CO_2. Moreover, no significative charge transfer was observed in the reactive complex due to the large separation between the fragments (Table S1 in Supporting Information).

3.2. CO_2 Activation. Once the reactive complex **R** is formed, the structural and electronic rearrangements start to take place, driving the reduction mechanism of CO_2. It is worth to mention that reactions take place by bubbling dry CO_2 gas in the presence of complex **1** or **2** in toluene (at ambient conditions) to afford the corresponding $Ge^{(II)}$ or $Sn^{(II)}$ formates, respectively.[25,26] To take into account solvent effects, we calculated electronic and free energies in toluene at 298.15 K using the polarizable continuum model (PCM). TS structures together with selected geometrical parameters are shown in Figure 4 for the six reactions under consideration. In

DOI: 10.1021/acs.jpcc.7b00278
J. Phys. Chem. C 2017, 121, 12127−12135

all the cases, the TS forms a four-membered ring delimited by the interaction between the CO_2 molecule and the **M**−H bond. The first mechanistic event is the σ(**M**−H) bond breaking that induces the hydride transfer to the carbon atom of CO_2. The second event is the nucleophilic attack of the oxygen (O1) atom on the metal core. At this point, the C−H and **M**−O1 distances become shorter and longer, respectively, going from the front- to the back-side mechanism, while going from $Ge^{(II)}$ to $Pb^{(II)}$ both distances become longer. This is a direct consequence of the increase in the atomic radii. To analize the charge transfer from the isolated reactant to the TS geometry, the charges of the M-H bond and the CO_2 moiety were analized. It was found that a larger charge transfer is evidenced for the back-side approach than for the front-side one for each metal (Table S2 in the Supporting Information).

Activation and reaction energies, together with the predicted rate constants, are quoted in Table 1. The activation energies, $\Delta E^{\ddagger}$, (the standard Gibbs free energy of activation, $\Delta G^{\ddagger}$) for the front-side reaction, decreases monotonically when going from Ge to Pb with values of 14.8 (24.8), 8.6 (19.3), and 3.8 (13.6) kcal mol^{-1}, respectively. For the back-side pathway, these energies were found to be 13.3 (24.6), 8.7 (19.2), and 4.4 (15.7) kcal mol^{-1}, respectively. The barriers are expected to be low enough to activate CO_2 at room temperature. This result validates our computational methodology and is in agreement with recent experimental studies,[25,26,39] where the CO_2 activation proceeds even without using a cocatalyst. Notice that the difference between the activation free energies of both approaches ($\Delta\Delta G^{\ddagger}$) are 0.2, 0.1, and 2.1 kcal mol^{-1} for complexes **1**, **2**, and **3**, respectively. The former values are small enough (lower than the chemical accuracy limit of 1 kcal mol^{-1} for Ge and Sn-based catalyst) that both activation pathways are equally feasible at ambient conditions. Regarding complex **3**, the front-side approach is preferred kinetically since it is favored by 2.1 kcal mol^{-1} over **R2**. Table 1 also reveals that the entropic contribution ($\%T\Delta S^{\ddagger}$) to the activation energy is very important in all cases, almost at the same extent when both mechanisms are compared, and becoming stressed when going down in the group. It can be suggested that the entropic effects are playing a significant role in the energy barrier contributing from 41% in (1 + CO_2)@R1 until 76%(3 + CO_2)@R2.

Analogously, $\Delta E^{\ddagger}$ and ΔE° were also computed in toluene with the extended 6-311+G(d,p) basis set at the M06-2*X*/6-31G(d,p) gas phase geometries. These values are reported in Table 1. As can be seen, although the activation barrier becomes lower with the increase of the basis set and inclusion of diffuse functions (with the largest difference of 2.5 kcal mol^{-1}), the energies follow a similar trend of those obtained with the 6-31G(d,p), indicating reliability of the computed energies. The same can be concluded with reaction energies when both basis sets are compared. Thus, hereafter the reported energies were computed with the 6-31G(d,p) basis.

Finally, given the low energy barriers and relative large exothermicities obtained for reactions (3 + CO_2)@R1 and (3 + CO_2)@R2, it can be concluded that the CO_2 activation mediated by the $Pb^{(II)}$ hydride complex would be both thermodynamically and kinetically viable under mild conditions, thus being the best catalyst for CO_2 activation. Moreover, the large values of the reverse activation energies make the CO_2 releasing process less probable for the series studied, but easier for complex **3**.

In the present contribution, special attention was attributed to the heavy group 14 elements. As for Pb, there are no reports of the synthesis of a stable NacNacSiH compound. Some reports of silicon(II) monohydride include stabilizing external agents as Lewis acids or TMs that can interact with the silylene lone-pair.[27,72] Although several Si-based examples have been prepared, its use in CO_2 activation is unknown.[73] For the sake of completeness, we have computed the activation of CO_2 by using the NacNacSiH (Si*) derivative (see bottom of Table 1). Activation energies of 21.2 and 20.0 kcal mol^{-1} were found for the **R1** and **R2** pathways, respectively. Moreover, the computed reaction energies (−21.2 and −19.4 kcal mol^{-1} for **R1** and **R2**) are quite similar to those obtained for complexes **1**, **2** and **3**. The activation energies displayed in Table 1 enable us to establish the trend in reactivity of this low valent group 14 hydrides toward the CO_2 activation. This reactivity increases as the atomic radii of the metal increases. The reason for this behavior is because the Lewis acid character of the metal center increases when going down in group 14, which generates a more polar $\mathbf{M}^{\delta+}$−$H^{\delta-}$ bond that will easily promote the hydride transfer reaction. This is confirmated by the bond polarity index (BPI; ΔQ_{M-H}) values of 1.04|*e*| (Si−H), 1.15|*e*| (Ge−H), 1.40|*e*| (Sn−H), and 1.43|*e*| (Pb−H). These values indicate that Sn and Pb complexes are expected to be more reactive toward CO_2 than Si and Ge complexes. In Figure 5, the activation

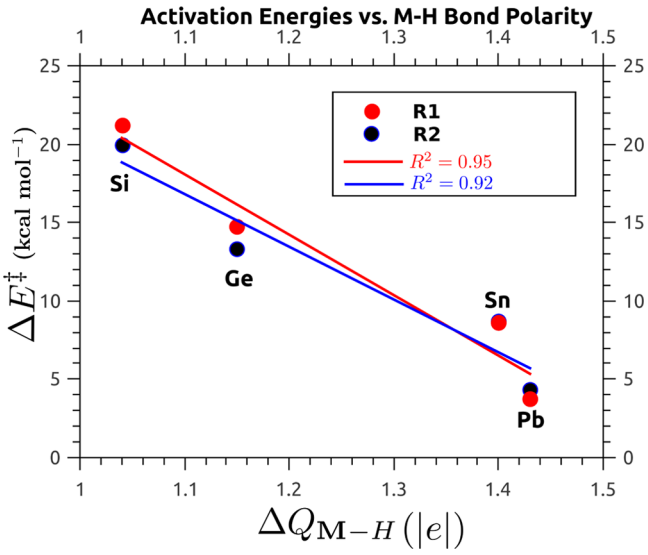

Figure 5. Linear relationship between activation energies ($\Delta E^{\ddagger}$) and bond polarity index (ΔQ_{M-H}) for complexes studied including silicon for the **R1** and **R2** pathways (**R1**, $\Delta E^{\ddagger} = -38.6\Delta Q_{M-H} + 60.5$; **R2**, $\Delta E^{\ddagger} = -33.7\Delta Q_{M-H} + 53.8$).

barriers obtained were plotted against the BPI for each reaction including silicon; it gives a clear view of the linear dependence of activation energies with the polarity of the **M**−H bond. It is interesting to note from the linear dependence of $\Delta E^{\ddagger}$ with the BPI that a barrierless reaction can be obtained when this index reaches the value of roughly 1.60|*e*|. This could be achieved tunning the polarity of the M−H bond, for example by means of electron-withdrawing groups at the vecinity of the M−H bond or by changing the polarity of the solvent. On the other hand, the same result shows that an eventual metallic behavior of $C^{(II)}$ seems difficult to be achieved for these reactions since high energy barriers would prevent it. In summary, we have provided evidence that the charge separation in the **M**−H bond seems to be responsible for the observed reactivity trend of

DOI: 10.1021/acs.jpcc.7b00278
J. Phys. Chem. C 2017, 121, 12127−12135

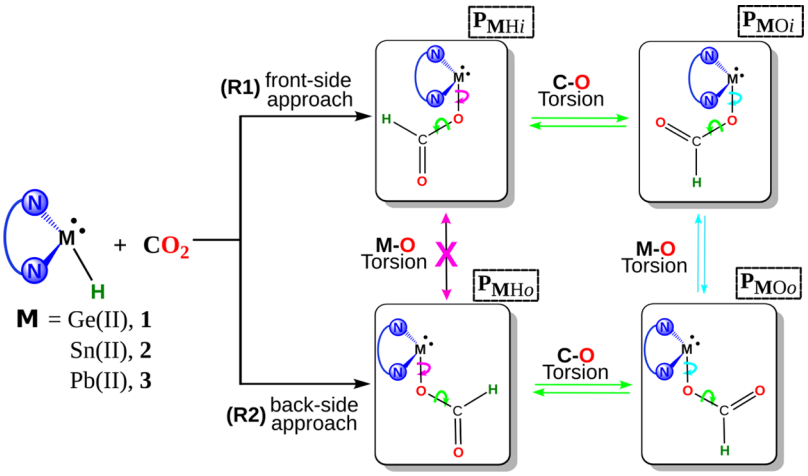

Figure 6. Representation of the conformational stereoisomers obtained as products of the reactions between complexes **1**−**3** and CO_2. The products from both approaches (**R1** and **R2**) are named $\mathbf{P}_{MHi}$ and $\mathbf{P}_{MHo}$, respectively. The free torsion around the C−O bond (green arrow) afford the more stable complexes $\mathbf{P}_{MOi}$ and $\mathbf{P}_{MOo}$, respectively. Other possible interconversions are also shown rotating the M−O bond (magenta and turquoise arrows). **M**−O torsion in magenta was found to be not possible. The bidentated NacNac ligand was schematized by connected nitrogen atoms (blue).

these catalysts toward CO_2, ordered as $Pb^{(II)}$ > $Sn^{(II)}$[26] > $Ge^{(II)}$[25] > $Si^{(II)}$.

Experimentally, addition of CO_2 to **1** initiates the reaction, the solution *slowly* changes color from red to yellow, giving place to the germanium formate,[25] whereas the same reaction using **2** *instantaneously* changes the color from yellow to colorless. The observed rates of these reactions are consistent with the computational estimated rate constants quoted in Table 1. As can be seen, reaction with **2** is four orders of magnitude faster than when complex **1** is used. As readily seen in Table 1, CO_2 activation with $Pb^{(II)}$ hydride complex is the fastest reaction in both pathways. A similar trend has been found by activation and subsequent hydroboration (using HBpin, pin = pinacolato) of bulky and unactivated carbonyl compounds by means of a low valent $Ge^{(II)}$ and $Sn^{(II)}$ catalyst.[42] It was found that hydroborations after activation of ketones is the rate-determining step, being the tin catalyzed reactions faster than those carried out using germanium. This was attributed to the polarity of the **M**−O bond that increases as the metal size increases along the group.

3.3. Conformational Stereoselectivity. For both reaction paths **R1** and **R2**, the CO_2 activation leads to the corresponding metal formates $\mathbf{P}_{MHi}$ and $\mathbf{P}_{MHo}$ (Figure 6). The notation comes from the spatial orientation of the hydride with respect to the NacNac ligand: pointing inside (H*i*) or outside (H*o*) the ligand. It was previously stablished that for complexes **1** and **2** both reaction mechanisms take place ($\Delta\Delta G^{\ddagger}$ < 0.2 kcal mol^{-1}) and thus both products are kinetically favored and equally expected to be formed (Table 1). Moreover, from the product stabilities plotted in Figures 7 and 8 (energies contain ZPE correction), for Ge and Sn the energy differences between both possible products $\mathbf{P}_{MHi}$ and $\mathbf{P}_{MHo}$ are also quite small (ΔE = 0.7 kcal mol^{-1} and ΔE = 0.2 kcal mol^{-1}, respectively) that they can be classified as almost isoenegetics (the thermal energy kT is 0.6 kcal mol^{-1} at 298 K, k stands for the Boltzmann constant). Regarding the Pb-based catalyst, the formation of the product $\mathbf{P}_{3Hi}$ is preferred under kinetic control, in view of the higher activation barrier ($\Delta\Delta G^{\ddagger}$ = 2.1 kcal mol^{-1}) computed for the **R2** pathway (Table 1). However, we will characterize both products since none of them have been reported before and in order to be consistent with the systematic study of the rotamers for both pathways along the group 14.

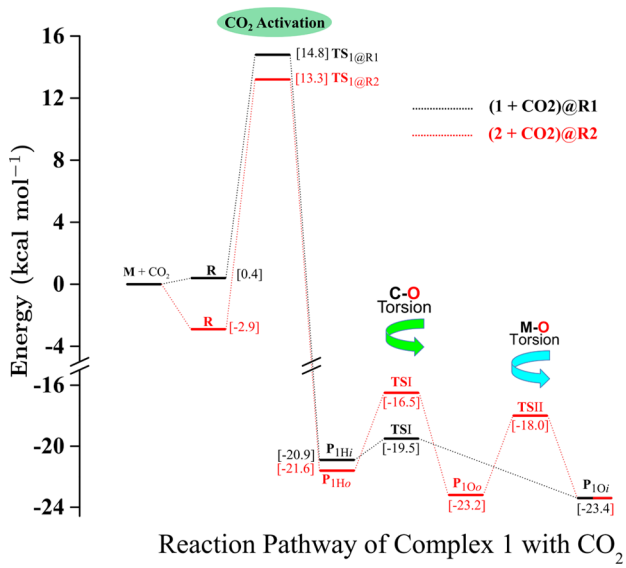

Figure 7. Potential electronic energy changes (in kcal mol^{-1}) for the front- and back-side reactions of $Ge^{(II)}$-hydride complexes (in black and red, respectively). Interconversion to different conformational stereoisomers are also shown: torsion around C−O and **M**−O bonds in green and turquoise arrows, respectively. Note that displayed values are relative to the **M** + CO_2 isolated reactants. All energies are given in kcal mol^{-1}, computed in toluene and corrected with zero point energies.

The crystallographic structure reported for the reaction between **1** and CO_2 corresponds to the $\mathbf{P}_{1Ho}$,[25] which comes from **R2** pathway. Although it is well-known that most of the crystal structures differ from the lowest energy conformations,[74] the existence of $\mathbf{P}_{1Ho}$ agrees well with our computations: $\mathbf{P}_{1Ho}$ is slightly stabilized compared to $\mathbf{P}_{1Hi}$ in 0.7 kcal mol^{-1}. This means that a mixture composed by a 77% $\mathbf{P}_{1Ho}$ and 23% $\mathbf{P}_{1Hi}$ will coexist in toluene solution at ambient temperature, in accordance with a standard Boltzmann distribution. It is worth to mention that taking into account rather low barriers of

DOI: 10.1021/acs.jpcc.7b00278
J. Phys. Chem. C 2017, 121, 12127−12135

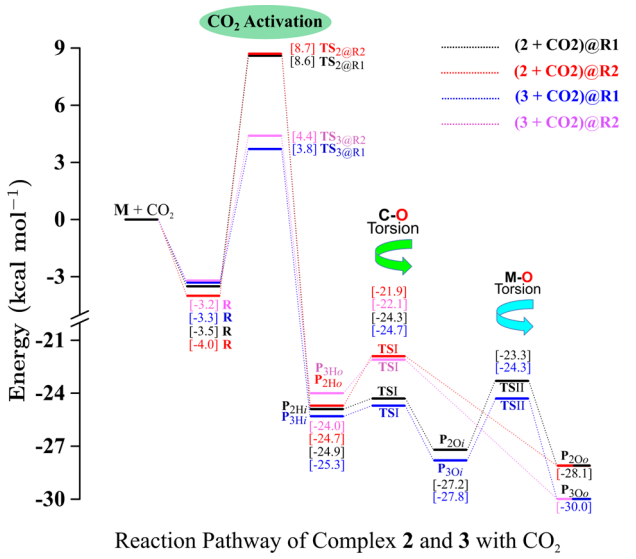

Figure 8. Potential electronic energy changes (in kcal mol^{-1}) for the front- and back-side reactions of Sn$^{(II)}$- (in black and red, respectively) and Pb$^{(II)}$-hydride complexes (in blue and pink, respectively) with CO_2. Interconversion to different conformational stereoisomers are also shown: torsion around C−O and **M**−O bonds in green and turquoise arrows, respectively. Note that displayed values are relative to the **M** + CO_2 isolated reactants. All energies are given in kcal mol^{-1}, computed in toluene and corrected with zero point energies.

conformational interconversions for the **P1** isomers (Figure 7), it should be expected that the mixture be also composed by $\mathbf{P}_{1Oo}$ and $\mathbf{P}_{1Oi}$.

Takagi and Sakaki have reported $\mathbf{P}_{1Ho}$ as the only product of both approaches, in apparent contradiction with our findings.[44] This result prompted us to perform a conformational study with the aim of connecting the obtained conformers. In this context, it was studied the rotation of the **M**−O bond, finding that **R1** and **R2** are not connected through the rotation of the **M**−O bond since the steric hindrance presented by the bulky aryl groups (2,6-iPr$_2$C$_6$H$_3$) of the NacNac prevents the straightforward interconversion between $\mathbf{P}_{1Hi}$ and $\mathbf{P}_{1Ho}$. Instead, a new set of conformers was found: $\mathbf{P}_{MOi}$ and $\mathbf{P}_{MOo}$ (labeled in accordance with spatial orientation of the carbonyl oxygen with respect to the NacNac ligand). These rotamers arise from the restricted rotation of the C−O bond and are also quoted in Figures 7 and 8.

The computed relative stabilities of the new "*inside*" rotamers $\mathbf{P}_{MOi}$ are enhanced by 2.5 (Ge), 2.3 (Sn), and 2.5 (Pb) kcal mol^{-1} with respect to the $\mathbf{P}_{MHi}$ rotamers; while the "*outside*" $\mathbf{P}_{MOo}$ are 1.6 (Ge), 3.4 (Sn) and 6.0 (Pb) kcal mol^{-1} more stable than their $\mathbf{P}_{MHo}$ conformers. Thus, all the rotamers that can be interconverted are very thermodynamically favored once the CO_2 reduction is carried out. Moreover, $\mathbf{P}_{2Oi}$ and $\mathbf{P}_{3Oi}$ conformers are obtained from barrierless rotations (0.6 kcal mol^{-1}). The crystal structure reported for the stannylene formate corresponds to the conformational stereoisomer $\mathbf{P}_{2Oo}$,[26] which our calculations confirm as the most stable isomer. Finally, Figure 8 evidence that our theoretically predicted plumbylene formates, $\mathbf{P}_{3Oi}$ and $\mathbf{P}_{3Oo}$, are more stable than their germylene and stannylene analogues being $\mathbf{P}_{3Oo}$ the most stable among all conformers. Therefore, this thermodynamic driving force reinforces our above-mentioned result that lead(II) hydride complex seems to be a more convenient alternative for CO_2 activation than the other congeners in the 14 group.

4. CONCLUSIONS

The CO_2 activation mechanism by low-valent Ge$^{(II)}$, Sn$^{(II)}$ and Pb$^{(II)}$ hydride complexes bearing a bidentate β-diketiminate (NacNac) ligand was studied in detail by DFT calculations. In general, it was found that as the reactants approach each other, the steric hindrance of the bulky aryl groups (2,6-iPr$_2$C$_6$H$_3$) of the ligand leads to two different transition states close in energy. Indeed, both reaction pathways were found to be feasible under mild conditions yielding the respective products of activation, except for Pb where **R1** was kinetically favored over **R2**. According to the computed activation and reaction energies along with the rate constants, the Pb based complex is by far the most reactive toward CO_2, followed in order by Sn, Ge, and Si analogues. This is a direct consequence of the enhanced polar character of the M−H bond, more Lewis acidic metal center, as the atomic radii of the metal increases when going down group 14. To validate this result, it was found a linear dependence between the polarity of the **M**−H bond and the activation energies for the reaction studied, including those by using a silicon(II) analogue. Even though, a low valent Pb formate has not been reported to date, different conformational isomers of plumbylene formate were characterized and are predicted to be extremely stable in toluene at room temperature. Indeed, the formation of these conformers is thermodynamically and kinetically favored with respect to Sn and Ge analogues. In summary, the computational study carried out herein proposes a lead(II) hydride complex as a more convenient alternative for CO_2 activation than the experimentally used germanium(II) and tin(II) hydride catalysts. Furthermore, the trend in reactivity found here will certainly help with a faster development in main group chemistry.

■ ASSOCIATED CONTENT

Supporting Information

The Supporting Information is available free of charge on the ACS Publications website at DOI: 10.1021/acs.jpcc.7b00278.

Charge transfer at selected points, gas phase energies, comparison between obtained X-ray and theoretical data and Cartesian coordinates for all structures (PDF)

■ AUTHOR INFORMATION

Corresponding Author

*E-mail: atola@uc.cl.

ORCID

Nery Villegas-Escobar: 0000-0002-6370-617X
Diego Cortés-Arriagada: 0000-0002-6709-1723
Diana Yepes: 0000-0003-4211-7162
Alejandro Toro-Labbé: 0000-0001-9906-2153

Notes

The authors declare no competing financial interest.

■ ACKNOWLEDGMENTS

Authors gratefully acknowledge referees' comments that helped to enrich this work. The authors are thankful for the financial support of the Nucleus Millenium "Chemical Processes and Catalysis" NC 120082 and FONDECYT Grant No. 1141098. N.V.-E and D.E.O. acknowledge CONICYT Ph.D. fellowship. D.C.-A. and D.Y acknowledge FONDECYT through Projects

DOI: 10.1021/acs.jpcc.7b00278
J. Phys. Chem. C 2017, 121, 12127−12135

No. 3140314 and 3150249, respectively. R.D. acknowledges VRI-PUC fellowship.

■ REFERENCES

(1) Piccot, S. D.; Watson, J. J.; Jones, J. W. A Global Inventory of Volatile Organic Compound Emissions from Anthropogenic Sources. *J. Geophys. Res. Atmos* **1992**, *97*, 9897−9912.

(2) United States Enviromental Protection Agency (EPA). *Overview of Greenhouse Gases*; http://www.epa.gov/climatechange/science/overview.html, 2015.

(3) Falkowski, P.; Scholes, R.; Boyle, E. e. a.; Canadell, J.; Canfield, D.; Elser, J.; Gruber, N.; Hibbard, K.; Högberg, P.; Linder, S. The Global Carbon Cycle: A Test of our Knowledge of Earth as a System. *Science* **2000**, *290*, 291−296.

(4) Lal, R. Sequestration of Atmospheric CO_2 in Global Carbon Pools. *Energy Environ. Sci.* **2008**, *1*, 86−100.

(5) Huang, K.; Sun, C.-L.; Shi, Z.-J. Transition-Metal-Catalyzed C-C Bond Formation Through the Fixation of Carbon Dioxide. *Chem. Soc. Rev.* **2011**, *40*, 2435−2452.

(6) Sakakura, T.; Choi, J.-C.; Yasuda, H. Transformation of Carbon Dioxide. *Chem. Rev.* **2007**, *107*, 2365−2387.

(7) Aresta, M. *Carbon Dioxide as Chemical Feedstock*; John Wiley & Sons, 2010.

(8) Darensbourg, D. J. Making Plastics from Carbon Dioxide: Salen Metal Complexes as Catalysts for the Production of Polycarbonates from Epoxides and CO_2. *Chem. Rev.* **2007**, *107*, 2388−2410.

(9) Sakakura, T.; Kohno, K. The Synthesis of Organic Carbonates from Carbon Dioxide. *Chem. Commun.* **2009**, 1312−1330.

(10) Boogaerts, I. I.; Nolan, S. P. Carboxylation of C-H Bonds Using N-Heterocyclic Carbene Gold (I) Complexes. *J. Am. Chem. Soc.* **2010**, *132*, 8858−8859.

(11) Boogaerts, I. I.; Fortman, G. C.; Furst, M. R.; Cazin, C. S.; Nolan, S. P. Carboxylation of N-H/C-H Bonds Using N-Heterocyclic Carbene Copper (I) Complexes. *Angew. Chem., Int. Ed.* **2010**, *49*, 8674−8677.

(12) Holbrey, J. D.; Reichert, W. M.; Tkatchenko, I.; Bouajila, E.; Walter, O.; Tommasi, I.; Rogers, R. D. 1, 3-Dimethylimidazolium-2-Carboxylate: The Unexpected Synthesis of an Ionic Liquid Precursor and Carbene-CO_2 Adduct. *Chem. Commun.* **2003**, 28−29.

(13) Duong, H. A.; Tekavec, T. N.; Arif, A. M.; Louie, J. Reversible Carboxylation of N-Heterocyclic Carbenes. *Chem. Commun.* **2004**, 112−113.

(14) Gaillard, S.; Slawin, A. M.; Nolan, S. P. A N-Heterocyclic Carbene Gold Hydroxide Complex: A Golden Synthon. *Chem. Commun.* **2010**, *46*, 2742−2744.

(15) Zhang, L.; Cheng, J.; Ohishi, T.; Hou, Z. Copper-Catalyzed Direct Carboxylation of C-H Bonds with Carbon Dioxide. *Angew. Chem.* **2010**, *122*, 8852−8855.

(16) Kayaki, Y.; Yamamoto, M.; Ikariya, T. N-Heterocyclic Carbenes as Efficient Organocatalysts for CO_2 Fixation Reactions. *Angew. Chem.* **2009**, *121*, 4258−4261.

(17) Zhou, H.; Zhang, W.-Z.; Wang, Y.-M.; Qu, J.-P.; Lu, X.-B. N-Heterocyclic Carbene Functionalized Polymer for Reversible Fixation-Release of CO_2. *Macromolecules* **2009**, *42*, 5419−5421.

(18) Lo, R.; Ganguly, B. Efficacy of Carbenes for CO_2 Chemical Fixation and Activation by their Superbasicity/Alcohol: A DFT Study. *New J. Chem.* **2012**, *36*, 2549−2554.

(19) Beyzavi, M. H.; Klet, R. C.; Tussupbayev, S.; Borycz, J.; Vermeulen, N. A.; Cramer, C. J.; Stoddart, J. F.; Hupp, J. T.; Farha, O. K. A Hafnium-Based Metal-Organic Framework as an Efficient and Multifunctional Catalyst for Facile CO_2 Fixation and Regioselective and Enantioretentive Epoxide Activation. *J. Am. Chem. Soc.* **2014**, *136*, 15861−15864.

(20) Vummaleti, S. V.; Talarico, G.; Nolan, S. P.; Cavallo, L.; Poater, A. How easy is CO_2 Fixation by M-C Bond Containing Complexes (M= Cu, Ni, Co, Rh, Ir)? *Org. Chem. Front.* **2016**, *3*, 19−23.

(21) Beccalli, E. M.; Broggini, G.; Martinelli, M.; Sottocornola, S. C-C C-O C-N Bond Formation on sp^2 Carbon by Pd(II)-Catalyzed Reactions Involving Oxidant Agents. *Chem. Rev.* **2007**, *107*, 5318−5365.

(22) Chin, C. S.; Won, G.; Chong, D.; Kim, M.; Lee, H. Carbon-Carbon Bond Formation Involving Reactions of Alkynes with Group 9 Metals (Ir, Rh, Co): Preparation of Conjugated Olefins. *Acc. Chem. Res.* **2002**, *35*, 218−225.

(23) Doyle, M. P.; Duffy, R.; Ratnikov, M.; Zhou, L. Catalytic Carbene Insertion into C-H Bonds. *Chem. Rev.* **2010**, *110*, 704−724.

(24) Chianese, A. R.; Lee, S. J.; Gagne, M. R. Electrophilic Activation of Alkenes by Platinum (II): So Much More than a Slow Version of Palladium (II). *Angew. Chem., Int. Ed.* **2007**, *46*, 4042−4059.

(25) Jana, A.; Ghoshal, D.; Roesky, H. W.; Objartel, I.; Schwab, G.; Stalke, D. A Germanium (II) Hydride as an Effective Reagent for Hydrogermylation Reactions. *J. Am. Chem. Soc.* **2009**, *131*, 1288−1293.

(26) Jana, A.; Roesky, H. W.; Schulzke, C.; Döring, A. Reactions of Tin (II) Hydride Species with Unsaturated Molecules. *Angew. Chem., Int. Ed.* **2009**, *48*, 1106−1109.

(27) Stoelzel, M.; Präsang, C.; Inoue, S.; Enthaler, S.; Driess, M. Hydrosilylation of Alkynes by $Ni(CO)_3$-Stabilized Silicon (II) Hydride. *Angew. Chem., Int. Ed.* **2012**, *51*, 399−403.

(28) Chen, M.; Fulton, J. R.; Hitchcock, P. B.; Johnstone, N. C.; Lappert, M. F.; Protchenko, A. V. Synthesis and Theoretical Studies on Rare Three-Coordinate Lead Complexes. *Dalton Trans.* **2007**, 2770−2778.

(29) Tam, E. C.; Coles, M. P.; Smith, J. D.; Fulton, J. R. The Steric Influence of β-Diketiminato Ligands on the Coordination Chemistry of Lead (II). *Polyhedron* **2015**, *85*, 284−294.

(30) Fulton, J. R.; Hitchcock, P. B.; Johnstone, N. C.; Tam, E. C. The Synthesis of Monomeric Terminal Lead Aryloxides: Dependence on Reagents and Conditions. *Dalton Trans.* **2007**, 3360−3362.

(31) Harris, L. A.-M.; Tam, E. C.; Coles, M. P.; Fulton, J. R. Lead and Tin β-Diketiminato Amido/Anilido Complexes: Competitive Nucleophilic Reactivity at the β-Diketiminato γ-Carbon. *Dalton Trans.* **2014**, *43*, 13803−13814.

(32) Yao, S.; Block, S.; Brym, M.; Driess, M. A New Type of Heteroleptic Complex of Divalent Lead and Synthesis of the Plumbyleniophosphasilene, R_2Si = P-Pb(L):(L= β-diketiminate). *Chem. Commun.* **2007**, 3844−3846.

(33) Tam, E. C.; Johnstone, N. C.; Ferro, L.; Hitchcock, P. B.; Fulton, J. R. Carbon Dioxide Activation by Non-nucleophilic Lead Alkoxides. *Inorg. Chem.* **2009**, *48*, 8971−8976.

(34) Jana, A.; Sarish, S. P.; Roesky, H. W.; Schulzke, C.; Doring, A.; John, M. Facile Access of Well-Defined Stable Divalent Lead Compounds with Small Organic Substituents. *Organometallics* **2009**, *28*, 2563−2567.

(35) Ferro, L.; Hitchcock, P. B.; Coles, M. P.; Cox, H.; Fulton, J. R. Activation of Carbon Dioxide by Divalent Tin Alkoxides Complexes. *Inorg. Chem.* **2011**, *50*, 1879−1888.

(36) Asay, M.; Jones, C.; Driess, M. N-Heterocyclic Carbene Analogues with Low-Valent Group 13 and Group 14 Elements: Syntheses, Structures, and Reactivities of a New Generation of Multitalented Ligands. *Chem. Rev.* **2011**, *111*, 354−396.

(37) Chu, T.; Korobkov, I.; Nikonov, G. I. Oxidative Addition of σ Bonds to an Al (I) Center. *J. Am. Chem. Soc.* **2014**, *136*, 9195−9202.

(38) Jones, C.; Junk, P. C.; Platts, J. A.; Stasch, A. Four-Membered Group 13 Metal (I) N-Heterocyclic Carbene Analogues: Synthesis, Characterization, and Theoretical Studies. *J. Am. Chem. Soc.* **2006**, *128*, 2206−2207.

(39) Mandal, S. K.; Roesky, H. W. Group 14 Hydrides with Low Valent Elements for Activation of Small Molecules. *Acc. Chem. Res.* **2012**, *45*, 298−307.

(40) Villegas-Escobar, N.; Gutiérrez-Oliva, S.; Toro-Labbé, A. Catalytic Mechanism of H_2 Activation by a Carbenoid Aluminum Complex. *J. Phys. Chem. C* **2015**, *119*, 26598−26604.

(41) Power, P. P. Main-Group Elements as Transition Metals. *Nature* **2010**, *463*, 171−177.

(42) Hadlington, T. J.; Hermann, M.; Frenking, G.; Jones, C. Low Coordinate Germanium (II) and Tin (II) Hydride Complexes:

DOI: 10.1021/acs.jpcc.7b00278
J. Phys. Chem. C 2017, 121, 12127−12135

Efficient Catalysts for the Hydroboration of Carbonyl Compounds. *J. Am. Chem. Soc.* **2014**, *136*, 3028−3031.
(43) Yao, S.; Xiong, Y.; Driess, M. Zwitterionic and Donor-Stabilized N-Heterocyclic Silylenes (NHSis) for Metal-Free Activation of Small Molecules. *Organometallics* **2011**, *30*, 1748−1767.
(44) Takagi, N.; Sakaki, S. Theoretical Study of Reactivity of Ge (II)-Hydride Compound: Comparison with Rh (I)-Hydride Complex and Prediction of Full Catalytic Cycle by Ge (II)-hydride. *J. Am. Chem. Soc.* **2013**, *135*, 8955−8965.
(45) Zhao, Y.; Truhlar, D. G. The M06 Suite of Density Functionals for Main Group Thermochemistry, Thermochemical Kinetics, Noncovalent Interactions, Excited States, and Transition Elements: Two New Functionals and Systematic Testing of Four M06-Class Functionals and 12 Other Functionals. *Theor. Chem. Acc.* **2008**, *120*, 215−241.
(46) Zhao, Y.; Truhlar, D. G. Exploring the Limit of Accuracy of the Global Hybrid Meta Density Functional for Main-Group Thermochemistry, Kinetics, and Noncovalent Interactions. *J. Chem. Theory Comput.* **2008**, *4*, 1849−1868.
(47) Valero, R.; Costa, R.; de P. R. Moreira, I.; Truhlar, D. G.; Illas, F. Performance of the M06 Family of Exchange-Correlation Functionals for Predicting Magnetic Coupling in Organic and Inorganic Molecules. *J. Chem. Phys.* **2008**, *128*, 114103.
(48) Hay, P. J.; Wadt, W. R. Ab Initio Effective Core Potentials for Molecular Calculations. Potentials for K to Au Including the Outermost Core Orbitals. *J. Chem. Phys.* **1985**, *82*, 299−310.
(49) Dill, J. D.; Pople, J. A. Self-Consistent Molecular Orbital Methods. XV. Extended Gaussian-Type Basis Sets for Lithium, Beryllium, and Boron. *J. Chem. Phys.* **1975**, *62*, 2921−2923.
(50) Francl, M. M.; Pietro, W. J.; Hehre, W. J.; Binkley, J. S.; Gordon, M. S.; Defrees, D. J.; Pople, J. A. Self-Consistent Molecular Orbital Methods. XXIII. A Polarization-Type Basis Set for Second-Row Elements. *J. Chem. Phys.* **1982**, *77*, 3654−3665.
(51) Scott, A. P.; Radom, L. Harmonic Vibrational Frequencies: An Evaluation of Hartree-Fock, Møller-Plesset, Quadratic Configuration Interaction, Density Functional Theory, and Semiempirical Scale Factors. *J. Phys. Chem.* **1996**, *100*, 16502−16513.
(52) Schlegel, H. B. Optimization of Equilibrium Geometries and Transition Structures. *J. Comput. Chem.* **1982**, *3*, 214−218.
(53) Schlegel, H. B. Optimization of Equilibrium Geometries and Transition Structures. *Adv. Chem. Phys.* **2009**, *67*, 249.
(54) Fukui, K. The Path of Chemical Reactions-The IRC Approach. *Acc. Chem. Res.* **1981**, *14*, 363−368.
(55) Hratchian, H. P.; Schlegel, H. B. Accurate Reaction Paths Using a Hessian Based Predictor-Corrector Integrator. *J. Chem. Phys.* **2004**, *120*, 9918−9924.
(56) Hratchian, H. P.; Schlegel, H. B. Using Hessian Updating to Increase the Efficiency of a Hessian Based Predictor-Corrector Reaction Path Following Method. *J. Chem. Theory Comput.* **2005**, *1*, 61−69.
(57) Tomasi, J.; Mennucci, B.; Cammi, R. Quantum Mechanical Continuum Solvation Models. *Chem. Rev.* **2005**, *105*, 2999−3094.
(58) Frisch, M. J.; Trucks, G. W.; Schlegel, H. B.; Scuseria, G. E.; Robb, M. A.; Cheeseman, J. R.; Scalmani, G.; Barone, V.; Mennucci, B.; Petersson, G. A. et al. *Gaussian 09*, Revision B.01; Gaussian Inc.: Wallingford, CT, 2009.
(59) Lu, T.; Chen, F. Multiwfn: A Multifunctional Wavefunction Analyzer. *J. Comput. Chem.* **2012**, *33*, 580−592.
(60) Reed, A. E.; Curtiss, L. A.; Weinhold, F. Intermolecular Interactions from a Natural Bond Orbital, Donor-Acceptor Viewpoint. *Chem. Rev.* **1988**, *88*, 899−926.
(61) Taylor, M. J.; Coakley, E. J.; Coles, M. P.; Cox, H.; Fulton, J. R. *β*-Diketiminato Organolead Complexes: Structures, ^{207}Pb NMR, and Hammett Correlations. *Organometallics* **2015**, *34*, 2515−2521.
(62) Pauling, L. The Nature of the Chemical Bond. IV. The Energy of Single Bonds and the Relative Electronegativity of Atoms. *J. Am. Chem. Soc.* **1932**, *54*, 3570−3582.
(63) Pauling, L. *The Nature of the Chemical Bond and the Structure of Molecules and Crystals: An Introduction to Modern Structural Chemistry*; Cornell University Press, 1960; Vol. *18*.
(64) Morell, C.; Grand, A.; Toro-Labbé, A. New Dual Descriptor for Chemical Reactivity. *J. Phys. Chem. A* **2005**, *109*, 205−212.
(65) Morell, C.; Grand, A.; Toro-Labbé, A. Theoretical support for using the Δf (r) descriptor. *Chem. Phys. Lett.* **2006**, *425*, 342−346.
(66) Fievez, T.; Sablon, N.; De Proft, F.; Ayers, P. W.; Geerlings, P. Calculation of Fukui functions without differentiating to the number of electrons. 3. Local Fukui function and dual descriptor. *J. Chem. Theory Comput.* **2008**, *4*, 1065−1072.
(67) Morell, C.; Ayers, P. W.; Grand, A.; Gutiérrez-Oliva, S.; Toro-Labbé, A. Rationalization of Diels-Alder reactions through the use of the dual reactivity descriptor Δ f (r). *Phys. Chem. Chem. Phys.* **2008**, *10*, 7239−7246.
(68) Chamorro, E.; Perez, P.; Duque, M.; De Proft, F.; Geerlings, P. Dual descriptors within the framework of spin-polarized density functional theory. *J. Chem. Phys.* **2008**, *129*, 064117.
(69) Geerlings, P.; Ayers, P. W.; Toro-Labbé, A.; Chattaraj, P. K.; De Proft, F. The Woodward-Hoffmann Rules Reinterpreted by Conceptual Density Functional Theory. *Acc. Chem. Res.* **2012**, *45*, 683−695.
(70) Tognetti, V.; Morell, C.; Ayers, P. W.; Joubert, L.; Chermette, H. A Proposal for an Extended Dual Descriptor: A Possible Solution When Frontier Molecular Orbital Theory Fails. *Phys. Chem. Chem. Phys.* **2013**, *15*, 14465−14475.
(71) De Proft, F.; Forquet, V.; Ourri, B.; Chermette, H.; Geerlings, P.; Morell, C. Investigation of Electron Density Changes at the Onset of a Chemical Reaction Using the State-Specific Dual Descriptor from Conceptual Density Functional Theory. *Phys. Chem. Chem. Phys.* **2015**, *17*, 9359−9368.
(72) Jana, A.; Leusser, D.; Objartel, I.; Roesky, H. W.; Stalke, D. A Stable Silicon (II) Monohydride. *Dalton Trans.* **2011**, *40*, 5458−5463.
(73) Blom, B.; Driess, M. *Functional Molecular Silicon Compounds II*; Springer, 2013; pp 85−123.
(74) Verdal, N.; Wilke, J. J.; Hudson, B. S. Conformational Distinguishability of Medium Cycloalkanes in Crystals via Inelastic Neutron Scattering. *J. Phys. Chem. A* **2006**, *110*, 2639−2646.

DOI: 10.1021/acs.jpcc.7b00278
J. Phys. Chem. C 2017, 121, 12127−12135